

NUNO MIGUEL MAGALHÃES DOURADO

***R*-Curve behaviour and size effect
of a quasibrittle material: Wood**

UNIVERSIDADE DE TRÁS-OS-MONTES E ALTO DOURO

THESIS

SUBMITTED TO

**UNIVERSIDADE DE TRÁS-OS-MONTES
E ALTO DOURO (UTAD)**

and

UNIVERSITÉ BORDEAUX I (UB1)

(under Tutorship)

By Mr. **Nuno DOURADO**

TO GET THE DEGREE OF

Doctor of Philosophy

Speciality: Mechanics

***R*-Curve behaviour and size effect
of a quasibrittle material: Wood**

Under supervision of

Mr. GÉRARD VALENTIN (Professor)
Mr. MARCELO de MOURA (Professor)

According to the
Convention de Cotutelle Internationale de Thèse
Signed on 14th November 2005 by

Mr. Armando Mascarenhas Ferreira	(Reitor UTAD)
Mr. Francis HARDOUIN	(Président de l'UB1)
Mr. Gérard Valentin	(Directeur de Thèse en France)
Mr. Marcelo de Moura	(Directeur de Thèse au Portugal)
Mr. Nuno Dourado	(PhD Student)

-- 2008 --

Este trabalho foi expressamente elaborado com vista
à obtenção do grau de Doutor em Ciências de Engenharia,
de acordo com o disposto no Decreto de Lei nº 216/92, de 31 de Outubro

Resumo

O trabalho apresentado nesta Tese de Doutorado é constituído por uma parte experimental, uma parte numérica e uma parte analítica, com o propósito de estudar o comportamento evidenciado pelo desenvolvimento de uma curva de *Resistência* e o efeito de escala em estruturas de madeira pré-entalhadas, sujeitas a fractura em Modo I. Os resultados providenciados pelos ensaios mecânicos são combinados com análises numéricas realizadas por Elementos Finitos (EF), no sentido de avaliar propriedades de fractura, recorrendo a um procedimento equivalente da Teoria da Mecânica da Fractura Linear Elástica (LEFM), baseado na flexibilidade da estrutura, e a um Algoritmo Genético. A curva de Resistência (curva-*R*), determinada a partir dos ensaios mecânicos, evidencia o desenvolvimento da Zona de Processo de Fractura (FPZ), que ocorre na frente de fenda, durante o processo de propagação. A taxa de libertação de energia de fractura, dada pela curva-*R*, exhibe, numa primeira fase, uma tendência crescente, convergindo continuamente para uma assíntota horizontal (patamar), à medida que o comprimento de fenda aumenta. Este patamar define a taxa crítica de libertação de energia de fractura (modo I), que constitui uma propriedade coesiva útil para reproduzir numericamente (modelação por EF) o processo de propagação da fenda. Assim, escolhida que seja a geometria da estrutura a analisar, bem como o modelo de dano a utilizar na simulação do processo de propagação da fenda, torna-se possível monitorizar o desenvolvimento da zona coesiva, equivalente à dimensão da FPZ (real), em função do comprimento de fenda equivalente. Os resultados decorrentes da modelação por EF da propagação da fenda, para além de dependerem do material simulado, revelam que a dimensão crítica da zona coesiva está associada ao início do patamar da curva-*R*. Esta observação permite especular quanto à exactidão na medição da taxa crítica de libertação de energia de fractura, em qualquer material quase-frágil, na medida em que a avaliação desta propriedade de fractura requer a constatação prévia de que a dimensão crítica evidenciada pela zona coesiva, permanece inalterada ao longo de um comprimento de fenda (equivalente) suficientemente extenso (estado de propagação auto-semelhante). Decorre deste ponto, a necessidade de observar atentamente a dependência da extensão da zona coesiva com a dimensão característica da estrutura, vulgo extensão do ligamento, na medida em que a modelação por EF revela a existência de uma dimensão crítica, abaixo da qual é impossível obter taxas críticas de libertação

de energia. A modelação da fenda por EF põe em evidência que a curva- R não depende da dimensão característica da estrutura, para uma dada geometria.

Surge a este propósito, o estudo do efeito de escala, no contexto de uma análise assintótica, recorrendo a um procedimento analítico, que tem por base a constatação de que a curva- R é única. Discute-se se o comprimento de fenda equivalente associado à carga máxima depende ou não da dimensão característica da estrutura. Da mesma forma, analisa-se a evolução da taxa de libertação de energia associada à carga máxima, quando a dimensão da estrutura aumenta. Atendendo a que a lei de efeito de escala de Bažant (SEL), determina a evolução da resistência nominal para estruturas de dimensão intermédia, a partir do ajuste assintótico efectuado a partir dos regimes previstos pela Teoria da Resistência de Materiais e pela LEFM, deve questionar-se se não seria mais exacto deduzir, para o regime intermédio, um regime adimensional assintótico baseado na curva- R determinada experimentalmente.

O conjunto de questões levantadas no parágrafo anterior, respeitantes ao comportamento evidenciado pelo material, suscitou a realização de ensaios mecânicos em estruturas geometricamente semelhantes, de dimensão diferente. Este estudo de efeito de escala envolveu a realização de ensaios mecânicos em estruturas de dimensão não desprezível, pelo que se justificou o desenvolvimento de um procedimento que visasse a compensação do peso próprio.

O tratamento estatístico, envolvendo os resultados experimentais obtidos nos ensaios de fractura (Modo I), providencia a informação necessária para confirmar a existência de uma curva- R única, para uma espécie de madeira correntemente utilizada em construção civil. Assim, o efeito de escala evidenciado pela resistência nominal da estrutura, em particular aquele que cobre a gama de dimensões características intermédias, pode então possibilitar a avaliação do regime adimensional assintótico baseado na curva- R (única) experimental. Este regime assintótico representa a transição exacta entre os regimes previstos pela Teoria da Resistência de Materiais, e pela LEFM, quando analisado de um ponto de vista energético. A evolução da resistência nominal da estrutura, baseada em informação experimental, constituir-se-á sob a forma de um domínio (ou envelope de tendência) em função da dimensão característica da estrutura (gráfico bi-logarítmico).

Abstract

This Thesis concerns the mechanical testing, numerical analysis and cohesive modelling of fracture (Mode I) on the purpose to study the *Resistance*-curve behaviour and the size effect in wooden notched structures in its unmodified form. The mechanical testing is combined with the numerical analysis to evaluate fracture properties by means of an equivalent LEFM approach based on the structure compliance. The *Resistance*-curve being revealed from the experiments puts into evidence that a non-negligible damaged domain (Fracture Process Zone) is under development in the crack front during the loading process. Additionally, it is possible to investigate if the raise of the energy release rate, necessary to initiate the crack propagation, is likely to reveal an asymptotic behaviour (plateau). This being the case, among other fracture parameters issued from the *Resistance*-curve, the critical (asymptotic) energy release rate is determined, turning possible to use it in combination with other cohesive crack properties in the crack modelling (in Mode I). Thus, for a given geometry it is feasible to monitor the critical dimension being revealed by the Fracture Process Zone (FPZ) during the crack propagation. Furthermore, the analyses may reveal that this critical extent depend on the material used in the numerical simulation. Thus, one can speculates that the accurate evaluation of the critical energy release rate in any material is subjected to the condition that the FPZ extent stays unaffected during a sufficiently large crack extension. Another subject which merits attention concerns the dependence of the FPZ extent with the structure size being analysed in the cohesive modelling, since a lower characteristic dimension ought to outcome from the numerical study, thus permitting to define a critical ligament length valid for a given geometry. The cohesive crack modelling is also likely to provide the evidence that the *Resistance*-curve is not dependent of the structure size being considered in the analysis.

The foreknowledge developments just described envisage that the *Resistance*-curve is unique, turning consequent the analysis of the size effect on an energy based asymptotic analysis, thus making use of an analytical development procedure. Accordingly, one can argue whether the relative crack length at the peak load depends or not on the characteristic structure size. In a like manner, a similar query might be addressed concerning the trend exhibited by energy release rate at the peak load with the increase in the structure size. As the predictions provided by the Bažant's size effect law

(SEL) are accomplished on the fitting basis of both the Strength Theory and the Linear Elastic Fracture Mechanics (LEFM) asymptotic regimes, one might wonder if the nominal strength in the intermediate size range would not be defined through an additional dimensionless asymptotic regime based on the evaluated *Resistance*-curve.

The above cited predictions involving the material behaviour somehow rouse the inevitable mechanical testing on geometrically similar structures of different sizes. With the required size effect study bringing about the mechanical testing of structures exhibiting non-negligible sizes, the self-weight is very likely to induce the results. This being observed, a self-weight compensation method turns crucial in the treatment of the experimental data.

The statistical handling issued by the fracture (Mode I) experiments, involving geometrically structures of different sizes, might provide the essentials to conclude for the unique *Resistance*-curve in a given wood species used in timber construction. The scaling of the nominal strength is then possible to perform for a set of tested characteristic sizes, spanning the predictions yield by the Strength Theory and LEFM. The accurate definition of the intermediate size regime is thus possible to achieve, sufficing that the *R*-curve is known for a given specimen geometry.

Résumé

Le travail détaillé de cette Thèse de Doctorat, est composé en partie par un travail expérimental, numérique et analytique. La dernière partie est présentée avec la proposition d'étudier le comportement qui met en évidence le développement d'une courbe de *Résistance*, et l'effet d'échelle, en charpentes de bois massif entaillé (Mode I de rupture). Les résultats, fournis par des essais mécaniques, sont combinés avec les analyses numériques réalisées par la Méthode des Éléments Finis (MEF), dans le but d'évaluer les propriétés mécaniques de rupture. Ceci est réalisé par une approche équivalente de la Mécanique de la Rupture Linéaire Élastique (Linear Elastic Fracture Mechanics : LEFM), basée par la flexibilité de la structure. Pour ceci, un Algorithme Génétique a été implémenté et testé. La courbe de *Résistance* (courbe-*R*), déterminée à partir des essais mécaniques expérimentaux, met en évidence le développement de la Zone de Rupture (Fracture Process Zone : FPZ), qui s'étend en fond de fissure au cours du processus de propagation. Dans une première phase, le taux de restitution d'énergie de rupture montre une tendance croissante, progressant vers une asymptote horizontale (*plateau*) avec la longueur de fissure. Ce *plateau* détermine la valeur critique du taux de restitution d'énergie de rupture (Mode I) utilisée comme une propriété cohésive nécessaire à la modélisation numérique (MEF) d'une fissure. Ainsi, une fois la géométrie de structure à analyser a été choisie, bien que le modèle d'endommagement pour traduire le comportement du matériau, il sera possible d'estimer la taille de la zone cohésive, équivalente à la dimension de la FPZ (donc réelle), en fonction de la longueur équivalente de la fissure. Les résultats de la propagation de la fissure obtenus par modélisation MEF, au delà d'être dépendants des matériaux simulés, ils montrent que la dimension critique de la zone cohésive est associée au début du *plateau* de la courbe-*R*. Cette observation permet d'évaluer la précision de mesure de la valeur critique du taux de restitution d'énergie indépendamment du matériau considéré. Cette évaluation de la propriété de rupture nécessite la constatation, au préalable, que la dimension critique de la zone cohésive reste inaltérée le long d'une grande longueur de fissure (équivalente).

En conséquence, il devient impératif d'examiner attentivement la dépendance de l'extension de la zone cohésive avec la taille caractéristique de la structure. Par conséquent la modélisation par MEF montre l'existence d'une dimension critique en dessous de laquelle est impossible de déterminer des taux de restitution d'énergie

critiques de rupture. La modélisation de la fissure par MEF montre que la courbe- R ne dépend pas de la dimension de la structure elle-même, pour une géométrie en particulier.

À la suite de ces observations, il devient pertinent de réaliser l'étude d'effet d'échelle dans le contexte d'une analyse asymptotique, basée sur le fait que la courbe- R est effectivement unique. L'importance d'évaluer si la longueur de fissure équivalente, associée à la charge ultime, dépend de la dimension caractéristique de la structure. De même, l'analyse de l'évolution du taux de restitution d'énergie associée à la charge ultime, quand la dimension de la structure augmente, est aussi très pertinente. Il est connu que pour le régime de taille intermédiaire, la loi d'effet d'échelle de Bažant (Size Effect Law : SEL), estime la résistance nominale par ajustement asymptotique, réalisée à partir des petites tailles (Théorie de Résistance des Matériaux) et des grandes (LEFM). Par conséquent, il devient approprié de proposer un régime adimensionnel asymptotique basé sur la courbe- R unique, sur la base d'une approche analytique. Ce régime asymptotique additionnel devrait, donc, être en fonction de l'information acquise dans les données expérimentales de rupture, notamment la courbe- R .

L'ensemble de questions et suppositions antérieurement énumérés, notamment à propos du comportement exhibé par le matériau, justifient bien la réalisation des essais mécaniques en structures géométriquement similaires de différentes dimensions. Cette étude d'effet d'échelle comporte ainsi la réalisation des essais en structures de taille importante. La conséquence inévitable, c'est donc l'influence du poids propre dans les résultats expérimentaux, surtout pour les grandes tailles de structures testées. Cette constatation justifie donc bien le développement d'une procédure qui considère l'effet du poids propre de la structure analysée (donc une correction).

Le traitement statistique réalisé sur les résultats du dépouillement expérimental, fourni l'information nécessaire pour confirmer l'existence d'une courbe- R unique, lorsque une essence de bois est utilisée comme matériau de teste. Ainsi, l'effet d'échelle sur la résistance nominale de la structure, en particulier celui qui couvre le régime de taille intermédiaire, rend possible l'évaluation du régime asymptotique adimensionnel basé dans la courbe- R expérimentale (unique). L'évolution de la résistance nominale de la structure, basée sur l'information expérimentale, est montrée sur la forme d'une enveloppe (domaine) de transition entre les petites et les grandes tailles de structure (en représentation bi-logarithmique).

D'abord je profite de cette occasion pour adresser mes sincères remerciements à M. Stéphane Morel, mon collègue et Ami de l'Université Bordeaux I, de m'avoir transmis des compétences scientifiques essentiels à la réalisation de ce travail. Je le remercie de l'intérêt et disponibilité toujours manifestés pour les éclaircissements sollicités au long de cette grande aventure.

Je dois également une grande partie de mon travail à M. Marcelo de Moura, mon Directeur de Thèse au Portugal, de m'avoir transmis des aptitudes indispensables à la modélisation par Eléments Finis, une compétence que je cherchais à acquière il y a long temps, et que j'en profiterai bien dans l'avenir.

Je tiens également à remercier vivement M. Gérard Valentin, mon Directeur de Thèse en France, de m'avoir fait bénéficier de ses conseils et de ses compétences, soulignant ainsi l'intérêt qu'il porte à mes travaux. Je suis très reconnaissant d'avoir reçu de lui le sens de la rigueur expérimentale, et de l'esprit critique nécessaire à la prise de décisions au long de ce travail.

Mes remerciements vont aussi adressés à M. Patrick Castéra, Directeur du magnifique Laboratoire de Rhéologie du Bois de Bordeaux (LRBB), pour le tendre accueil toujours manifesté.

Je suis aussi très remercié à M. Pierre Morlier, de m'avoir invité et accueilli, dans le cadre de deux Stages réalisés au LRBB, en bénéficiant d'une bourse Marie Curie Fellowships, et dans une deuxième fois, comme Professeur invité par l'Université Bordeaux I.

Je tiens également à remercier vivement mon Chef José Morais, pour m'avoir incité à débiter mon activité de recherche dans le sujet de la Mécanique de la Rupture du bois, et d'y chercher des compétences hors barrières. Je lui manifeste ma gratitude de m'avoir aidé et conseillé dans plusieurs étapes de ce long processus.

Je suis reconnaissant à M. Pedro Melo, Président du CETAV/UTAD, de m'avoir engagé des efforts pour me rembourser des frais réalisés au long de ce travail.

Je ne peux pas oublier Pierrette Wyss, de m'avoir facilité l'accès au Labo puis l'heure de fermeture du portail et dans l'Week-end. J'en profite aussi de l'occasion pour remercier les gens du LRBB, comme Jean-Luc Coureau, Christophe Lespine, Myriam Chaplain, Bernard Solbes, Philippe Taris, Jérôme Malvestio, Jean-Marc Sibaud, Jean-Louis et Françoise Rodriguez.

Dirijo-me agora à Coordenação do Departamento de Engenharias da UTAD, para manifestar o meu agradecimento e apreço pela criação das condições necessárias à realização desta Tese.

Devo uma palavra de grande agradecimento ao Sr. Professor José Luis Lousada, pelo interesse manifestado pelo meu trabalho, dando indicações preciosas quanto aos cuidados a ter na selecção e conservação do material utilizado na preparação dos provetes. Fico igualmente reconhecido ao Sr. Armindo Teixeira, pelos conhecimentos que me soube transmitir durante a árdua tarefa de maquinagem dos provetes, prestando um importante auxílio.

Fico reconhecido aos colegas e amigos que me ajudaram muito em fases cruciais da realização deste trabalho, como o Cristóvão Santos, o Abílio de Jesus, o Marcelo Oliveira, o José Xavier, o Amadeu Borges, o Engenheiro Domingos Guimarães, o Abel Rouboa, o Jorge Godinho e o José Luis Pereira.

Uma palavra de gratidão ao Sr. Engenheiro Jorge Martins, Director do Curso de Engenharia de Madeiras, pela autorização concedida para utilizar as oficinas do Instituto Politécnico de Viseu, numa fase inicial de preparação de provetes.

Estou obviamente muito reconhecido à minha Mulher, Paula Peixoto Dourado, e aos meus Filhos, Gonçalo Nuno Dourado e à Lídia Jorge Dourado, pelo apoio incansável e o carinho manifestados em todas as fases desta longa etapa da minha carreira.

Estou muito grato aos meus Pais e ao meu irmão, Telmo Dourado, pelo incentivo dado em muitos momentos deste trabalho.

Contents

Nomenclature	23
Introduction	26
Chapter I	
Overview of the cohesive failure and main consequences	30
1.1 Introduction	31
1.2 Quasibrittle behaviour	31
1.3 Equivalent LEFM: <i>Resistance-curve</i>	35
1.4 Cohesive crack models	37
1.5 Size effect	41
Chapter II	
Quasibrittle Fracture	46
2.1 Introduction	47
2.2 Experiments	47
2.2.1 Material and specimens	47
2.2.2 Fracture tests	48
2.3 Equivalent LEFM	50
2.4 Cohesive crack modelling	55
2.4.1 Interface finite element	55
2.4.2 Bilinear stress-softening model	56
2.4.3 FEM calculations	57
2.5 Formulation of the inverse problem	59
2.6 Results and discussion	59

Chapter III

Size Effect in Notched Structures	65
3.1 Introduction	66
3.2 Derivation of the energetic Size Effect Law based on the equivalent LEFM and the asymptotic analysis	67
3.2.1 <i>Size effect on the relative crack length and resistance at the peak load</i>	69
3.2.2 <i>Size effect on the nominal strength</i>	74
3.2.2.1 <i>Asymptotic regime at large sizes</i>	74
3.2.2.2 <i>Asymptotic regime at intermediate sizes</i>	75
3.2.2.3 <i>Asymptotic regime at small sizes</i>	76
3.3 Validation procedure from numerical analysis: discussion	83
3.3.1 <i>R-curve estimate</i>	85
3.3.2 <i>Relative crack length at the peak load</i>	90
3.3.3 <i>Size effect on the nominal strength</i>	95

Chapter IV

Experiments on Size Effect	99
4.1 Introduction	100
4.2 Experiments	100
4.3 Self-weight compensation	103
4.3.1 Load equivalent to the specimen self-weight: static approach	103
4.3.2 Load equivalent to the specimen self-weight: kinematic approach	104

4.3.3 Exact self-weight compensation method	109
4.3.3.1 <i>Estimate of the equivalent crack length</i>	112
4.3.3.2 <i>R-curve estimate</i>	114
4.3.3.3 <i>Cohesive crack modelling validation</i>	118
4.4 Results of the Size Effect experiments: discussion	125
4.4.1 Variability and sampling	125
4.4.2 Estimate of the R-curves (Exact self-weight compensation)	127
Conclusions	135
Appendices	
Appendix A2.1	140
Appendix A2.2	142
Appendix A2.3	148
Appendix A3.1	151
Appendix A3.2	153
Appendix A4.1	155
Appendix A4.2	156
Appendix A4.3	158
Appendix A4.4	160
Appendix A4.5	171
References	174
Annex	178

List of Figures

Figure 1.1	Fracture Process Zone (FPZ) at the crack tip of a quasibrittle material and stress distribution along the crack line	32
Figure 1.2	Propagation of the main crack with its Fracture Process Zone (FPZ)	34
Figure 1.3	Typical load-displacement curve and corresponding <i>R</i> -curve obtained in spruce for the SEN-TPB test in the TL system	37
Figure 1.4	Sketch of the cohesive zone behaviour: comparison of the numerical crack length with the equivalent LEFM crack length for different stages of the numerical crack propagation	40
Figure 1.5	Size effect on the nominal strength	43
Figure 2.1	Parts set up before bonding	48
Figure 2.2	Sketch of TPB test set-up	49
Figure 2.3	Typical load-displacement curves (Mode I) obtained in wood fracture	49
Figure 2.4	FE-modelling used in ABAQUS® 6.5-1 compliance computations performed using 352 isoparametric 8-node plane strain elements	51
Figure 2.5	Procedure used to assess the elastic energy release rate in wood	53
Figure 2.6	<i>R</i> -curves obtained in wood from <i>P</i> - δ curves	54
Figure 2.7	Bilinear Petersson's softening stress-softening model used to describe the natural phenomena occurring in the cohesive zone during wood fracture (Mode I): micro-cracking and fibre-bridging	58
Figure 2.8	Energies attributed to micro-cracking and fibre-bridging phenomena for both sets of tested wood	60
Figure 2.9	Superposition of bilinear diagrams showing obtained mean values of achieved independent damage parameters using the proposed IP, for both wood tested species	62
Figure 2.10	Results of the IP for both wood tested species, regarding mean values of energy ascribed to phenomena of micro-cracking $G_{f\mu}$ and fibre-bridging	62
Figure 2.11	Bilinear Petersson's law	63
Figure. 2.14	Results of FEA showing the evolution of the extent of the cohesive zone with the numerical crack length for both tested wood	64
Figure 3.1	Plotting of Eq. (3.6) used to estimate α_{u*} in a positive specimen geometry	70

Figure 3.2	Size effect on the ratio $G'_R/G_R(\alpha)$ revealing the decrease of α_u with the structure size for the SEN-TPB	71
Figure 3.3	Plotting of the scaling of the relative crack length at the peak load against the structure size according to Eq. (3.8)	72
Figure 3.4	Size effect on the resistance at the peak load according to Eqs. (3.11) and (3.12)	73
Figure 3.5	Size effect on the nominal strength	78
Figure 3.6	Comparison of the asymptotic behaviours estimated by Eq. (3.20) and the fitting of Bažant's SEL (Eq. 1.3) for two distinct values of the exponent β which characterize the curvature of the R -curve	79
Figure 3.7	Underestimated design (more leftwards centreline) and nominal strength given by LEFM (Eq. 3.17)	82
Figure 3.8	Approximate size effect generated by fitting of the nominal strength (Eq. 1.4) and the asymptote of LEFM (Eq. 3.17)	82
Figure 3.9	Sketch of the SEN-TPB showing the wood anatomic directions in the front plane	83
Figure 3.10	Load-deflection curves obtained in the CCM under displacement control. Curves labelling is in agreement with Table 3.1	84
Figure 3.11	Normalised R -curves (by $G_f = G_{Rc} = 0.1 \text{ N/mm}$) obtained in the numerical analyses	86
Figure 3.12	Influence of the specimen (SEN-TPB) size D on the normalized extent of the cohesive zone	86
Figure 3.13	Unique R -curve revealed through the CCM	87
Figure 3.14	Linear regression plot performed on the rising part of the R -curves which exhibit an undoubted plateau, used to define the curvature exponent of the R -curve	89
Figure 3.15	Plotting of the normalized R -curve according to Eq. (3.1) ($\phi=1$ and $\beta=0.27$) and the numerical results plotted in Fig. 3.11 for those series which exhibit an undoubted plateau	89
Figure 3.16	Plotting of Eq. (3.6) used to estimate α_{u*} . Comparison with the plotting of Eq. (3.7) obtained from the R -curve computed for series D_3	91
Figure 3.17	Plotting of Eq. (3.6) used to estimate α_{u*} . Comparison with the plotting of Eq. (3.7) obtained from the R -curve computed for series D_4	92

Figure 3.18	Plotting of Eq. (3.6) used to estimate α_{u^*} . Comparison with the plotting of Eq. (3.7) obtained from the <i>R</i> -curve computed for series D_5	92
Figure 3.19	Plotting of Eq. (3.6) used to estimate α_{u^*} . Comparison with the plotting of Eq. (3.7) obtained from the <i>R</i> -curve computed for series D_6	93
Figure 3.20	Plotting of Eq. (3.6) used to estimate α_{u^*} . Comparison with the plotting of Eq. (3.7) obtained from the <i>R</i> -curve computed for series D_7	93
Figure 3.21	Scaling of the relative crack length at the peak load α_u as a function of the characteristic size	95
Figure 3.22	Size effect on the resistance at the peak load according to Eqs. (3.11 and 3.12)	96
Figure 3.23	Size effect on the nominal strength (Eq. 3.17, 3.18 and 3.20)	97
Figure 4.1	SEN-TPB geometry used in the experiments showing the initial crack length	101
Figure 4.2	Sketch of the TPB test set-up showing the displacement monitoring	102
Figure 4.3	Superposition of typical load-deflection curves obtained for each series	103
Figure 4.4	Load-displacement curve for the uncompensated TPB test	104
Figure 4.5	Schematization of the simply supported beam subjected to the superposition of the central load <i>P</i> and the distributed load	105
Figure 4.6	Load–deflection curve in the elastic domain	106
Figure 4.7	Self-weight compensation of the load–deflection curve	108
Figure 4.8	Simply supported beam subjected to the superposition of the central load and the distributed load	109
Figure 4.9	Superposition of load–displacement curves obtained in the experiments and through FE analysis in the linear elastic domain	112
Figure 4.10	Modified load–deflection curve due to the compensation of the specimen self-weight	113
Figure 4.11	Partial strain energy associated to the external load in two consecutive points of the modified load-displacement curve	115
Figure 4.12	Schematic representation of the vertical displacement fields (absolute values) obtained for the SEN-TPB specimen along the middle-axis corresponding to two consecutive points of the load-displacement curve	116

Figure 4.13	Load-displacement curves obtained through FEM computations	119
Figure 4.14	Evolution of the numerical FPZ extent with the numerical crack length for densities in the interval $[300, 700]$ kg/m ³	120
Figure 4.15	<i>R</i> -curves obtained for material densities in the interval $[300, 700]$ kg/m ³	122
Figure 4.16	Evolution of $G_P(a)$ and $G_q(a)$ using material densities in the interval $[300, 700]$ kg/m ³	123
Figure 4.17	<i>R</i> -curves obtained for material densities in the interval $[300, 700]$ kg/m ³	123
Figure 4.18	<i>R</i> -curves obtained for material densities in the interval $[300, 700]$ kg/m ³	125
Figure 4.19	Unitary initial compliances obtained in the experiments showing the huge scattering of the tested material	126
Figure 4.20	<i>Resistance</i> -curves obtained in the experiments after application of the Exact self-weight compensation method	128
Figure 4.21	Mean <i>R</i> -curves obtained in the experiments	129
Figure 4.22	Mean values of the critical energy release rate G_{Rc} obtained in the experiments for the specimens which exhibited an undoubted plateau on the <i>R</i> -curve	129
Figure 4.23	Envelop estimated for the size effect on the nominal strength in wood spruce using the mean values obtained for each tested series	132
Figure 4.24	Progress of ratios used to estimate the nominal strength according to Eq. (3.17) and Eq. (3.18), showing the calculated limits for each ratio, according to the estimate performed for the structure sizes $D=210 - D=23.3$ (mm)	133
Figure A2.1.1	Axis directions in wood	141
Figure A2.1.2	Identification of wood fracture systems	141
Figure A2.2.1	<i>Ranking</i> of solutions in generation t showing subsets disposition	144
Figure A2.2.2	Couples resulting from <i>Selection</i> with the chromosomes display	145
Figure A2.2.3	Arrangement of solutions performed by Elimination	146
Figure A2.2.4	Sketch of the Inverse Problem	147
Figure A3.1.1	<i>Stiffness</i> calibration curve for the SEN-TPB	152

Figure A3.1.2	Dimensionless energy release rate	152
Figure A3.2.1	Symmetric FE-mesh used in ABAQUS® 6.5-1 simulations	154
Figure A4.1.1	Load-displacement curves obtained in the experiments	155
Figure A4.3.1	Plotting of the ratio $\lambda_{Pq}^*(\alpha)/\lambda_{PP}^*(\alpha)$ obtained in the cohesive crack modeling conditions referred in Section 4.3.3.3	158
Figure A4.3.2	Load-displacement curves obtained in the cohesive crack modelling after reset and corresponding compensation	159
Figure A4.4.1	Plotting of unitary compliances due to the applied external load	161
Figure A4.4.2	Plotting of unitary compliances due to the distributed load corresponding to the specimen self-weight	162
Figure A4.4.3	Plotting of the dimensionless energy release rate function for each series	163
Figure A4.4.4	Linear regression plot performed on the rising part of the <i>R</i> -curve and corresponding normalized <i>R</i> -curve for the data got in the experiments	165
Figure A4.4.5	Plotting of Eq. (3.6) used to estimate α_{u*} . Comparison with the plotting of Eq. (3.7) obtained from the <i>R</i> -curve computed for specimen size $D=280$ mm	167
Figure A4.4.6	Plotting of Eq. (3.6) used to estimate α_{u*} . Comparison with the plotting of Eq. (3.7) obtained from the <i>R</i> -curve computed for specimen size $D=210$ mm	167
Figure A4.4.7	Plotting of Eq. (3.6) used to estimate α_{u*} . Comparison with the plotting of Eq. (3.7) obtained from the <i>R</i> -curve computed for specimen size $D=140$ mm	168
Figure A4.4.8	Plotting of Eq. (3.6) used to estimate α_{u*} . Comparison with the plotting of Eq. (3.7) obtained from the <i>R</i> -curve computed for specimen size $D=70$ mm	168
Figure A4.4.9	Plotting of Eq. (3.6) used to estimate α_{u*} . Comparison with the plotting of Eq. (3.7) obtained from the <i>R</i> -curve computed for specimen size $D=35$ mm	169
Figure A4.4.10	Plotting of Eq. (3.6) used to estimate α_{u*} . Comparison with the plotting of Eq. (3.7) obtained from the <i>R</i> -curve computed for specimen size $D=23.3$ mm	169
Figure A4.5.1	Measured densities at 12% EMC in the totality of specimens which exhibited an undoubted plateau on the <i>Resistance</i> -curve	171

Figure A4.5.2	Mean values of the ultimate load obtained in the experiments for the specimens which exhibited an undoubted plateau on the <i>R</i> -curve	172
Figure A4.5.3	Mean values of the relative crack length associated to the ultimate load obtained in the experiments for the specimens which exhibited an undoubted plateau on the <i>R</i> -curve	172
Figure A4.5.4	Mean values of the energy release rate associated to the ultimate load obtained in the experiments for the specimens which exhibited an undoubted plateau on the <i>R</i> -curve	173
Figure A4.5.5	Mean values of the relative crack length associated to the critical energy release rate, obtained in the experiments for the specimens which exhibited an undoubted plateau on the <i>R</i> -curve	173

List of Tables

Table 2.1	Elastic properties of Maritime pine and Norway spruce	51
Table 2.2	Mean values obtained in TPB fracture tests for Pine wood	54
Table 2.3	Mean values obtained in TPB fracture tests for Norway spruce	54
Table 2.4	Comparison between numerical and experimental mean values obtained for Maritime pine	60
Table 2.5	Comparison between numerical and experimental mean values obtained for Norway spruce	60
Table 2.6	Summary of mean values obtained by the inverse problem regarding the bilinear constitutive model	61
Table 3.1	Series identification	84
Table 3.2	Resume of parameters obtained in the numerical simulation of SEN-TPB	88
Table 4.1	Specimen sizes used in the experiments	102
Table 4.2	Resume of mean values obtained in the experiments	130
Table 4.3	Results obtained in the size effect study for the experimental data	133
Table A2.2.1	Lower and upper limits of the search domain attributed to each design variable	142
Table A2.2.2	Resume of genetic parameters	147
Table A2.3.1	(Complete recording of Table 2.2) Resume of main values obtained in TPB for Pine wood	148
Table A2.3.2	(Complete recording of Table 2.3) Resume of main values obtained in TPB for Norway spruce	148
Table A2.3.3	(Complete recording of Table 2.4) Comparison between numerical and experimental mean values obtained for Maritime pine	149
Table A2.3.4	(Complete recording of Table 2.5) Comparison between numerical and experimental mean values obtained for Norway spruce	149
Table A2.3.5	(Complete recording of Table 2.6) Summary of main values (12 specimens of each wood species) obtained in the inverse problem regarding the bilinear constitutive model	150
Table A3.1.1	Elastic properties of Norway spruce	151

Table A3.2.1	Elastic properties of Norway spruce	154
Table A3.2.2	Petersson's model softening properties used in the simulations	154
Table A4.3.1	Load equivalent to the specimen self-weight	158
Table A4.4.1	Elastic properties of Norway spruce (based on Guitard D, 1987) used in the FEA for each series	162
Table A4.4.2	Parameters obtained in the size effect study for the experimental data	170
Table A1	Parameters obtained in the experiments regarding series with the characteristic size $D=280$ mm	179
Table A2	Parameters obtained in the experiments regarding series with the characteristic size $D=210$ mm	180
Table A3	Parameters obtained in the experiments regarding series with the characteristic size $D=140$ mm	181
Table A4	Parameters obtained in the experiments regarding series with the characteristic size $D=70$ mm	182
Table A5	Parameters obtained in the experiments regarding series with the characteristic size $D=35$ mm	183
Table A6	Parameters obtained in the experiments regarding series with the characteristic size $D=23.3$ mm	184

Nomenclature

a	Equivalent crack length	$f(w)$	Stress softening function
a_c	Critical equivalent crack length	$f(\alpha)$	Dimensionless function
a_{lim}	Limit value of a used in the IP	F_{max}	Arbitrary constant
a_{num}	Numerical crack-length	g	Acceleration of gravity
a_u	Equivalent crack length at P_u	$g(\alpha)$	Dimensionless energy rel. rate funct.
a_0	Traction free crack length	G_d	Critical damage energy dissipation rate
b	Width of the structure cross section	G_f	Cohesive fracture energy
\mathbf{b}	Vector of design variables	G_{fb}	Fracture energy due to fibre-bridging
$\underline{\mathbf{b}}$	Lower bound of design variables	$G_{f\mu}$	Fracture energy due to micro-cracking
$\overline{\mathbf{b}}$	Upper bound of design variables	$G_p(a)$	Energy release rate associated to P
B	Empirical constant	$G_q(a)$	Energy release rate due to q
c_N	Coefficient introduced for convenience	$G_R(a)$	Energy release rate
d_n	Normal stiffness at the interface	G_{RC}	Critical energy release rate
d_s	Shear stiffness at the interface	h	Specimen height
D	Characteristic structure dimension	h_{FPZ}	Height of the FPZ
D_c	Crossover size (in terms of energy)	\mathbf{I}	Identity matrix
D_{min}	Crossover size (lower bound of α_{u^*})	j	Specimen label
D_{num}	Intermediate size in crossover regime	k	Total number of design variables
\mathbf{D}	Matrix of penalty parameters	l_{FPZ}	Extent of the FPZ
D_z	Domain of the state variables	L	Beam span
D_0	Crossover structure size	m	Mass
D_1^*	Crossover size (in terms of strength)	m_i	Number of bits of design variable i
\mathbf{E}	Matrix of damage parameter	N	Number of points of the P - δ curve
E	Young modulus	N_g	Number of constraints of the IP
E_L	Longitudinal modulus of wood	P	External applied central load
E_T	Tangential modulus of wood	p	Precision required to determine $y(\mathbf{b})$
E'	Longitudinal elastic modulus	$P(t)$	Population in generation t
E^*	Effective Young modulus	P_c	Probability of Crossover
f_b	Strength at the onset of bridging	p_m	Probability of Mutation
f_u	Arbitrary measure of material strength	P_q	Statically equivalent load
f_t	Local strength	$\text{Pop}(t)$	Number of solutions in generation t

P_u	Peak/ultimate load	δ_{Pq}	Displacement due q in axis of P
q	Distributed load corresp. self-weight	δU	Complementary energy
$R(a)$	Structure unloading stiffness	δU_q	complementary energy of q
S	Data structure to store design variabl.	$\delta(x, a_i)$	Displacement field associated to a_i
t	Generation label	l_{coh}	Extent of the cohesive zone
\mathbf{v}_i	Chromosome label	δW	Work of the external applied load
V_{FPZ}	Critical volume of the FPZ	Δa	Equivalent crack length increment
w	Crack opening width	Δa_c	Equivalent length of the FPZ
w_b	Crack opening at onset of bridging	$\Delta \delta_{PP}(a_0)$	Variation of δ_{PP} when $a = a_0$
w_c	Ultimate crack opening	$\Delta P_{\text{exp}}(a_0)$	Loading variation when $a = a_0$
w_f	Energy required during crack advance	ϕ	Arbitrary constant
w_o	Damage onset relative displacement	γ	Brittleness number
\mathbf{w}_r	Vector of relative displacements	$\lambda(a)$	Numerical compliance function
$W(a)$	Elastic strain energy	$\lambda_{\text{cor}}(a)$	Corrected numerical compliance
W^*	Complementary strain energy	$\lambda_{\text{exp}}(a)$	Experimental compliance
x_i^t	Potential solution in generation t	$\lambda_{\text{mod}}(a)$	Modified compliance
$y(\mathbf{b})$	Objective function	$\lambda_{qP}(x, a_i)$	Compliance field due δ_{Pq} when $a = a_i$
\mathbf{z}	Vector of the state variables	$\lambda_{qP}^*(x, a_i)$	Best fit of in-plane $\lambda_{qP}(x, a_i)$
\mathbf{z}^*	Vector of prescribed state variables	$\lambda_{qq}(x, a_i)$	Compliance field due to q ($a = a_i$)
α	Relative (equivalent) crack length	$\lambda_{qq}^*(x, a_i)$	Best fit of in-plane of $\lambda_{qq}(x, a_i)$
α_c	Critical relative crack length	λ_{PP}	Compliance associated to δ_{PP}
α_u	Relative crack length at P_u	$\lambda_{PP}^*(a)$	Best fit of in-plane FEA of $\lambda_{PP}(a)$
α_{u^*}	Single solution of α_u	λ_{Pq}	Compliance associated to δ_{Pq}
β	Curvature exponent of the R -curve	$\lambda_{Pq}^*(a)$	Best fit of in-plane FEA of $\lambda_{Pq}(a)$
δ	Displacement (vertical)	ν	Poisson ratio
δa	Infinitesimal crack propagation ext.	θ	Relative length of the FPZ
$\delta_{\text{exp}}(a)$	Displacement recording in experim.	ψ	Multiplicative correction factor
δ_i	Displacement in each specimen side	$\boldsymbol{\sigma}$	Vector of normal tractions
δE	Elastic strain energy release	σ_N	Nominal stress
δ_F	Displacement of load-point	$\sigma(x)$	Transfer normal stress
δ_{PP}	Vertical displacement due to P	ρ	Material (specific) density

Notation:

CCM	Cohesive Crack Modelling
COV	Coefficient of Variation
EMC	Equilibrium Moisture Content
ESWCM	Exact self-weight compensation method
FEA	Finite Element Analysis
FEM	Finite Element Method
FPZ	Fracture Process Zone
GA	Genetic Algorithm
IP	Inverse Problem
LEFM	Linear Elastic Fracture Mechanics
LSSW	Load equivalent to the specimen-self-weight
OS	Optimisation Strategy
RH	Relative Humidity
SE	Size Effect
SEN-TPB	Single-Edge-Notched beam loaded in Three-Point-Bending
SEL	Size Effect Law
SSW	Specimen self weight
TPB	Three point bending

Introduction

Fracture of quasibrittle materials, such as concrete, mortar, rocks, sea ice, dental cements, fibre composites, bone, wood, among others, is characterised by the existence of a non-negligible Fracture Process Zone (FPZ) which develops ahead of the crack-tip (Bažant ZP and Planas J, 1998). In these materials, the FPZ undergoes softening damage such as microcracking, crack-branching or crack-bridging, which may represent almost the entire nonlinear zone at the crack-tip, with normal stresses progressively declining along the FPZ domain (Bažant ZP, 2004). The experimental praxis in notched structures involving fracture reveals that the crack monitoring in these materials is very difficult to accomplish with accuracy, due to the cited fracture phenomena taking place ahead of the crack-tip. Due to the development of this FPZ, these materials typically fail only after a large crack has grown in a stable manner (Bažant ZP, 1997 c). As this softening zone attends a non-negligible dimension on the structure scale, Linear Elastic Fracture Mechanics (LEFM) cannot be directly applied, but rather Non-Linear Elastic Fracture Mechanics (NLEFM). Nevertheless, an adaptation of LEFM is possible to execute, known as *equivalent* LEFM, which provides a useful approximation of quasibrittle fracture.

The main consequence of the FPZ development is the observation of the so-called *Resistance-curve* (*R-curve*), in which the resistance to crack growth depends on this *equivalent* linear elastic crack length $G_R(a)$. The resistance to crack growth $G_R(a)$ has firstly been regarded as a fixed material property, as defended by Irwin GR (1960) and more assumedly by Kraft et al. (1961). More recently, however, it has been found that the shape of the *R-curve* is considerably influenced by the structure geometry (Bažant ZP and Li Y-N, 1997; Morel et al., 2003), as well as by the structure size (Bažant ZP and Planas J, 1998). This raises the issue regarding the relation which seems to exist between the energetic fracture properties, estimated from the *R-curve*, and the specimen geometry.

Conceptually, the most straightforward and efficient method to typify the quasibrittle failure in notched structures is the cohesive crack model (Elices M et al.,

2002; Planas et al., 2003). According to this NLFM model the entire FPZ is gathered into the crack line being characterized on the basis of a stress-displacement law which exhibits softening. In most of the analyses which involve the cohesive crack modelling (CCM), the structural model in a whole remains elastic, turning thus possible to get the mechanical response on each side of the crack on the linear elasticity basis, with the nonlinearity being included through boundary conditions along the crack line. Among the different possible softening behaviours used to characterize this nonlinearity, the bilinear softening function is well known to describe accurately the quasibrittle failure, since it reproduces well the most important phenomena taking place under crack propagation (*i.e.*, microcracking and crack-bridging). Regardless of the success revealed by the efficiency shown by the cohesive crack models to typify the quasibrittle failure in notched structures, the estimate of the cohesive properties with respect to a given experimental Load-Deflection response is yet a tiring task (Wang J, 2006; Dourado et al., 2008). Since this estimate provides a way to measure the development of the FPZ, as well as possible interactions with the structure boundaries, it turns that the issue deserves attention, also focused on the context of the *R*-curve behaviour. Therefore, the bilinear softening function (Petersson PE, 1981) has recently been used to estimate the connections between the *R*-curve and the cohesive crack properties in the one-to-one correspondence which seems to exist between the *R*-curve and the softening curve pointed out by Planas et al. (2003), using different specimen geometries (DCB, TDCB and SENB) (Lespine C 2007, Morel S et al. 2008). However, despite the efficiency of the CCM to describe the quasibrittle failure, the cohesive crack properties (as well as the *R*-curve properties) appear dependent on the specimen geometry.

One of the main consequences of the behaviour manifested through the *R*-curve is the effect of the structure size on its nominal strength. The size effect on the structural strength may be defined as the deviation, engendered by the change of structure size, of the actual load capacity of a structure from the load capacity predicted by plastic limit analysis (or any theory based on critical stresses or strains) (Bažant ZP and Planas J, 1998). In a unlike manner as previewed by the weakest link model (Weibull W, 1939) the size effect in notched structures is related to existence of the *R*-curve, through what it is referred as a energetic size effect rather than a statistical one (Bažant ZP, 1984; Bažant ZP, 1997 a; Bažant ZP c).

Since 1984, the Bažant's size effect law (SEL) (Bažant ZP, 1997 c) provides the alone efficient description of the size effect phenomenon in geometrically similar notched structures of different sizes D . In its most recent development, Bažant's SEL is obtained from an asymptotic analysis performed for small and large structure sizes and leads to a size effect expected to be transitional between two corresponding asymptotic behaviours : Strength Theory (or plastic limit analysis) for small structure sizes and LEFM for large structure sizes. As a consequence, the size effect for the intermediate structure sizes is not accurately defined, since it is obtained from an asymptotic matching procedure, performed from both extreme asymptotic regimes. Since the intermediate structure sizes correspond to the range of the experimental data usually available, it turns that the issue ought to be analysed in detail. In addition, the size effect study on the intermediate size range might be supported on credible experimental data, thus allow verifying its adequacy to predict the evolution of the nominal stress in a given geometry.

After an overview of the quasibrittle failure and its main consequences in Chapter I, the second Chapter is devoted to an experimental study consisting in fracture tests in a quasibrittle material. The consequences motivated by the development of a non-negligible non-linear domain are discussed in the context of an equivalent Linear Elastic Fracture Mechanics approach, with the resistance to crack growth being evaluated as a function of the equivalent crack length (R -curve). The experimental results are then simulated from CCM and it is shown that the developed cohesive zone might interact with the structure boundaries, leading to corresponding underestimation of energetic properties. This interaction between the cohesive zone and the structure boundaries emphasizes the required minimum specimen dimension necessary to perform accurate estimate of the energetic properties and leads naturally to the introduction of the size effect phenomenon.

The third Chapter is focused in the size effect phenomenon in quasibrittle fracture. In this chapter, an evaluation of the size effect on the relative crack length at the peak load, on the corresponding resistance to crack growth, and on the nominal strength, is proposed. An analytical development procedure is presented, and an additional asymptotic regime is detailed for the intermediate size range. The predictions of this size effect model are

validated from CCM simulations performed on geometrically similar notched structures of different sizes.

The ending Chapter presents the experiments on the size effect. The *R*-curve is estimated through a compensation procedure which takes into account the specimen self-weight. The size effect on the nominal strength is presented revealing the intermediate size regime estimated by means of experimental data.

Chapter I

**Overview of the cohesive failure and
main consequences**

Chapter I

1.1 Introduction

The first Chapter of the present Thesis starts by framing the reader to the quasibrittle behaviour when a notched structure is subjected to an external load. The main consequences originated by the development of a non-negligible non-linear domain are discussed in the framework of an equivalent Linear Elastic Fracture Mechanics approach. The estimate of the resistance to crack growth is made as a function of the equivalent crack length, revealing a rising *Resistance*-curve, with turned out stress redistributions and stored energy release in the non-linear domain. On the other hand, cohesive crack models are referred as a very useful way to mimic damage development in materials which exhibit this non-linear domain through Finite Element Analysis. A first mention is made to the Size Effect on the nominal strength, since it comes out as the main consequence of the noticed *R*-curve behaviour observed in quasibrittle materials.

1.2 Quasibrittle behaviour

In notched structures, the fracture behaviour of *quasibrittle* materials is characterized by the existence of a large Fracture Process Zone (FPZ) where various toughening mechanisms take place such as microcracking, crack branching or crack bridging (Morel S 2008). This domain (*i.e.*, the FPZ) is composed by a softening zone enclosed by a non-softening nonlinear zone which undergoes hardening or perfect plasticity (Fig. 1.1), with stress increase at increasing deformation, or held unchanged as the material deformation develops (Bažant ZP and Planas J 1998). As fracture in

quasibrittle materials is characterized by the existence of this large FPZ, Linear Elastic Fracture Mechanics (LEFM) can not be applied, but rather Non-Linear Fracture Mechanics. Nevertheless, an adaptation of LEFM (known as *equivalent* LEFM) provides a useful approximation of the quasibrittle failure, attributing the increase in the structure compliance, owing to the development of the FPZ, to the propagation of an *effective* crack, *i.e.*, a sharp traction-free crack of length a (called equivalent linear elastic crack length) which gives, according to LEFM, the same compliance as the one of the actual crack with its FPZ (Bažant ZP and Kazemi MT 1990, Bažant ZP 2002).

In *quasibrittle* materials the relative size of this nonlinear (*i.e.*, softening) zone and the characteristic structure dimension D is considerably higher than in materials characterized by a very brittle behaviour, or in those materials in which a ductile behaviour is observed. Indeed, as for the very brittle behaviour, this ratio is practically neglected, while as to the materials exhibiting a ductile behaviour the ratio is not sufficiently small so that LEFM may be fully applied (mostly treated by the elasto-plastic fracture mechanics).

In most of the FPZ (Fig. 1.1) the material undergoes progressive damage with corresponding material softening, due to microcracking, void coalescence, crack-

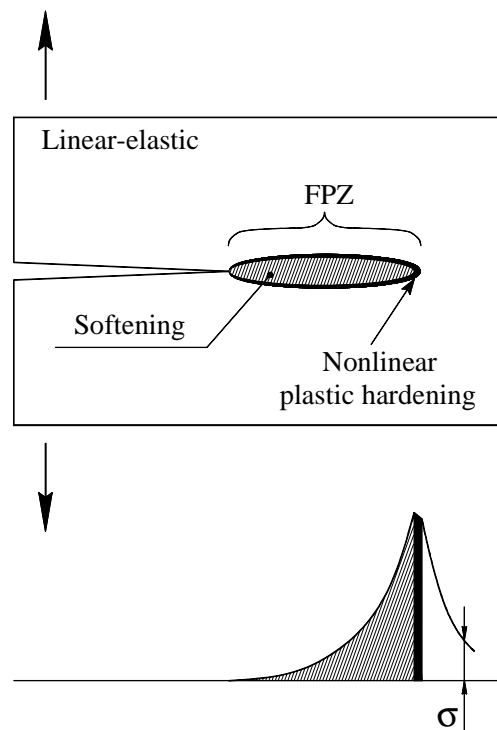


Figure 1.1 Fracture Process Zone (FPZ) at the crack tip of a quasibrittle material and stress distribution along the crack line. Adapted from Bažant ZP (1985).

bridging, frictional slips, and other analogous phenomena. In the envelope of the softening zone the nonlinear plastic hardening domain in quasibrittle materials, being negligible in volume, represents barely the transition between the elastic response and the material damaged volume. Materials as different as concrete, rock, cement mortars, sea-ice, tough fibre composites, ceramics, stiff clays, dental cements, bone and wood belong to this category (Bažant ZP 2004).

The denomination of *quasibrittle* is used to classify these materials since it is noticed that even when the plastic deformations are found irrelevant, the extent of the FPZ is *large* enough to have to be taken into account in the calculations, in total contrast with the genuine brittle materials in which LEFM is fully applied (Bažant ZP and Planas J 1998).

In quasibrittle failure of notched structures (in Mode I) the increase in the applied load at the early stage of the loading process leads to the development of a FPZ (Fig. 1.2 a) with the material undergoing progressive damage (with the equivalent crack length increment: $\Delta a < \Delta a_c$). In sufficiently large specimens, for which the softening zone is not affected by boundary effects, as the loading process progresses the FPZ reaches a critical size (Fig. 1.2 b), for which $\Delta a = \Delta a_c$. This means that, at stable crack growth FPZ is compelled to move forward (Fig. 1.2 c), with non corresponding increase in size. In such a case, one sustains that crack grows in a self-similar way.

Due to their heterogeneity and to the development of a large FPZ, these quasibrittle materials usually fail only after a large crack has grown in a stable manner, contrasting with metallic materials that fail before crack reaches macroscopic dimensions. Due note should be taken to the meaning of a so called *large* FPZ, as it indicates that the distance between the tip of the actual crack traction-free a_0 and the tip of the equivalent LEFM crack when the FPZ is fully developed (critical size) is equal to a given characteristic length Δa_c , as shown in Fig. 1.2 (b). This leads to non-negligible macroscopic stress redistribution with a non negligible amount of energy release from the structure.

Regarding the fracture length a_0 shown in Figs. 1.2 (b-c), two basic situations ought to be distinguished: (i) $a_0 = 0$, which conforms an un-notched structure, with the ultimate load P_u occurring at the onset of the fracture propagation, and (ii) $a_0 > 0$ not negligible in size compared to D , for which the ultimate (or peak) load P_u occurs after a

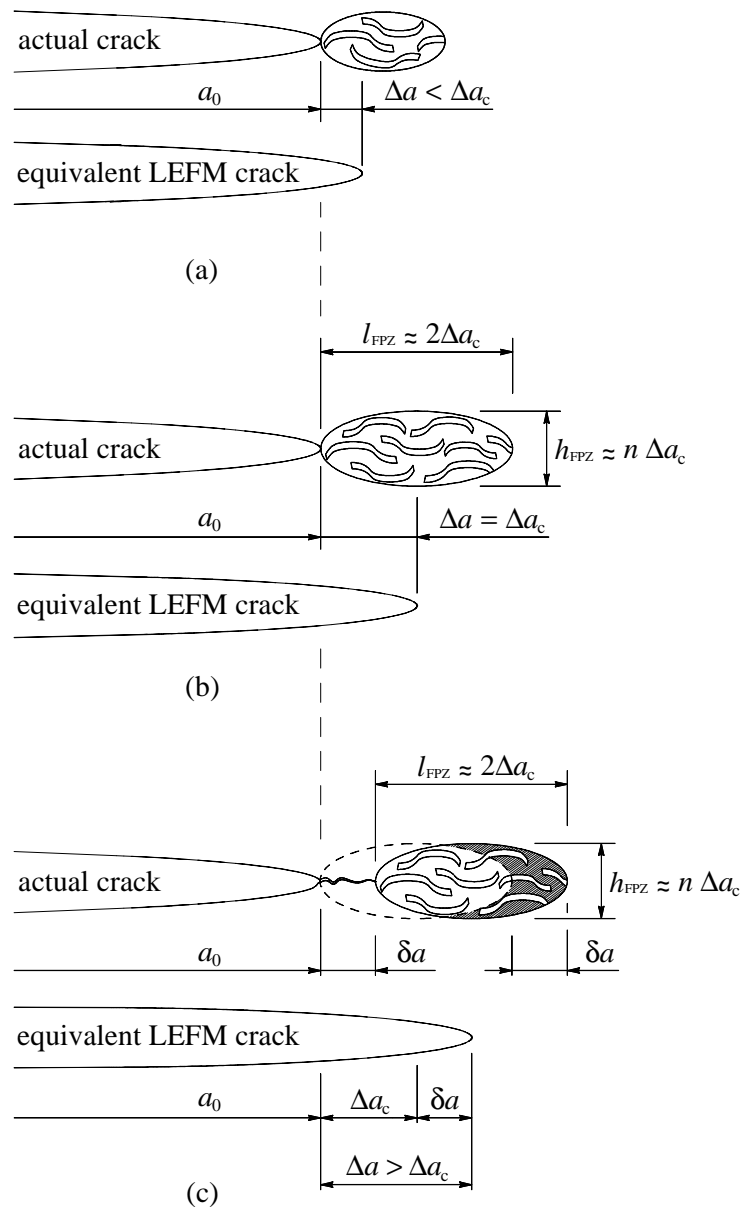


Figure 1.2 Propagation of the main crack with its Fracture Process Zone (FPZ): (a) FPZ development, (b) critical size of the FPZ (*i.e.*, fully developed) and (c) FPZ under crack propagation. Parameters: a_0 , initial crack length (actual traction-free crack length); $\Delta a = a - a_0$, equivalent crack length increment; δa , infinitesimal crack propagation extension; l_{FPZ} , extent of the FPZ. Adapted from Bažant ZP and Kazemi MT (1990).

given crack propagation has been monitored. In this Thesis only the later is a subject of concern, with corresponding failure types regarded as to exhibit a strong size effect (Gettu R et al. 1990).

1.3 Equivalent LEFM: *Resistance-curve*

Fracture of quasibrittle materials can be described with success through an equivalent linear elastic approach. According to this standard, acquainted with as ‘equivalent LEFM’, the compliance increase caused by the FPZ development and by the propagation of the main crack is attributed to the propagation of an elastic equivalent crack length (Bažant ZP and Kazemi MT 1990), which produces (on the framework of LEFM) the same structure compliance as the actual crack with its FPZ. Therefore, the complementary energy W^* might be used as a way to characterize the strain energy stored in the structure,

$$W^* = \frac{P^2}{E'b} f(\alpha) \quad (1.1)$$

in which P is the applied load, E' is the effective elastic modulus ($E'=E$ for plane stress and $E'=E/(1-\nu^2)$ for plane strain; E = Young modulus and ν the Poisson’s ratio), b is the width of the structure cross section, α the relative equivalent crack length (*i.e.*, $\alpha=a/D$), and $f(\alpha)$ a dimensionless function characterising the geometry of the structure. Actually, $f(\alpha)$ is a function of the specimen compliance $\lambda(\alpha)$ defined as $f(\alpha)=E'b\lambda(\alpha)/2$.

According to LEFM, during crack propagation the elastic energy release rate $G(\alpha)$ (either under load P or displacement δ control) must equal the resistance to crack growth $G_R(\alpha)$,

$$G(\alpha) = \frac{1}{bD} \left[\frac{\partial W^*(\alpha)}{\partial \alpha} \right] = \frac{P^2}{E'b^2 D} g(\alpha) = G_R(\alpha) \quad (1.2)$$

with the dimensionless energy release rate function $g(\alpha)$ defined as a function of the structure compliance $\lambda(\alpha)$ as follows $g(\alpha)=E'b[\partial\lambda(\alpha)/\partial\alpha]/2$.

When the resistance to crack growth G_R is estimated as a function of the equivalent crack length a (or in other terms, the relative crack length $\alpha=a/D$), the quasibrittle failure leads to a *Resistance-curve* (or *R-curve* as first pointed by Lawn BR 1993), which emphasizes the stress redistributions and stored energy release taking place during the crack growth before failure (Morel S 2008). Hence, as shown in Figs. 1.3 a-b for a Single-Edge-Notched Beam loaded in Three-Point-Bending (SEN-TPB), the *R-*

curve in wood obtained from the load-displacement curve is characterised by the existence of a rising part, for which the resistance to crack growth increases with the crack length, followed by a plateau which denotes that the influence of the toughening mechanisms is not indefinite (Morel et al. 2005). Hence, the rising portion of the R -curve ($\alpha < \alpha_c$ in Fig. 1.3-b) might be interpreted as the energetic response of the FPZ development observed in Fig. 1.2-a (with $\Delta a < \Delta a_c$) up to the attainment of the critical size of the FPZ (*i.e.*, $\Delta a = \Delta a_c$ in Fig. 1.2-b), with a fully developed FPZ. The second part of the R -curve ($\alpha \geq \alpha_c$ in Fig. 1.3-b) might correspond to the crack propagation with non-corresponding increase in volume of the FPZ (Fig. 1.2-c), with the resistance to crack growth G_R becoming independent of the equivalent crack length (Fig. 1.3-b). The reported behaviour observed in the second part of the R -curve (for $\alpha \geq \alpha_c$ in Fig. 1.3-b), defines an horizontal asymptote (known as the *plateau* of the R -curve) with the retrieved critical resistance value noted as G_{Rc} . The onset of the R -curve *plateau* defines the so called critical energy release rate G_{Rc} , with the corresponding abscissa α_c (Fig. 1.3-b) referred to as the critical (or characteristic) relative (equivalent) LFM crack length. The extent of α_c provides an approximation of the effective length of the FPZ (Morel et al. 2008), since $\alpha_c = \alpha_0 + \theta = a_0/D + \Delta a_c/D$. Accordingly, θ is designated the relative length of the FPZ and Δa_c the equivalent length of the FPZ.

Though G_{Rc} is regarded as an intrinsic material property (Irwin GR 1960, and Krafft et al. 1961), experimental evidences on the R -curve however revealed that the assumption is only valid in a very narrow range of specimen geometries and structure sizes. These dependences in wood were firstly investigated by Morel S et al. (2002 a, 2002 b and 2003) and Morel S (2007).

Experiments performed with the SEN-TPB in spruce (Figs. 1.3 a-b) also revealed that the R -curve develops both in the pre and in the post peak regime (*i.e.*, turning $G_R(\alpha_u) < G_{Rc}$). Indeed, as shown in Fig. 1.3-b the (equivalent) relative crack length α_u corresponding to the peak-load P_u is smaller than the critical relative crack length α_c . This behaviour is observed in specimens currently tested on the lab's scale, except in certain geometries for which $g'(\alpha) = 0$ as noticed by Morel et al. (2005), as the TDCB (*i.e.*, the Tapered Double Cantilever Beam).

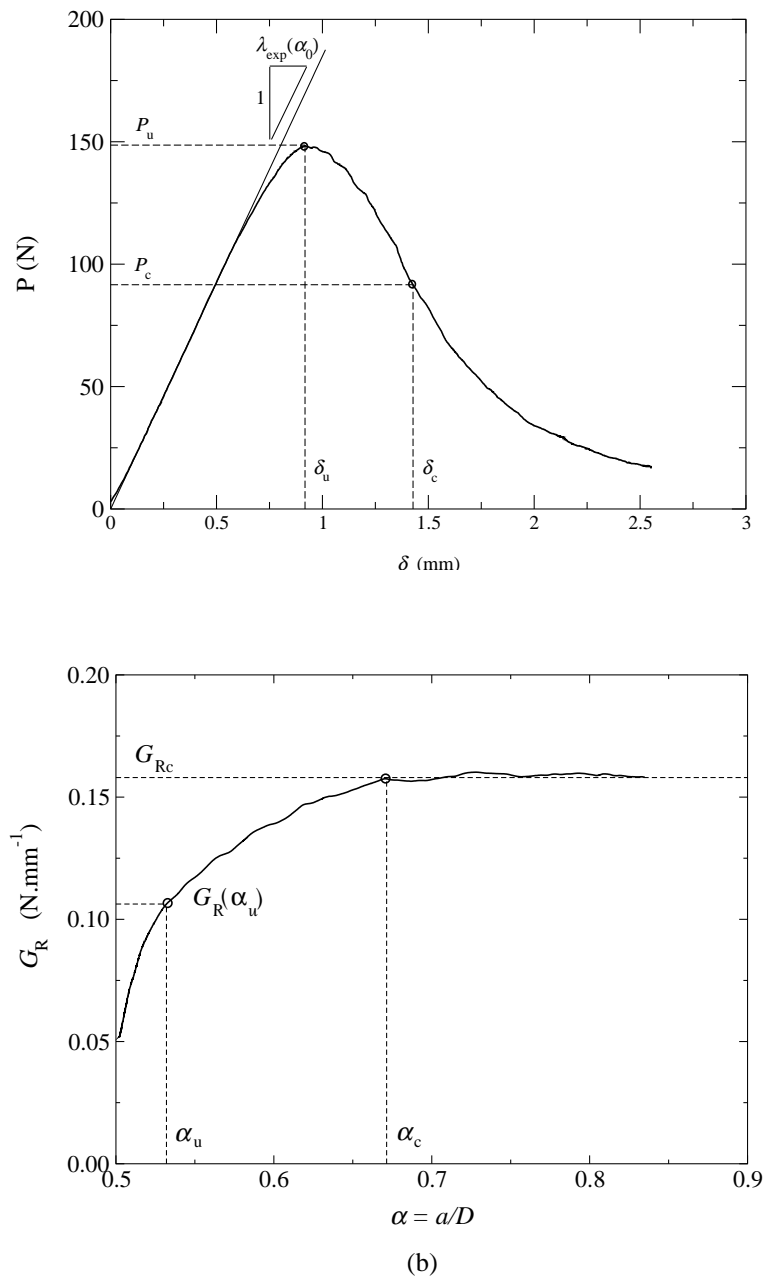


Figure 1.3 Typical (a) load-displacement curve and corresponding (b) R -curve obtained in spruce for the SEN-TPB test in the TL system (Appendix A2.1). Adapted from Morel S et al. (2005).

1.4 Cohesive crack models

Linear Elastic Fracture Mechanics (LEFM) theory takes for granted that a sharp crack tip does exist in a solid body for which stress fields may be determined. Although the elastic solutions envisage infinite stresses at the crack tip, *authentic* materials experience damage and yielding phenomena providing against this from actually occurring. Although linear elastic stress-relative displacement relationships are

considered to describe rupture in materials such as cast iron or glass, they can barely be well thought-out in materials which exhibit toughening mechanisms such as wood.

The degree to which toughening mechanisms influence fracture behaviour dictates whether LEFM can be applied to a certain material, bringing into the discussion how relevant are the dimensions of the fracture process zone (FPZ) compared to the structure size (Fig. 1.2). Usually, FPZ can be described by two basic approaches. One sustains that (a) the whole FPZ is lumped into the crack-line and is characterised in the form of a stress relative-displacement law which exhibits softening; whereas in the other (b) the inelastic deformations in the FPZ are smeared over a band of a definite width, supposed to exist ahead of the main crack. Only the first approach will be in the limelight in this Thesis, which may be found in the literature under a variety of names, e.g., cohesive crack model, fictitious crack model, Dugdale-Barenblatt model, and crack with bridging stresses (Bažant ZP and Planas J 1998, Morel S et al. 2002 and 2005).

The cohesive crack is the simplest model that permits to describe in full the progressive fracture process, taking into account the basic aspects of the non-linear behaviour of the material ahead of the tip of a pre-existent crack. The fundamental assumption of the cohesive crack model (e.g., in Mode I), is that FPZ of a finite length can be described by a fabricated chink able to transfer normal stress $\sigma(x)$ by means of a function (monotonically decreasing) of the opening width w , of the type $\sigma = f(w)$.

The most important feature of the cohesive crack model is the softening curve of the material, which in a certain sense replaces the stress-strain curve in theories such as plasticity. In this context, every material has its own softening curve which ought to be determined by means of experiments on this particular material.

First reported studies on cohesive crack models are attributed to Dugdale DS (1960) and Barenblatt GI (1962). These researchers separately treated a crack with a plastic zone as a slightly larger fictitious crack with closing stresses applied at the tips. Subsequently, cohesive cracks have largely been used to describe the material behaviour close to the near-tip non-linear zone for cracks in a multiplicity of materials such as metals, ceramics, geomaterials and polymers. In the seventies, Hillerborg et al. (1976) applied an alike approach to Dugdale and Barenblatt to simulate the effects of the FPZ in concrete, accounting for observed mechanisms of micro-cracking and bridging. According to the proposed model, the crack-tip was replaced by an equivalent crack

containing closing stresses. Instead of remaining constant during fracture alike Dugdale's model, stress rather follows a measurable function of crack opening. Nonlinear fracture mechanics modelling in wood has been preferably performed through the application of fictitious or cohesive crack models, which in essential comprise variations of a model proposed by Hillerborg et al. (1976) and Hillerborg (1991). A cohesive zone is typically modelled using FE calculations through a made up line crack transmitting tractions σ as a function of the crack opening w , by means of interface (finite) elements (Rice JR 1972, de Moura MFSF et al. 1997) with predetermined stress-softening properties along the crack path. Pioneering works involving the elaboration of fictitious crack models applied to wood are attributed to Boström L (1992). Since then the bilinear stress-softening model (Fig. 1.4), initially proposed by Petersson PE (1981) to simulate crack growth in concrete, was used by Stanzl-Tschegg et al. (1995) to obtain wood load–displacement curves in a developed wedge-splitting test protocol.

A recent method involving the single edge notched beam loaded in three-point bending (SEN-TPB) was developed (Dourado et al. 2008) to identify the material cohesive properties in two wood species, combining experimental data and a developed Genetic Algorithm (GA). The work revealed the existence of a non-negligible damaged zone as well as the growth perturbation of this zone along crack propagation in the SEN-TPB shape.

In regards to the cohesive zone modelling schematically represented in Fig. 1.4 (for the bilinear softening law), the FEM simulations permit to estimate the extent of the cohesive zone l_{coh} as the distance (measured along the crack path) between the numerical crack tip and the position of the integration point in the interface, for which the stress is equal to the tensile strength f_t (providing that the crack is already in progress). The numerical crack length a_{num} on its turn is defined by the distance measured from the axis of the applied load (hidden line in Figs. 1.4 a-c) up to the first integration point of the interface for which the normal stress is non-null. Therefore, as long as the equivalent crack length a (*i.e.*, αD) does not reach the critical extent a_c (*i.e.*, $a < a_c$ shown in Fig. 1.3-b and Figs. 1.4 a-b) the size of the cohesive zone l_{coh} does not attain its critical dimension $l_{\text{coh } c}$. In such a case, establishing a relation with

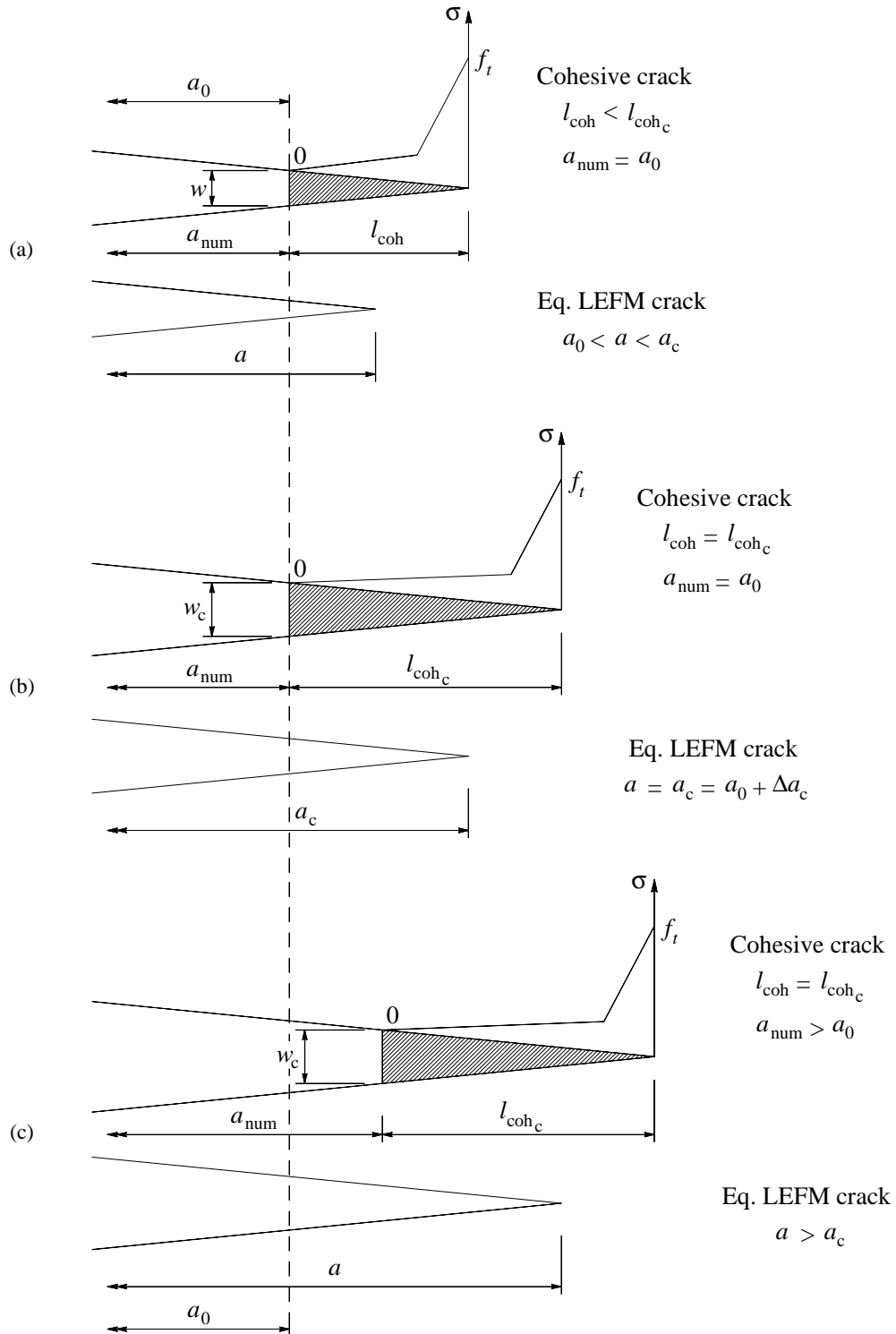


Figure 1.4 Sketch of the cohesive zone behaviour: comparison of the numerical crack length a_{num} with the equivalent LFM crack length a for different stages of the numerical crack propagation. Stages: cohesive zone (a) under development, (b) once attained its critical size and (c) fully developed at the crack tip (under crack propagation). Additional parameters: a_0 , initial crack length; l_{coh} , extent of the cohesive zone ; w , crack opening; Δa_c , equivalent length of the FPZ ($\Delta a_c = a_c - a_0$). The vertical hidden line represents the axis of the applied load. In: Morel S et al. (2008).

the evolution of the resistance to crack growth G_R (Section 1.3), the actual regime (*i.e.*, $l_{\text{coh}} < l_{\text{coh}_c}$) corresponds to the ascending part of the R -curve. As the local stress σ increases (provided that crack progresses in a self-similar way) the size of the cohesive zone attains its critical dimension, as shown in Fig. 1.4 (b) (*i.e.*, $l_{\text{coh}} = l_{\text{coh}_c}$). Indeed, as will be discussed in Chapters II and III, the progress of the extent l_{coh} (Fig. 1.4) is drastically influenced by the ligament length (*i.e.*, $D - a_0$). With the attainment of a fully developed cohesive zone (*i.e.*, size of the FPZ), the equivalent LEFM crack length turns out $a = a_c$ (Fig. 1.4 b) and the crack opening reaches the critical extent (*i.e.*, $w = w_c$). In an energetic point of view, the actual state corresponds to the onset of the plateau of the *Resistance*-curve shown in Fig. 1.3-b, with the energy release rate $G_R = G_{Rc}$. Since the toughening mechanism is not indefinite in quasibrittle failure (Section 1.3), the extent of the cohesive zone l_{coh} in the course of the loading process remains $l_{\text{coh}} = l_{\text{coh}_c}$ (Fig. 1.4 c). In such a case, the local crack opening w is kept unchanged (*i.e.*, $w = w_c$) while the equivalent crack length a propagates.

As observed by Morel et al. (2008) and Lespine I (2007), when the equivalent LEFM crack length $a \geq a_c$ (or in other terms: $\alpha \geq \alpha_c$ as illustrated in Fig. 1.3 b), then (i) the length of the cohesive zone remains constant (Fig. 1.4 c) and (ii) the stress profile at the crack front $\sigma = f(w)$ remains unchanged (Fig. 1.4 c). As a consequence, the cohesive zone can be considered in an energetic steady state, in the sense that it does not require more energy involved in the modification of its length and/or in its stress distribution. Therefore, the propagation of the numerical crack length a_{num} of an extent δa , with its critical cohesive zone, is expected to give rise to the energy release $dW = G_f (b \delta a)$; where G_f corresponds to the energy required to separate completely the crack faces at a given loading step, and $(b \delta a)$ corresponds to the cracked surface originated during the increment δa .

1.5 Size effect

The change of the mechanical response due to similarity preserving modifications of the dimension of a physical system is one of the most fundamental aspects of every physical theory, generally referred to as Size Effect (SE). Unlike other branches of Physics, scaling in Solid Mechanics has been largely neglected until recent times. A

plausible reason for this probably lies on the fact that theories of structural failure that have succeeded for a long period of time, exhibit no deterministic Size Effect (Bažant ZP 1993). That is the case of (a) Plasticity as well as other theories founded on the concept of a critical stress (strength) or a critical strain, and (b) Fracture Mechanics applied to a critical crack which size at incipient failure is independent of the structure size D and negligible when compared to D , as is typical of most metal structures embrittled by fatigue (Bažant ZP 1997 a). As a result, experimental evidences showing size effects were commonly explained on the context of the randomness phenomena affecting the material strength, as proposed by Weibull W (1939). Size Effect is considered a key issue particularly in the case of quasibrittle materials which are known to exhibit a large FPZ where a variety of toughening mechanisms take place.

Within the framework of Bažant's theory (Bažant ZP 1997 b and Bažant ZP 1997 c) the size effect for geometrically similar notched structures of different sizes D can be described by means of the nominal stress

$$\sigma_N = c_N \frac{P}{bD} \quad (1.3)$$

with P standing for the external load, b for the width of the structure cross section, D for the characteristic structure dimension, and c_N a coefficient introduced for convenience. Ever since the analysis regards the ultimate load P_u (*i.e.*, $P = P_u$), the nominal stress is called the nominal strength of the structure. For the test involving the simply supported beam in three-point-bending, the coefficient c_N may be chosen in order to make σ_N to coincide with the maximum normal stress. In such a case, if h is the beam height ($D=h$), and L the beam span, then $\sigma_N = 3/2(PL)/bh^2 = c_N(P/bD)$, with $c_N = 3/2(L/h)$. It turns thus out that c_N depends on the span-to-depth ratio, which obviously varies according to the beam size selection. This draws to the important conclusion that size effect is firmly defined only when geometrically similar specimens (or structures) with geometrically similar notches are analysed under similar loading conditions (Bažant ZP and Planas J 1998). Indeed, if this is not taken into account shape dissimilarities in size effect results may some-how be erroneous. Doing so, c_N yields to a constant, since the ratio L/h is kept unchanged by definition (Bažant ZP and Kazemi TK 1990).

A variety of possible plots showing particular aspects of the size effect do exist in the literature, however the most widely divulged is the bilogarithmic plot exhibited in Fig. 1.5, according which the nominal strength σ_N is represented against the characteristic specimen size D . This plotting is performed using the original form of the size effect law (SEL) (Bažant ZP 1984),

$$\sigma_N = \frac{B f_u}{\sqrt{1+\gamma}} \quad (1.4)$$

according which f_u is an arbitrary measure of the material strength, γ is the relative structure size ($\gamma = D/D_0$) and B an empirical constant. The relative structure size γ is also called the brittleness number because as $\gamma \rightarrow \infty$ the material turns more worthy of a fully brittle behaviour, whereas when $\gamma \rightarrow 0$ the material turns fully non-brittle, or plastic (Bažant ZP 1997 c). Hence, the size effect (SE) curve shown in Fig. 1.5 represents the transition from an horizontal asymptote (domain of the Strength Theory), to a descending asymptote which corresponds to a power law of exponent $-1/2$ (characterising LEFM). The point of interception of both asymptotes is identified by D_0 (Fig. 1.5).

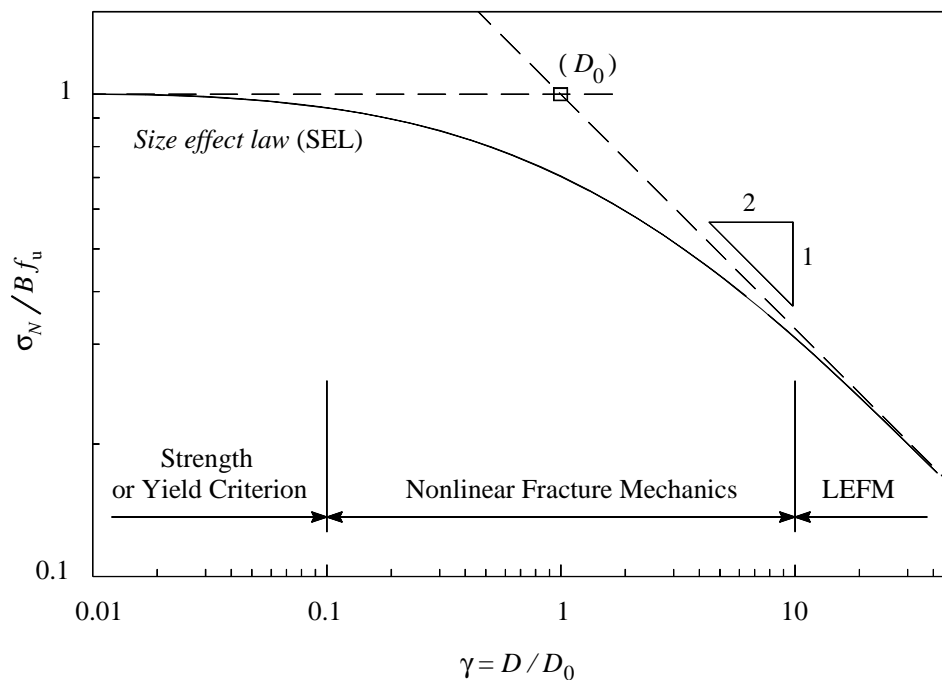


Figure 1.5 Size effect on the nominal strength (Adapted from Bažant ZP and Kazemi TK 1990).

Therefore, if $D \ll D_0$ (*i.e.*, on the micro-scale) the brittles number $\gamma \rightarrow 0$, and $\sigma_N \cong B f_u = \text{constant}$ (Eq. 1.4). Thus, no size effect is expected to occur on the micro-scale. Moreover, in structures of this size the FPZ is expected to occupy the whole volume of the structure, inducing no stress concentration (energy release is negligible), with failure occurring with no crack propagation.

For large structure sizes $D \gg D_0$ (*i.e.*, on the macro-scale) the brittles number $\gamma \rightarrow \infty$, leading to $\sigma_N \approx D^{-1/2}$ (Eq. 1.4). On the macro-scale, the size effect curve follows a power law which coincides in the log-log plot of Fig. 1.5 with the least straight line of slope $-1/2$ expected from LEFM. Indeed, in large structure sizes, the FPZ is expected to lie within an infinitesimal volume fraction of the structure, with corresponding stress and displacement fields surrounding the FPZ being estimated from LEFM.

The Bažant's size effect law (SEL) in Eq. (1.4) applies to several geometries tested in Labs all over the world. It was verified experimentally and justified theoretically for a broad range of many different materials and structures (Jirásek M and Bažant ZP 2002). The law was derived from asymptotic analysis performed both on small (Strength Theory) and on large (LEFM) structure sizes D . This means that the estimate of the nominal strength σ_N over the range $0.1 < \gamma < 10$ in Fig. 1.5 (*i.e.*, in the *crossover* regime) is the consequence of the asymptotic matching of the other two regimes. As a consequence, the regime proposed for the intermediate structure sizes does not appear accurately defined, deserving thus some more thinking, mainly because this is usually the range of the experimental data. Bearing this matter in mind, the numerical simulation of the quasibrittle fracture turns a key issue, since one can dispose of a method to validate any proposed law to describe more in detail the progress of σ_N with the structure size D , over the *crossover* regime.

Hence, as exposed in Chapter II the study first involved the evaluation of the *Resistance*-curve in two wood species commonly used in timber construction (for the SEN-TPB). The cohesive crack modelling has then been performed, revealing that the energetic state is not stationary for both wood species during crack propagation. This behaviour clearly unfolded the problematic interaction of the cohesive zone with the

structure boundaries, which turns crucial when the size effect study is to be conducted on the energetic basis.

Then, Chapter III is presented on the basis of a derivation of the energetic size effect law based on the equivalent LEFM and on the asymptotic analysis. Since one of the main consequences of the *R*-curve behaviour in quasibrittle materials is the effect of the structure size on its nominal strength (Morel S 2008), the energetic size-effect is essential to characterise an additional asymptotic regime which stands in the *crossover* regime. The additional asymptotic behaviour is validated by means of the cohesive crack modelling.

Chapter IV is presented much to the purpose of the size effect study revealing the results obtained in the experiments. Since testing involved the examination of structures of different sizes, the self-weight plays an important role, turning thus vital to introduce corrections to take it into account. The results issued from size effect on the nominal strength, were found quite in accordance with the additional asymptotic behaviour defined in Chapter III.

Chapter II

Quasibrittle Fracture

Chapter II

2.1 Introduction

The present Chapter aims at simulate the quasibrittle failure in two wood species frequently used in timber construction: Maritime pine (*Pinus pinaster* Ait.) and Norway spruce (*Picea abies* L.). With such a purpose, experiments were performed involving the single-edge-notched beam loaded in three-point-bending (SEN-TPB) and corresponding *Resistance*-curves determined by means of an equivalent LEFM approach based on the compliance. An inverse method is then detailed to identify the cohesive properties of a bilinear stress-softening law, combining the obtained experimental data with a developed Genetic Algorithm (GA). Quasibrittle failure is simulated using the identified cohesive properties in both wood species. Performed (FEM) computations revealed that a non-negligible cohesive zone do exist interacting (in different scales) with the structure boundaries. Based on the confinement of the cohesive zone, concerns are revealed regarding the required specimen (critical) dimension necessary to perform size effect studies in wood, ever since the SEN-TPB shape is used. Identical concerns are addressed to other specimen geometries (and/or sizes) which may induce compressive stress fields over the ligament length.

2.2 Experiments

2.2.1 *Material and specimens*

Maritime pine (*Pinus pinaster* Ait., 647 kgm^{-3}) and Norway spruce (*Picea abies* L.; 420 kgm^{-3}) were used in this study as testing material proceeding each from one single stem with a diameter approximately equal to 400 mm. Equilibrium Moisture Content (EMC) in wood has been found in 12%, after had been conditioned in a climate of 20°C

and 65 RH (Relative Humidity) until equilibrium. Wood (see Appendix 2.1) was machined far enough away from the stem pith to comply with anatomic axis orientations and nominal dimensions represented in Fig. 2.1, and clear parts (free from knots and material defects) bonded with a suitable epoxy adhesive (geometry adapted from Gustafsson PJ 1988). Starter notches were made along the composite beam mid-section using a band saw (1 mm thick) and initial crack notches sharpened using a razor blade (depth of sharp notch: 1-1.5 mm) up to $h/2$ (i.e. $a_0 = 35$ mm), just a little while before conducting experimental tests.

2.2.2 Fracture tests

Twelve single-edge-notched beams with the same size (Fig. 2.1) were tested to determine load-displacement curves up to complete rupture, for each wood species. The initial crack/depth ratio a_0/h was set to 0.5 (Fig. 2.1) and the span/depth ratio s/h to 6 (Fig. 2.2). A mechanical spindle-driven tension-compression machine (20 kN total capacity) was used to induce fracture in mode I. A load cell with the capacity of 1 kN has been installed and crosshead displacement rate regulated to reach the peak load, P_u , in 3 ± 1 minute during fracture tests, thus minimizing possible viscoelastic effects in wood. Measurement of load-point absolute displacement values, δ_F , has been attained setting one LVDT (range ± 2.5 mm) in contact with a reference surface rigidly attached to the load application device (Fig. 2.2). Two metal bars were set on metal pins previously bonded to each side of the composite beam in alignment with the beam supporting plans. Displacement values δ_i ($i = 1, 2$) were continually measured by means of LVDTs (2: range: ± 1.0 mm) positioned in contact with each metal bar mid-span

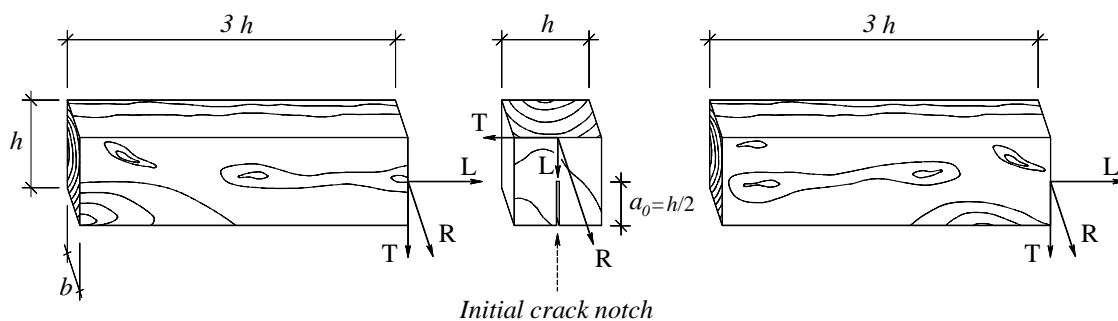


Figure 2.1 Parts set up before bonding ($h = 70$ mm, $b = 40$ mm and $a_0 = h/2$). Wood anatomic axis: (L) Longitudinal, (R) Radial and (T) Tangential. (In: Dourado N. et al. 2008).

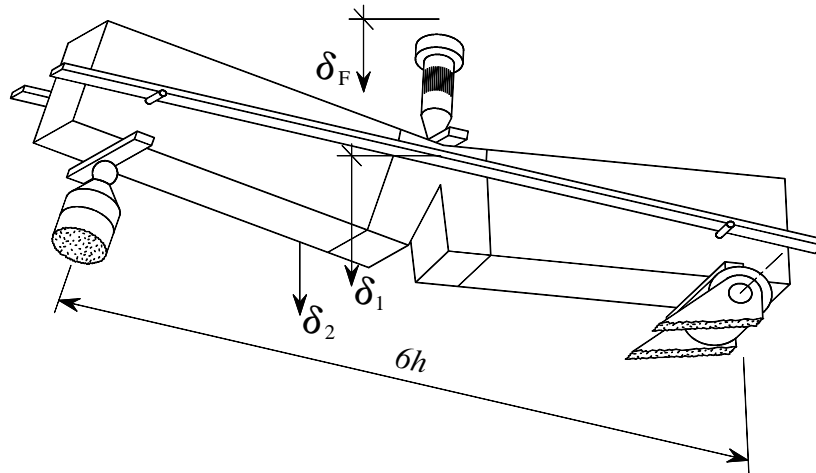


Figure 2.2 Sketch of TPB test set-up. δ_F : Load-point displacement; δ_i : Metal bar mid-span displacement-points in both sides ($i = 1, 2$) of the specimen. Recorded displacements : $\delta = \delta_F - (\delta_1 + \delta_2) / 2$. (In: Dourado N. et al. 2008).

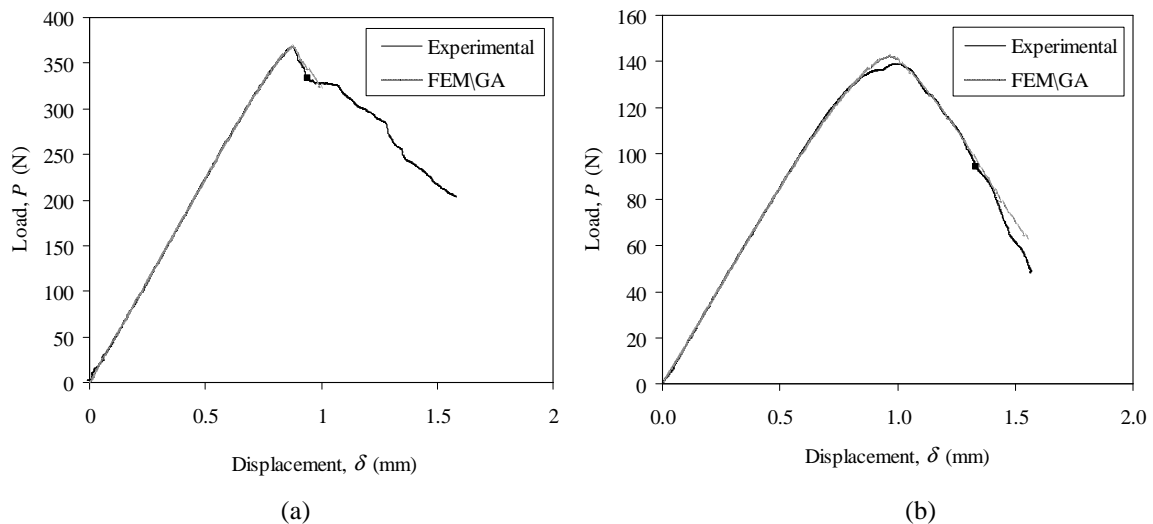


Figure 2.3 Typical load-displacement curves (Mode I) obtained in wood fracture: (a) Maritime pine (*Pinus pinaster* Ait.) and (b) Norway spruce (*Picea abies* L.). Fine thread shows the agreement between numerical and experimental data obtained through the Inverse Method (Section 2.5). Printed black square labels correspond to the end of the *Resistance*-curve: ($a_{lim} = a_c + 2$ mm in pine; $a_{lim} = a_i + 2$ mm in spruce). (In: Dourado N. et al. 2008).

points. Recording acquisition frequency during fracture tests was set to 5 Hz. Recorded load-displacement values (δ_F) were subsequently corrected accounting for potential specimen's rotation movement during bending, through the equation: $\delta = \delta_F - (\delta_1 + \delta_2) / 2$. Figure 2.3 illustrates typical load-displacement curves (P - δ curves) obtained for both wood species. A divergence from the linearity is observed

before the ultimate load attainment in both wood species. This phenomenon is attributed to the development of the FPZ at the crack-tip and has been shown by Vasic S and Smith I (2002), making use of *in situ* scanning electron microscopy, that crack bridging is the main toughening mechanism mobilised in wood fracture. Though recognised as a local phenomenon at the specimen scale, a mechanism of this type is itself at the source of the impossibility to apply LEFM directly to estimate failure in quasi-brittle materials, requiring the application of nonlinear fracture theories. However, an adaptation of LEFM referred to as an *equivalent linear elastic approach* can provide a useful approximation of the quasi-brittle behaviour.

2.3 Equivalent LEFM

In order to validate the applicability of an equivalent LEFM approach specimens taken from tested wood were submitted to cyclic loading until final fracture (Morel S et al. 2005). It has been proved that quasi-brittle behaviour of tested wood can be described in the frame of an equivalent linear elastic analysis, where observed compliance increase can be attributed to the extension of an equivalent elastic crack, *i.e.* a sharp traction-free crack of length a in the sense of LEFM (Bažant ZP 2002, Bažant ZP and Kazemi MT 1990). Accordingly, as reported in Section 1.2 the tip of the elastic equivalent crack is neither at the beginning of the FPZ nor at the end of it. It is considered to be given by $a = a_0 + \Delta a$ (Fig. 1.2 c), being a_0 the actual traction free initial crack length and Δa the equivalent crack length increment.

Compliance evolution as a function of the numerical crack length $\lambda(a)$ is firstly computed through linear elastic FE analyses (Fig. 2.4) using the set of elastic properties presented in Table 2.1 ($a_0 \leq a < h$). To account for scattering of wood mechanical properties, compliance evolution $\lambda(a)$ is corrected for each specimen using a multiplicative correction factor $\psi = \lambda_{\text{exp}}(a_0) / \lambda(a_0)$, with $\lambda_{\text{exp}}(a_0)$ standing for the compliance value obtained experimentally in the ascending linear domain, and $\lambda(a_0)$ the compliance value resulting from FEM calculations for the initial crack notch extent. The correction factor ψ is thus evaluated no more than once per specimen, since the only known value of a in the experiments is the initial crack notch extent a_0 . Indeed, for values of $a > a_0$ the damage extent which develops ahead of the crack-tip leads to

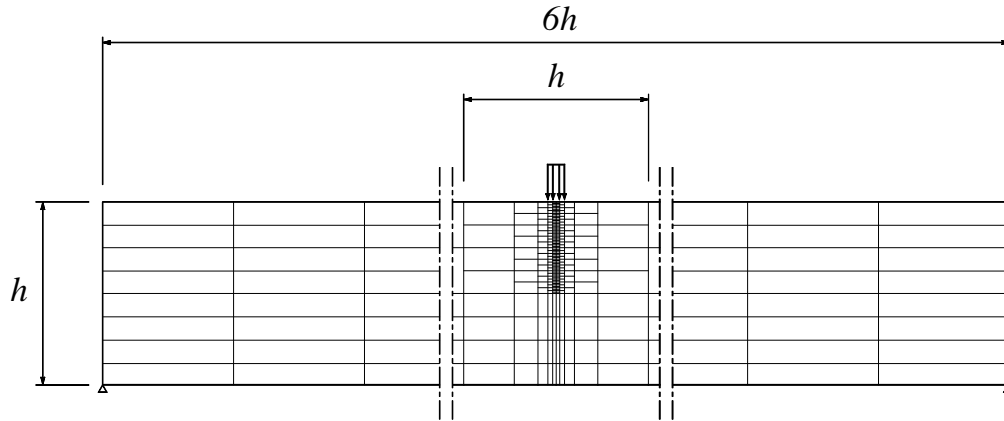


Figure 2.4 FE-modelling used in ABAQUS[®] 6.5-1 compliance computations performed using 352 isoparametric 8-node plane strain elements ($h = 70$ mm).(In: Dourado N. et al. 2008).

Table 2.1 Elastic properties of Maritime pine (*Pinus pinaster* Ait.) (Xavier J et al. 2004) and Norway spruce (*Picea abies* L.) (Guitard D 1987)

Wood Species	E_L (MPa)	E_R (MPa)	E_T (MPa)	ν_{TL}	ν_{RL}	ν_{TR}	G_{TL} (MPa)	G_{RT} (MPa)	G_{RL} (MPa)
Maritime pine	15 133	1 912	1 010	0.034	0.060	0.309	1 042	286	1 115
Norway spruce	9 900	730	410	0.018	0.032	0.306	610	22	500

equivalent crack length extents (evaluated from the experimental compliance) different of the actual crack length. A corrected numerical compliance function $\lambda_{\text{cor}}(a)$ is therefore required: $\lambda_{\text{cor}}(a) = \psi \times \lambda(a)$. References found in the literature (Ferreira LET et al. 2002, Ebrahimi et al. 2003, and Morel et al. 2002, 2003) sustain the idea that a multiplicative correction factor can be applied to those cases for which the specimen compliance is essentially found as a function of a single elastic modulus. Thus, if one examines the specimen constitutive parts disposal along the axial orientation (Fig. 2.1), and observes that in wood the Tangential elastic modulus E_T is much lower than the Longitudinal modulus E_L , then it turns that the specimen compliance (*i.e.*, the numerical compliance λ_{num}) is mainly a function of the central modulus E_T (*i.e.*, $\lambda_{\text{num}} = f(E_T^{-1})$ when the shearing forces are neglected) (Morel et al., 2005). This observation enables to establish the comparison on the modulus basis considering another beam of identical dimensions, for which the elastic modulus (unknown) is E_T^* ,

doing $\psi = E_T / E_T^*$. Consequently, as $\lambda^* \propto E_T^{*-1}$, it turns $\lambda^* / \lambda \cong E_T / E_T^* = \psi$. In other terms, this equivalence may be established setting $\psi \cong E_{\text{num}} / E_{\text{exp}}$, with E_{num} standing for the numerical modulus, while E_{exp} represents the experimental modulus (both attributed to the specimen central part). As a result of this compliance correction procedure, it is possible to determine the equivalent linear elastic crack length a , corresponding to any point of the experimental load-displacement curve (Fig. 2.3). Hence, for a given point of this load-displacement curve (Fig. 2.5) the compliance, $\lambda_{\text{exp}}(a)$, is determined and the corresponding equivalent linear elastic crack length computed through a process of dichotomy applied to the corrected numerical compliance function $\lambda_{\text{cor}}(a)$ previously evaluated. This corrected function enables to perform continuous computations of the elastic energy release rate for each load-displacement values recorded all along fracture tests. Usually the energy release rate is determined through analytical expressions generally obtained from FE analysis (Ferreira LET et al. 2002, Ebrahimi ME et al. 2003, Tanaka K et al. 2003), or by means of analytical procedures (Fett T et al. 2000). In the alternative method (Morel S et al. 2005) the energy release rate is directly evaluated from the experimental load-displacement curve using only the compliance function (Morel S et al. 2002, 2003), obtained from FE analysis.

As shown in Fig. 2.5, for a given experimental equivalent crack length a , the elastic energy release rate G_R is calculated dividing the elastic strain energy $W(a)$ released during a small crack extent δa (dashed area) by the corresponding crack surface $b \delta a$ (b : specimen width). The small crack extent δa was set to 1% of the initial notch extent (*i.e.*, $\delta a = 0.3$ mm), since it has been found to be the average value for which the estimated R -curves converges to a single curve. The strain energy $W(a)$ is evaluated using the experimental load-displacement curve (curve $P-\delta$) and the straight lines passing through the points corresponding to equivalent crack lengths: $a - \delta a / 2$ and $a + \delta a / 2$ (both deduced by a process of dichotomy from the corrected compliance values: $\lambda_{\text{cor}}(a - \delta a / 2)$ and $\lambda_{\text{cor}}(a + \delta a / 2)$, respectively).

Typical R -curves obtained by means of the described procedure are presented in Fig. 2.6.a and 2.6.b for pine and spruce, respectively. After a characteristic crack length a_c , the resistance does not evolve with respect to the crack length a but exhibits a plateau

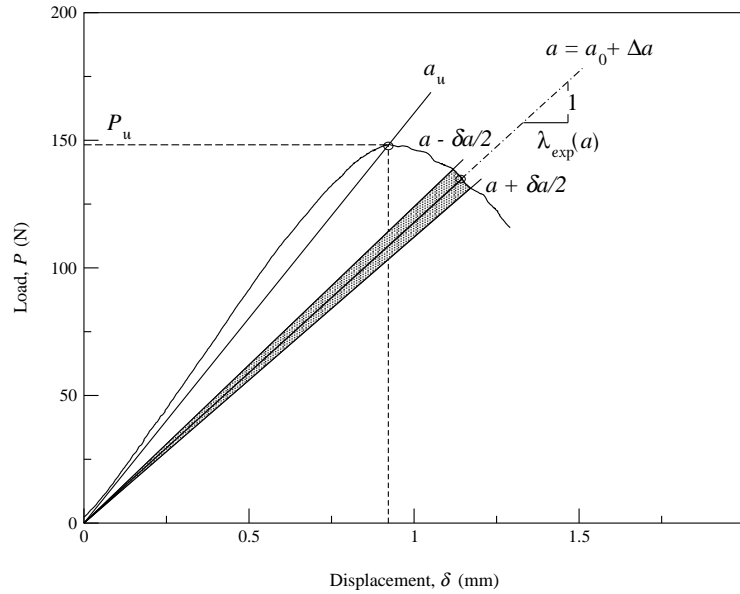


Figure 2.5 Procedure used to assess the elastic energy release rate $G_R(a) = W(a) / (b \delta a)$ in wood. P_u : ultimate load; a_u : equivalent crack length corresponding to P_u . (Adapted from Morel S et al. 2002).

value, denoted as G_{Rc} (Fig. 2.6.a). This phenomenon indicates that the influence of the toughening mechanism is not infinite at longer crack lengths, thus far tending to a stationary regime for crack lengths $a > a_c$.

Unlike pine wood, R -curves obtained for Norway spruce did not exhibit such an undoubted plateau, revealing instead an inflexion point or a short segment of nil slope before a new increase of the resistance (Fig. 2.6.b) has been obtained. In the absence of an unquestionable plateau of the resistance for this wood species, it has been decided to report the value of the resistance $G_R(a_i)$ to the referred inflexion point, or to the beginning of the short segment of nil slope a_i , depending on the cases.

Both wood species revealed resistances at the peak load $G_R(a_u)$ less significant than that which is attained at the plateau G_{Rc} (Fig. 2.6.a for pine) and $G_R(a_i)$ (Fig. 2.6.b for spruce). This indicates that the R -curve develops in the post peak regime of the load-displacement curve (Figs 2.3.a and b) (Morel S et al. 2005), resulting $a_u < a_c$ (in pine) and $a_u < a_i$ (in spruce). Tables 2.2 and 2.3 both report mean values obtained for the multiplicative correction factor ψ , compliance in the ascending linear domain $\lambda_{exp}(a_0)$, ultimate load P_u , corresponding equivalent crack length a_u , and the energy

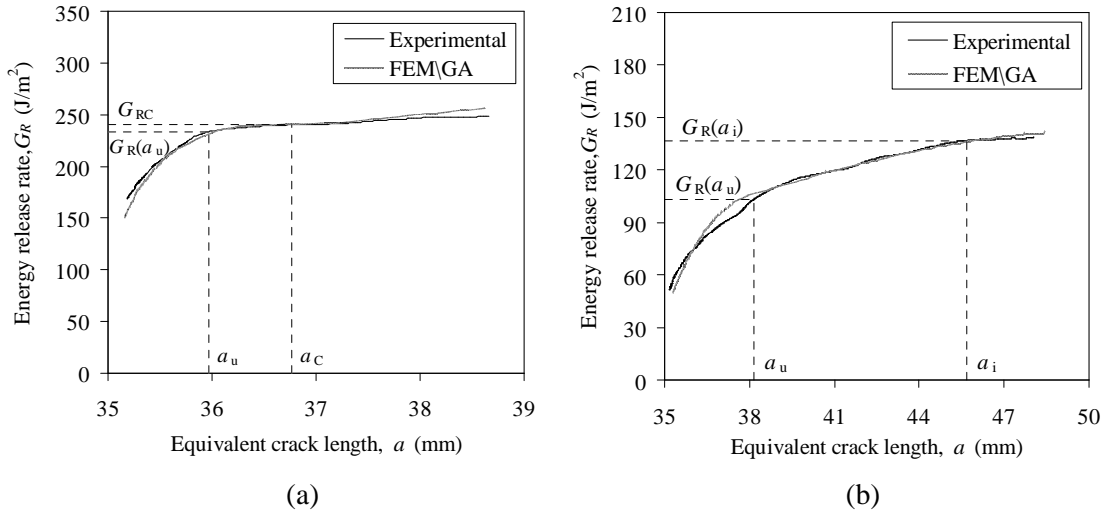


Figure 2.6 R -curves obtained in wood from P - δ curves presented in Figure 2.3.a and 2.3.b: (a) Maritime pine and (b) Norway spruce. Fine thread shows obtained R -curves by means of the Inverse Problem. G_{RC} : Critical energy release rate; a_c : Characteristic equivalent crack length; $G_R(a_u)$: Energy release rate corresponding to ultimate load P_u ; a_u : Equivalent crack length corresponding to P_u . (In: Dourado N. et al. 2008).

Table 2.2 Mean values obtained in TPB fracture tests for Pine wood (*Pinus pinaster* Ait.). ψ : Multiplicative correction factor; $\lambda_{exp}(a_0)$: Experimental compliance obtained for the initial notch a_0 ; P_u : Ultimate load; a_u : Elastic equivalent crack length corresponding to P_u ; $G_R(a_u)$: Energy release rate corresponding to P_u ; a_c : Characteristic value of elastic equivalent crack length corresponding to the plateau value of the R -curve; G_{RC} : Plateau value of the R -curve. (Consult Appendix A2.3 for complete record exhibition). (In: Dourado N et al. 2008)

<i>Pinus pinaster</i> Ait.	ψ	$\lambda_{exp}(a_0)$ (10^{-3} mm/N)	P_u (N)	a_u (mm)	$G_R(a_u)$ (J/m^2)	a_c (mm)	G_{RC} (J/m^2)
Average (12 Specimens)	1.21	2.21	330.4	36.9	201.6	37.6	209.2
St. Dev.	0.09	0.15	26.1	0.6	24.8	0.6	27.5

Table 2.3 Mean values obtained in TPB fracture tests for Norway spruce (*Picea abies* L.). $G_R(a_i)$: Energy release rate at the slender rising trend segment of the R -curve. Remaining parameters are as defined in Table 2.2. (Consult Appendix A2.3 for complete record exhibition). (In: Dourado N et al. 2008)

<i>Picea abies</i> L.	ψ	$\lambda_{exp}(a_0)$ (10^{-3} mm/N)	P_u (N)	a_u (mm)	$G_R(a_u)$ (J/m^2)	a_i (mm)	$G_R(a_i)$ (J/m^2)
Average (12 Specimens)	1.25	5.48	145.8	37.3	101.6	47.0	144.6
St. Dev.	0.09	0.37	6.1	0.6	7.7	2.6	17.8

release rate associated to the ultimate load $G_R(a_u)$, for each wood species. In addition, for Maritime pine, Table 2.2 exhibits mean values of the resistance at the plateau G_{Rc} and corresponding critical crack lengths a_c . Table 2.3 reports the mean values of the energy release rate at the slender rising trend segment of the R -curve obtained for Norway spruce $G_R(a_i)$, and corresponding equivalent crack length a_i .

2.4 Cohesive crack modelling

A bilinear stress-softening model was used to simulate mode I crack propagation in wood using the finite element code ABAQUS[®] 6.5-1 through a programmed user subroutine.

2.4.1 Interface finite element

The interface finite element used in this work is detailed in de Moura MFSF et al. (1997). It is compatible with used 2D solid element of the ABAQUS[®] library, and its formulation is based on the penalty function method. Stresses in interpolation points, for an undamaged material, are determined from the relative displacements: $\boldsymbol{\sigma} = \mathbf{D}\mathbf{w}_r$. Accordingly, \mathbf{w}_r represents the vector of the relative displacements between two homologous points and can be determined from the displacements field of both crack faces (face 1 and 2),

$$\mathbf{w}_r = \begin{Bmatrix} w_s \\ w_n \end{Bmatrix} = \begin{Bmatrix} w_s \\ w_n \end{Bmatrix}_1 - \begin{Bmatrix} w_s \\ w_n \end{Bmatrix}_2 \quad (2.1)$$

and indexes s and n stand for local tangential and normal directions of the interface element, respectively. Matrix \mathbf{D} establishes the relation between stresses and relative displacements,

$$\mathbf{D} = \begin{bmatrix} d_s & 0 \\ 0 & d_n \end{bmatrix} \quad (2.2)$$

Matrix components are the shear (d_s) and the normal (d_n) interface stiffnesses defined by the user. Since the thickness of the interface FE is null, then d_s and d_n in matrix \mathbf{D}

must be set to a very high value, thus preventing the interpenetration of the finite element faces, too. In this context, it has been noticed that small values induce large interpenetrations, incompatible with the physical reality, while large values lead to numerical problems. Thus, the optimum interface stiffness parameters are the largest values that do not produce numerical problems. Interface stiffness values (d_s, d_n) were set to 10^6 N/mm^3 (de Moura MFSF et al. 1997).

2.4.2 Bilinear stress-softening model

According to this model, after the peak-point (w_o, f_t) the stress-softening zone is defined by two descending lines (Fig. 2.7). The first one spans the peak-point and the break-point (w_b, f_b), and the corresponding amount of energy (represented by the first triangle) is attributed to “micro-cracking” phenomenon (Stanzl-Tschegg SE et al. 1995). Resulting energy is defined as the cohesive microcracking energy $G_{f\mu}$. The second branch is drawn from the break-point towards ($w_c, 0$), and the amount of energy represented by the dashed triangle is attributed to the “fibre-bridging” phenomenon (Stanzl-Tschegg SE et al. 1995). Resulting energy is defined as the cohesive fibre-bridging energy G_{fb} . The total area under the bilinear softening-stress model corresponds to the cohesive fracture energy G_f , *i.e.*, the energy required to completely separate two nodes of the interface, and is equal to the sum of both cited energies, *i.e.*, $G_f = G_{f\mu} + G_{fb}$. The cohesive fracture energy can also be written as,

$$G_f = \frac{f_t w_b}{2} + \frac{f_b w_c}{2} \quad (2.3)$$

Since the energy associated to the elastic domain is negligible when compared to the other regimes (d_s and d_n in Section 2.4.1), G_f in Eq. (2.3) is not defined as function of w_o . Accordingly, the softening relation is given by the equation,

$$\boldsymbol{\sigma} = (\mathbf{I} - \mathbf{E}) \mathbf{D} \mathbf{w}_r \quad (2.4)$$

with \mathbf{I} representing the identity matrix and \mathbf{E} the diagonal matrix containing the damage parameter

$$e = \frac{w_b (w_r - w_o)(1 - \gamma)}{w_r (w_b - w_o)}, \quad w_o \leq w_r \leq w_b \quad (2.5)$$

$$e = 1 - \frac{\gamma w_b (w_c - w_r)}{w_r (w_c - w_b)}, \quad w_b \leq w_r \leq w_c \quad (2.6)$$

with

$$\gamma = \frac{f_b w_o}{f_t w_b} \quad (2.7)$$

The stress-softening model is thus defined by the independent parameters: w_b , f_b , f_t and G_f .

2.4.3 FEM calculations

In the built up bi-dimensional FE model the SEN-TPB specimen was divided into 352 8-node anisotropic plane elements according to the mesh sketch shown in Fig. 2.4. A total of 64 interface plane elements (IPE) were positioned all through an upright central line sited ahead of the initial crack notch $a_0 = 35 \text{ mm}$ ($\cong 1 \text{ IPE}/0.55 \text{ mm}$). In-plane strain analyses were performed modelling Maritime Pine (*Pinus pinaster* Ait.) and Norway spruce (*Picea abies* L.) as linear elastic orthotropic materials with engineering constants presented in Table 2.1. Boundary conditions were imposed according to performed TPB tests.

Owing to the symmetry of the FE model (Fig. 2.4), during the simulations the displacement values were monitored considering the nodal displacements at the specimen middle-height (I) in alignment with one beam supporting plan δ_I (e.g., position of left metal pin according to Fig. 2.2) and (II) close to one side (e.g., left) of the crack plane δ_{II} , at a distance Δ below the top prescribed displacement line (Fig. 2.4). At this distance Δ the compression stresses perpendicular to the longitudinal direction (see specimen orientation in Fig. 2.1) were found negligible during the crack propagation, avoiding thus the indentation phenomenon. Displacement values in FEM calculations were obtained computing: $\delta = \delta_{II} - \delta_I$.

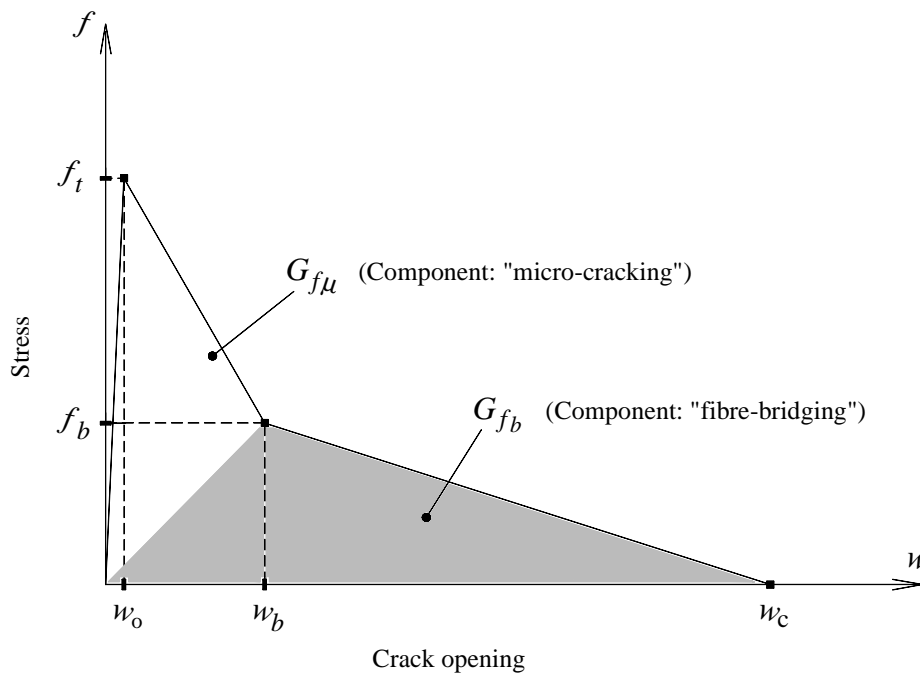


Figure 2.7 Bilinear Petersson's softening stress-softening model used to describe the natural phenomena occurring in the cohesive zone during wood fracture (Mode I): micro-cracking and fibre-bridging (with $G_f = G_{f\mu} + G_{fb}$). (Adapted from Stanzl-Tschegg SE et al. 1995).

A potential way to estimate the cohesive properties could lie in the one-to-one correspondence which seems to exist between the R -curve and the softening curve (Planas et al., 1993). In addition, it has been suggested by Planas et al. 2003, that, for a given specimen geometry and size, the relation between the R -curve and the softening curve is unique (though recognized that the R -curve is itself geometry and size dependent).

A recent study already mentioned in Chapter I, focused on the relation between the R -curve and the cohesive crack properties (Morel S et al. 2008) demonstrated the equality between the plateau value of the R -curve G_{Rc} and the cohesive fracture energy G_f (i.e., $G_f = G_{Rc}$, with G_f representing the energy corresponding to the total area under the cohesive function as represented in Fig. 2.7). On this basis, for each specimen of Maritime pine, the cohesive fracture energy G_f was fixed to the estimated value of the resistance at the plateau of the R -curve G_{Rc} (Table 2.2), whereas in the case of Normay spruce, for which the R -curves did not exhibit undoubted plateaus of the resistance, the cohesive fracture energy G_f was fixed, in a first approximation, to the values of the resistance denoted as $G_R(a_i)$ (Table 2.3).

In regard to the set of four independent parameters required to define the bilinear stress-softening model (Section 2.3.2), the cohesive fracture energy G_f being fixed to the plateau value of the resistance G_{Rc} for Maritime pine, and to $G_R(a_i)$ for Norway spruce, the other cohesive crack properties δ_b , f_b , and f_t (Fig. 2.7) were estimated by means of a developed Genetic Algorithm, in the context of the inverse problem, performed for each specimen. For both wood species, the cohesive fracture energy was fixed to the value of G_{Rc} for pine and $G_R(a_i)$ for spruce (in a first approximation, to be modified if necessary).

2.5 Formulation of the inverse problem

The formulation of the inverse problem (IP) detailed in Appendix A2.2 is established on the basis of the minimization of an objective function $y(\mathbf{b})$, which quantifies the agreement between two P - δ curves. Thus, for a given specimen tested in the experiments (Appendix A2.3), the right set of the cohesive properties of the bilinear Petersson's softening law (Fig. 2.7) is identified, when the corresponding numerical load-displacement curve generated in the FEM computations, provides a fine agreement with the experimental P - δ curve (Fig. 2.3 a-b). The numerical procedure used to seek the independent cohesive crack properties (*i.e.*, w_b , f_b and f_t in Fig. 2.7) is based on a developed Genetic Algorithm (detailed in Appendix A2.2). The method mimics the evolutionary natural systems on the seeking task to identify the most fitting solution which satisfies a given purpose (in this particular case, a fine agreement between the numerical and the experimental P - δ curve).

2.6 Results and discussion

Figures 2.3.a and 2.3.b both exhibit the achieved agreement between numerical and experimental data regarding the P - δ curves, by means of the developed IP for both wood species. The objective function $y(\mathbf{b})$ defined in Appendix A2.2 (Eq. A2.2.1) has been delineated to concern the set of points in both numerical and experimental P - δ curves up to the limit-point (black square label printed in Figs 2.3.a and 2.3.b) corresponding to $a_{lim} = a_c + 2$ mm, since this limit value matches the end of the *Resistance*-curves obtained for both wood species. Numerical P - δ curves thus obtained

were subsequently treated taking place of experimental data using the method described in Section 2.3. A fine agreement has been achieved for each tested specimen (Figs 2.6.a and 2.6.b) which demonstrates the accuracy of the proposed methodology to determine the cohesive parameters. Tables 2.4 and 2.5, on its turn, permit to establish a comparison between numerical and experimental mean values obtained for pine and spruce, respectively. Corresponding mean values obtained in the plateau of the R -curve G_{Rc} for pine, and in the short segment of nil slope $G_R(a_1)$ for spruce, retrieved the cohesive fracture energy G_f used in the IP. On the other hand, calculated energies attributed both to micro-cracking and fibre-bridging (Eq. 2.3) have been plotted in Fig. 2.8 for each specimen.

Table 2.4 Comparison between numerical and experimental mean values obtained for Maritime pine. (Consult Appendix A2.3 for complete record exhibition)

12 Specimens	Numerical results		Experimental results			Error (%)	
	P_u (N)	$G_R(a_u)$ (J/m ²)	P_u (N)	$G_R(a_u)$ (J/m ²)	G_{Rc} (J/m ²)	P_u	$G_R(a_u)$
Avg.	330.8	198.4	330.4	201.6	209.2	0.15	-1.67
St. Dev.	25.7	26.0	26.1	24.8	27.5		

Table 2.5 Comparison between numerical and experimental mean values obtained for Norway spruce. (Consult Appendix A2.3 for complete record exhibition)

12 Specimens	Numerical results		Experimental results			Error (%)	
	P_u (N)	$G_R(a_u)$ (J/m ²)	P_u (N)	$G_R(a_u)$ (J/m ²)	G_{Rc} (J/m ²)	P_u	$G_R(a_u)$
Avg.	148.9	102.3	145.8	101.6	144.6	2.13	0.76
St. Dev.	6.5	9.1	6.1	7.7	17.8		

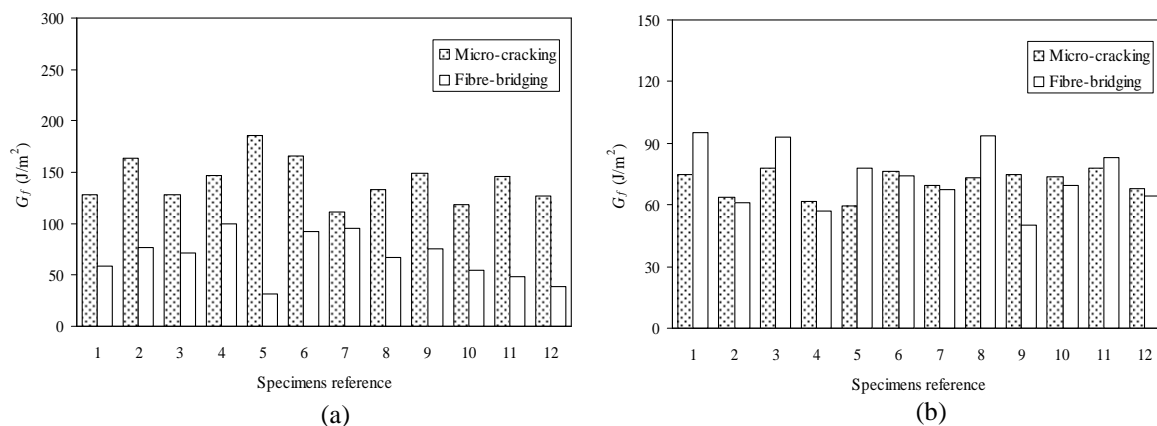


Figure 2.8 Energies attributed to micro-cracking $G_{f\mu}$ and fibre-bridging G_{fb} phenomena for both sets of tested wood (a) Maritime pine and (b) Norway spruce, according to Eq. (2.3) and Table 2.6. (In: Dourado N. et al. 2008).

Mean values of the cohesive crack properties and corresponding fracture energies obtained for each wood species are reported in Table 2.6. Making use of the mean values: f_t , f_b and w_b , together with the energy release rate resulting from values $G_f = G_{f\mu} + G_{fb} = G_{Rc}$ (Table 2.6), two stress-softening diagrams have been plotted (Fig. 2.9). Although a non-negligible scattering (Table 2.6) has been registered for stress parameter f_b , the procedure enables to settle a legitimate comparison between both wood species regarding the ultimate stress f_t (Fig. 2.7). Ahead of the statement that Maritime pine in the experiments has been found on average stiffer than Norway spruce (ratio of 2.48 in Tables 2.2 and 2.3), mean values of the ultimate stress f_t found by the IP revealed a ratio of 2.81 favourable to pine. At this purpose, it has been noticed that mean values of sought f_t (Table 2.6) have been found close to the bulk tensile strength (4.20 MPa) obtained by the experiments on un-notched specimens for Maritime pine (Pereira JL. 2004), revealing that local and global strengths may be considered as similar for this studied wood. As a consequence of the set of results obtained in the performed simulations, fracture energy attributed to micro-cracking $G_{f\mu}$ is on average considerably higher in Maritime pine than in spruce. A ratio of 2.10 has been found in fracture energies comparing micro-cracking with fibre-bridging for Maritime pine (Fig. 2.10). A non-remarkable difference has however been noticed for spruce. Based on these results (namely Fig. 2.9) it is foreknowable that the total extent of the fracture process zone (FPZ) in Norway spruce is higher than in pine wood. Consequently, a numerical

Table 2.6 Summary of mean values (12 specimens of each wood species) obtained by the inverse problem regarding the bilinear constitutive model (Figure 2.7). f_t : ultimate stress value; f_b and w_b : coordinates of the break-point; $G_{f\mu}$: fracture energy attributed to micro-cracking; G_{fb} : fracture energy ascribed to fibre-bridging phenomenon; G_f : cohesive fracture energy. (Consult Appendix A2.3 for complete record exhibition)

	f_t (MPa)	f_b (MPa)	w_b (mm)	$G_{f\mu}$ (J/m ²)	G_{fb} (J/m ²)	G_f (J/m ²)
Pine						
Average	4.66	0.72	0.06	141.83	67.39	209.22
St. Dev.	0.65	0.33	0.01	20.87	21.00	27.49
Spruce						
Average	1.66	0.30	0.09	70.91	73.91	144.81
St. Dev.	0.13	0.05	0.01	6.12	14.38	17.97

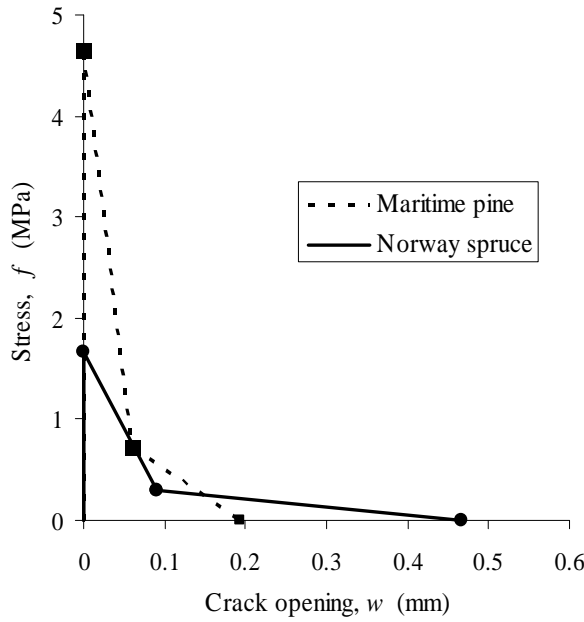


Figure 2.9 Superposition of bilinear diagrams showing obtained mean values of achieved independent damage parameters using the proposed IP, for both wood tested species. (In: Dourado N. et al. 2008).

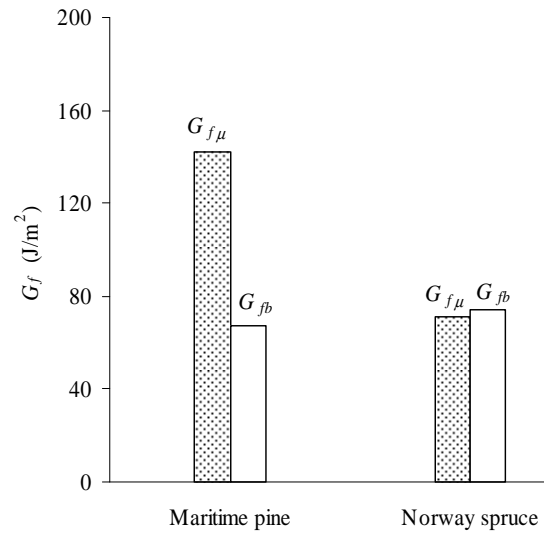


Figure 2.10 Results of the IP for both wood tested species, regarding mean values of energy ascribed to phenomena of micro-cracking $G_{f\mu}$ and fibre-bridging G_{fb} . (In: Dourado N. et al. 2008).

evaluation of the total extent of the damage extent developed ahead of the numerical crack-tip (*i.e.*, the critical extent of the cohesive zone $l_{coh\ c}$), has been conducted using the set of parameters identified by the IP for each specimen, and obtained results plotted against the numerical crack length a_{num} . As sketched in Fig. 2.11, the material localised ahead of the crack-tip experiences damage subsequent to the attainment of the ultimate stress (point A). Further increase in the crack opening w , leads gradually to a state of progressively more damage, up to fracture (cross-section B). The critical extent of the cohesive zone $l_{coh\ c}$ was continually computed during the performed FEM simulations, and corresponds to the set of points undergoing softening sited ahead of the crack-tip. As illustrated in Fig. 2.12, the $l_{coh\ c}$ in Norway spruce attains the available specimen ligament extent (thick centre-line) since the instant of numerical propagation onset, unlike Maritime pine. Subsequent trend in Norway Spruce shows a remarkable decrease in the $l_{coh\ c}$ with numerical crack size, revealing a cohesive zone markedly perturbed by the specimen boundary. In fact, the normal compressive stresses developed above the neutral axis (Fig. 2.2) avoid a self-similar propagation process. Note that this phenomenon is consistent with the some-how

continuous trend revealed in the rising R -curves observed in Norway spruce (Fig. 2.6.b), resulting in the reported slight extent in the plateau of this curve. As a result of this behaviour, it is worthwhile to use a higher specimen height (*i.e.*, h in Fig. 2.1) in order to avoid this phenomenon. In regards to the set of simulations performed for Maritime pine, though affected by scattering in results (Fig. 2.12), a mean critical value of the cohesive zone extent ($l_{\text{coh}_c} \cong 15 \text{ mm}$) seems to be revealed, since a plateau appears to take shape in the early stage of the crack propagation.

The trend revealed by the set of FEM results presented in Fig. 2.12 indicates that for most of the cases, the cohesive zone develops freely in Maritime pine in the early stages of the crack propagation leading to the appearance of a corresponding plateau value G_{Rc} on the R -curve (Fig. 2.6.a) for this wood species.

Taking into account the set of results regarding the critical extent of the cohesive zone l_{coh_c} , one can conclude that a strong perturbation of the damaged zone (FPZ) does exist in Norway spruce. A reasonable surveillance is also legitimate since the specimen height h (Fig. 2.1) used in the experiments may be limit for in pine wood. This numerical report draws to the important conclusion that a careful size effect study has to be put into practice if fracture properties are to be accurately evaluated in these wood species involving the SEN-TPB shape (or other shapes which may lead to compressive stress fields in the ligament length).

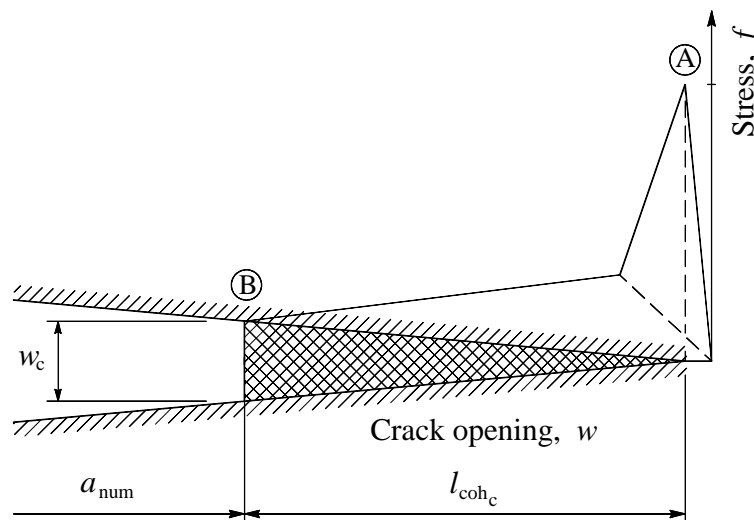


Figure 2.11 Bilinear Petersson's law. a_{num} : numerical crack length; l_{coh_c} : critical extent of the cohesive zone. (Adapted from Dourado N. et al. 2008).

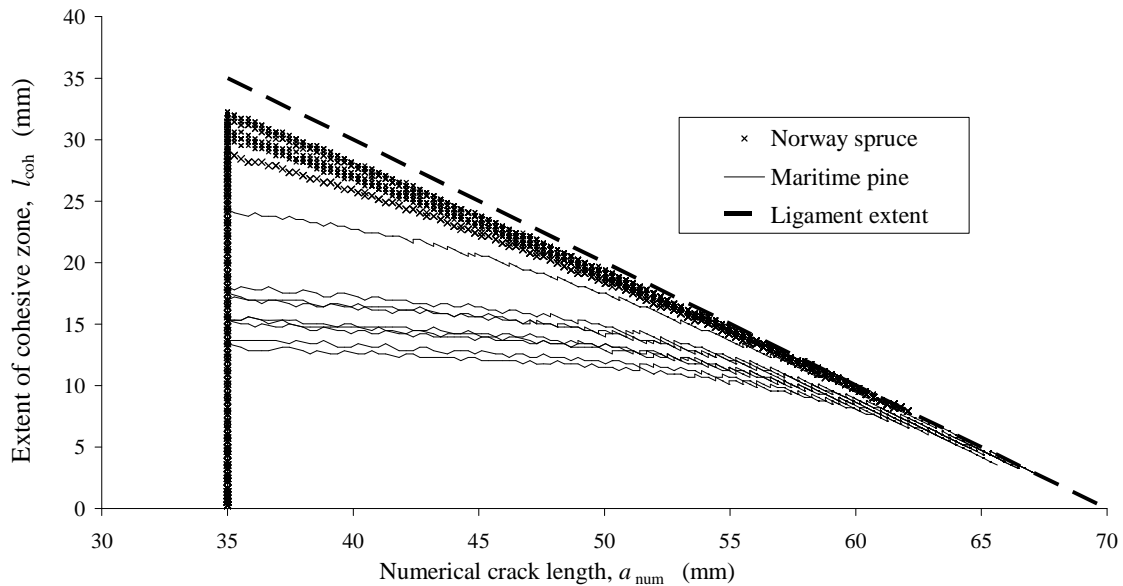


Figure. 2.14 Results of FEA showing the evolution of the extent of the cohesive zone with the numerical crack length for both tested wood (Norway spruce and Maritime pine), using the cohesive crack properties sought by the developed Inverse Problem. The Ligament extent is evaluated computing $h - a_{num}$. (In: Dourado N. et al. 2008).

The numerical simulations revealed that if the *Resistance*-curve is to be used on the basis of an accurate assessment of the size effect, namely on the nominal strength (Section 1.5), one must observe two important circumstances:

- (a) The Fracture Process Zone must be fully developed (Section 1.2) and keep its critical size over a reasonable crack extent during the loading process;
- (b) The plateau of the *Resistance*-curve must be undoubtedly revealed.

Taking into account the set of results obtained in the FEM-computations (using the IP outcome) one may conclude that both above cited conditions were reasonable satisfied for pine wood. On the other hand, the attained data clearly revealed that the experiments (and the numerical analysis) in spruce ought to be carried out with specimen dimensions of higher sizes h .

These important remarks some-how dictated the research path reported in the subsequent Chapters, since barely wood spruce has been used in the size effect study detailed therein. Indeed, since the results obtained for spruce seem to be strongly perturbed by the effect of the specimen size (chosen in this study), further analysis involving the size effect both on the numerical (Chapter III) and on the experimental (Chapter IV) standpoints were all performed for spruce.

Chapter III

Size Effect in Notched Structures

Chapter III

3.1 Introduction

The present Chapter is focused on the evaluation of the size effect on the relative crack length at the peak load α_u , the corresponding resistance to crack growth $G(\alpha_u)$ and the nominal strength σ_N defined in Section 1.5. Making use of an analytical development procedure, it is shown that an additional dimensionless asymptotic regime exists for the intermediate size range. A numerical (FEM) validation procedure is put into practice using a given set of cohesive properties.

Hence, the effect of the structure size D on the ultimate fracture properties is studied, performing an energy based asymptotic analysis for which the resistance to crack growth (R -curve) in a notched structure (Mode I) is considered as a size independent property and described according to an analytical expression. Scaling evaluations involving the relative crack length together with the resistance to crack growth are performed when the ultimate load acting on the structure is attained. For the intermediate size range, the relative crack length at the peak load α_u is found to decrease with the structure size, whereas the corresponding resistance to crack growth $G(\alpha_u)$ shows an increasing trend.

Results of FEM computations involving geometrically similar notched orthotropic structures (SEN-TPB) of different sizes performed with the same combination of cohesive crack properties are presented. The bi-logarithmic plot of the nominal strength versus the characteristic structure size is in agreement with the Bažant's size effect law

(SEL) for most of the size spectrum, with the exception of the intermediate sizes, for which an additional asymptotic regime is identified. Considerations regarding the extent together with the slope of this additional asymptotic regime are made, based on the exponent characterizing the curvature of the *Resistance*-curve.

3.2 Derivation of the energetic Size Effect Law based on the equivalent LEFM and the asymptotic analysis

Let us consider an *R*-curve independent of the structure size D , defined through an analytical single expression, evolving as a power law (Morel S 2008),

$$G_R(\Delta a) = \begin{cases} \phi \Delta a^\beta & \text{if } \Delta a < \Delta a_c \\ \phi \Delta a_c^\beta & \text{if } \Delta a \geq \Delta a_c \end{cases} \quad (3.1)$$

with $\Delta a = a - a_0$ standing for the equivalent crack length increment, the exponent β selected to reproduce the negative curvature of the rising portion of the *R*-curve (*i.e.*, $0 < \beta < 1$), and the equivalent length of the FPZ is given by $\Delta a_c = a_c - a_0$. The remainder term ϕ is the pre-factor of the power law which does not depend on the structure size D . Though the *R*-curve is recognized as geometry-dependent, the proposed formulation is based on the assumption that the exponent β does not change significantly with the structure size D , when geometrically similar notched structures are analysed (different characteristic sizes D). This assumption is to be verified in the following.

It should be noted that the analytical expression provided by Eq. (3.1) defines two different regimes observed during the crack propagation (Fig. 1.3). By this means, no accurate account of the smooth transition observed in the *R*-curve is possible to capture between the ascending part (*i.e.*, $\Delta a < \Delta a_c$) and the stationary regime (*i.e.*, $\Delta a > \Delta a_c$), with an angulate point being thus possible to be revealed through Eq. (3.1).

In quasibrittle fracture the characteristic equivalent crack length increment Δa_c is proportional to the ratio: $\Delta a_c \propto G_{Rc}/G_d$, with G_d representing the energy associated to the damage dissipation rate defined per unit volume of the damaged material (in J/m^3), *i.e.*, per unit volume of the FPZ. Indeed, as shown in Fig. 1.2(b), once the FPZ attains its critical size $l_{FPZ} \approx 2\Delta a_c$ (Bažant ZP and Kazemi MT, 1990), then the height

of the FPZ turns a fraction n (independent of the structure size) of the characteristic equivalent crack length increment Δa_c , *i.e.*, $h_{\text{FPZ}} \approx n \Delta a_c$, where n is a constant whatever the structure size D . As mentioned in Chapter I, during the propagation of the main crack (with its critical FPZ), the FPZ can be considered in an energetic steady state. Hence, the FPZ does not consume more energy other than to be displaced. Hence, if the crack propagates by the infinitesimal extent δa , then the new damage volume generated by the crack advance corresponds to the dashed *area* printed in Fig. 1.2 (c), with the revealed volume approximately estimated through,

$$V_{\text{FPZ}}(\delta a) = b \delta a h_{\text{FPZ}} = b \delta a n \Delta a_c \quad (3.2)$$

with b representing the width of the structure cross-section. Hence, the energy required during the infinitesimal crack advance δa can be expressed by

$$w_f = G_d V_{\text{FPZ}}(\delta a) \quad (3.3)$$

with the energy released at the macroscopic level, estimated through

$$w_f = G_{\text{Rc}} b \delta a \quad (3.4)$$

The product $b \delta a$ in Eq. (3.4) represents the elastic equivalent cracked surface. Thus, combining Eqs. (3.3) and (3.4) with Eq. (3.2), one can obtain the characteristic equivalent crack length increment (or in other terms, the equivalent LEFM length of the FPZ), through,

$$\Delta a_c = \frac{G_{\text{Rc}}}{n G_d} \quad (3.5)$$

As long as crack evolves in a self-similar way the characteristic equivalent crack length increment Δa_c should be considered as an internal length of the considered quasibrittle material, and n a corresponding extent (constant) used to quantify the FPZ height.

Equations (3.2) and (3.3) establish that the effective length of the FPZ, Δa_c is a constant, and thus it turns independent of the structure size D . The relative critical crack length of the FPZ (*i.e.*, $\theta = \Delta a_c / D$) by definition evolves as a power law of the structure size D : $\theta \propto D^{-1}$. It means that for small structure sizes D (*i.e.*, $D \rightarrow 0$), the relative critical crack length of the FPZ tends to infinity (*i.e.*, $\theta \rightarrow \infty$), with the resulting

structure ligament length being entirely occupied by the FPZ (Fig. 1.1). On the other hand, for large structure sizes D (*i.e.*, $D \rightarrow \infty$) resulting $\theta \rightarrow 0$, with the FPZ lying in an infinitesimal volume fraction of the ligament, as expected from the SEL (Bažant ZP 1984)

3.2.1 Size effect on the relative crack length and resistance at the peak load

Let us consider the case of geometrically similar structures characterized by the dimensionless energy release rate function $g(\alpha)$ defined in Section 1.5 [*i.e.*, $g(\alpha) = E' b \lambda(\alpha)/2$] and the estimate of the scaling of the relative crack length at the peak load $\alpha_u(D)$. The well known condition verified at the peak load (Bažant ZP and Cedolin L 1991, Morel S et al. 2005) when an R -curve behaviour is observed, provides the relative crack length at the peak load α_u from the equality,

$$\frac{G'_R(\alpha)}{G_R(\alpha)} = \frac{g'(\alpha)}{g(\alpha)} \quad (3.6)$$

with $G'_R(\alpha) = \partial G_R(\alpha) / \partial \alpha$ and $g'(\alpha) = \partial g(\alpha) / \partial \alpha$. Equation (3.6) is valid for both load and displacement-controlled fracture tests, and reveals that the relative crack length at the peak load α_u , does not necessarily correspond to the critical relative crack length α_c (Fig. 1.3) (Morel S et al. 2005).

Combining both Eqs. (3.6) and (3.1) for the rising part of the R -curve (*i.e.*, for $\Delta a < \Delta a_c$), it turns

$$\frac{G'_R(\alpha)}{G_R(\alpha)} = \frac{\beta}{\alpha - \alpha_0} \quad (3.7)$$

with α denoting the relative crack length (*i.e.*, $\alpha = a/D = a_0/D + \Delta a/D = \alpha_0 + \Delta a/D$), and α_0 the relative length of the initial notch (Fig. 1.2 b-c). Equation (3.7) shows that $G'_R/G_R(\alpha)$ is independent of the structure size D , and the consequence of this is that Eq. (3.6) leads to a unique solution α_{u*} for the relative crack length at the peak load (Fig. 3.1), *i.e.*, a solution independent of the structure size D . It should be noticed that Eq. (3.7) would have been reached if another R -curve shape had been considered (Morel S., 2007). It is also worth-while to notice that the increase in the

characteristic structure size D leads to the decrease in the relative crack length at the peak load α_u , as exemplified in Fig. 3.2 using two geometrically similar structure sizes (with $D_2 > D_1$) (Morel S 2008).

The achieved solution α_{u^*} (constant) is revealed providing that $\alpha_{u^*} < \alpha_0 + \theta$ as shown in Fig. 3.2 for the structure size D_1 (with θ standing for the relative length of the FPZ, defined through $\theta = \Delta a_c / D$). Hence, as D increases in size, the relative length of the FPZ, decreases ($\theta \rightarrow 0$).

Let us consider a characteristic structure size D_c quantified by $D_c = \Delta a_c / (\alpha_{u^*} - \alpha_0)$, for which the unique solution $\alpha_{u^*} = \alpha_0 + \theta$. For a structure of such a size (*i.e.*, D_c) one assumes that the peak load P_u is reached at the onset of the R -curve plateau (Section 1.3). This means that, for structures of size $D > D_c$ the relative crack length at the peak load α_u , is no longer equal to the unique solution α_{u^*} , but rather to $\alpha_0 + \theta$ (as shown in Fig. 3.2 for $D = D_2$). Indeed, the characteristic structure size D_c (Fig. 3.3) plays the role of the upper bound of the single solution α_{u^*} regime.

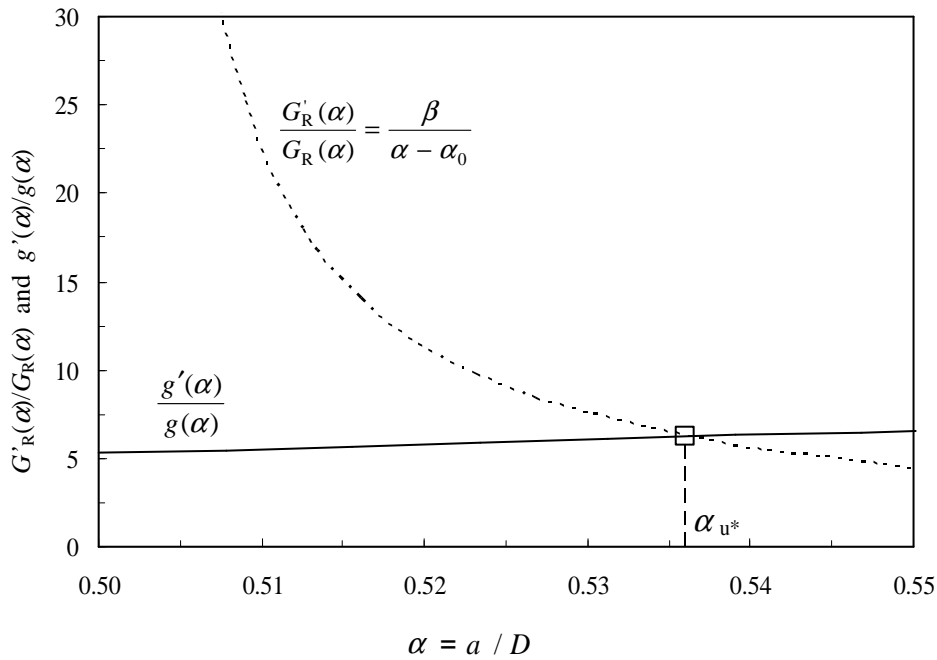


Figure 3.1 Plotting of Eq. (3.6) used to estimate α_{u^*} in a positive specimen geometry (*i.e.* $g'(\alpha) > 0$) : the SEN-TPB.

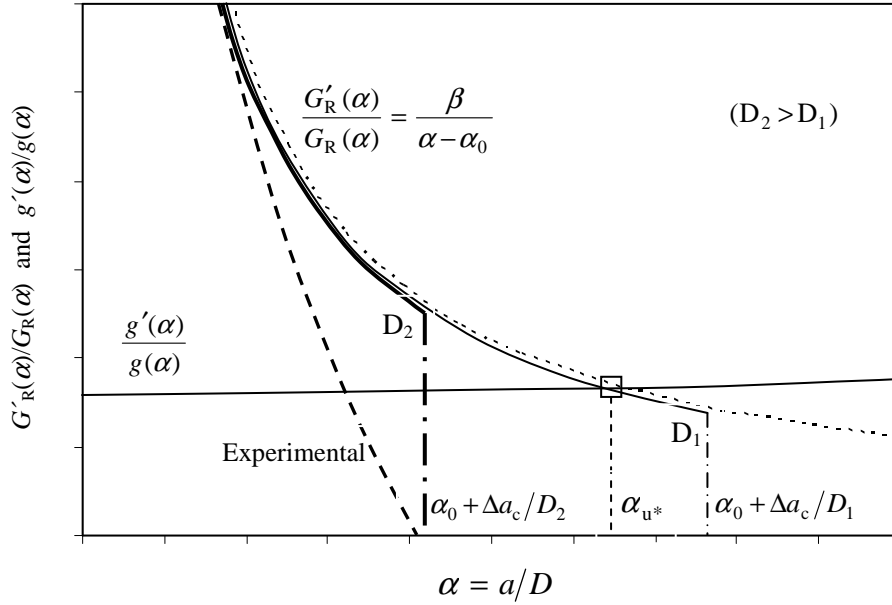


Figure 3.2 Size effect on the ratio $G'_R/G_R(\alpha)$ revealing the decrease of α_u with the structure size for the SEN-TPB.

On the other hand, there exists a lower bound (*i.e.*, D_{\min}) for this regime (Fig. 3.3), which corresponds to the case for which the FPZ is expected to occupy the entire crack ligament, such that $\Delta a_c = (1 - \alpha_0) D_{\min}$. Therefore, for structure sizes smaller than D_{\min} , the FPZ occupies the whole crack ligament, with failure occurring with no crack propagation. This is the domain characterized by the Strength Theory (Section 1.5), with the R -curve turning irrelevant to describe the failure mechanisms which takes place.

The centreline represented under the scaling law in Fig. 3.3 mimics the plotting of the experimental data, showing that no angulate point is expected to exist in the crossover regime but rather a smooth transition. Figure 3.3 clearly shows that ever since the structure size tends to infinite (*i.e.*, $D \rightarrow \infty$), the relative crack length at the peak load vanishes (*i.e.*, $\alpha_u \rightarrow \alpha_0$), which reveals that in large structure sizes the FPZ lies within an infinitesimal volume of the structure, as postulated through the Bažant's SEL (Bažant ZP 1997 b). As a consequence, one can summarize the scaling of α_u as follows,

$$\alpha_u(D) = \begin{cases} \text{'Strength theory'} & \text{if } D < D_{\min} \\ \alpha_{u^*} & \text{if } D_{\min} < D < D_c \\ \alpha_0 + \theta & \text{if } D > D_c \end{cases} \quad (3.8)$$

with,

$$D_{\min} = \frac{\Delta a_c}{1 - \alpha_0} \quad (3.9)$$

$$D_c = \frac{\Delta a_c}{\alpha_{u^*} - \alpha_0} \quad (3.10)$$

Once evaluated the R -curve (Eq. 3.1) and performed the scaling of α_u at the peak load (Eq. 3.8), it is possible to assess the size effect on the corresponding resistance to crack propagation at the peak load $G_R(\alpha_u, D)$. As referred above, the relative crack length at the peak load in the interval $D_{\min} < D < D_c$, is the single solution α_{u^*} . Consequently, combining Eqs. (3.1) and (3.9), the resistance at the peak load yields,

$$G_R(\alpha_u, D_{\min} < D < D_c) = \phi[(\alpha_{u^*} - \alpha_0)D]^\beta \quad (3.11)$$

Equation (3.11) indicates that the regime related to the single solution α_{u^*} leads to a resistance at the peak load, regarding the structure size D , evolving as a power law

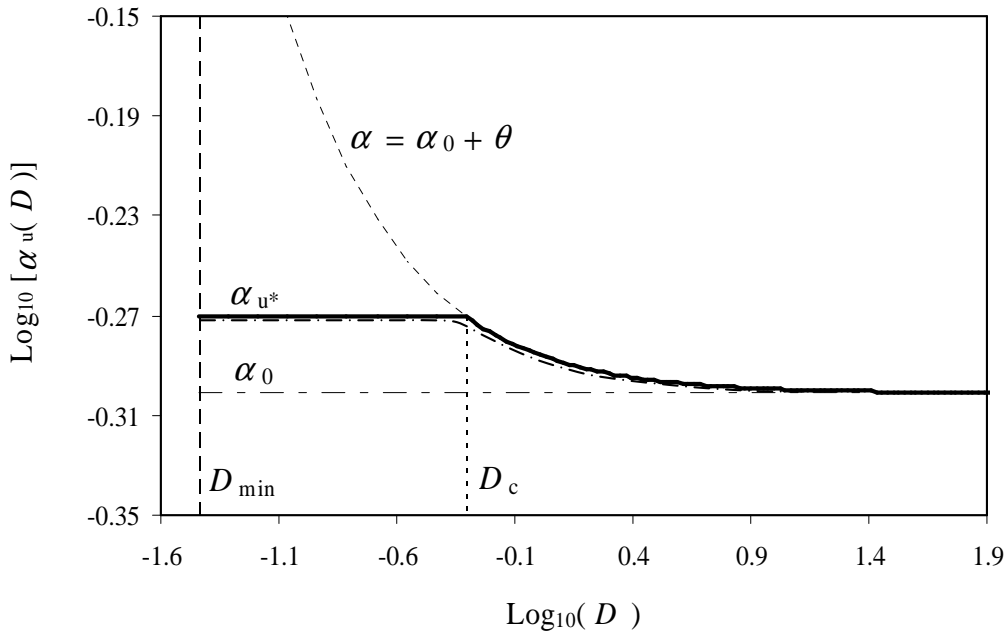


Figure 3.3 Plotting of the scaling of the relative crack length at the peak load α_u against the structure size D according to Eq. (3.8). Parameters D_{\min} and D_c are the lower and upper bounds of the single solution α_{u^*} , respectively defined through Eqs. (3.9) and (3.10). $\theta = \Delta a_c/D$ is the relative length of the FPZ. The centreline mimics the trend expected for the experimental data.

governed by the exponent β . As reported in Eq. (3.8) for structure sizes $D > D_c$, the relative crack length at the peak load is $\alpha_u = \alpha_0 + \theta$ (with $\theta = \Delta a_c / D$), leading to a constant resistance at the peak load $G_R(\alpha_u, D) = G_{Rc}$ (i.e., the horizontal asymptote of the R -curve shown in Fig. 1.3-b). Accordingly, three distinct asymptotic regimes are observed regarding the size effect on the resistance to crack growth,

$$G_R(\alpha_u, D) \propto \begin{cases} \text{'Strength theory'} & \text{if } D < D_{\min} \\ D^\beta & \text{if } D_{\min} < D < D_c \\ G_{Rc} = \text{constant} & \text{if } D > D_c \end{cases} \quad (3.12)$$

A plotting of the size effect on the resistance at the peak load is illustrated in Fig. 3.4. Equation (3.12) indicates that the increase in the structure size D is followed by a resistance raise up to G_{Rc} . Hence, once attained the peak load P_u , the resistance to crack growth (i.e., $G_R(\alpha_u)$) increases with the specimen size D , whereas the relative crack length at the peak load decreases from α_{u*} to α_0 (as illustrated in Fig. 3.3). In a like manner as performed for Fig. 3.3, the centreline represented in Fig. 3.4 imitates the trend expected for the experimental data in the crossover regime.

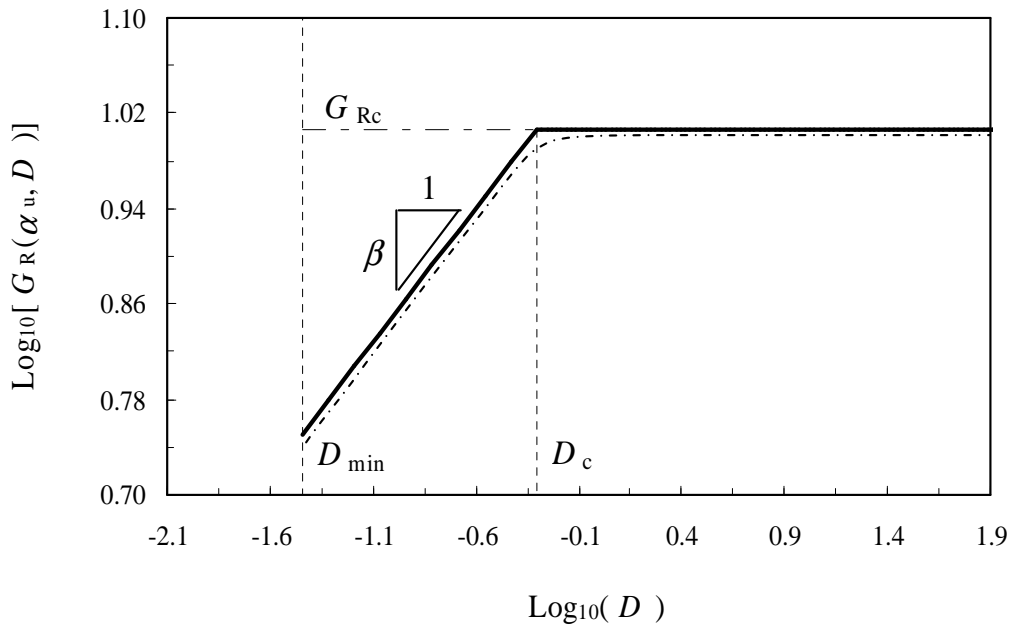


Figure 3.4 Size effect on the resistance at the peak load according to Eqs. (3.11) and (3.12). Parameters D_{\min} and D_c are the lower and upper bounds of the single solution α_{u*} , respectively defined through Eqs. (3.9) and (3.10). The centreline mimics the trend expected for the experimental data.

3.2.2 Size effect on the nominal strength

As mentioned in Section 1.5 the strength concept is generally revealed by the value of the nominal stress at the ultimate load P_u . Consequently, once the load P reaches P_u , Eq. (1.3) yields the nominal strength σ_N . The scaling assessment of both relative crack length $\alpha_u(D)$ and the corresponding resistance $G_R(\alpha_u, D)$ at the peak load renders likely to estimate the resulting size effect on the nominal strength. Consequently, combining Eqs. (1.3) and (1.2) it turns,

$$\sigma_N(D) = c_N \sqrt{\frac{E' G_R(\alpha_u, D)}{D g[\alpha_u(D)]}} \quad (3.13)$$

with E' standing for the effective elastic modulus ($E' = E$ for plane stress and $E' = E/(1-\nu^2)$ for plane strain; $E =$ Young modulus and ν the Poisson's ratio) as first defined in Section 1.3. The coefficient $c_N = 3/2(L/h)$ is in accordance with the assumption referred to in Section 1.5.

In the following a discussion involving the three different regimes for the size effect on the nominal strength σ_N is made, from the analysis of Eqs. (3.8) and (3.12).

3.2.2.1 Asymptotic regime at large sizes

According to Eq. (3.12), for large structure sizes, *i.e.*, $D > D_c$ the energy release rate remains unchanged, *i.e.*, $G_R(\alpha_u, D) = G_{Rc}$, whereas the relative crack length at the peak load (Eq. 3.8) is given by $\alpha_u = \alpha_0 + \theta$, with $\theta = \Delta a_c / D$. In this expression the relative length of the FPZ $\theta \rightarrow 0$ as the structure increases in size (*i.e.*, $D \rightarrow \infty$). Hence, expanding in Taylor series the dimensionless energy release rate function $g(\alpha_u)$ around $\alpha_u = \alpha_0$, reported in Eq. (3.13), yields

$$\sigma_N(D) = c_N \sqrt{\frac{E' G_{Rc}}{D}} \left[g(\alpha_0) + g_1(\alpha_0) \frac{\Delta a_c}{D} + \frac{g_2(\alpha_0)}{2!} \left(\frac{\Delta a_c}{D} \right)^2 + \frac{g_3(\alpha_0)}{3!} \left(\frac{\Delta a_c}{D} \right)^3 + \dots \right]^{-\frac{1}{2}}$$

$$= \sigma_{Mc} \left[1 + \frac{D}{D_{Nc}} + b_2 \left(\frac{D_{Nc}}{D} \right) + b_3 \left(\frac{D_{Nc}}{D} \right)^2 + \dots \right]^{-\frac{1}{2}} \quad (3.14)$$

with,

$$g_i(\alpha_0) = \frac{\partial^i g(\alpha_0)}{\partial \alpha^i} \quad \text{and} \quad b_i = \frac{g(\alpha_0)^{i-1} g_i(\alpha_0)}{i! g_1(\alpha_0)^i} \quad (i = 1, 2, 3, \dots)$$

and

$$\sigma_{Mc} = c_N \sqrt{\frac{E' G_{Rc}}{g(\alpha_0) D_{Nc}}} \quad (3.15)$$

$$D_{Nc} = \frac{g_1(\alpha_0)}{g(\alpha_0)} \Delta a_c \quad (3.16)$$

The asymptotic regime at large sizes provided by Equation (3.14) leads to,

$$\sigma_N(D) = c_N \sqrt{\frac{E' G_{Rc}}{g(\alpha_0)}} D^{-1/2} \quad (3.17)$$

with both the critical energy release rate G_{Rc} and the dimensionless energy release rate function for the initial crack notch $g(\alpha_0)$ (Appendix A3.1) assuming constant values whatever the structure size D .

It should be noted that the asymptotic behaviour at large sizes estimated through Eq. (3.14) is attained for a relative crack length at the peak load equal to α_0 (Fig. 3.3), whereas for intermediate sizes it is accomplished for α_{u^*} .

3.2.2.2 Asymptotic regime at intermediate sizes

This is the field of structure sizes lying in the interval $D_{\min} < D < D_c$ (Fig. 3.4). Recovering Eq. (3.11) one observes that the resistance at the peak load progresses (Fig. 3.4) according to a power law $G_R(\alpha_u, D_{\min} < D < D_c) \propto D^\beta$. According to Eq. (3.8) the relative crack length α_u at the peak load is supposed to remain unchanged and equal to α_{u^*} (Fig. 3.3). Applying Eq. (3.13) to this regime leads to

$$\sigma_N(D) = c_N \sqrt{\frac{E' \phi (\alpha_{u^*} - \alpha_0)^\beta}{g(\alpha_{u^*}) D^{1-\beta}}} \quad (3.18)$$

with the coefficient $\phi = G_{Rc} / \Delta a_c^\beta$. Therefore, it turns out that the nominal strength at intermediate sizes evolves in an asymptotic manner according to a power law $\sigma_N(D) \propto D^{-1/2+\beta/2}$. This regime is in disagreement with LEFM, since G_R evolves as a power law as a function of the structure size D . Unlike LEFM (Fig. 1.5) the resistance at the peak load raises with the structure size $G_R(\alpha_u, D) \propto D^\beta$ as is revealed by Eq. (3.11). Since the exponent β must lie in the interval $0 < \beta < 1$ (Section 3.2), the outcome is that the exponent of the power law of σ_N must vary between $-1/2$ (size effect described by LEFM) and 0 (no size effect).

The asymptotic regime at intermediate sizes (*i.e.*, in the *crossover* region) is delimited by D_{\min} (Eq. 3.9) and the characteristic size noted as D_1^* , which is defined as the crossover size between the asymptotic regime (Eq. 3.17) and Eq. (3.18),

$$D_1^* = \left[\frac{g(\alpha_{u^*})}{g(\alpha_0)} \right]^{1/\beta} D_c \quad (3.19)$$

It gives thus rise to the clearing up that this quantity does not coincide with D_c defined as the crossover size (Eq. 3.10) on the relative crack length and on the resistance at the peak load (Fig. 3.4). Indeed, each one of the asymptotic regimes is not obtained for the same relative crack length at the peak load. Hence, the single solution α_{u^*} is used to define the asymptotic regime in the intermediate size range, while α_0 is used to characterize the asymptotic regime at large sizes.

3.2.2.3 Asymptotic regime at small sizes

As referred in Section 3.2.1, in small structure sizes (*i.e.*, $D < D_{\min}$) the ligament length is fully occupied by the FPZ. In these circumstances, failure arises with no crack propagation, with the *R*-curve turning irrelevant to describe the failure process. This is the field of the Strength Theory (Bažant ZP 1997 a, 1997 b) (Fig. 1.5) with the failure load evolving proportionally to the strength of the material, $\sigma_N(D \leq D_{\min}) = \text{constant}$.

Hence, this strength corresponds to the maximum nominal strength $\sigma_{N \max}$ which may be computed according to Eq. (3.18), considering $D = D_{\min}$,

$$\sigma_{N \max} = c_N \sqrt{\frac{E' \phi (\alpha_{u^*} - \alpha_0)^\beta}{g(\alpha_{u^*}) D_{\min}^{1-\beta}}} \quad (3.20)$$

In other terms, the maximum nominal strength $\sigma_{N \max}$ is estimated from the asymptotic behaviour at intermediate structure sizes, considering the value of the nominal strength obtained for the lower bound $D = D_{\min}$.

The bi-logarithmic plotting shown in Fig. 3.5 illustrates the progress of the nominal strength σ_N with the structure size D , presenting the three different asymptotic regimes,

$$\sigma_N(D) \propto \begin{cases} \sigma_{N \max} & \Leftarrow D < D_{\min} \text{ (strength theory)} \\ D^{-1/2 + \beta/2} & \Leftarrow D_{\min} < D < D_1^* \\ D^{-1/2} & \Leftarrow D > D_1^* \end{cases} \quad (3.21)$$

It turns thus clear that the actual size effect curve agrees with both the horizontal (Strength theory) and the lean (LEFM) asymptotic plotting (slope: $-1/2$). The major divergence is observed in the regime expected for the intermediate size, for which an additional asymptotic regime develops.

A more convenient way to express the range of the intermediate size consists to combine Eqs. (3.19) with (3.9) and (3.10),

$$\frac{D_1^*}{D_{\min}} = \frac{1 - \alpha_0}{\alpha_{u^*} - \alpha_0} \left[\frac{g(\alpha_{u^*})}{g(\alpha_0)} \right]^{1/\beta} \quad (3.22)$$

Equation (3.22) noticeably makes the ratio D_1^*/D_{\min} independent of the extent of the R -curve, Δa_c . As a consequence, D_1^* and D_{\min} are expected to be dependent of the structure geometry. This means that it is possible to express the range of sizes in the *crossover* region as a function of the curvature of the R -curve β , not relying it on the extent of the *Resistance*-curve (*i.e.*, on the equivalent LEFM length of the FPZ). The asymptotic regime expected for the relative crack length and for the resistance at the

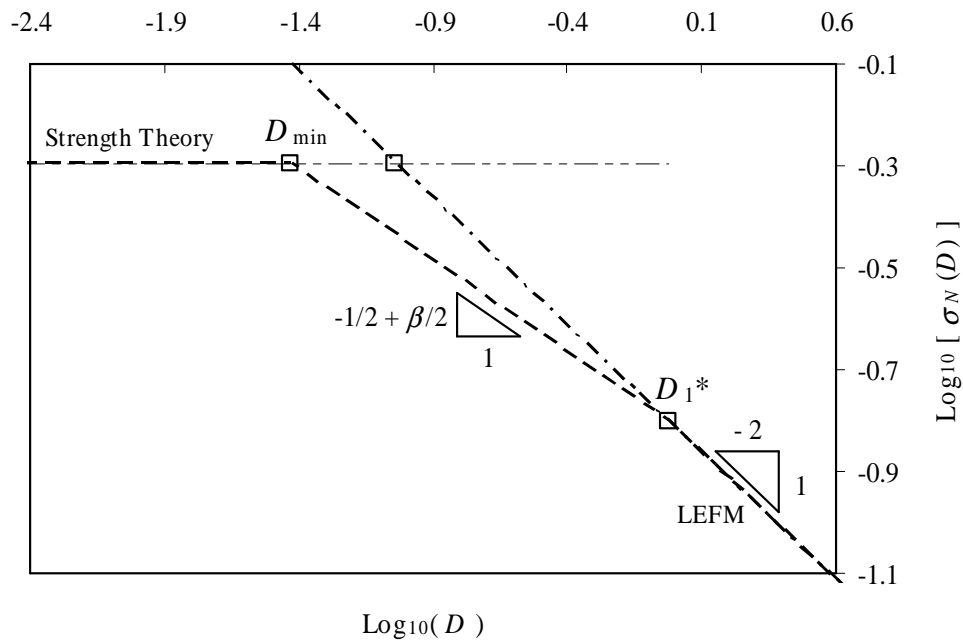


Figure 3.5 Size effect on the nominal strength.

peak load (*i.e.*, $\alpha_u(D)$ and $G_R(\alpha_u, D)$, respectively) turns also possible to express the ratio D_c/D_{\min} independently of Δa_c .

As the R -curve evolves in a progressive way from the rising domain up to the plateau (Fig. 1.3 b) it is unexpected to turn to angulate points in the bi-logarithmic plotting of σ_N versus D shown in Fig. 3.5 (D_{\min} and D_1^*). Therefore, one might expect to obtain smooth transitions (*i.e.*, crossover) between the two successive asymptotic regimes: (i) Strength Theory and the regime at intermediate sizes, and (ii) the intermediate sizes regime and LEFM.

The comparison of the asymptotic behaviours for the nominal strength (Eq. 3.21) with the Bažant's SEL (Eq. 1.3) has been made taking two different values of the exponent β used to characterize the curvature of the *Resistance*-curve ($\beta = 0.8$ and 0.2), thus reproducing respectively the effect of a slight and a very strong curvature of the R -curve. Hence, as shown in Fig. 3.6 (a-b) for the FEM-computation of the SEN-TPB on the Lab's (or experimental) scale (using spruce as testing material, $D_{\text{exp}} = 140$ mm, $b = 40$ mm, as well as $G_{Rc} = 0.1 \text{ N}\cdot\text{mm}^{-1}$ and $\Delta a_c = 25$ mm), the fitting of the SEL has been achieved establishing the transition between the horizontal asymptote provided by the Strength Theory and the lean asymptote previewed by LEFM. In both plotting representations (Fig. 3.6 a-b) one can conclude that in the

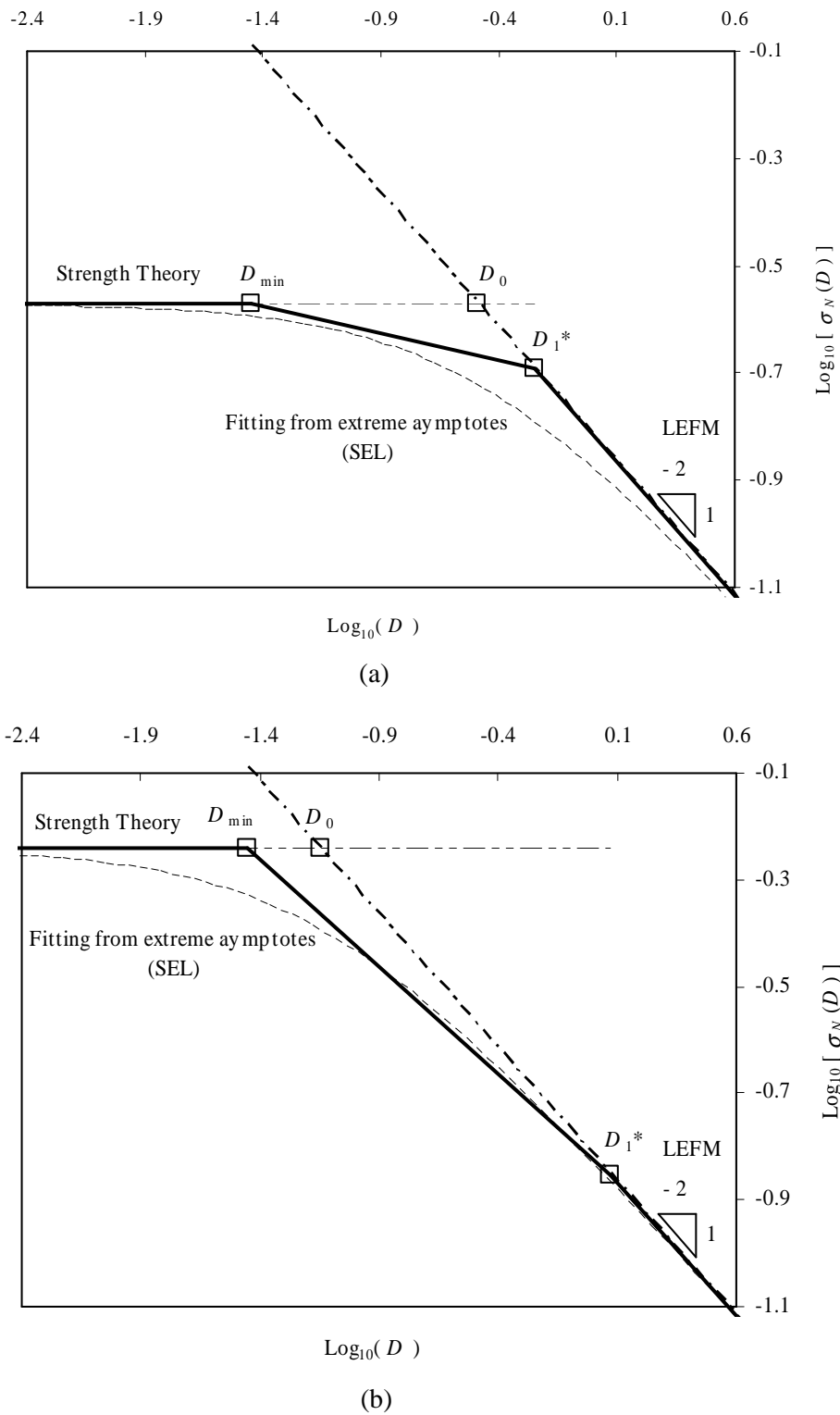


Figure 3.6 Comparison of the asymptotic behaviours estimated by Eq. (3.20) and the fitting of Bažant’s SEL (Eq. 1.3) for two distinct values of the exponent β which characterize the curvature of the R -curve. (a) $\beta=0.8$ for a slight curvature of the R -curve and (b) $\beta=0.2$ for a very strong curvature of the R -curve.

intermediate domain (*i.e.*, $D_{\min} < D_{\exp} < D_1^*$) the agreement between the fitted SEL and the estimate performed by means of Eq. (3.21) is not completely satisfactory. Indeed, it

is an evidence that the curvature of the fitted function of the SEL (Eq. 1.4) stays unaffected if the parameters B , f_u and D_0 are modified, thus proving that it is not possible to change the curvature of the SEL in order to fit the plotting provided by Eq. (3.21). It ought to be noticed as well that the main differences between the two asymptotic behaviours (SEL and the one estimated through Eq. 3.21) arise when the R -curve curvature is too slight (Fig. 3.6 a), or in the case that a strong curvature is reported for the R -curve (Fig. 3.6 b). In such circumstances, the optimum structure design (*i.e.*, less conservative) inclines towards the solution provided by Eq. (3.21). On the other hand, it is revealed that the asymptotic regime expected at intermediate sizes can extend from 1 decade, for slight curvatures of the R -curve (Fig. 3.6 a), up to more than 3 decades, for very strong curvatures (Fig. 3.6 b).

Thus, in conclusion one should put in relief the following aspects:

- For small structure sizes (*i.e.*, $D < D_{\min}$) it makes no sense to perform the size effect study since the ligament *volume* is often small when compared to the characteristic volume of material required to develop a full damaged domain. Consequently, the failure process arises as very theoretical, with the corresponding results being used cautiously.
- In intermediate structure sizes (*i.e.*, $D_{\min} < D < D_c$), one also notices that as according to the energy release rate at the ultimate load $G_R(\alpha_u, D)$ increases, the relative crack length at the peak load $\alpha_u(D)$ decreases, tending thus to the relative crack length value of the initial notch α_0 [*i.e.*, $\alpha_u(D) \rightarrow \alpha_0$]. This makes the ratio $G_R(\alpha_u, D)/g[\alpha_u(D)]$ to increase with D , which establishes by evidence that the size effect on the nominal strength $\sigma_N(D)$, estimated through Eq. (3.13), develops in a less pronounced way than that predicted by LEFM (*i.e.*, $\propto D^{-1/2}$). This leads to the asymptotic plotting estimated by LEFM more rightwards than such which is estimated through Eq. (3.18), *i.e.*, according to a power law $\sigma_N(D) \propto D^{-1/2 + \beta/2}$.
- For very large structure sizes (*i.e.*, with $D \rightarrow \infty$) the accurate positioning of the leant asymptote given by LEFM, is barely driven by the horizontal asymptote of the R -curve (*i.e.*, G_{Rc}). Indeed, in such cases the analysis of Eq. (3.14) leads to,

$$\sigma_N(D) = c_N \sqrt{\frac{E' G_{Rc}}{g(\alpha_0)}} D^{-1/2}$$

The available FEM data has been used to perform the computation of D_1^* through Eq. (3.19), providing the definition of the intermediate size domain (*i.e.*, $D_{\min} < D_{\exp} < D_1^*$) represented in Fig. 3.7. The intermediate dimension labelled as D_{\exp} in Fig. 3.7 (for the structure size $D_{\exp} = 140$ mm mentioned above), has been represented for convenience, since this is usually the structure size of available experimental data. In this range of structural sizes, as previously reported in this Section, the relative crack length at the peak load $\alpha_u(D_{\exp})$ is higher than α_0 (Fig. 3.3). It has also been shown that the energy release rate at the peak load $G_R[\alpha_u(D_{\exp})]$ is smaller than G_{Rc} (Fig. 3.4). As a consequence, if one considers the descending straight centreline (slope: $-1/2$) passing through D_{\exp} (Fig. 3.7) it turns out that the predicted nominal strength $\sigma_N(D_{\exp})$ thus provided is visibly underestimated (*i.e.*, is more likely to correspond to the *safety design*). A more convenient way to quantify this undervaluing may be achieved through,

$$\sigma_N(D) = c_N \sqrt{\frac{E' G_R[\alpha_u(D_{\exp})]}{g[\alpha_u(D_{\exp})]}} D^{-1/2} \quad (3.23)$$

with the corresponding position in the bilogarithmic graph being influenced by the ratio $G_R(\alpha_u, D_{\exp})/g[\alpha_u(D_{\exp})]$, setting $D = D_{\exp}$. Thus, the relative position of this descending centreline (more leftwards in Fig. 3.7) is not surprising, since the ratio $G_R[\alpha_u(D_{\exp})]/g[\alpha_u(D_{\exp})]$ in Eq. (3.23) is smaller than $G_{Rc}/g(\alpha_0)$ defined in Eq. (3.17). The fact that Eq. (3.23) leads to an underestimate of the nominal strength $\sigma_N(D)$, unquestionably brings about to the overestimate of the structure dimension D . The corresponding solution provided by LEFM's descending asymptote is more likely to match the optimal solution. However, this result requires the estimate of the R -curve, together with the critical energy release rate G_{Rc} . Notwithstanding this, one can notice that the estimate of the required experimental data is possible to achieve from a single structure size, $D = D_{\exp}$. In such a case, an approximate size effect (Fig. 3.8) is likely to

be obtained fitting the SEL (Bažant ZP 1984; Eq. 1.4) from the nominal strength $\sigma_N(D_{exp})$ up to the asymptote of LEFM defined by Eq. (3.17).

In the following Section a numerical (FEM) validation procedure is put into practice using a given set (constant) of cohesive properties (bilinear softening model), in

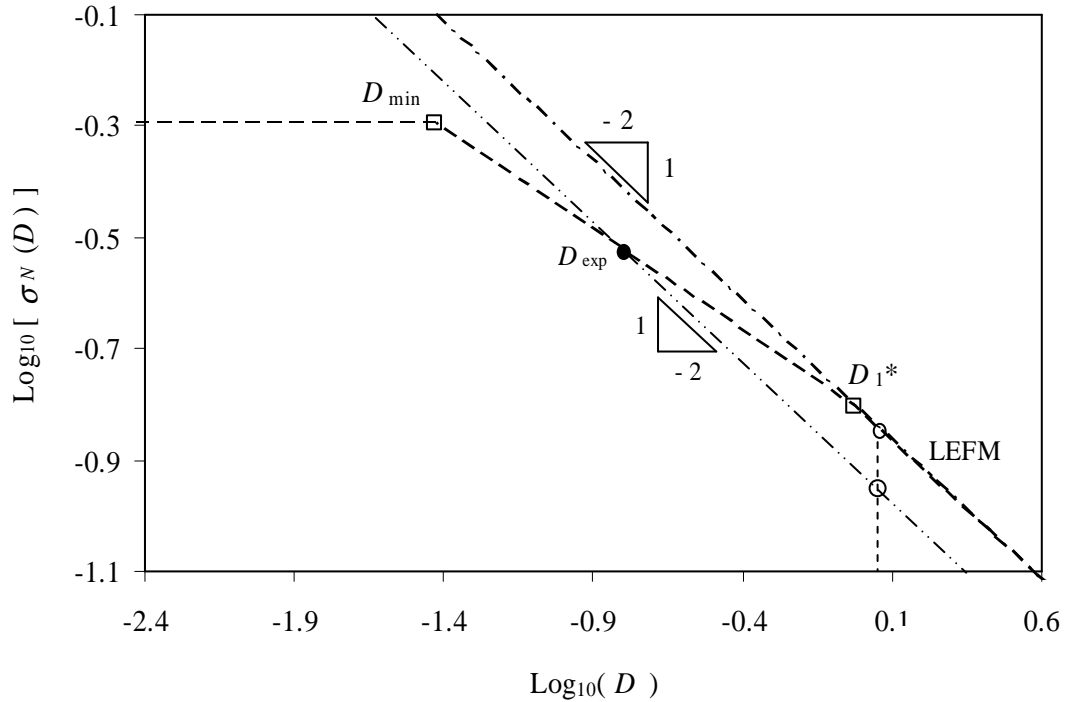


Figure 3.7 Underestimated design (more leftwards centreline) and nominal strength given by LEFM (Eq. 3.17).

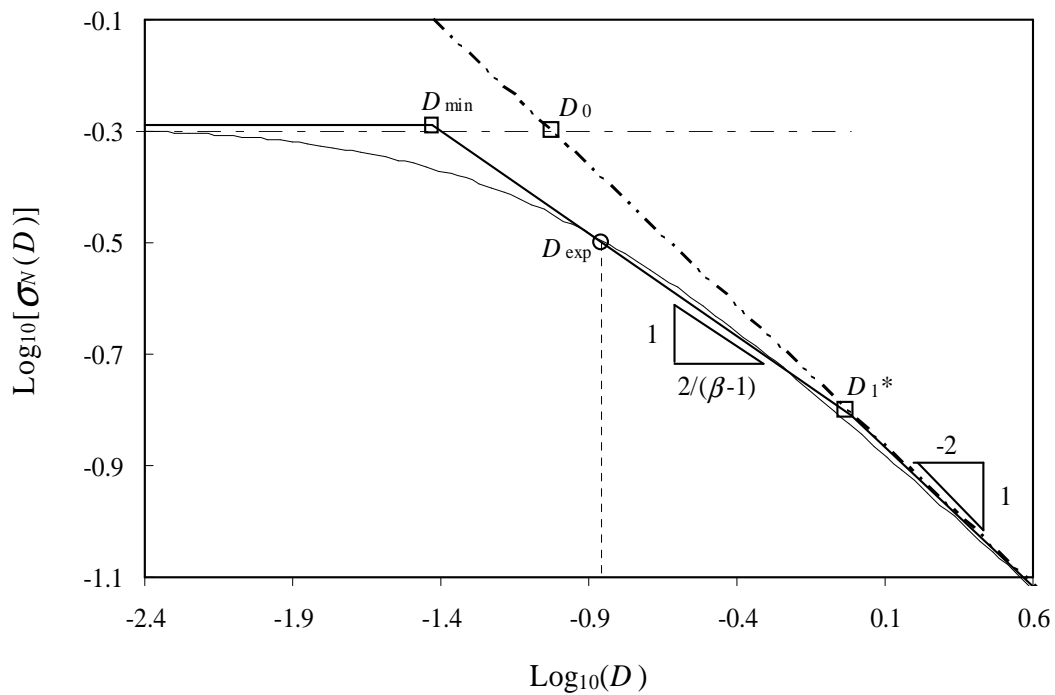


Figure 3.8 Approximate size effect generated by fitting of the nominal strength (Eq. 1.4) and the asymptote of LEFM (Eq. 3.17).

geometrically similar specimens (SEN-TPB) of different sizes. The purpose of doing so is to validate the just exposed derivation of the Size Effect Law, relying on the one-to-one correspondence referred by Planas et al. (1993) (Section 2.4.3) which seems to exist between the R -curve and the softening curve. Hence, the same combination of the cohesive crack properties is to be used in the whole FEM analyses, with the additional intent of verifying if a unique R -curve is revealed.

3.3 Validation procedure from numerical analysis: discussion

This Section presents results of the Cohesive Crack Modelling (CCM) of the Single-Edge Notched Beam loaded in Three-Point-Bending (SEN-TPB) involving geometrically similar specimens (Fig 3.9) of different sizes D (Table 3.1), setting the size range 1:128. The FE-modelling presented in more detail in Appendix A3.2 has been performed using the set of wood engineering constants exhibited in Table A3.2.1 (Appendix A3.2), with the crack propagation model proposed by Petersson PE (1981) (Fig. 2.7) being governed by the same combination of cohesive properties (Table A3.2.2 of Appendix A3.2) for whole specimen sizes D . In regards to the FE-model used in the numerical simulations, the mesh has been implemented to provide a ligament length uniformly divided in every 0.5 mm for the totality of the performed analyses.

Figures 3.10(a) and (b) together illustrate the superposition of load-deflection ($P-\delta$) curves obtained under displacement control, through the CCM for the series set presented in Table 3.1.

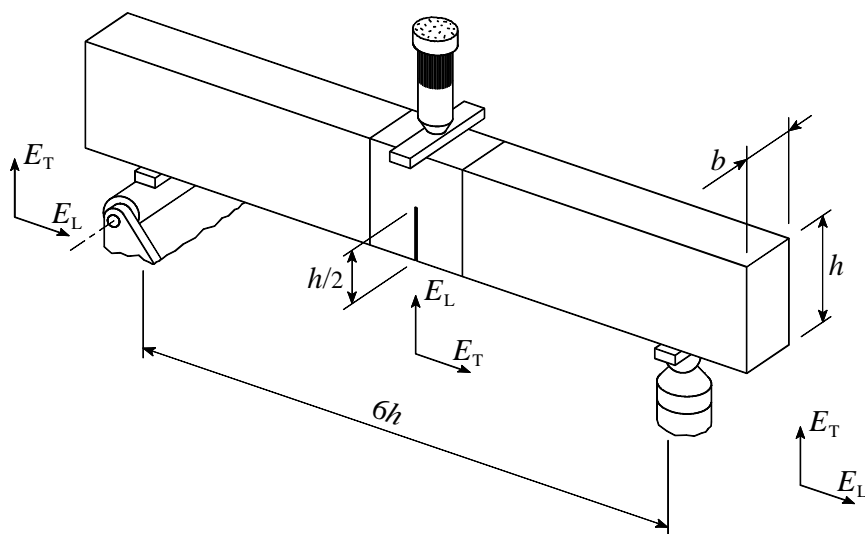
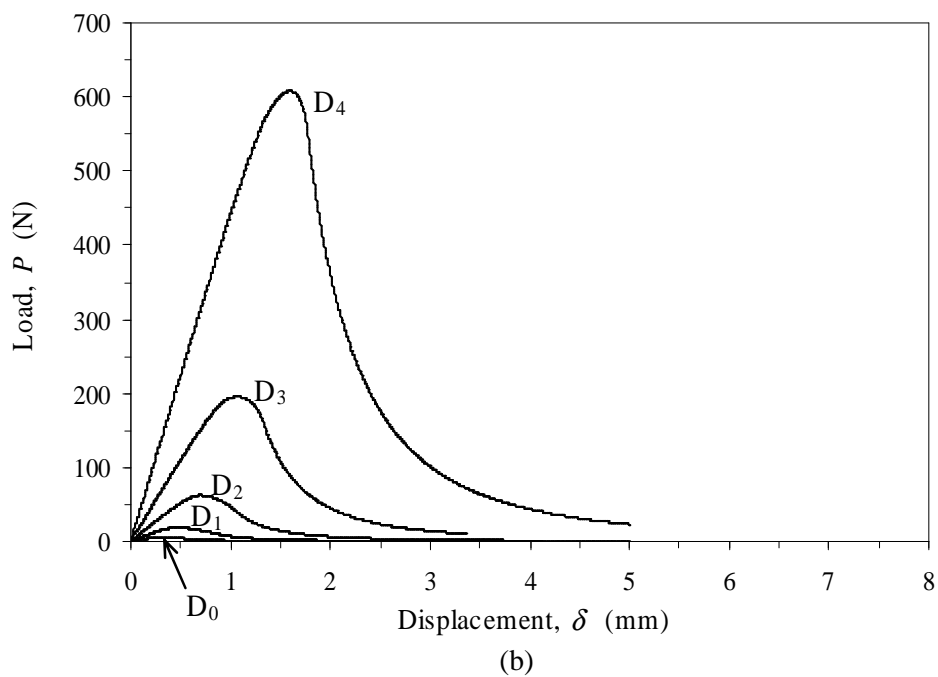
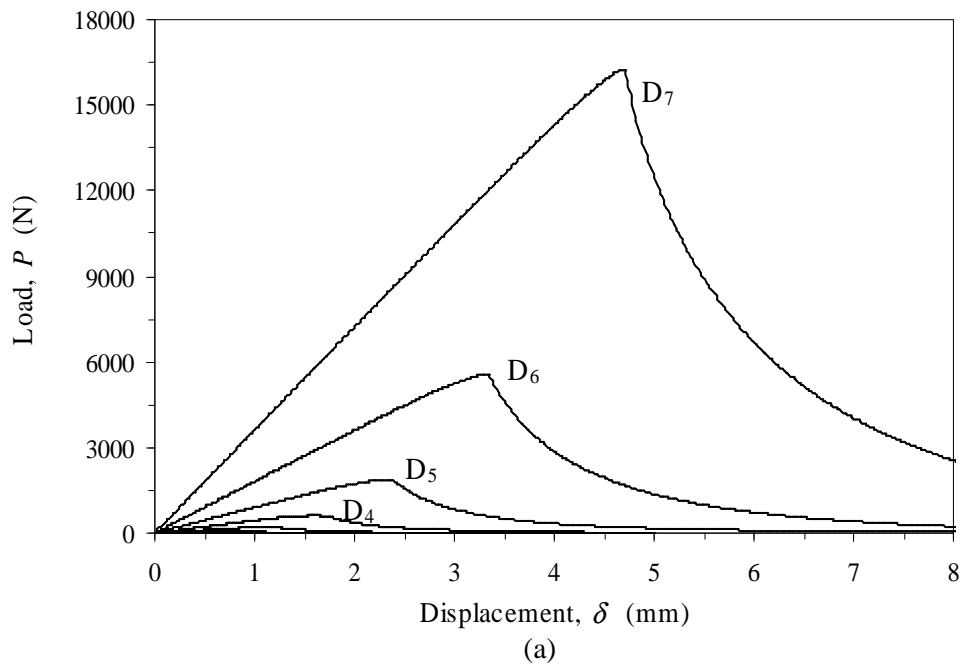


Figure 3.9 Sketch of the SEN-TPB showing the wood anatomic directions in the front plane: Longitudinal (L) and Tangential (T). Dimensions shown in Table 3.1.

Table 3.1 Series identification with corresponding dimensions according to Fig. 3.9

Series label	$D=h$ (mm)	b (mm)	Series label	$D=h$ (mm)	b (mm)
D_0	17.5	5	D_4	280	80
D_1	35	10	D_5	560	160
D_2	70	20	D_6	1 120	320
D_3	140	40	D_7	2 240	640

**Figure 3.10** Load-deflection curves obtained in the CCM under displacement control. Curves labelling is in agreement with Table 3.1.

3.3.1 *R-curve estimate*

Making use of the numerical $P-\delta$ curves (Figs. 3.10 a-b), corresponding R -curves have been estimated using the method detailed in Chapter II (Section 2.3). Since the ligament length varies with the specimen size D the equivalent crack length a has been normalized by the specimen height (*i.e.*, $\alpha=a/h$) to render possible a more convenient way to compare the whole R -curves, as illustrated in Fig. 3.11.

Though the present study had not been carried out using a determined (right-purpose) set of wood cohesive crack properties (as in Chapter II), one can anyway look to the achieved results and legitimately conclude that the choice of the SEN-TPB specimen dimensions used to perform a size effect study on the energy release rate G_R , might be preceded by the definition of a criterion to choose the suitable specimen size range. Indeed, as reported in neither Fig. 3.11, nor all the specimen sizes exhibit an undoubted plateau on the R -curve, with a clear rise in the energy release rate G_R as the specimen decreases in size D . A clearer emphasis on this issue is possible to attain representing the influence of the specimen size D on the evolution of the normalized extent of the cohesive zone l_{coh} , as has been plotted in Fig. 3.12. Thus, it is unquestionable that specimen sizes smaller than D_4 (*i.e.*, $D < 280$ mm according to Table 3.1) ought not to be used in a size effect study on the energy release rate G_R , since an increasingly steeper trend in the (normalized) extent of the cohesive zone l_{coh} is revealed for those sizes, with no subsequent plateau on the R -curve being thus observed. This hinders a self-similar crack propagation which is fundamental to perform accurate measurements of G_{Rc} . Reminding what has been written in Section 1.4 in regards to the self-similar crack propagation, it turns out that under crack growth, the cohesive zone l_{coh} is compelled to move forward (Fig.1.4.c), without increasing in size (*i.e.*, $l_{\text{coh } c}$), and is associated to an equivalent LEFM stable crack growth in the post peak regime (as reported in Figs. 1.4 a-b).

The numerical simulations also show that the extent of the cohesive zone (Fig. 3.12) becomes progressively negligible when compared to the structure size D (LEFM domain).

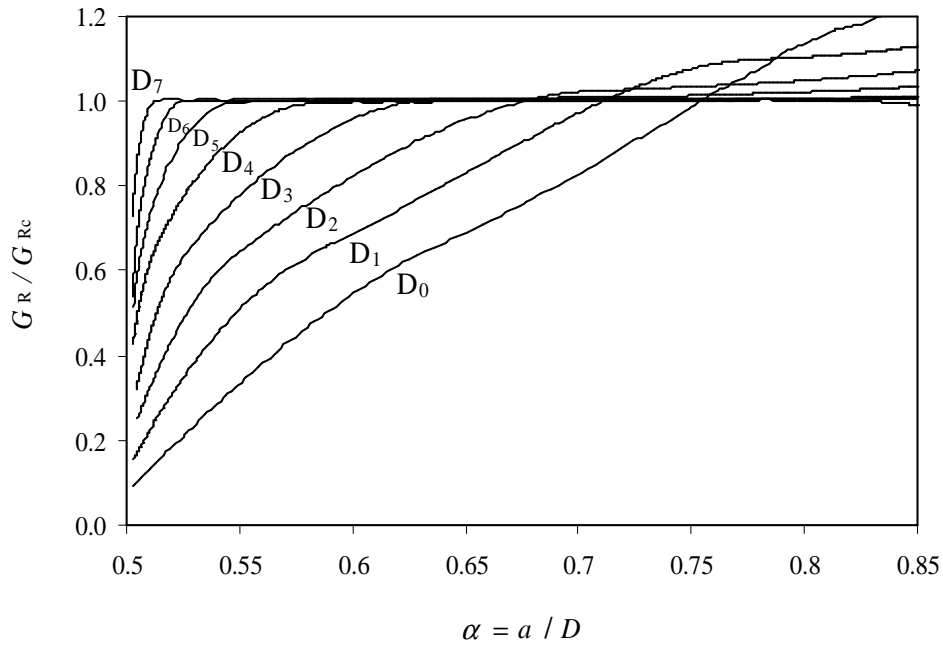


Figure 3.11 Normalised *R*-curves (by $G_f = G_{Rc} = 0.1$ N/mm) obtained in the numerical analyses. Labelling is in agreement with Table 3.1.

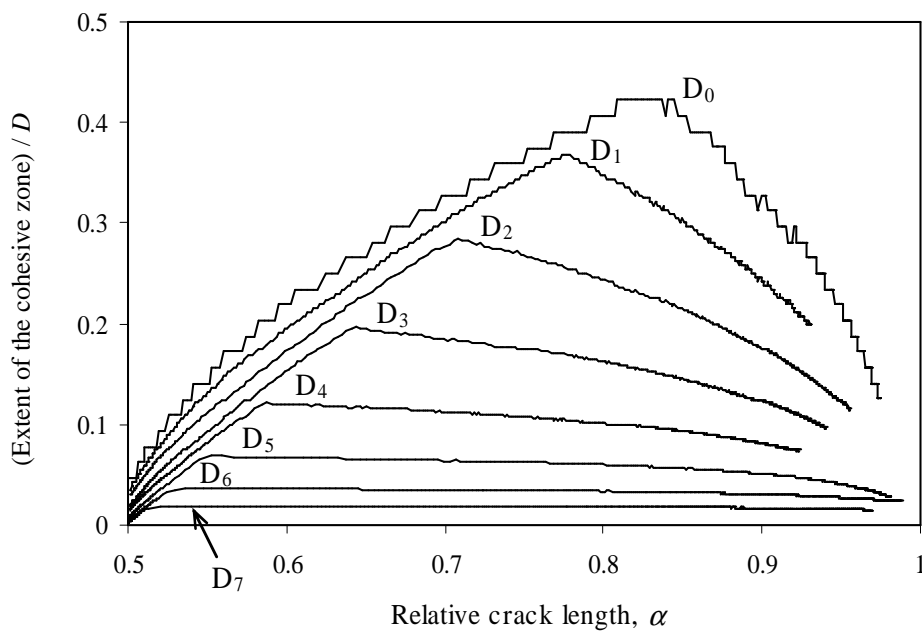


Figure 3.12 Influence of the specimen (SEN-TPB) size D on the normalized extent of the cohesive zone (consult Table 3.1 for labelling identification).

An important conclusion drawn from the numerical analysis has to do with the fact that if the extent of the cohesive zone (Fig. 3.12) does not configure a *plateau* over a considerable (wide) range during the fracture process, then the corresponding *R*-curve does not show an undoubted *plateau*, as it is clearly observed comparing Fig. 3.11 with Fig. 3.12. Another issue of major importance, rouse by the CCM just exposed, is the numerical confirmation that the *R*-curve is unique (*i.e.*, independent of the structure characteristic size D), as is illustrated in Fig. 3.13. It is thus verified what has constituted one of the most important aims of the present numerical study, as evoked in precedent Sections.

The resume of the main results obtained in the numerical study presented in Table 3.2, shows that the relative crack length corresponding to the peak load α_u tends to α_0 as the specimen increases in size (*i.e.*, $D \rightarrow \infty$). As a consequence, the achieved energy release rate associated to the ultimate load P_u also evolves towards the value of the critical energy release rate [*i.e.*, $G_R(\alpha_u) \rightarrow G_{Rc} = 0.1 \text{ N.mm}^{-1}$] as D increases in size. Accordingly, the relative length of the FPZ, *i.e.*, $\theta = \Delta a_c / D$, decreases in size (*i.e.*, $\theta \rightarrow 0$) as $D \rightarrow \infty$, as previewed with the plotting shown in Fig. 3.3.

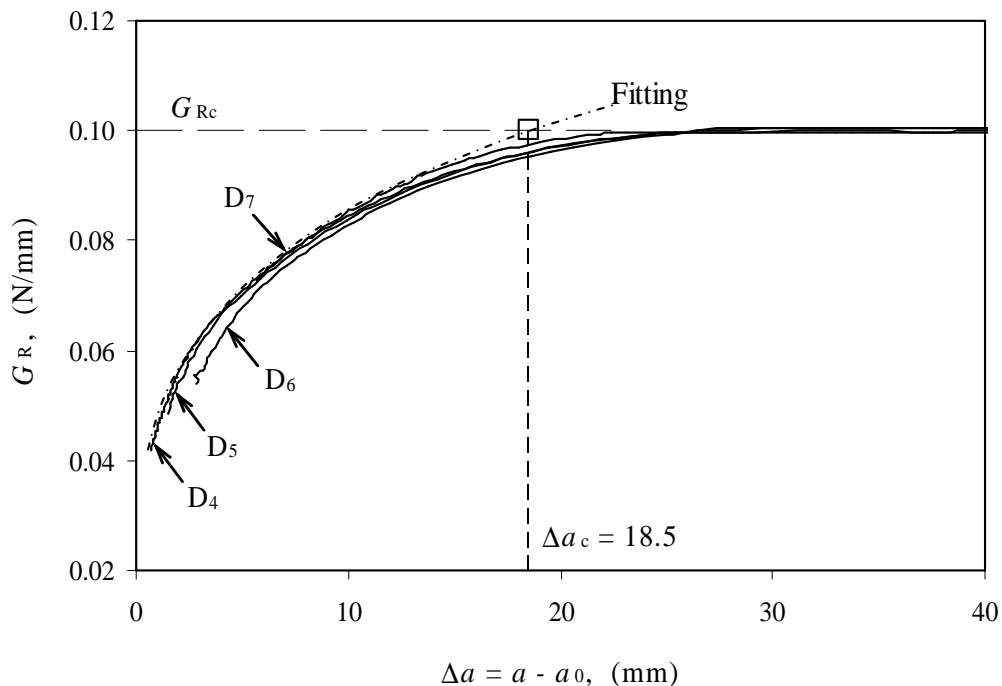


Figure 3.13 Unique *R*-curve revealed through the CCM (consult Table 3.1 for labelling identification).

On the other hand, the dimensionless energy release rate function $g(\alpha)$ (*i.e.*, $g(\alpha) = E' b [\partial \lambda(\alpha) / \partial \alpha] / 2$) has been plotted for a specimen size $D = h$ (Appendix 3.1) and the corresponding polynomial function evaluated by means of the best fit of the set of points obtained for each relative crack length α , as shown in Fig. A3.1.2 (Appendix A3.1). The fitting represented in Fig. 3.14 has been made gathering the data obtained from the rising part of the numerical R -curves [*i.e.*, $G_R(\alpha_0)/G_{Rc} < G_R(\alpha)/G_{Rc} < 1$] represented in Fig. 3.11, corresponding to those curves which exhibit an undoubted plateau (*i.e.*, series: D_4 , D_5 , D_6 and D_7). The curvature exponent of the R -curve β used in the size effect formulation (Section 3.2) is obtained from the slope of the linear regression plot which passes through the origin, revealing $\beta = 0.27$. In such a circumstance, the energy release rate at the onset of the R -curve $G_R(\Delta a_c)$ is the critical value given by the horizontal asymptote [*i.e.*, $G_R(\Delta a_c) = G_{Rc}$].

The R -curve shown in Fig. 3.15 has been outlined plotting the energy release rate G_R as a function of the crack length increment Δa (similarly to Fig. 3.13), by means of Eq. (3.1), using the curvature exponent β obtained in the linear regression plotting of Fig. 3.14. Both axis have been normalized to render possible the comparison between

Table 3.2 Resume of parameters obtained in the numerical simulation of SEN-TPB. Parameters: $\lambda(\alpha_0)$ is the initial compliance; α_u the relative crack length at the peak load P_u ; $G_R(\alpha_u)$ the energy release rate at P_u ; $\theta = \Delta a_c / D$ the relative length of the FPZ.

Series label	$D = h$ (mm)	$\lambda(\alpha_0)$ (mm/N $\times 10^{-3}$)	α_u	$G_R(\alpha_u)$ (N/mm)	θ
D_0	17.5	37.19	0.60	0.053	-
D_1	35	18.41	0.57	0.059	0.265
D_2	70	9.21	0.54	0.062	0.213
D_3	140	4.53	0.55	0.077	0.126
D_4	280	2.26	0.54	0.087	0.085
D_5	560	1.12	0.53	0.094	0.045
D_6	1 120	0.56	0.52	0.099	0.024
D_7	2 240	0.28	0.51	0.100	0.013

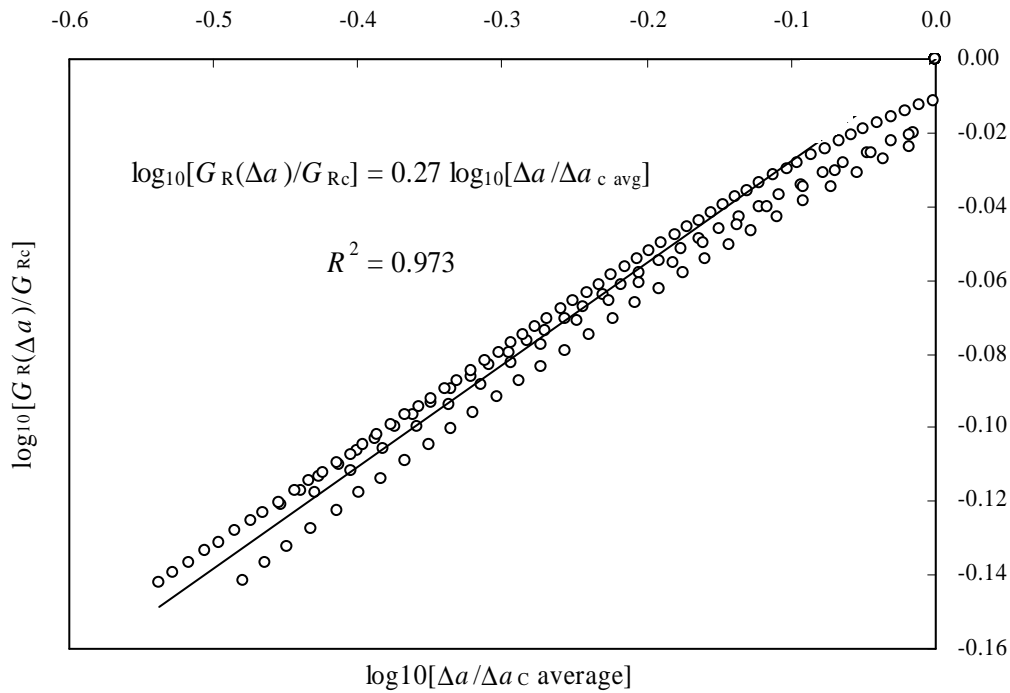


Figure 3.14 Linear regression plot performed on the rising part of the R -curves which exhibit an undoubted plateau (*i.e.*, series D_4 , D_5 , D_6 and D_7 according to Fig. 3.12), used to define the curvature exponent of the R -curve (*i.e.*, $\beta = 0.27$).

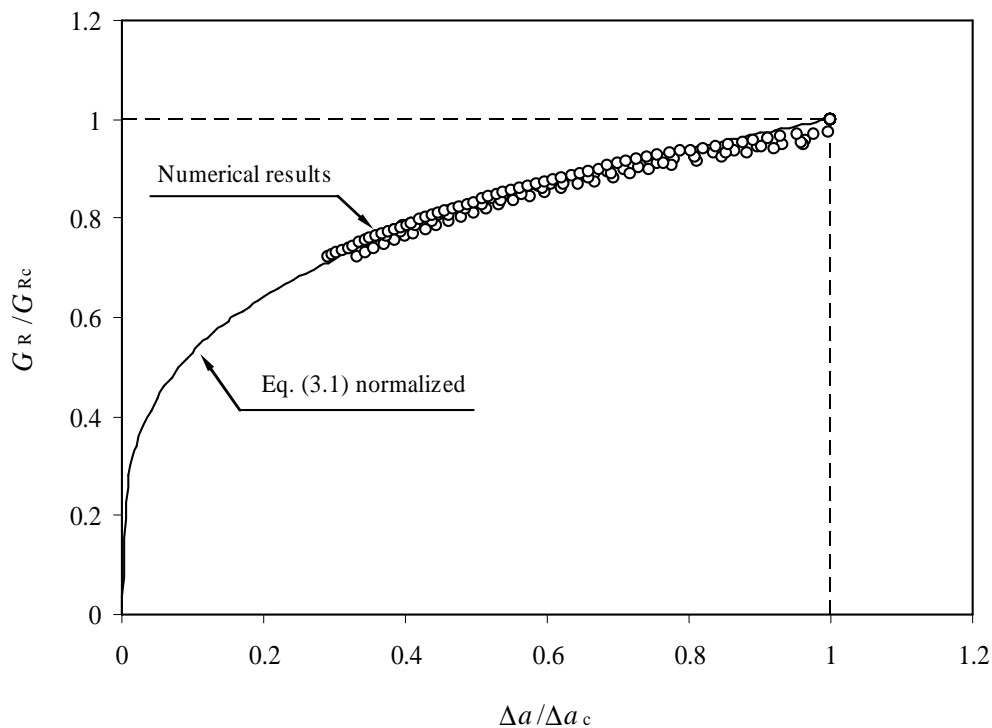


Figure 3.15 Plotting of the normalized R -curve according to Eq. (3.1) ($\phi=1$ and $\beta=0.27$) and the numerical results plotted in Fig. 3.11 for those series which exhibit an undoubted plateau (*i.e.*, series D_4 , D_5 , D_6 and D_7 as plotting of Fig. 3.12). $G_{Rc} = G_f = 0.1 \text{ N/mm}$.

the theoretical and the numerical results obtained in Fig. 3.11 for $G_R/G_{Rc} < 1.0$. The numerical results are barely those which exhibited an undoubted plateau (*i.e.*, series D_4 , D_5 , D_6 and D_7).

3.3.2 Relative crack length at the peak load

The CCM detailed in the previous Section brought to the important conclusion that the R -curve is unique (*i.e.*, independent of the structure characteristic size D), as illustrated through the superposition of the set of R -curves which exhibited an undoubted plateau on the extent of the cohesive zone (Fig. 3.13). This being revealed, the fitting of those R -curves by a power law (centreline shown in Fig. 3.13) rendered possible to estimate the equivalent length of the FPZ, $\Delta a_c = 18.5$ mm. Following on, the linear regression plot executed on the rising part of the same set of R -curves (Fig. 3.14), brought about the curvature exponent of the unique R -curve $\beta = 0.27$. Then, the plotting of the unique R -curve was performed according to Eq. (3.1), revealing the accuracy of the obtained fitting operation, when the comparison is made with the numerical data obtained through the CCM ($G_{Rc} = G_f = 0.1$ N/mm) (*i.e.*, the numerical results printed in Fig. 3.15). Therefore, the transitional regime (*i.e.*, the *crossover* zone in Fig. 3.15: $\Delta a = \Delta a_c$) between the ascending part of the R -curve and the plateau (*i.e.*, $G_R = G_{Rc} = G_f$) is not described by the analytical analysis which is being followed. Indeed, the observation of Fig. 3.15 permits to detect an angulate point in the referred *crossover* zone.

The plotting of Eq. (3.6) exhibited in Figs. 3.16 – 3.20, for most of the series shown in Table 3.1, provide the estimate of the single solution $\alpha_{u^*} = 0.54$, revealed by the interception between $g'/g(\alpha)$ and $G'_R/G_R(\alpha)$. Therefore, computing the size limits D_{\min} and D_c (Eqs. 3.9 and 3.10),

$$D_{\min} = \frac{\Delta a_c}{1 - \alpha_0}$$

$$D_c = \frac{\Delta a_c}{\alpha_{u^*} - \alpha_0}$$

which characterize the domain of α_{u^*} (Fig. 3.3), yield $D_{\min} = 37$ mm and $D_c = 462.5$ mm, taking $\alpha_0 = 0.5$ (Fig. 3.9) and $\Delta a_c = 18.5$ mm (Fig. 3.13). The estimate of the size limits D_{\min} and D_c rendered possible to classify the series set D_2 , D_3 , and D_4 as eligible to figure in the intermediate size range (Table 3.1), with $\alpha_{u^*} \cong \alpha_u$. Increasing in the specimen size D , it turns clear that the relative crack length at the peak load α_u becomes quite unlike the single solution α_{u^*} , since the ultimate load P_u is attended closer and closer the onset of the R -curve plateau. Indeed, as reported in Table 3.2 the current numerical study revealed that as $D \rightarrow \infty$, then $\theta \rightarrow 0$ (*i.e.*, with the FPZ turning irrelevant when compared with the structure size D). Therefore, since Eq. (3.8) establishes that $\alpha_u(D) = \alpha_0 + \theta$, for $D > D_c$, then it seems quite reasonable that the trend revealed by the numerical results (Figs. 3.19-3.20), lean towards $\alpha_u \rightarrow \alpha_0$, as appears in specimens of larger sizes (*i.e.*, for series D_5 , D_6 and D_7 , in Figures 3.18, 3.19 and 3.20).

The poor agreement revealed by the plotting of Eq. (3.7) and $G'_R/G_R(\alpha)$ directly obtained from the R -curve (Fig. 3.11), shown in Figs. 3.16 (over half the range) is

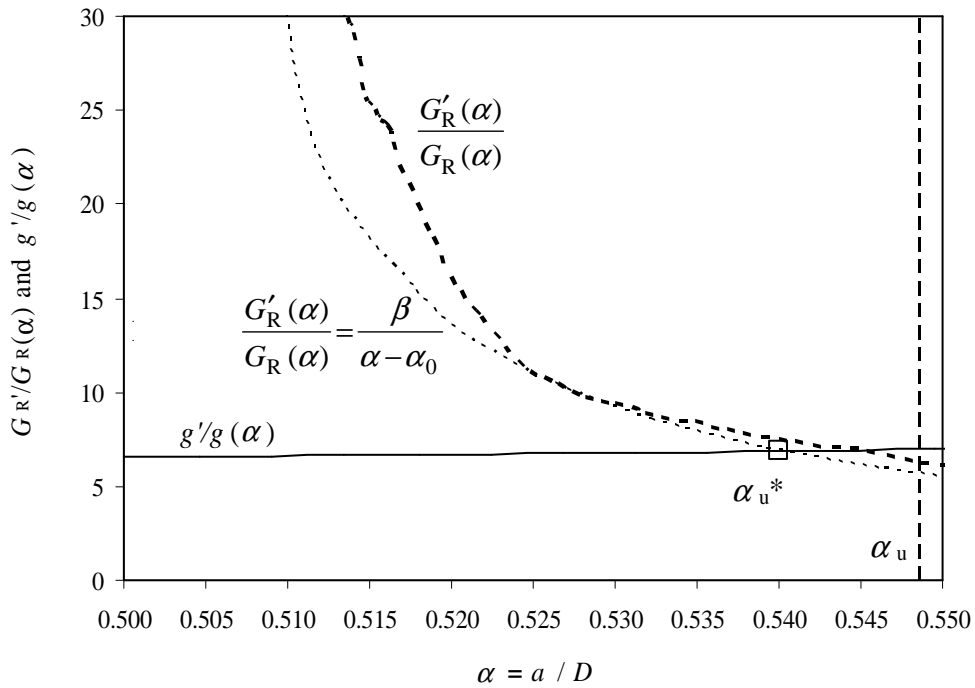


Figure 3.16 Plotting of Eq. (3.6) used to estimate α_{u^*} . Comparison with the plotting of Eq. (3.7) obtained from the R -curve computed for series D_3 (see Fig. 3.11).

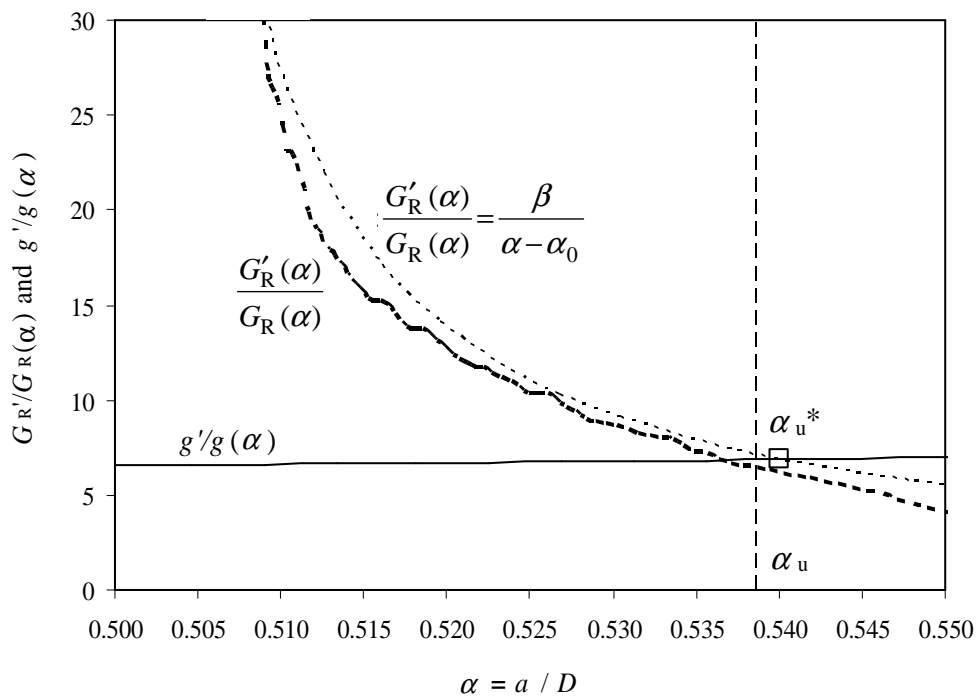


Figure 3.17 Plotting of Eq. (3.6) used to estimate α_{u^*} . Comparison with the plotting of Eq. (3.7) obtained from the R -curve computed for series D_4 (see Fig. 3.11).

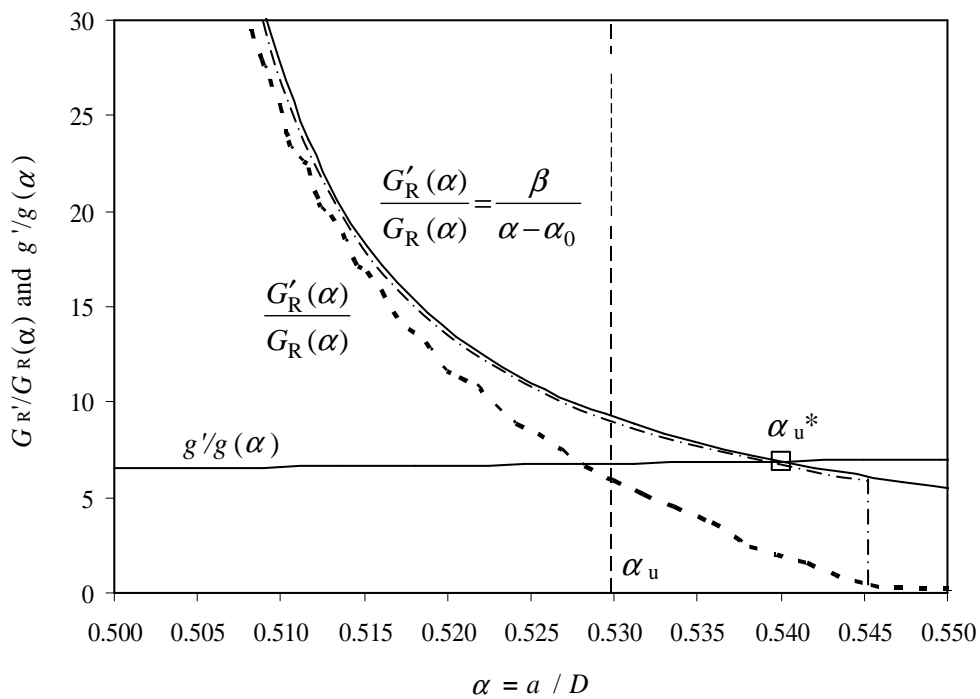


Figure 3.18 Plotting of Eq. (3.6) used to estimate α_{u^*} . Comparison with the plotting of Eq. (3.7) obtained from the R -curve computed for series D_5 (see Fig. 3.11).

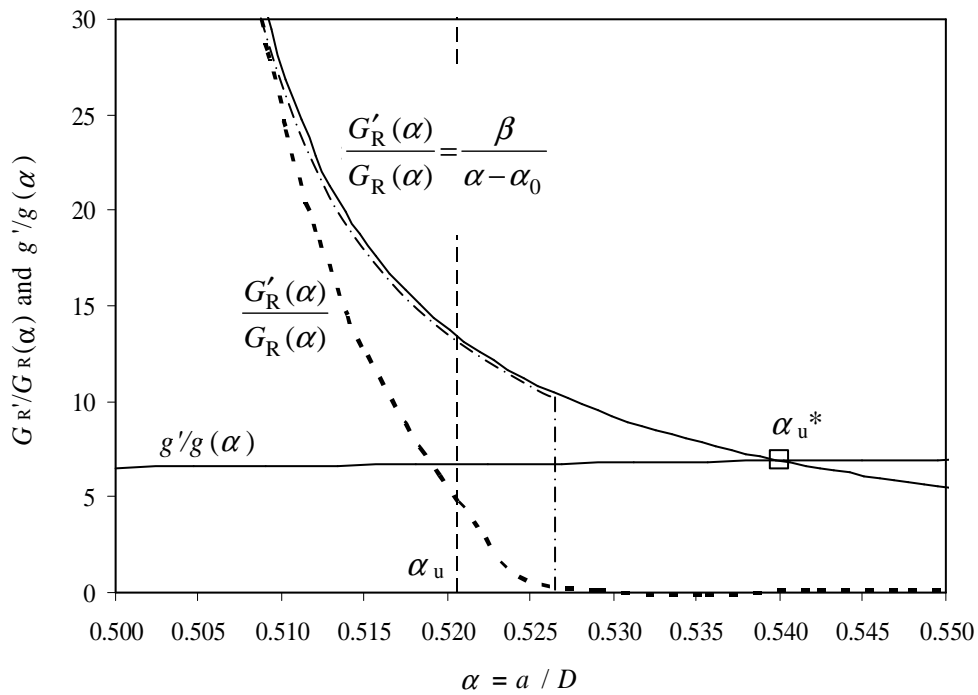


Figure 3.19 Plotting of Eq. (3.6) used to estimate α_{u^*} . Comparison with the plotting of Eq. (3.7) obtained from the R -curve computed for series D_6 (see Fig. 3.11).

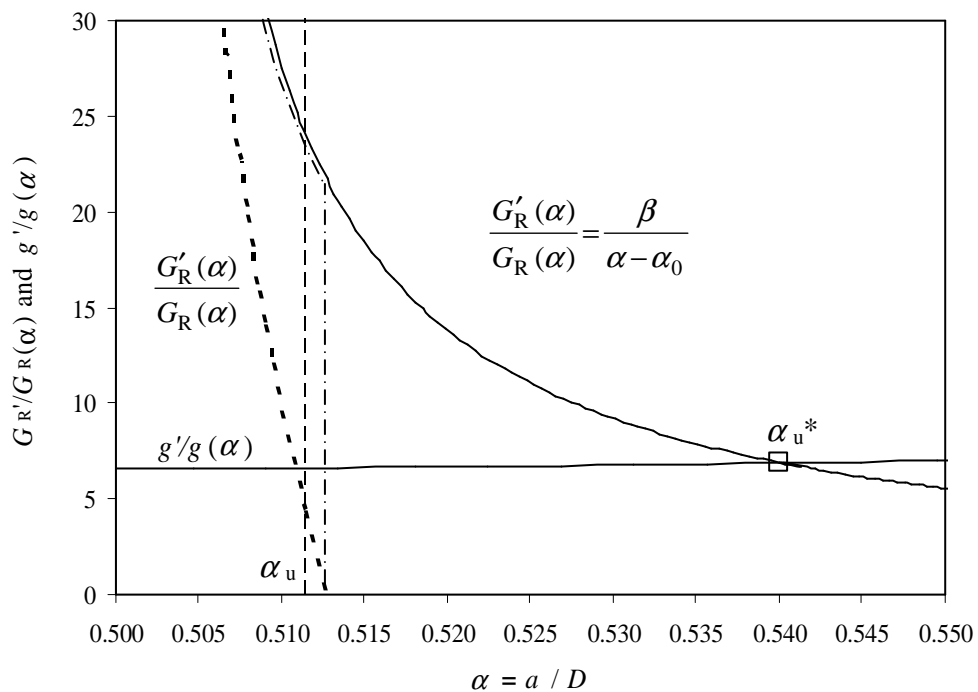


Figure 3.20 Plotting of Eq. (3.6) used to estimate α_{u^*} . Comparison with the plotting of Eq. (3.7) obtained from the R -curve computed for series D_7 (see Fig. 3.11).

justified by the inexistence of a clear (an undoubted) plateau for series D_3 , as mentioned above (Figs. 3.11 and 3.12). As according to the specimen increases in size D , the interception of $G'_R(\alpha)/G_R(\alpha)$ with the axis of the abscissas outlined in Figs. 3.16 – 3.20 (descending thicker hidden line), gets closer and closer the relative crack length at the peak load α_u (which, it turn, gets closer and closer to α_0). This trend is not surprising, bearing in mind that α_u is obtained closer and closer the plateau of the R -curve (*i.e.*, $\alpha_c \rightarrow \alpha_u$) as may be confirmed from analysis of the set of results reported in Table 3.2.

The scaling of the relative crack length at the peak load $\alpha_u(D)$ has been plotted in Figure 3.21, for the available data provided by the FEM computations (structure sizes D as in Table 3.1). As previously performed for Fig. 3.3, the plotting shows the minor and the upper size bounds (D_{\min} and D_c) which set out the intermediate size range. In regards to the included sizes printed in Fig. 3.21 (*i.e.*, labels D_3, D_4, \dots, D_7), it is clear that the revealed FEM data follows a trend which is in fine agreement with both predictions established for the intermediate size range (*i.e.*, $D_{\min} < D < D_c$) and for large sizes (*i.e.*, $D > D_c$: series D_5, D_6 and D_7). Hence, in the former regime one observes that the relative crack length at the peak load α_u is set equal to the single solution α_{u*} , whereas for the later regime (*i.e.*, for large sizes D), the FEM-computations revealed a trend evolving close to the law $\alpha_0 + \theta$. It is worth-while to notice that the plotted circles in Fig. 3.21 follow the tendency outlined by the centreline plotted under the scaling law in Fig. 3.3, mainly in the neighbourhood of the transitional regimes, *i.e.*, from the intermediate size range (*i.e.*, $D_{\min} < D < D_c$) to the large size regime (*i.e.*, $D > D_c$).

The size effect results (Eq. 3.12) on the resistance at the peak load $G_R(\alpha_u, D)$ have been plotted in Fig. 3.22, together with the two asymptotic regimes both for small and for large structure sizes D . Accordingly, the available data generated by means of the FEM computations turned out values of $G_R(\alpha_u)$ evolving with the structure size D in agreement both with the power law $G_R(\alpha_u, D) \propto D^\beta$, in the intermediate regime (*i.e.*, $D_{\min} < D < D_c$: series D_3 and D_4), and with G_{Rc} (with $G_{Rc} = G_f$), in the regime of

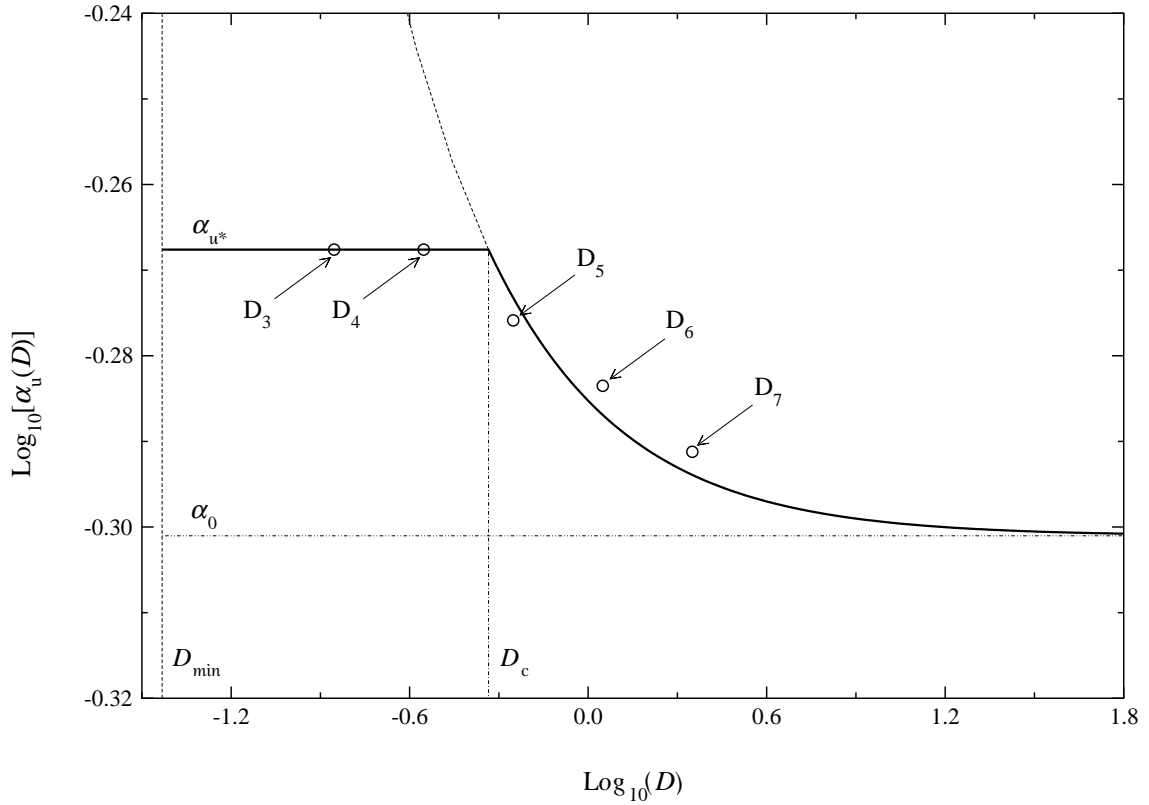


Figure 3.21 Scaling of the relative crack length at the peak load α_u as a function of the characteristic size D . Parameters D_{\min} and D_c represent the lower and upper bounds of α_{u^*} (Eqs. 3.9 and 3.10). Plotted circles indicate the available data provided by the FEM computations (Table 3.1).

large structure sizes D (i.e., $D > D_c$: D_5 , D_6 and D_7). The asymptotic behaviour put into evidence by the size D_5 in Fig. 3.22, confirms the outlined trend shown in Fig. 3.4.

3.3.3 Size effect on the nominal strength

Taking into account the crossover size value ($D_c = 462.5$ mm), the estimate of the single solution ($\alpha_{u^*} = 0.54$) and the curvature exponent of the unique R -curve ($\beta = 0.27$), obtained in the last two Sections, together with the dimensionless energy release rate function $g(\alpha)$ deduced in Appendix A3.1, it is possible to estimate the characteristic size through Eq. (3.19),

$$D_1^* = \left[\frac{g(\alpha_{u^*})}{g(\alpha_0)} \right]^{1/\beta} D_c$$

leading to $D_1^* = 680$ mm, for the initial relative crack length ($\alpha_0 = 0.5$).

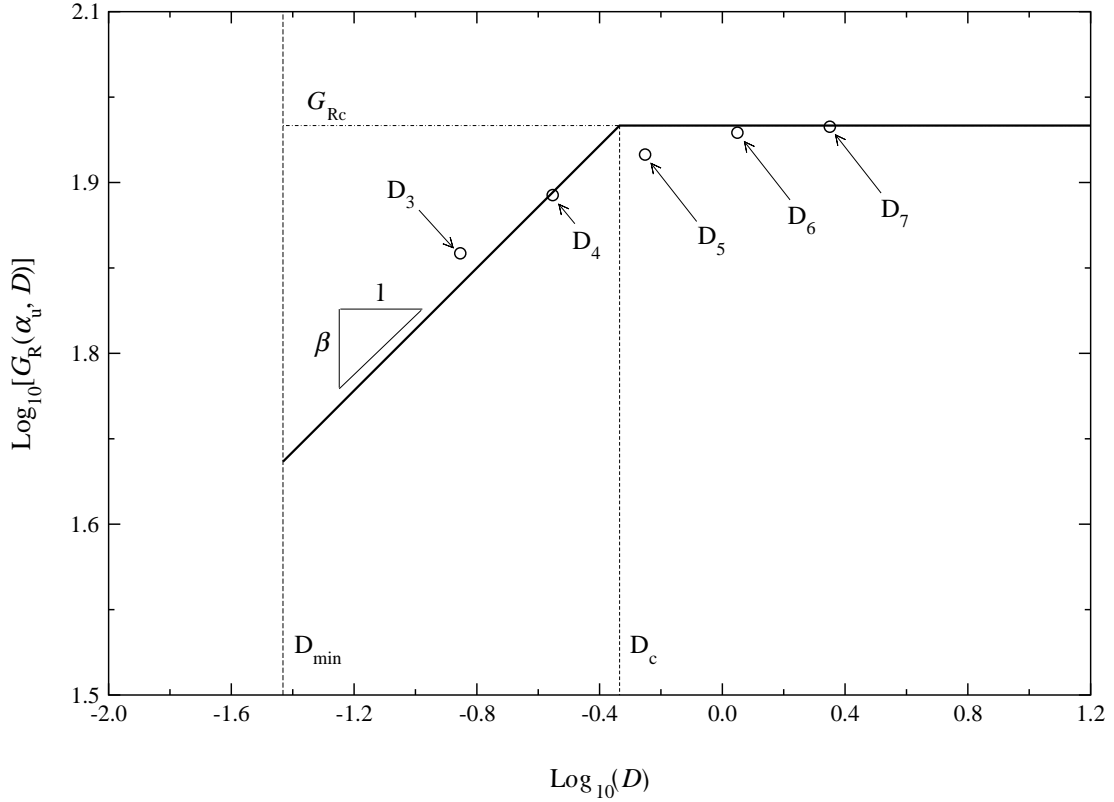


Figure 3.22 Size effect on the resistance at the peak load according to Eqs. (3.11 and 3.12). Parameters D_{\min} and D_c represent the lower and upper bounds of α_{u^*} (Eqs. 3.9 and 3.10). Plotted circles indicate the available data provided by the FEM computations.

The nominal strength $\sigma_N(D)$ expected for the three asymptotic regimes, comprising (i) the large, (ii) the intermediate and (iii) the small sizes D are to be evaluated through Eqs. (3.17), (3.18) and (3.20), listed below:

$$\sigma_N(D) = c_N \sqrt{\frac{E' G_{Rc}}{g(\alpha_0)}} D^{-1/2}$$

$$\sigma_N(D) = c_N \sqrt{\frac{E' \phi(\alpha_{u^*} - \alpha_0)^\beta}{g(\alpha_{u^*}) D^{1-\beta}}}$$

$$\sigma_{N \max} = c_N \sqrt{\frac{E' \phi(\alpha_{u^*} - \alpha_0)^\beta}{g(\alpha_{u^*}) D_{\min}^{1-\beta}}}$$

Hence, bearing in mind that $c_N = 3/2(L/h) = 9$ as deduced in Section 3.2.2.2, the effective Young modulus $E' = 709.8$ MPa and the dimensionless energy release rate function $g(\alpha)$ estimated in Appendix A3.1, together with the critical energy release

rate $G_{Rc} = 0.1 \text{ N.mm}^{-1}$, the initial relative crack length $\alpha_0 = 0.5$, the equivalent length of the FPZ $\Delta a_c = 18.5 \text{ mm}$, the curvature exponent of the unique R -curve $\beta = 0.27$, the pre-factor $\phi = G_{Rc} / \Delta a_c^\beta = 270 \text{ J/m}^{2+\beta}$ defined through Eq. (3.1), the single solution $\alpha_{u^*} = 0.54$ and the size limits $D_{\min} = 37 \text{ mm}$ and $D_1^* = 680 \text{ mm}$, it is possible to estimate the nominal strength $\sigma_N(D)$ expected for the three asymptotic regimes, setting D according to Eq. (3.21),

$$\sigma_N(D) \propto \begin{cases} \sigma_{N \max} & \Leftrightarrow D < D_{\min} \text{ (strength theory)} \\ D^{-1/2 + \beta/2} & \Leftrightarrow D_{\min} < D < D_1^* \\ D^{-1/2} & \Leftrightarrow D > D_1^* \end{cases}$$

Figure 3.23 shows the plotting of these Equations thus providing the necessary data to accomplish the size effect on the nominal strength $\sigma_N(D)$. Figure 3.23 also shows the fine agreement obtained by the inclusion of the set of circles corresponding to the

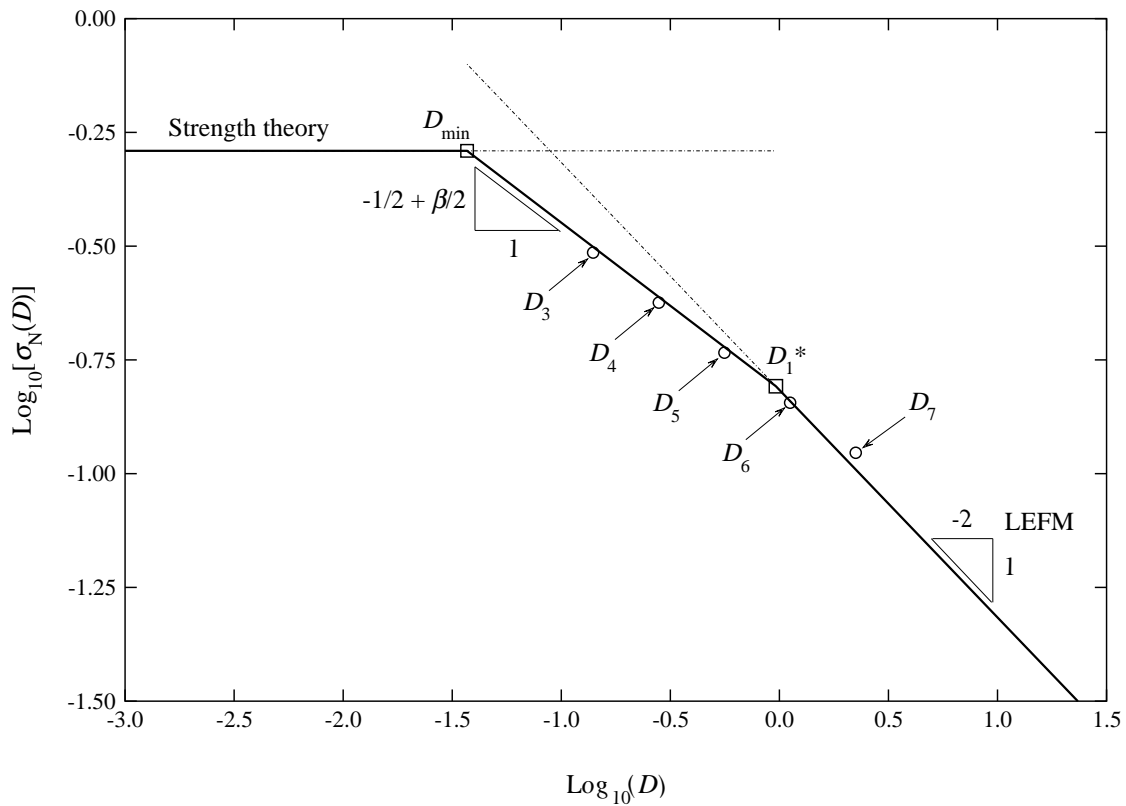


Figure 3.23 Size effect on the nominal strength (Eq. 3.17, 3.18 and 3.20). Included circles are labelled according to specimen sizes listed in Table 3.1.

It should be noted that sizes D_0 , D_1 and D_2 were not included in Fig. 3.23 because the CCM revealed the absence of an undoubted plateau on the R -curve for these specimen sizes (Figs. 3.11 and 3.12). On the other hand, it turns quite dubious to describe accurately the cracking phenomenon taking place in such a narrow ligament volume.

Notwithstanding the even more massive time consuming necessary to perform the CCM, the inclusion of a specimen of larger size (*i.e.*, $D > D_7$) among the set of dimensions of Table 3.1 is well worth-while, to provide a more convincing trend revealed in the domain estimated by LEFM (Fig. 3.23).

Summing up, the CCM presented in this Section has demonstrated that the derivation of the energetic Size Effect Law based on the equivalent LEFM, as detailed in Section 3.2, is valid.

Still focused on the evaluation of the Size effect on the nominal strength $\sigma_N(D)$, once determined the position of the experimental data (Fig. 3.23), the LEFM asymptotic regime might be plotted using the Bažant's Size Effect Law (SEL) through Eq. (1.4).

Following the procedure issued from the derivation law exposed in Section 3.2, based on reliable experimental data, one can predict the Size Effect of a quasibrittle material of a given structure geometry. This is the subject of main concern treated in the ending Chapter of this Thesis.

Chapter IV

Experiments on Size Effect

Chapter IV

4.1 Introduction

In this Chapter a description of the experiments on size effect in wood is made involving the Single-Edge-Notched beam loaded in Three-Point-Bending (SEN-TPB). A method is proposed on the regards of the evaluation of the *Resistance*-curve taking into account the correction needed to take into account the specimen self-weight. A verification of the attained accurateness in the evaluation of the critical energy release rate is made through cohesive crack modelling. Size effect results are revealed arising from the experiments performed in wood spruce SEN-TPB specimens.

4.2 Experiments

Norway spruce (*Picea abies* L.; 405 kgm⁻³ on average: ANNEXE) was used in this study as testing material. Moisture content in wood was found in 11-13% after conditioning at 20°C and 65 RH until equilibrium. Wood was machined far enough away from the stem pith complying with anatomic axis orientations and nominal dimensions represented in Figure 4.1 and clear parts (free from knots and material defects) bonded with a suitable epoxy adhesive (ARALDITE® AW106/953U). Starter notches were made along the composite beam central-section using a band saw (1 mm thick) and initial crack notches a_0

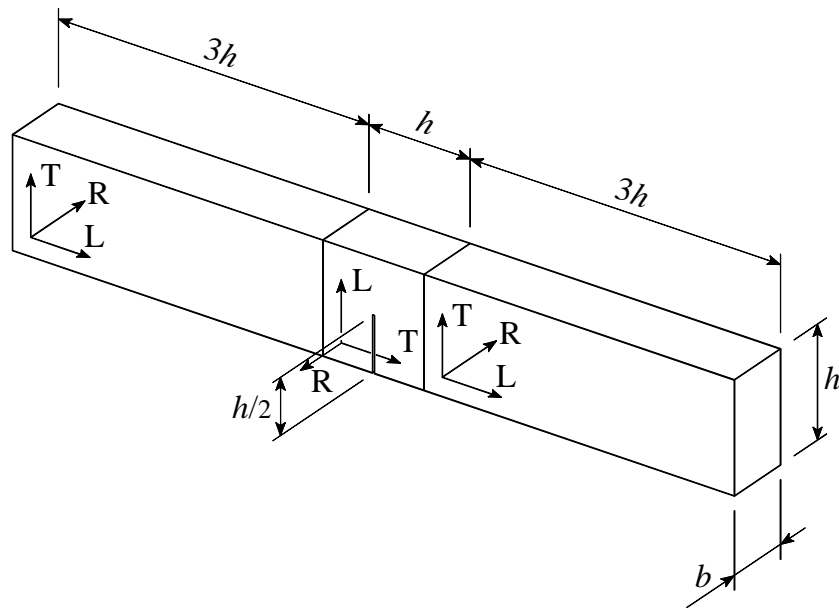


Figure 4.1 SEN-TPB geometry used in the experiments showing the initial crack length $a_0 = h/2$. Triad indexes L , R and T represent the Longitudinal, Radial and Tangential wood anatomic directions. Values of h and b are listed in Table 4.1.

sharpened using a fine cutter blade (depth of sharp notch: 1.0 - 1.5 mm) up to $h/2$ just a little while before conducting experimental tests. Taking due note of the reference characteristic structure size h regarding the dimension $D=70$ mm (Table 4.1), five additional homothetic series were machined from this one, composing a size range of 1:12.

Geometrically similar SEN-TPB were tested to determine load-displacement curves up to complete rupture under displacement control. The initial crack/depth ratio was set to 0.5 and the span/depth ratio was fixed to 6 (Figure 4.2.a and b). A mechanical spindle-driven tension-compression machine (20 kN total capacity) was used to induce fracture in Mode I. A load cell with the capacity of 1 kN was installed and the crosshead displacement rate regulated to reach the peak load P_u in 3 ± 1 minute during fracture tests, thus minimizing possible viscoelastic effects in wood. An optical extensometer was used to monitor two displacement values during the experiments: δ_1 regarding the mid-span target bonded on a long light-weight rigid bar supported on two small metal pins previously stuck onto the specimen in alignment with the supports (Figure 4.2.a); and δ_2 , referring to another target

Table 4.1 Specimen sizes used in the experiments according to Fig. 4.1

Quantity	$h=D$ (mm)	b (mm)
11	280	80
18	210	60
19	140	40
16	70	20
19	35	10
12	23.3	6.7

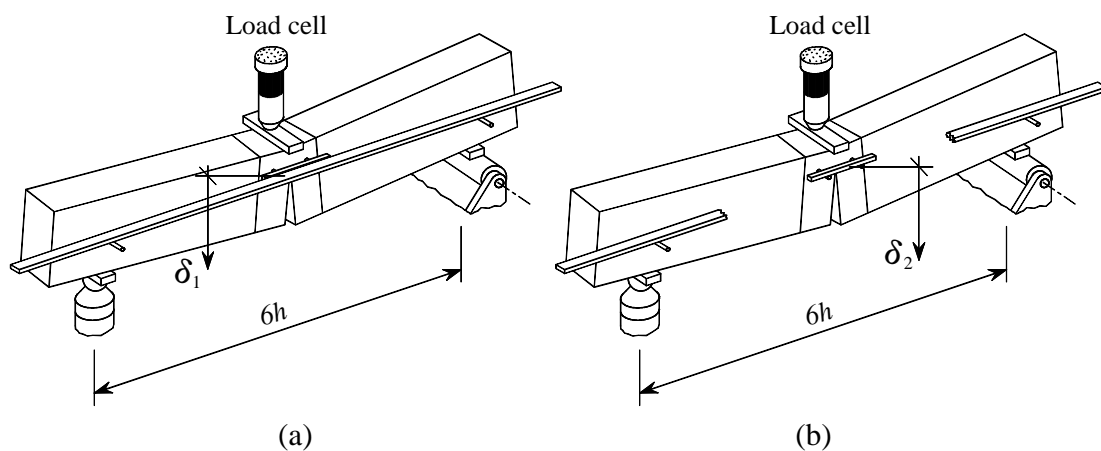


Figure 4.2 Sketch of the TPB test set-up showing the displacement monitoring in the mid-span of the : (a) δ_1 : long light-weight rigid bar and (b) δ_2 : short light-weight rigid bar supported on tiny metal pins also bonded to the specimen surface.

bonded onto the mid-span of a short light rigid bar hold on two additional tiny metal pins, firmly fixed to the central span, positioned at $2h/3$, at $h/10$ apart from the central section (Figure 4.2.b). Displacement values were monitored computing $\delta = (\delta_2 - \delta_1)$, exerting no mechanical contact with the specimen during the experiments.

The superposition of typical $P-\delta$ curves shown in Figure 4.3 reveals the obvious decrease of the initial compliance $\lambda_{\text{exp}}(a_0)$ with the increase in the structure size D , together with the natural increase in the ultimate load P_u (ANNEXE). The configuration revealed by the $P-\delta$ curves (Appendix A4.1) also indicates that crack propagation occurred in a stable way.

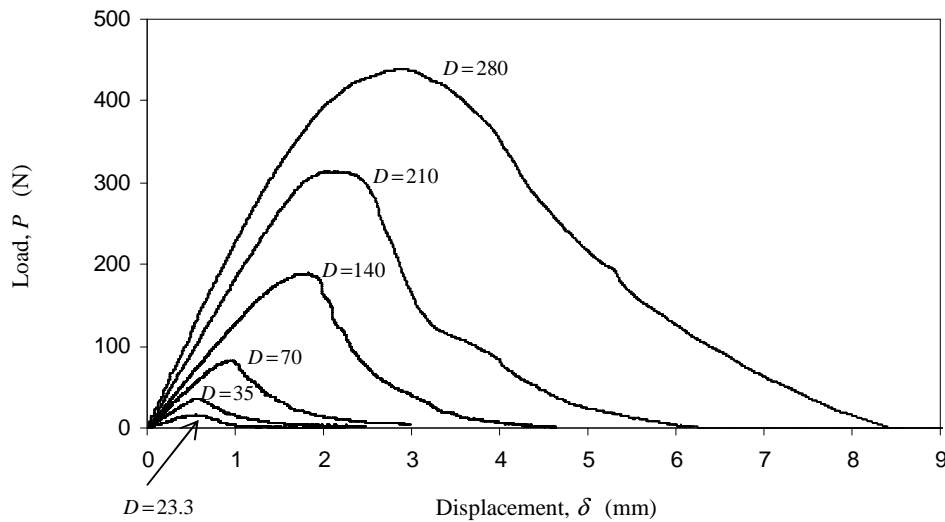


Figure 4.3 Superposition of typical load-deflection curves obtained for each series according to dimensions shown in Table 4.1.

4.3 Self-weight compensation

In fracture testing involving Single-Edge-Notched beams loaded in Three-Point-Bending (SEN-TPB) as well as in other specimen shapes, the specimen weight contributes to the overall loading of the system. Unless special methods are put into practice, the contribution of the specimen weight is not compensated, leading thus to misevaluations of fracture parameters obtained in the experiments.

4.3.1 Load equivalent to the specimen self-weight: static approach

As illustrated in Fig. 4.4 for the simple test configuration, the load cell has been zeroed (point O) when the self-weight was already acting on the specimen (Bažant Z and Planas J, 1998). This means that at zero applied load ($P=0$), a bending moment $qL^2/8$ already exists at the central cross section (with q standing for the distributed load corresponding to the specimen self-weight and L for the beam span). Consequently, if one considers a statically equivalent load acting on the mid-span P_q , which gives the same bending moment as the one obtained from the distributed load q , corresponding to the specimen self-weight, the resultant bending moment will turn $M_q = P_q L/4$. Thus, establishing the equality between the former bending moments, it is possible to get the constant central load $P_q = qL/2$, with

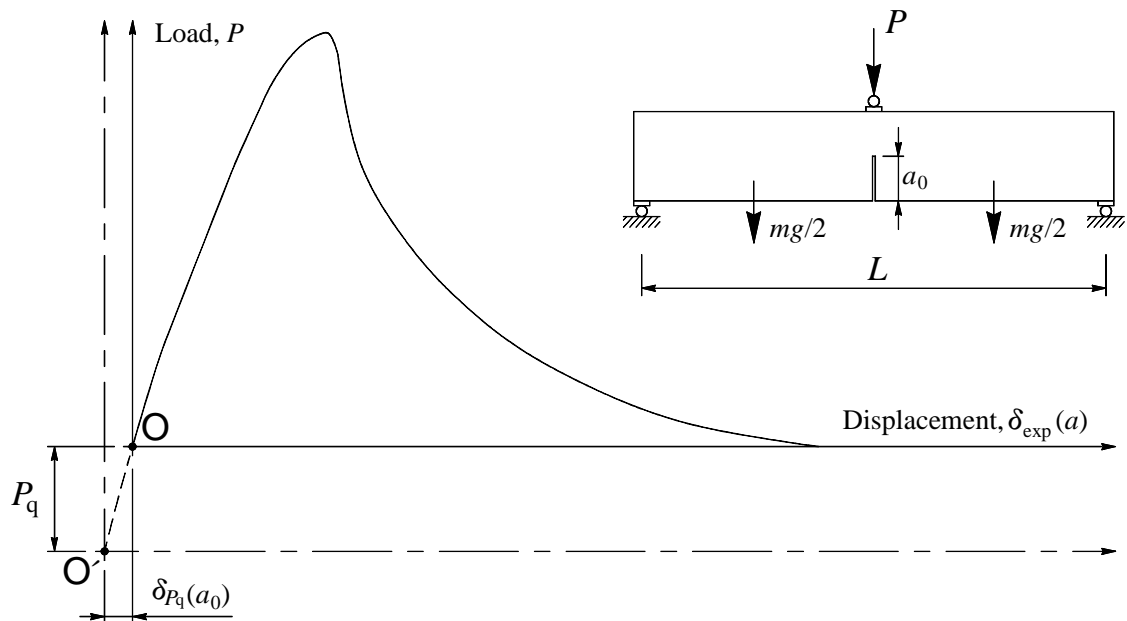


Figure 4.4 Load-displacement curve for the uncompensated TPB test. Adapted from Bažant Z and Planas J (1998).

$qL = mg$ (being m the specimen mass and g the acceleration of gravity). In a strictly theoretical point of view, if this statically equivalent load P_q could act alone in the system, it would produce the load-deflection curve represented by the dashed line in Fig. 4.4 (origin at O'). Nevertheless, in the experiments the recorded curve is simply the one illustrated by the full line, which obviously is the result of the applied load P and its own-weight. It should be emphasized however that the recording provides the external applied load P (given by the load cell) while the displacement δ is due to the combined action of P and the specimen self-weight.

In the following, two methods are proposed to put into practice the self-weight compensation in the context of the R -curve evaluation using the SEN-TPB geometry. The first one is an approximate method based on the kinematic approach, whereas the second is the Exact method, which provides the accurate evaluation of the self-weight compensation.

4.3.2 Load equivalent to the specimen self-weight: kinematic approach

Consider the testing notched beam in TPB represented in Fig. 4.5, subjected both to an external load P acting on the half-span and the beam weight represented by the linear

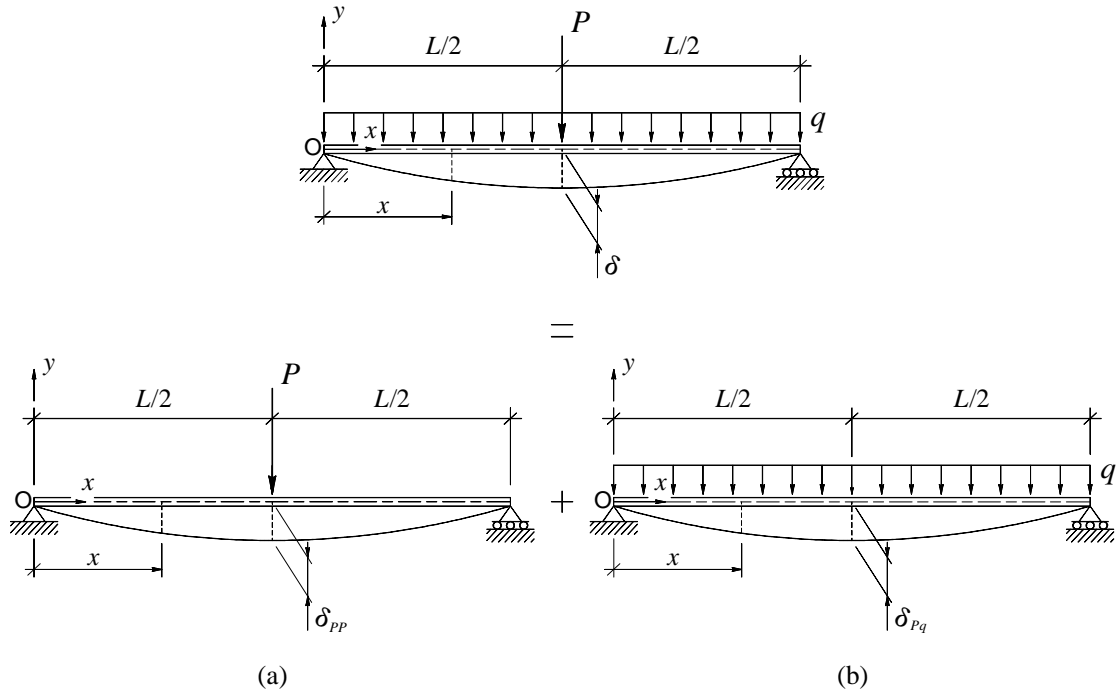


Figure 4.5 Schematization of the simply supported beam subjected to the superposition of (a) the central load P [N] and (b) the distributed load q [N/m]. Parameters: δ_{PP} , displacement due to P ; δ_{Pq} , displacement due to q . Both displacement values are read in the central load axis P , with $\delta = \delta_{PP} + \delta_{Pq}$.

distributed load q . The displacement of point C is given by the contribution of the central load P and the linear distributed load q ,

$$\delta = \delta_{PP} + \delta_{Pq} = \lambda_{PP} P + \lambda_{Pq} q \quad (4.1)$$

where λ_{PP} and λ_{Pq} represent the compliance due to P and q , respectively (with λ_{PP} expressed in [m/N] and λ_{Pq} in [m²/N]) measured in the axis of P .

The initial compliance $\lambda_{\text{exp}}(a_0)$ is evaluated considering the recorded values (Fig. 4.6) got hold of the experiments, computing

$$\lambda_{\text{exp}}(a_0) = \frac{\Delta \delta_{\text{exp}}(a_0)}{\Delta P_{\text{exp}}(a_0)} \quad (4.2)$$

with $\delta_{\text{exp}}(a_0)$ defined in Fig. 4.6 as

$$\delta_{\text{exp}}(a_0) = [\delta_{PP}(a_0) + \delta_{Pq}(a_0)] - \delta_{Pq}(a_0) \quad (4.3)$$

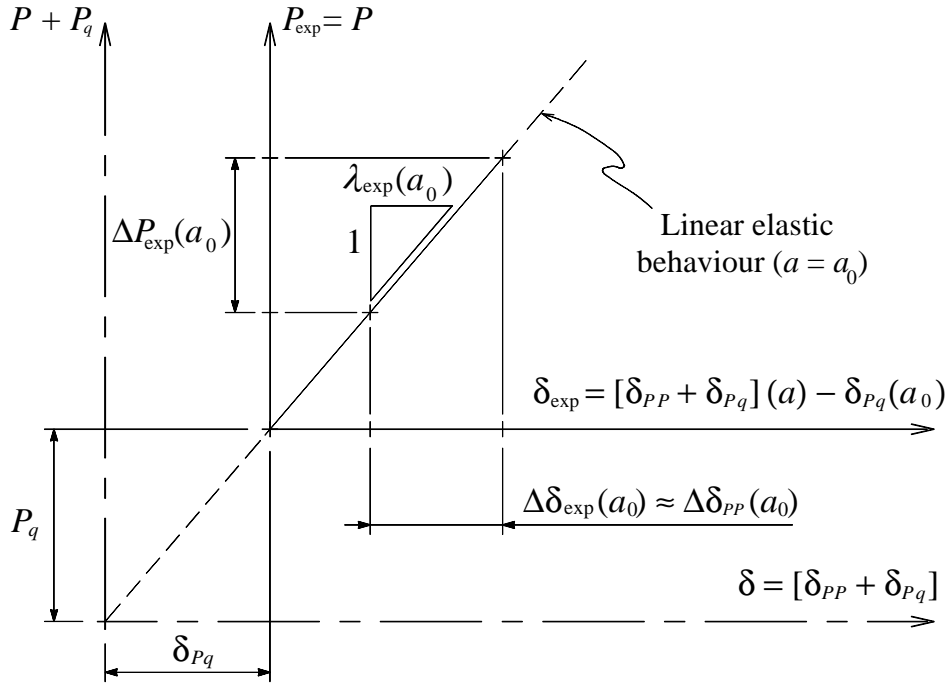


Figure 4.6 Load–deflection curve in the elastic domain ($a = a_0$).

In Eq. (4.3) $\delta_{PP}(a_0)$ is the only quantity which varies. Indeed, the quantity $\delta_{Pq}(a_0)$, though impossible to measure in the experiments, is kept up unchanged (providing that $a = a_0$), thus leading to,

$$\delta_{\text{exp}}(a_0) = \delta_{PP}(a_0) \quad (4.4)$$

Hence, rearranging Eq. (4.2), it may be established that (Fig. 4.6),

$$\lambda_{\text{exp}}(a_0) = \frac{\Delta \delta_{PP}(a_0)}{\Delta P_{\text{exp}}(a_0)} = \lambda_{PP\text{exp}}(a_0) \quad (4.5)$$

The second term of Eq. (4.1) may be rearranged in order to incorporate an external central load P_q , which in practice produces the same displacement of the beam weight δ_{Pq} in point C (kinematic equivalence) (Fig. 4.5), so that

$$\delta = \lambda_{PP}(P + P_q) \quad (4.6)$$

Thus, eliminating δ among Eqs. (4.1) and (4.6), it turns

$$P_q = \frac{\lambda_{Pq}(a)}{\lambda_{PP}(a)} q \quad (4.7)$$

which is valid if the ratio

$$\lambda_{Pq}(a)/\lambda_{PP}(a) \equiv \text{constant} \quad \forall a \in [a_0, a_{\text{expl}}] \quad (4.8)$$

with the range of validity $[a_0, a_{\text{expl}}]$ to be estimated numerically.

Therefore, using the recorded load–deflection curve obtained in the experiments (Fig. 4.7), and providing that the *equality* settled through Eq. (4.8) is verified, Eq. (4.7) enables to establish

$$\lambda_{Pq}(a_0) q = \lambda_{PP \text{ exp}}(a_0) P_q = \delta_{Pq \text{ exp}}(a_0) \quad (4.9)$$

with $\lambda_{PP \text{ exp}}(a_0)$ as defined through Eq. (4.5),

$$\lambda_{PP \text{ exp}}(a_0) = \lambda_{\text{exp}}(a_0)$$

Hence, for a given point M of the load-deflection curve (Fig. 4.7), for which an equivalent crack length a is to be computed, the compensation due to the self-weight is performed setting

$$\lambda_{\text{exp comp}}(a) = \frac{\delta}{P + P_q} \quad (4.10)$$

which, according to Eqs. (4.1) and (4.6), results

$$\lambda_{\text{exp comp}}(a) = \frac{\delta_{PP} + \delta_{Pq}}{P + P_q} = \frac{\lambda_{PP}(a)(P + P_q)}{P + P_q} = \lambda_{PP}(a) \quad (4.11)$$

Resulting values of $\lambda_{\text{exp comp}}(a)$ are subsequently used to perform computations on the equivalent crack length a and resultant energy release rate $G_R(a)$ quantities by means of the equivalent LEFM approach proposed by Morel S. *et al.* (2005) (also detailed in Section 2.3). It should be noted that both terms $\lambda_{PP}(a)$ and $\lambda_{Pq}(a)$ in Eqs. (4.6) - (4.8) and (4.11) represent corrected values of the compliance polynomial functions which result, respectively, from the best fit of FEM computations for the central P and distributed q loads acting on the specimen for different crack lengths a ,

$$\lambda_{PP}(a) = \psi \lambda_{PP}^*(a) \quad (4.12)$$

$$\lambda_{Pq}(a) = \psi \lambda_{Pq}^*(a) \quad (4.13)$$

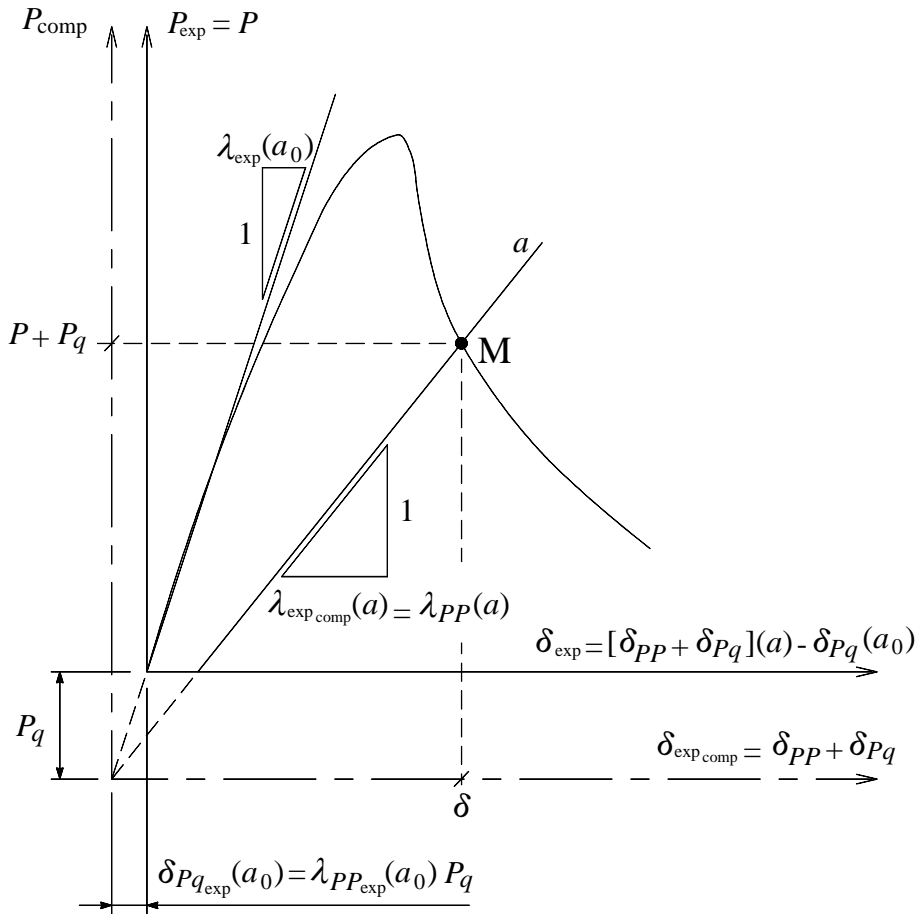


Figure 4.7 Self-weight compensation of the load–deflection curve.

The purpose of this correction, as proposed by Morel S. et al. (2005), is to take into account the scattering of mechanical properties observed in the material. The parameter ψ in Eqs. (4.12) and (4.13) stands for the multiplicative correction factor estimated once per specimen as,

$$\psi = \frac{\lambda_{\text{exp}}(a_0)}{\lambda_{PP}^*(a_0)} \quad (4.14)$$

As observed in Section 2.3, in view of the fact that in in-plane analysis the quantity $1/E$ is essentially proportional to the compliance $\lambda_{PP}(a)$ (with $E = E_T$ according to specimen sketch of Fig. 4.1), as detailed in Morel S et al. (2005), the multiplicative correction factor defined in Eq. (4.14) turns,

$$\psi \cong \frac{E_{\text{num}}}{E_{\text{exp}}} \tag{4.15}$$

The kinematic approach detailed in the present Section ought to be compared on the energetic point of view, in regards to the evaluation of the *Resistance*-curve. This idea rouse up the development of an alternative method which is presented as the Exact self-weight compensation method presented in detail in the next Section.

4.3.3 Exact self-weight compensation method

Regarding once more the testing beam loaded in TPB now represented in Fig. 4.8, subjected to the superposition of an external load P acting on the half-span and to the beam self-weight represented by the linear distributed load q , the displacement δ of a given point localised in the specimen central section (*i.e.*, in the axis of the central load) is the result of the contribution of both loading systems (*i.e.*, P and q). Since the result $\delta(a)$ is conditioned by the extent of the crack length a in the mid-section (Fig. 4.4), the former

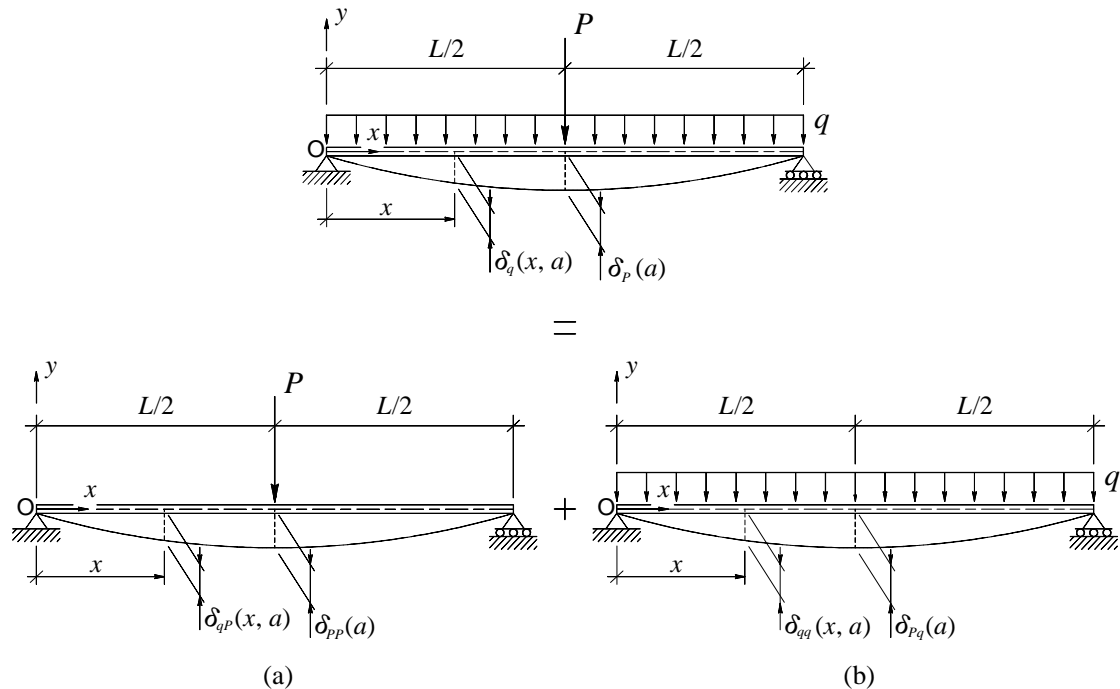


Figure 4.8 Simply supported beam subjected to the superposition of (a) the central load P [N] and (b) the distributed load q [N/m]. Parameters δ_{iP} and δ_{iq} represent respectively the displacements due to P and to q measured in axis i .

displacement will be designated in the following by $\delta_{PP}(a)$, though the later will be referred to as $\delta_{Pq}(a)$, leading, in a like manner as through Eq. (4.1), to

$$\delta_P(a) = \delta_{PP}(a) + \delta_{Pq}(a) \quad (4.16)$$

with the second index (in δ) being used to designate the applied loading system (P or q), while the first one (*i.e.*, P) is used to refer to the axis used to estimate the displacement δ . An alternative notation may be preferred to express the displacements $\delta_P(a)$ on the compliance basis for a given crack length a ,

$$\delta_P(a) = \lambda_{PP}(a)P + \lambda_{Pq}(a)q \quad (4.17)$$

(with λ_{PP} expressed in [m/N] and λ_{Pq} in [m²/N], since P and q are stated in [N] and [N/m], respectively).

On the other hand, it is possible to define the displacement *field* obtained along the specimen axis (middle-axis denoted as x in Fig. 4.8), with respect to the abscissa x , and for a given crack length a , as

$$\delta_q(x, a) = \delta_{qP}(x, a) + \delta_{qq}(x, a) \quad (4.18)$$

which, on the compliance basis is expressed through,

$$\delta_q(x, a) = \lambda_{qP}(x, a)P + \lambda_{qq}(x, a)q \quad (4.19)$$

The set of functions $\lambda_{PP}(a)$ and $\lambda_{Pq}(a)$ in Eq. (4.17), as well as $\lambda_{qP}(x, a)$ and $\lambda_{qq}(x, a)$ in Eq. (4.19) represent, respectively, corrected compliances and corrected compliance *fields* (Fig. 4.8) estimated through,

$$\lambda_{PP}(a) = \psi \lambda_{PP}^*(a) \quad (4.20)$$

$$\lambda_{Pq}(a) = \psi \lambda_{Pq}^*(a) \quad (4.21)$$

$$\lambda_{qP}(x, a) = \psi \lambda_{qP}^*(x, a) \quad (4.22)$$

$$\lambda_{qq}(x, a) = \psi \lambda_{qq}^*(x, a) \quad (4.23)$$

In Eqs. (4.20) and (4.21) the compliance functions $\lambda_{PP}^*(a)$ and $\lambda_{Pq}^*(a)$ are obtained from the best fit of in-plane FEM computations (elastic strain analyses) performed for different

values of a_0 in the interval $[h/2, h]$ (Fig. 4.1). As to Eqs. (4.22) and (4.23), the compliance fields $\lambda_{qp}^*(x, a)$ and $\lambda_{qq}^*(x, a)$ are achieved by means of the best fit of in-plane strain FEM computations performed along the axis Ox of Fig. 4.8 (*i.e.*, along the centreline) for each crack length a . Indeed, the calculation is made in the integration points sited along the mid-height of the FEM mesh used to compute the displacement values. Hence, $\lambda_{pp}^*(a)$ and $\lambda_{qp}^*(x, a)$ are expressed in [m/N], whereas $\lambda_{pq}^*(a)$ and $\lambda_{qq}^*(x, a)$ are defined in [m²/N], since P and q are stated in [N] and [N/m], respectively. In regards to the multiplicative correction factor ψ defined by Eq. (4.14),

$$\psi = \frac{\lambda_{\text{exp}}(a_0)}{\lambda_{pp}^*(a_0)}$$

in a like manner as has been seen in Section 4.3.2, the extent $\lambda_{\text{exp}}(a_0)$ represents the initial compliance (for $a=a_0$) obtained in the experiments (Fig. 4.9),

$$\lambda_{\text{exp}}(a_0) = \frac{\Delta \delta_{\text{exp}}(a_0)}{\Delta P_{\text{exp}}(a_0)} \quad (4.24)$$

with $\delta_{\text{exp}}(a_0)$ given by Eq. (4.3),

$$\delta_{\text{exp}}(a_0) = [\delta_{pp}(a_0) + \delta_{pq}(a_0)] - \delta_{pq}(a_0)$$

Therefore, regarding that the structure (Fig. 4.4) does not undergo damage (at least) before the central load P has been applied one can observe that $\delta_{pp}(a_0)$ in the above Equation (*i.e.*, Eq. 4.3) is the single quantity which actually varies. Indeed, the displacement $\delta_{pq}(a_0)$ though impossible to measure in the experiments, is kept unchanged, leading to

$$\delta_{\text{exp}}(a_0) = \delta_{pp}(a_0) \quad (4.25)$$

In fact, the quantity $\lambda_{\text{exp}}(a_0)$ in Eq. (4.14) should be reformulated to fit with the notation $\lambda_{pp \text{ exp}}(a_0)$ of Fig. 4.9. Hence, introducing the modification at once in Eq. (4.24), yields,

$$\lambda_{\text{exp}}(a_0) = \frac{\Delta \delta_{pp}(a_0)}{\Delta P_{\text{exp}}(a_0)} = \lambda_{pp \text{ exp}}(a_0) \quad (4.26)$$

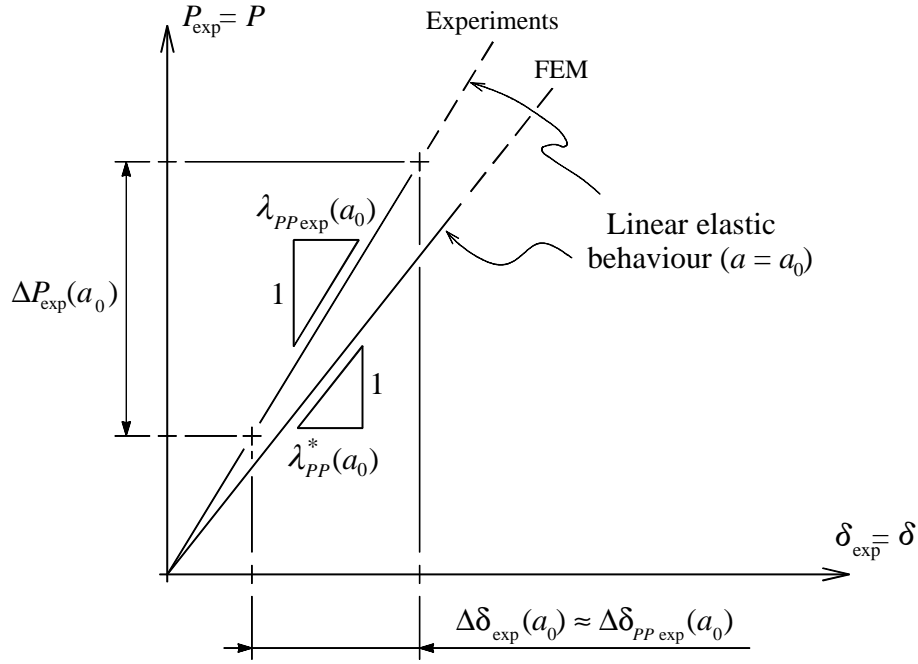


Figure 4.9 Superposition of load–displacement curves obtained in the experiments and through FE analysis in the linear elastic domain (for $a = a_0$).

4.3.3.1 Estimate of the equivalent crack length

In the course of the fracture test illustrated in Fig. 4.4 the displacement monitoring provides the result associated to both loading systems acting on the specimen (*i.e.*, P and q). In such a circumstance, one gets

$$\delta_{\text{exp}}(a) = [\delta_{PP}(a) + \delta_{Pq}(a)] - \delta_{Pq}(a_0) \quad (4.27)$$

The self-weight compensation however, implies the modification of the displacements recording schematized in Fig. 4.10,

$$\delta_{\text{mod}}(a) = \delta_{\text{exp}}(a) + \delta_{Pq}(a_0) \quad (4.28)$$

with $\delta_{Pq}(a_0)$ standing for the displacement which result from the structure self-weight prior to the load-cell zeroing operation (point O Fig. 4.4). The second term of Eq. (4.28) may be defined as follows

$$\delta_{Pq}(a_0) = \lambda_{Pq}(a_0)q \quad (4.29)$$

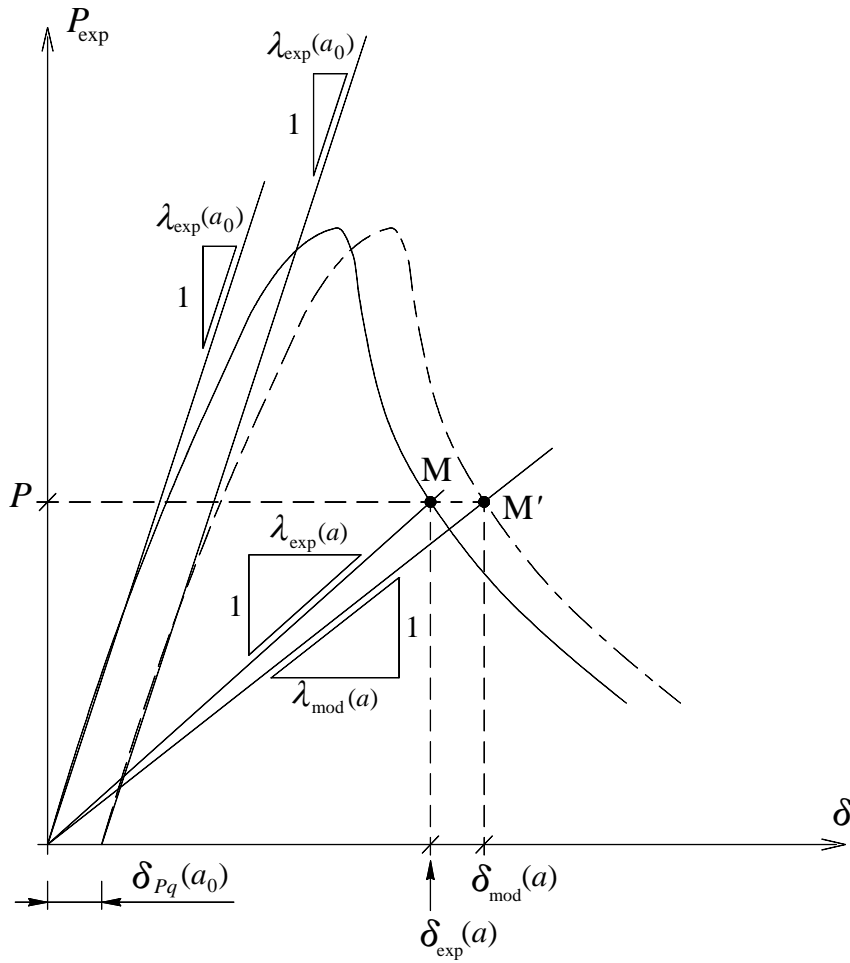


Figure 4.10 Modified load–deflection curve due to the compensation of the specimen self-weight (dashed line).

which is established as a function of the corrected compliance $\lambda_{Pq}(a_0)$, possible to be obtained from the computation of Eq. (4.21) for $a = a_0 = h/2$ (Fig. 4.1).

Still focused on the modification of the displacements recording schematically shown in Fig. 4.10, one can rewrite Eq. (4.28) on the compliance basis for a given crack length a ,

$$\delta_{\text{mod}}(a) = \lambda_{PP}(a)P + \lambda_{Pq}(a)q = \lambda_{\text{mod}}(a)P \tag{4.30}$$

with the corresponding modified compliance $\lambda_{\text{mod}}(a)$ defined as,

$$\lambda_{\text{mod}}(a) = \lambda_{PP}(a) + \lambda_{Pq}(a) \frac{q}{P} \tag{4.31}$$

with both functions $\lambda_{pp}(a)$ and $\lambda_{pq}(a)$ being corrected by means of Eqs. (4.20) and (4.21), respectively ($a \geq a_0$). Hence, combining Eq. (4.31) with Eqs. (4.20) and (4.21), yields

$$\lambda_{\text{mod}}(a) = \psi \left[\lambda_{pp}^*(a) + \lambda_{pq}^*(a) \frac{q}{P} \right] \quad (4.32)$$

Therefore, the first step consists to obtaining the modified load-displacement curve (Eqs. 4.14, 4.21 and 4.28) making use of the compliance calibration functions $\lambda_{pp}^*(a)$ and $\lambda_{pq}^*(a)$ previously evaluated in the interval $a \in [h/2, h]$. Subsequently, for a given point M' (Fig. 4.10) of the modified load-displacement curve (which corresponds to an *unknown* equivalent crack length a) the corresponding compliance $\lambda_{\text{mod}}(a)$ is calculated (*i.e.*, $\delta_{\text{mod}}(a)/P$ as the *first member* of Eq. 4.32). Then, making use of the corresponding load P quantity, together with the scalar constants ψ and q evaluated once per specimen, a given (*i.e.*, taken by hazard) crack length $a = a_i$ extent is used, to evaluate the *second member* of Eq. (4.32). The equivalent crack length a is the used value of a_i which provides the equality between both members of Eq. (4.32). The bisection method (Chapra SC and Canale RP 1985) has been applied as the seeking routine for the equivalent crack length a tracking.

In the following, the method used to evaluate the R -curve is detailed, using the modified load-displacement curve, together with corresponding values of the equivalent crack length a (*i.e.*, P, δ, a).

4.3.3.2 R -curve estimate

Consider two consecutive points of the modified load-displacement curve (Fig. 4.10) with the coordinates $[\delta_{\text{mod}}(a_1), P_1]$ and $[\delta_{\text{mod}}(a_2), P_2]$, as sketched in Fig. 4.11, with corresponding compliances represented by $\lambda_{\text{mod}}(a_1)$ and $\lambda_{\text{mod}}(a_2)$, respectively.

The elastic strain energy release δE associated to the corresponding infinitesimal crack

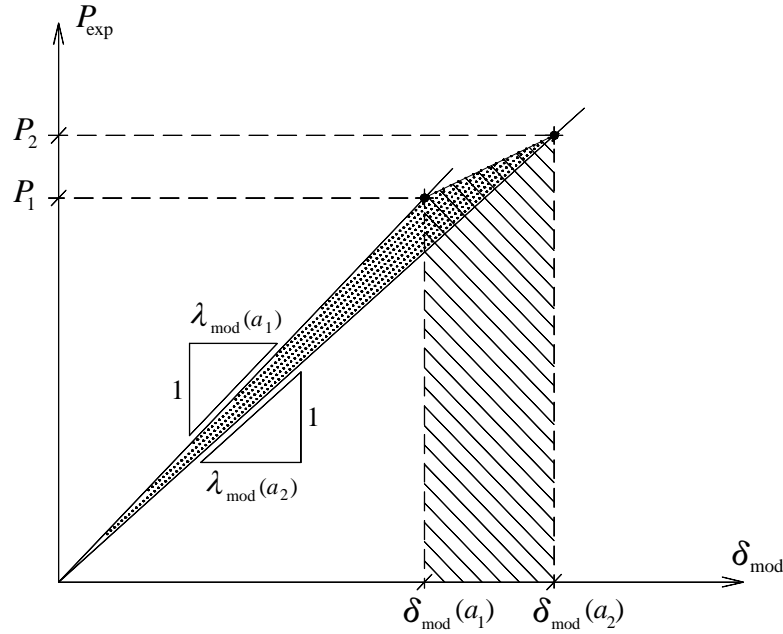


Figure 4.11 Partial strain energy associated to the external load P in two consecutive points of the modified load-displacement curve.

propagation δa (with $\delta a = a_2 - a_1$), is generically given by

$$\delta E = \delta W - \delta U \quad (4.33)$$

with δW and δU denoting, respectively, the work of the external applied load and the corresponding system complementary energy. As the self-weight counts, Eq. (4.33) may be rewritten in a more detailed form, taking into account the contribution of both central P and distributed q loads,

$$\delta E = (\delta W_P + \delta W_q) - (\delta U_P + \delta U_q) \quad (4.34)$$

The computation of the work of the external applied load (Fig. 4.11) in Eq. (4.34) leads to

$$\delta W_P = \frac{P_1 + P_2}{2} [\delta_{\text{mod}}(a_2) - \delta_{\text{mod}}(a_1)] \quad (4.35)$$

The work due to the distributed load δW_q in Eq. (4.34), is computed in the integral form through,

$$\delta W_q = \int_0^L q [\delta_q(x, a_2) - \delta_q(x, a_1)] dx \quad (4.36)$$

Both displacement fields $\delta_q(x, a_1)$ and $\delta_q(x, a_2)$ in Eq. (4.36) are estimated through FEM computations along the middle-axis ($y=h/2$) of the FE model (Appendix A3.2), following the resulting trend sketch depicted in Fig. 4.12. It is thus quite accountable that each of the above displacement field includes a term associated to the central load P , plus a second one coupled with the distributed load q , in such a way that,

$$\delta_q(x, a_i) = \delta_{qP}(x, a_i) + \delta_{qq}(x, a_i) \quad , (i = 1, 2) \quad (4.37)$$

$$= \lambda_{qP}(x, a_i) P_i + \lambda_{qq}(x, a_i) q \quad , (i = 1, 2) \quad (4.38)$$

with both quantities $\lambda_{qP}(x, a_i)$ and $\lambda_{qq}(x, a_i)$ denoting normalized compliance functions ($0 < x < L$) computed for crack lengths $a \geq a_0$, as performed through Eqs. (4.22) and (4.23), for a given equivalent crack length a .

The term δU_P in Eq. (4.34) refers to the complementary energy of the applied load P (Fig. 4.11), which is computed through,

$$\delta U_P = \frac{1}{2} P_2 \delta_{\text{mod}}(a_2) - \frac{1}{2} P_1 \delta_{\text{mod}}(a_1) \quad (4.39)$$

while the complementary energy of the distributed load δU_q , corresponding to the specimen self-weight (the last term of Eq. 4.34) is evaluated as follows,

$$\delta U_q = U_{q_2} - U_{q_1} = \frac{1}{2} \int_0^L q [\delta_q(x, a_2) - \delta_q(x, a_1)] dx \quad (4.40)$$

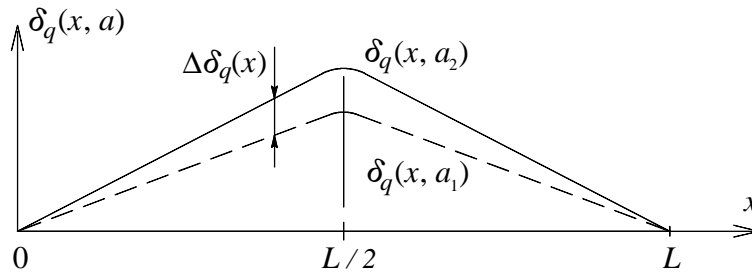


Figure 4.12 Schematic representation of the vertical displacement fields (absolute values) obtained for the SEN-TPB specimen along the middle-axis corresponding to two consecutive points of the load-displacement curve ($L=6h$).

Consequently, one can demonstrate the equality (from Eq. 4.36),

$$\delta U_q = \frac{1}{2} \delta W_q \quad (4.41)$$

The quantity $(\delta W_p - \delta U_p)$ reported in Eq. (4.34) can be estimated combining Eqs. (4.35) and (4.39),

$$\delta W_p - \delta U_p = \frac{P_1 - P_2}{2} [\delta_{\text{mod}}(a_1) + \delta_{\text{mod}}(a_2)] \quad (4.42)$$

which corresponds to the filled area represented in Fig. 4.11 for the equivalent crack length a_1 , as proposed by Morel S et al. (2005).

Additionally, according to the Maxwell's reciprocal theorem ($\lambda_{ij} = \lambda_{ji}$) one can establish the equality (Dato MH 1991),

$$\int_0^L \lambda_{qp}(x, a) dx = \lambda_{pq}(a) \quad (4.43)$$

which visibly gives rise to the simplification of the problem since it is not required to estimate the four compliance functions defined through Eqs. 4.20 - 4.23, but only three of them.

On the other hand, Eq. (4.34) establishes

$$\delta E = (\delta W_p - \delta U_p) + (\delta W_q - \delta U_q) = \delta E_p + \delta E_q \quad (4.44)$$

where $\delta E_p = \delta W_p - \delta U_p$ and $\delta E_q = \delta W_q - \delta U_q$.

Therefore, for a given elastic crack length a , the energy released during an infinitesimal crack extension δa , is obtained dividing both terms of Eq. (4.44) (i.e., δE_p and δE_q) by the infinitesimal crack surface (i.e., $b \delta a$), such that

$$G(a) = \frac{\delta E_p}{b \delta a} + \frac{\delta E_q}{b \delta a} = G_p(a) + G_q(a) = R(a) \quad (4.45)$$

Through Eq. (4.45) it is stated that the energy release rate $G(a)$ equalizes the *Resistance* to crack growth $R(a)$.

An ordering of the whole Formulary has been typed in Appendix A4.2 to provide a more comprehensive way to follow the main steps of the proposed algorithm (based on the Exact self-weight compensation method).

The validation of the proposed method used to take into account the structure self-weight in specimens of non-negligible sizes D is well worth doing, to prove the adequacy of the proposed method to measure accurate fracture parameters (*i.e.*, given by the R -curve) in quasibrittle materials. With such a purpose, the self-weight compensation method may be applied to a set of load-displacement curves obtained through the cohesive crack modelling for a given G_f (Fig. 2.7). The validation might be settled in the basis of $G_{Rc} = G_f$, since this is the only valid worth noticed fact. Additionally, a comparison might be made regarding the evaluated R -curve provided by each method used to perform the self-weight compensation (Sections 4.3.2 and 4.3.3). The uncompensated method used in Section 2.3 might be used for comparison. This corresponds exactly to what is reported and discussed in the following Section.

4.3.3.3 Cohesive crack modelling validation

In the following a description of the proposed R -curve validation procedure is made using the FE-mesh exhibited in Fig. A3.2.1 (Appendix A3.2), setting h to 210 mm. The distributed load q has been chosen to correspond to several density values ρ contained in the interval $[300, 700]$ kg/m³. Hence, a cohesive zone has been modelled by means of interface finite elements (de Moura MFSF 1997) through a made up line-crack disposed along the central section, in the specimen ligament length. As previously carried out in this Thesis, the bilinear stress-softening model proposed by Petersson PE (1981) was used to simulate crack growth in spruce. A set of cohesive properties has been chosen (following Fig. 2.7, $w_b = 0.045$ mm, $f_b = 0.63$ MPa, $f_t = 2.1$ MPa and $G_f = 0.1$ N/mm) to assure the self-similar crack propagation in a given range, as duly discussed in Chapter II. The elastic properties used in the in-plane strain FE analysis are exhibited in Appendix A3.2. The loading process was planned in two independent steps: (a) the first one, through a distributed load q corresponding to the specimen own-weight (agreeing with the material

density ρ); while (b) the second one, has been performed through a prescribed vertical displacement δ , with the first solicitation (*i.e.*, q) constantly applied on the specimen.

Accordingly, load-displacement curves were obtained from numerical simulations of the SEN-TPB test using the set of material densities ρ listed in Fig. 4.13. This plotting shows that increasing values of the material density ρ give rise to higher displacement values which resulted from the accommodation of the specimen to the structure own-weight, *i.e.*, $\delta_{Pq}(a_0)$, prior to the second loading (*i.e.*, displacement) step (b). The FEM computations revealed that the initial compliance $\lambda_{\text{exp}}(a_0)$ is not affected by the material density ρ used in the cohesive modeling (as expected from Eq. 4.26). Another conclusion arising from this study is related to the fact that nor just the ultimate load decreases with the material density, but also the energy corresponding to the area under the load-displacement

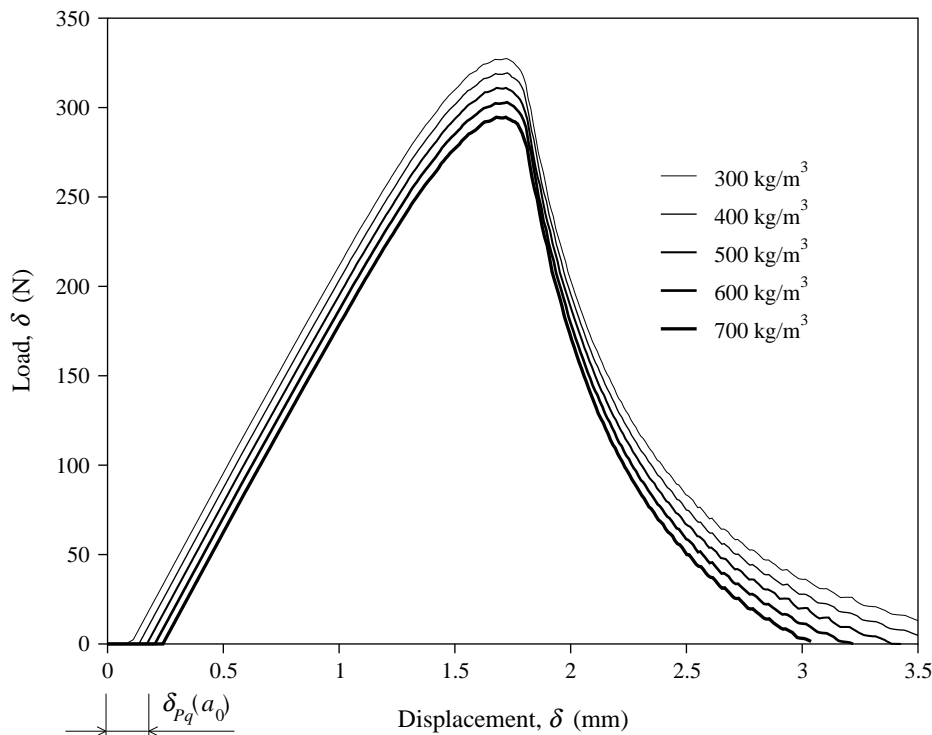


Figure 4.13 Load-displacement curves obtained through FEM computations (Appendix A3.2) for densities in the interval $[300, 700]$ kg/m^3 using $h = 210$ and $b = 60$ (mm), according to Fig. 4.1.

curve [*i.e.*, the integral $\int_{\delta_{pq}(a_0)}^{\delta_c} P(\delta) d\delta$] required to conduct the total rupture, decreases with ρ . Figure 4.14 reports the trend of the extent of the cohesive zone l_{coh} as a function of the numerical (*i.e.*, the real) crack length obtained for the simulated set of material densities. According to these results a critical extent of the cohesive zone $l_{\text{coh } c}$ is clearly revealed when the material density is set to 300 kg/m^3 ($l_{\text{coh } c} \approx 19 \text{ mm}$). One may also observe that simulations performed with higher material densities provide the same critical extent (*i.e.*, $l_{\text{coh } c}$) before the crack propagation onset (*i.e.*, for $a = a_0 = 105 \text{ mm}$), whereas the amplitude of the interval of the numerical crack length for which this extent remains unchanged, radically decreases with the material density when crack propagates (*i.e.*, for $a > a_0$). This behaviour signs the confinement of the cohesive zone with the increase in ρ .

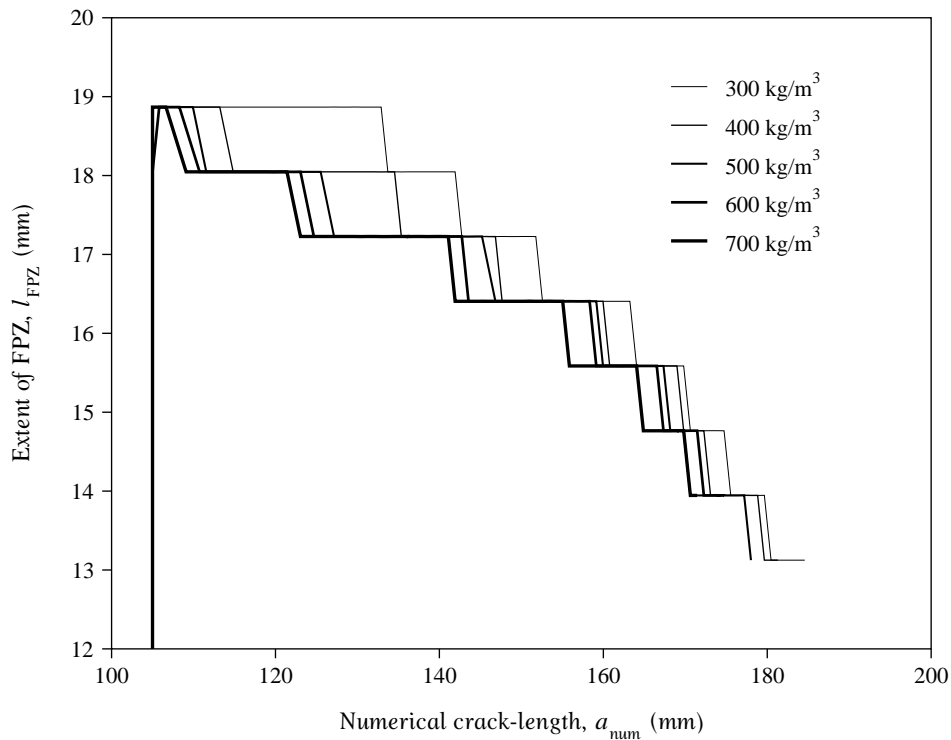


Figure 4.14 Evolution of the numerical FPZ extent with the numerical crack length for densities in the interval $[300, 700] \text{ kg/m}^3$ using $h = 210$ and $b = 60$ (mm), according to Fig. 4.1.

The set of load-displacement curves exhibited in Fig. 4.13 has firstly been used in the context of the self-weight compensation by means of the methodology based on the evaluation of the load equivalent to the specimen self-weight (Section 4.3.2) to evaluate corresponding R -curves. The method requires the previous verification of the condition established by Eq. (4.8), namely the constancy of the ratio $\lambda_{P_q}^*(\alpha)/\lambda_{P_P}^*(\alpha)$ over an interval $a \in [a_0, a_{\text{expl}}]$, together with the reset (Fig. 4.7) of the load-displacement curve after the equivalent load P_q evaluation, as properly reported in Appendix A4.3. In regards to the numerical compliance functions $\lambda_{P_P}^*(\alpha)$ and $\lambda_{P_q}^*(\alpha)$, the FEM computations provided the set of polynomial functions exhibited in Appendix A4.4. Subsequent evaluations of the numerical (*i.e.*, for $\psi = 1.0$) R -curve associated to each density in the interval $[300, 700]$ kg/m³ led to the plotting shown in Fig. 4.15, using the equivalent LEFM approach proposed by Morel S. *et al.* (2005) (also detailed in Section 2.3). It is noticed that the horizontal asymptote revealed by the set of *Resistance*-curves (Fig. 4.15) overestimates the critical energy release rate G_{Rc} in 2.3%. This surplus in G_{Rc} once compared with the value of G_f used as input in the CCM, is naturally found irrelevant. Nevertheless, one can not exclude the possibility that higher differences might be obtained if one would have used higher values of the material density ρ , as well as different combinations of Young modulus E (namely E_T). One also observes that the evaluated R -curve does not depend on the modeled material densities.

Figure 4.16 on its turn, shows the evolution of both quantities reported in Eq. (4.45) against the equivalent crack length a for each material density ρ using the exact self-weight compensation method (Section 4.3.3). As reported (Fig. 4.16), both energy release rate functions evolve monotonically towards a horizontal asymptotic value. Indeed, in the early stage of the crack propagation (*i.e.*, for $a \cong a_0$) it is noticed that the strong reduction in the amount of energy due to the distributed load equivalent to the self-weight $G_q(a)$, is *compensated* by an equivalent increase in the energy associated to the external central load acting on the specimen $G_p(a)$. Hence, according to Eq. (4.45) the resulting energy release rate $G(a)$ in this extent (*i.e.*, for $a \cong a_0$) is essentially that which elapses from the material

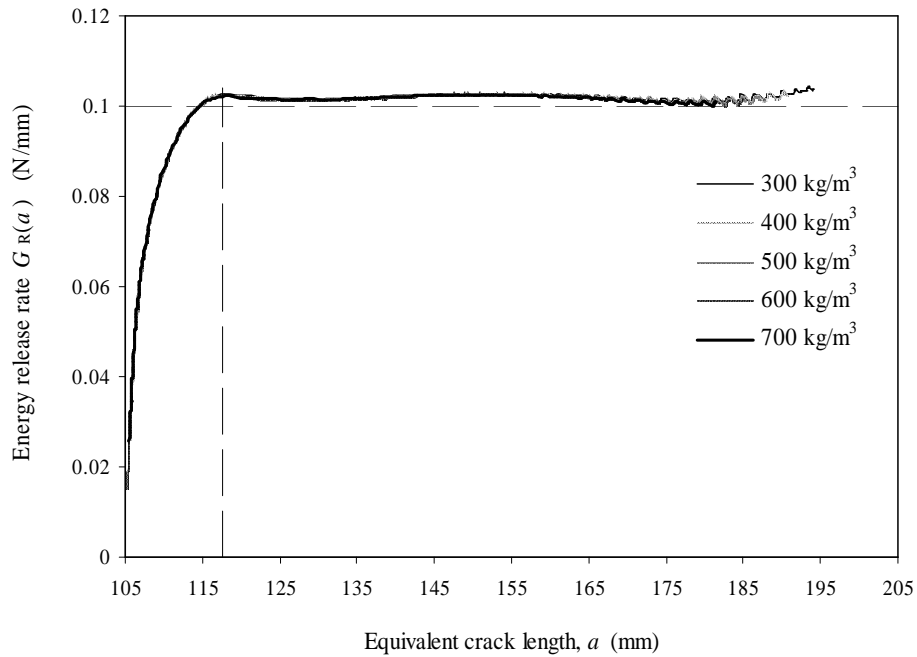


Figure 4.15 R -curves obtained for material densities in the interval $[300, 700]$ kg/m^3 with $h = 210$ and $b = 60$ (mm), according to the method of the Load equivalent to the specimen self-weight (Section 4.3.1).

own-weight, as intuitively expected. As the equivalent crack length a progresses the term $G_q(a)$ nearly vanishes in an initial phase, turning increasingly higher again with the reduction of the crack ligament. The trend exhibited by the energetic term $G_p(a)$, in turn, somehow compensates the later (*i.e.*, $G_q(a)$), leading to $G(a) = G_{Rc} = 0.1 \text{ N/mm}$, used as input value as one of the cohesive properties.

At last, executing the sum of both functions $G_p(a)$ and $G_q(a)$ reported in Eq. (4.45) one gets the plotting exhibited in Fig. 4.17. It turns clear from the estimation of the exhibited plotting that the R -curve is independent of the (simulated) material densities ρ . Furthermore, the energy release rate $G_R(a)$ being obtained under self-similar crack propagation revealed an undoubted horizontal asymptote for 0.1 N/mm , *i.e.*, corresponding precisely to the value of G_f used as input in the cohesive model (*i.e.*, the softening diagram shown in Fig. 2.7).

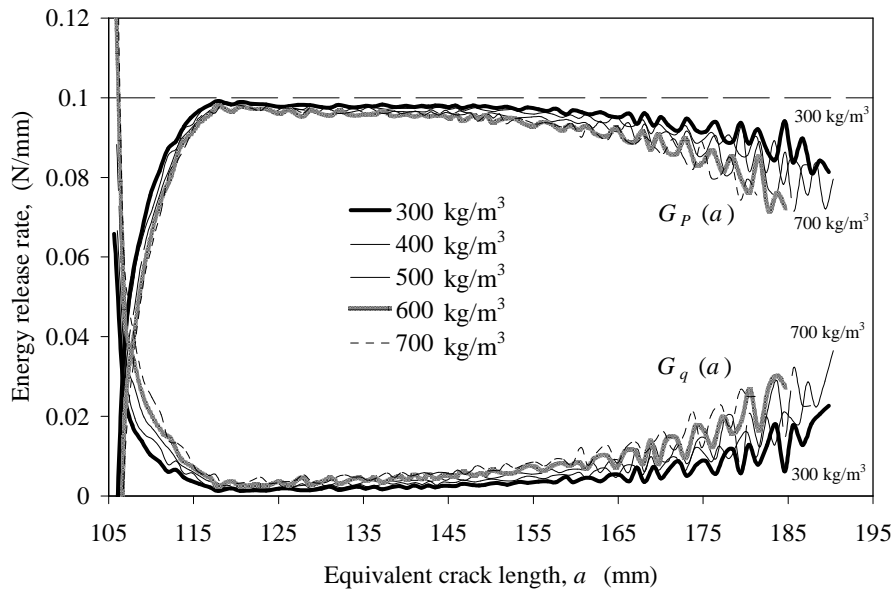


Figure 4.16 Evolution of $G_p(a)$ and $G_q(a)$ using material densities in the interval $[300, 700]$ kg/m³ with $h = 210$ and $b = 60$ (mm), following the exact self-weight compensation method (Section 4.3.3).

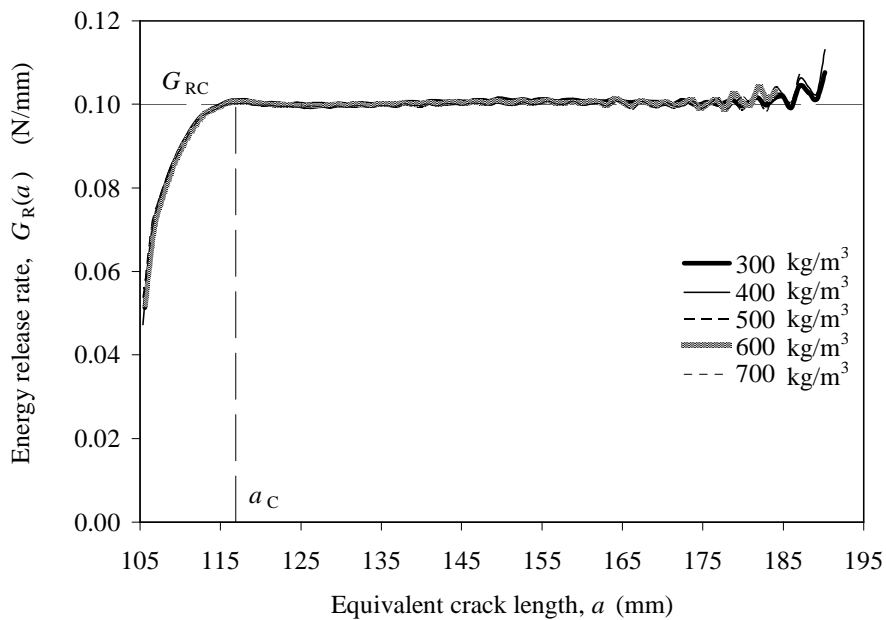


Figure 4.17 R-curves obtained for material densities in the interval $[300, 700]$ kg/m³ with $h = 210$ and $b = 60$ (mm), following the Exact self-weight compensation method (Section 4.3.3).

In short, in view of the results revealed in the present Section, it is possible to conclude for the adequacy of the *Exact self-weight compensation method* detailed in Section 4.3.3 to evaluate the R -curve, when the specimen self-weight plays an important role in the SEN-TPB structure. Consequently, barely this method deserves attention in the following Sections of this Thesis in what regards the evaluation of the R -curve in wood.

It should be emphasized that the purpose of these numerical simulations was barely to test for the accuracy of the developed algorithm to retrieve the right value of G_{Rc} (*i.e.*, $G_{Rc} = G_f$), together with the accurate progress of the corresponding R -curve, taking into account the effect of the specimen self-weight. Therefore, no concern has been devoted into the seeking of the *true* set of cohesive properties which would retrieve appropriate fittings of a given set of experimental P - δ curves (as duly discussed in Chapter II and in Dourado N et al. 2008).

The evaluation of the R -curve, with no regard to the self-weight compensation, by means of the equivalent LEFM approach (Section 2.3), has also been conducted with the set of load-displacement curves obtained in the cohesive crack modelling (Fig. 4.13) after the zeroing operation. The obtained plotting shown in Fig. 4.18 emphasises the great importance of the proposed (numerical) correction, as the evaluated R -curves are far from revealing the right value of G_f used as one of the input cohesive properties. It is shown that as the material used in the simulations increases in density ρ , the retrieved plateau is less distinct and the obtained asymptotic value less important.

Bearing in mind the main aspects issued from the Quasibrittle Fracture modelling discussed in Chapter II regarding the development of the FPZ, together with the derivation of the energetic size effect law, based on the equivalent LEFM and the asymptotic analysis, treated in Chapter III, as well as the methodology just detailed (and validated) to take into account the structure self-weight when the R -curve is to be evaluated, one can consider that the indispensable conditions (numerical tools) have been gathered to put into practice the Size Effect Study on the experimental data. That is precisely the aim of the next Section.

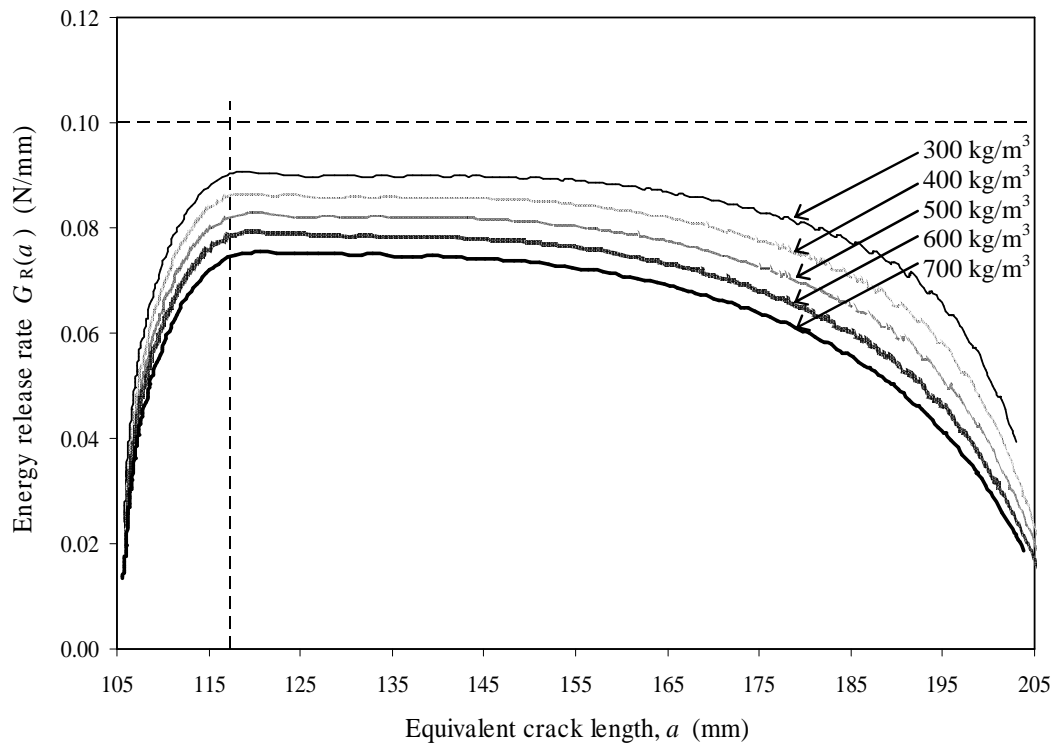


Figure 4.18 *R*-curves obtained for material densities in the interval $[300, 700]$ kg/m³ with $h = 210$ and $b = 60$ (mm), for the uncompensated approach presented in Section 2.3.

4.4 Results of the Size Effect experiments: discussion

4.4.1 Variability and sampling

With the purpose to *eliminate* the size effect among the specimens used in the experiments, an evaluation of the unitary compliances [*i.e.*, $b\lambda_{\text{exp}}(a_0)$] has been performed, thus providing a way to compare the whole specimens in regards to the material elastic response. Hence, observing the plotting of the unitary initial compliances obtained in the experiments (ANNEXE) for the set of specimens which exhibited an undoubted plateau on the *Resistance*-curve, shown in Fig. 4.19, it is clearly put into evidence that a strong scattering does exist in the tested material.

Though a careful selection of the raw material has been carried out in the specimens preparation, revealed by the material density spectrum exhibited in Appendix A4.5 (Fig. A4.5.1), as well as with watchful machining operations (wood dully aligned, free from

notches and natural imperfections), and adequate warehousing in every stages of the specimens preparation, the results will certainly render the dispersion shown in Fig. 4.19.

A possible cause for the noticed scattering is the well known spontaneous micro-crack propagation which occurs during the drying process in wood. Indeed, the humidity concentration gradients which occur in the material during the drying process lead to the internal stress field formation with the micro-cracking phenomenon being the most serious consequence of this natural phenomenon. Consequently, a damaged domain is very likely to exist due to the natural drying process of wood pieces during the sequence of machining operations. This phenomenon is particularly noticed in the selected specimen orientation (Fig. 4.1) according which fracture is induced in the TL system, since the micro-cracking phenomenon during wood natural drying processes occurs preferably along the longitudinal (L) axis. Hence, in addition to the Size Effect influence which is expected to arise from the experiments, it is necessary to account for the material it-self, since the initial damage state is not the same for the whole specimens. This being the case, different and unknown *drying stories* may have occurred with the raw material, leading thus to a sampling problem among the specimens selected for testing.

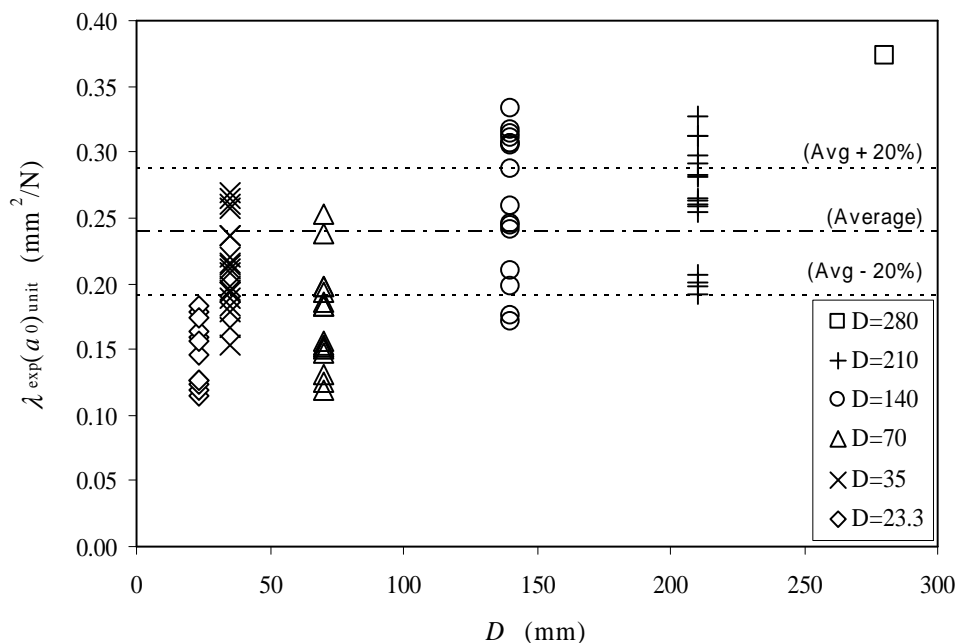


Figure 4.19 Unitary initial compliances obtained in the experiments showing the huge scattering of the tested material. Printed labelling is in accordance to Table 4.1

The wooden boards selected for the specimens' preparation presented at the origin different sizes (cross-sectional dimensions) according to the final dimension required by the series for which they were intended for. Accordingly, boards presenting smaller cross sectional areas were chosen for those series which required the preparation of specimens with smaller dimensions (*e.g.*, $D=35$ mm and smaller in Fig. 4.1 and Table 4.1), while specimens with higher cross-sectional areas ($D=210$ mm and bigger) were machined from those beams which presented extreme dimensions (commercially available).

Measurements performed on wood boards' surface during the raw material provisioning revealed values between 11 and 13% for the RH. Since it was necessary to reduce the original cross-sectional dimensions in every wooden boards selected to prepare the testing specimens, the whole material involved in the experiments had to undergo a natural drying process (conditioning at 20°C and 65 RH until equilibrium as referred in Section 4.2) during the specimens preparation.

4.4.2 Estimate of the R -curves (Exact self-weight compensation)

The load-displacement curves obtained (under displacement control) in the experiments have been printed in Appendix A4.1. Figure 4.20 shows the plotting of the *Resistance*-curves which exhibit an undoubted plateau, by means of the Exact self-weight compensation method (Section 4.3.3) with the compliance calibration functions $\lambda_{pp}^*(a)$ and $\lambda_{pq}^*(a)$ shown in Appendix A4.4. In order to dispose of a general view of the R -curve evolution with the specimen characteristic size D (yet in homothetic SEN-TPB structures), the mean values of G_R have been plotted in Fig. 4.21 as a function of the relative crack length $\alpha = a/D$, suggesting that a non-negligible difference in terms of G_R may exist when similar structures of different sizes D are compared. Figure 4.22, on its turn, shows the influence of the specimen size D on the mean critical energy release rate G_{Rc} obtained in the experiments for those specimens which exhibited an undoubted plateau on the R -curve (consult the ANNEXE). Hence, though a huge scattering is recognized to arise from the evaluated R -curves (Fig. 4.20 a-f), also confirmed by a non-negligible coefficient of variation (COV) of the energy release rate associated to the ultimate load $G_R(\alpha_u)$, as well

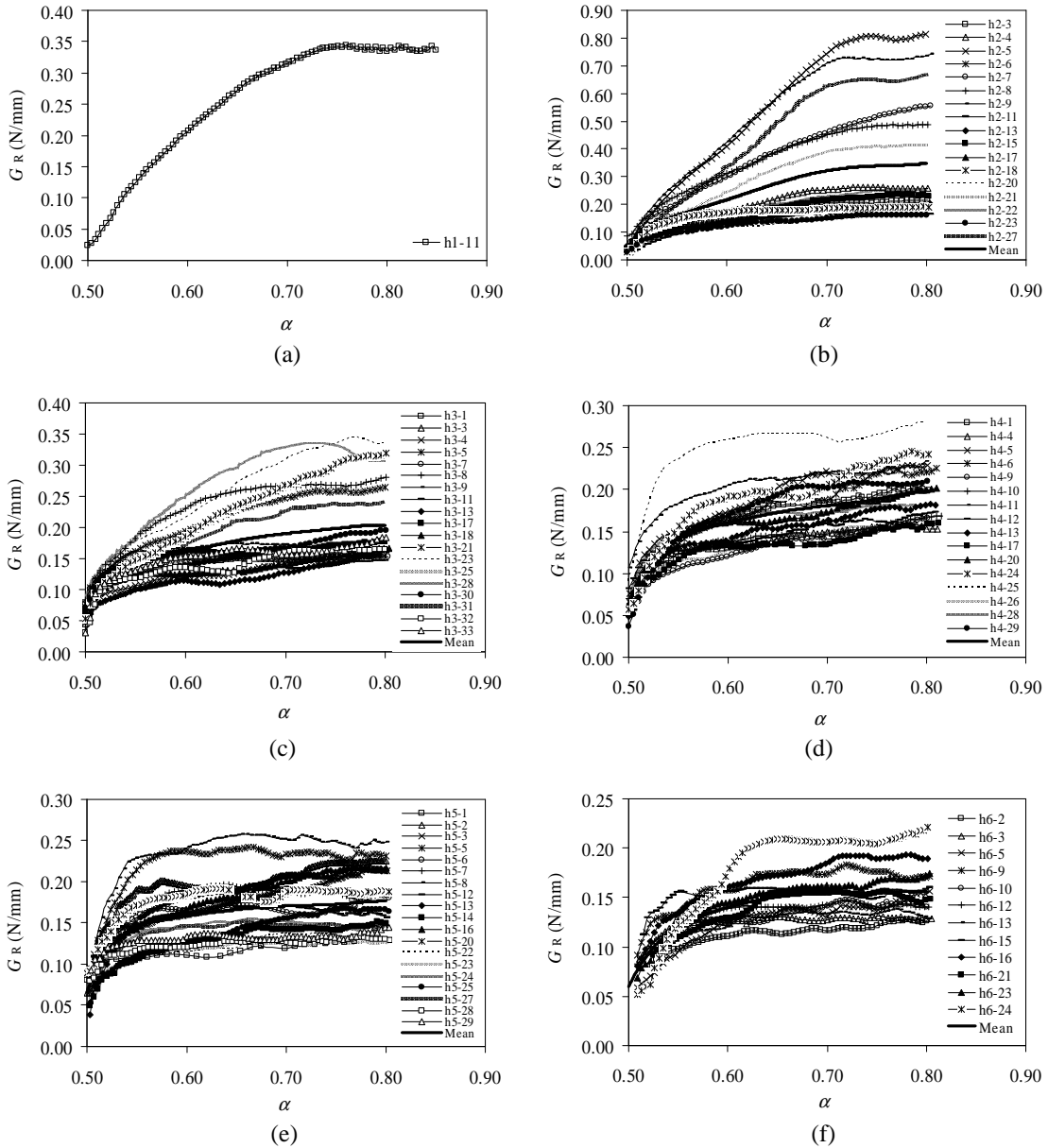


Figure 4.20 Resistance-curves obtained in the experiments after application of the Exact self-weight compensation method (Section 4.3.3). The plotting shows the curves which exhibit an irrefutable plateau. Exhibited graphics correspond to specimen characteristic dimensions: (a) $D=280$ mm, (b) $D=210$ mm, (c) $D=140$ mm, (d) $D=70$ mm, (e) $D=35$ mm and (f) $D=23.3$ mm, as listed in Table 4.1.

as the critical energy release rate G_{Rc} (Table 4.2), one observes that the relative crack lengths associated to these energy release rates (*i.e.*, α_u and α_c) however, are significantly less perturbed by the scattering. This ultimate experimental observation seems to suggest

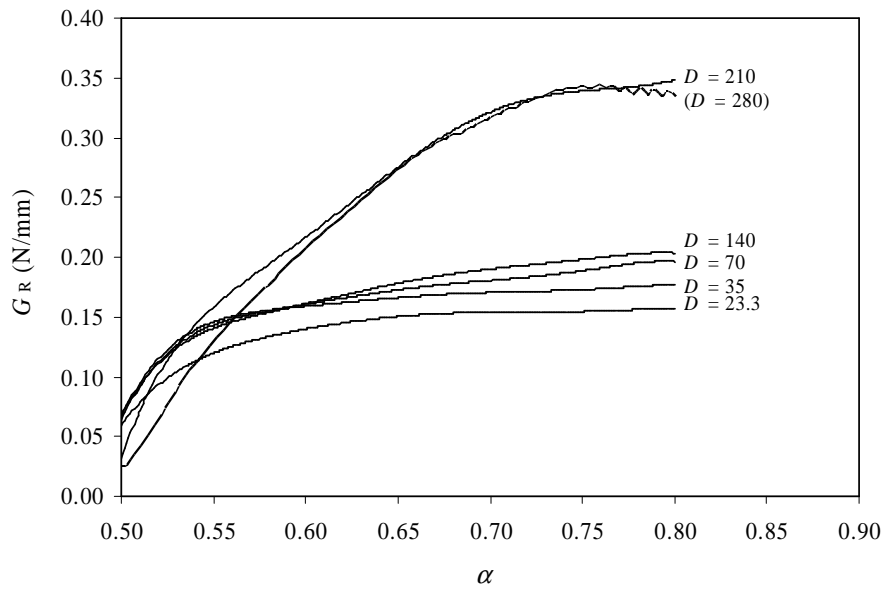


Figure 4.21 Mean R -curves obtained in the experiments. Labelling is in accordance with Table 4.1. Series labelled in parenthesis has no statistic meaning since only one R -curve has been obtained for this size.

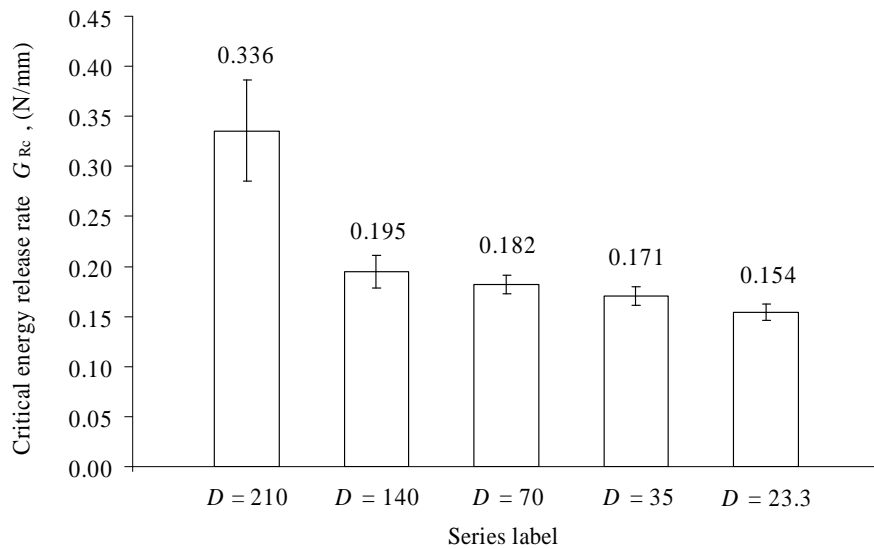


Figure 4.22 Mean values of the critical energy release rate G_{Rc} obtained in the experiments (see ANNEXE) for the specimens which exhibited an undoubted plateau on the R -curve.

that both parameters α_u and α_c slightly increase with the raise of the specimen size D . Nevertheless, this observation is in complete disagreement with the conclusions drawn from the Cohesive Crack Modelling presented in Section 3.3 (namely Table 3.2). Indeed,

those computations indicated the opposite trend, with both α_u and α_c (with $\alpha_c = \theta + a_0$) decreasing with the raise of D . One should notice however that the suspicions regarding the evolution of both parameters α_u and α_c (Appendix A4.5), ought to be confirmed through additional experimental data provided with specimens

Table 4.2 Resume of mean values obtained in the experiments according to structure sizes printed in Table 4.1. Values in parenthesis represent COV in percentage (consult the ANNEXE and Appendix A4.5 for more details). Listed parameters represent: ψ , multiplicative correction factor; $\lambda_{\text{exp}}(a_0)$, initial experimental compliance; P_u , ultimate load; α_u , relative crack length corresponding to P_u ; $G_R(\alpha_u)$, energy release rate associated to P_u ; α_c , relative crack length associated to the critical energy release rate; G_{Rc} , critical energy release rate; θ , relative critical crack length of the FPZ; β , curvature exponent of the raising portion of the R -curve; α_{u^*} , single solution of α_u (as in Figure 3.1). $\theta = \Delta a_c / D$ and $\Delta a_c = a_c - a_0$

D (mm)	ψ	$\lambda_{\text{exp}}(a_0)$ (10^{-3}mmN^{-1})	ρ (12%MC) (kg m^{-3})	P_u (N)	α_u	$G_R(\alpha_u)$ (Nmm^{-1})
280	1.01 (20.4)	3.69 (21.9)	453.45 (21.4)	464.7 (18.8)	0.593	0.156
210	1.06 (17.3)	4.37 (17.3)	405.18 (11.7)	397.6 (31.2)	0.570 (4.2)	0.198 (56.4)
140	1.07 (26.3)	6.68 (20.1)	418.35 (12.5)	210.5 (19.6)	0.541 (2.2)	0.189 (12.3)
70	1.01 (22.1)	8.63 (22.1)	425.80 (10.0)	93.9 (15.2)	0.544 (2.2)	0.141 (21.6)
35	1.02 (15.9)	21.31 (15.9)	369.49 (4.7)	30.8 (9.5)	0.537 (2.0)	0.140 (27.4)
23.3	0.95 (16.7)	22.11 (16.7)	415.62 (10.1)	18.5 (9.6)	0.540 (4.0)	0.117 (20.7)
D (mm)	α_c	θ	Δa_c (mm)	G_{Rc} (Nmm^{-1})	β	α_{u^*}
280	0.744	0.244	68.3	0.341	0.64	0.582
210	0.731 (5.3)	0.231 (5.3)	48.5	0.336 (63.7)	0.40	0.557
140	0.665 (11.4)	0.166 (11.4)	23.2	0.195 (36.4)	0.23	0.535
70	0.683 (9.4)	0.183 (9.4)	12.8	0.182 (19.9)	0.19	0.528
35	0.641 (9.1)	0.141 (9.1)	4.9	0.171 (22.9)	0.21	0.537
23.3	0.661 (5.6)	0.161 (5.6)	3.8	0.154 (17.8)	0.24	0.525

with higher sizes D . Hence, no absolutely conclusive remark can be made in regards to the evolution of α_u and α_c with the characteristic size D obtained in the experiments (*i.e.*, sampling problem among the specimens selected for testing as reported in Section 4.4.1).

A description regarding the details of the mean values evaluation of the curvature exponent of the R -curve β , the single solution of α_u (*i.e.*, α_{u*}), and corresponding limits (*i.e.*, D_{\min} and D_c) necessary to outline the log-log plotting in the context of the Size Effect study, is made in Appendix A4.4. As to the energy release rate associated to the ultimate load $G_R(\alpha_u)$, though strongly affected by scattering (values in parenthesis in Table 4.2), the experimental data seems to indicate the increasing trend with the raise of the structure size D . This being the case, the results issued from the cohesive crack modelling (Section 3.3, namely Table 3.2) are in agreement with the experiments.

The plotting of the size effect on the nominal strength $\sigma_N(D)$ represented in Fig. 4.23 has been made using the mean values represented in Table 4.2 and Table A4.4.2 (Appendix A4.4), for each tested size D . The outlined envelop circumscribed by the hidden-lines corresponds to what can be estimated for the size effect on the nominal strength $\sigma_N(D)$ in wood (spruce), when the R -curve is known. Indeed, this is the pattern shape of what is expected for a material such as wood. The inflected shape revealed by the circumscribed domain is not surprising, since it integrates the intermediate size range estimated through the derivation of the energetic Size Effect Law (Section 3.2), and the domain of LEFM. Table 4.3 reports the set of results which permit to justify the progress verified in the nominal strength $\sigma_N(D)$ through the bilogarithmic plot of Fig. 4.23, namely those which are estimated through Eqs. (3.17) and (3.18) for the domain of LEFM and for the intermediate size range, respectively.

$$\sigma_N(D) = c_N \sqrt{\frac{E' G_{Rc}}{g(\alpha_0)}} D^{-1/2}$$

$$\sigma_N(D) = c_N \sqrt{\frac{E' \phi(\alpha_{u*} - \alpha_0)^\beta}{g(\alpha_{u*}) D^{1-\beta}}}$$

Accordingly, both ratios: $\sqrt{[E' \phi (\alpha_{u*} - \alpha_0)^\beta] / g(\alpha_{u*})}$ and $\sqrt{(E' G_{Rc}) / g(\alpha_0)}$ were calculated in Table 4.3 and outlined in graph of Fig. 4.24.

It should be noted that the envelop outlined in Fig. 4.23 renders possible to estimate the approximately ratio of 0.13 in the $\log_{10} \sigma_N(D)$ between the highest and the smallest value estimated for the LEFM regime. Therefore, though affected by the noticed sampling problem (Section 4.4.1), the evaluated ratio yields roughly 35%, which is quite acceptable in view of the scattering normally associated to the estimate of elastic and fracture parameters in wood.

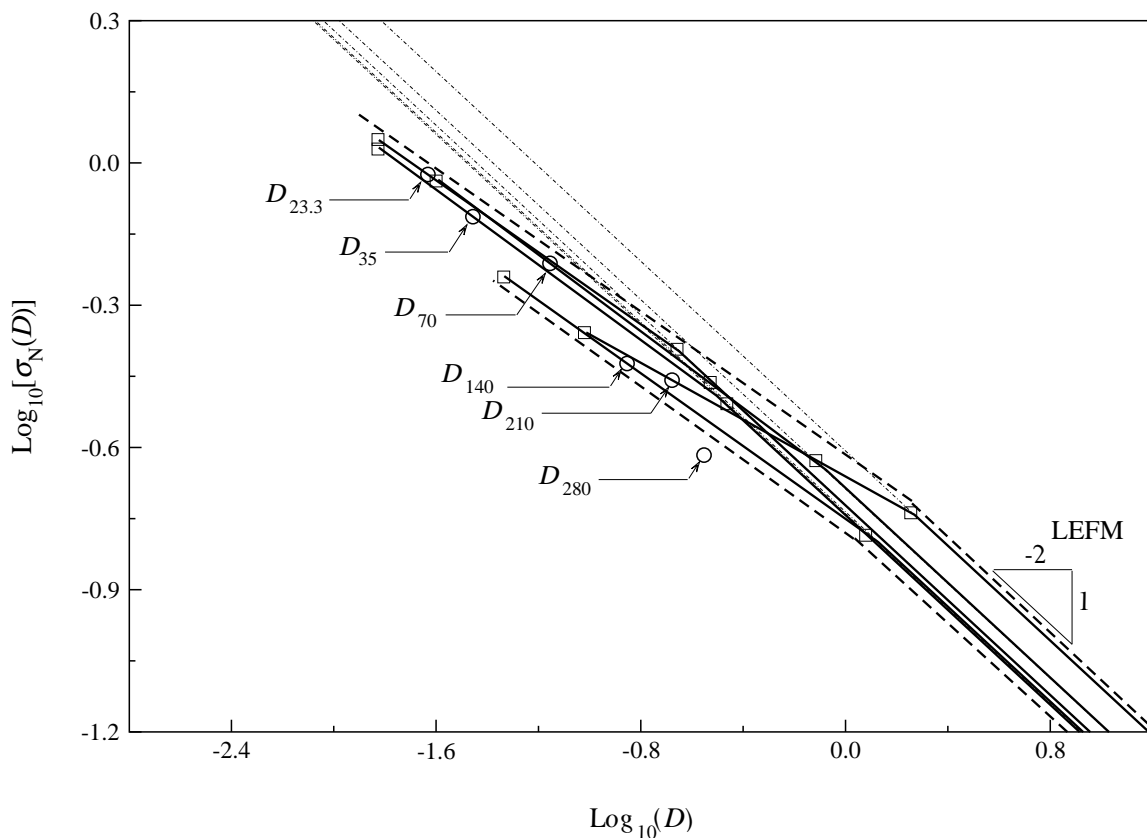


Figure 4.23 Envelop (hidden line) estimated for the size effect on the nominal strength in wood spruce using the mean values obtained for each tested series (Table 4.2 and Table A4.4.2 in Appendix A4.4).

Table 4.3 Results obtained in the size effect study for the experimental data. Parameters: E' , Longitudinal elastic modulus ($E' = E^*$ as defined in Appendix A3.1); G_{Rc} , Critical energy release rate; α_{u*} , Single solution of α_u ; $g(\alpha_0)$, Dimensionless energy release rate function; $\sqrt{(E' G_{Rc})/g(\alpha_0)}$, Ratio of Eq. (3.17) characterized by LEFM; $\sqrt{[E' \phi(\alpha_{u*} - \alpha_0)^\beta]/[g(\alpha_{u*})]}$, Ratio of Eq. (3.19) used to estimate the nominal strength in the intermediate size range

Series	E' (MPa)	G_{Rc} (Jm ⁻²)	α_{u*}	$g(\alpha_0)$	$g(\alpha_{u*})$	$\sqrt{\frac{E' G_{Rc}}{g(\alpha_0)}}$ (N ² /m ³) ^{1/2}	$\sqrt{\frac{E' \phi(\alpha_{u*} - \alpha_0)^\beta}{g(\alpha_{u*})}}$ [N ² /(m ^{3+β})] ^{1/2}
$D=280$	476.17	341	0.582	305.94	455.23	23038	15390
$D=210$	552.9	336	0.557	291.00	380.19	25266	20826
$D=140$	526.0	195	0.535	294.39	302.61	18666	19366
$D=70$	710.1	182	0.528	273.87	267.59	21723	24245
$D=35$	583.0	171	0.537	255.07	292.43	19770	22750
$D=23.3$	709.6	154	0.525	227.16	231.93	21933	28484

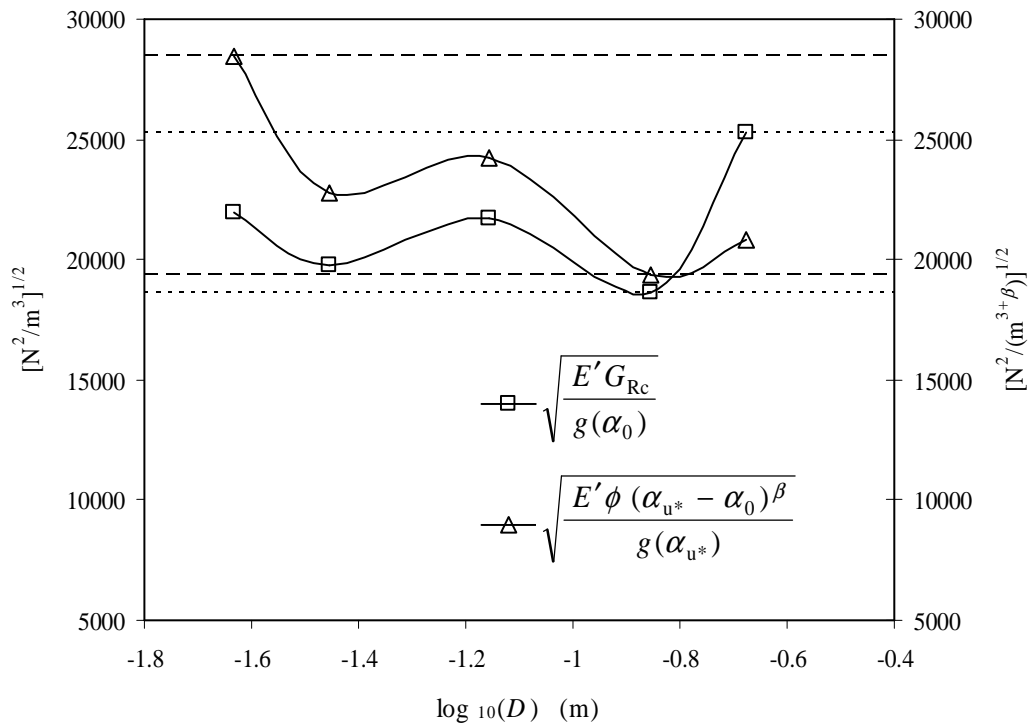


Figure 4.24 Progress of ratios used to estimate the nominal strength according to Eq. (3.17) and Eq. (3.18), showing the calculated limits for each ratio, according to the estimate performed for the structure sizes $D=210 - D=23.3$ (mm) in Table 4.3.

Hence, taking notice of the sketched out envelop of Fig. 4.23, as well as of the set of parameters used to characterize in full the R -curve in wood spruce [*i.e.*, $G_{Rc} = \overline{G}_{Rc} \pm \Delta G_{Rc}$; $\Delta a_c = \overline{\Delta a}_c \pm \Delta(\Delta a_c)$ and $\beta = \overline{\beta} \pm \Delta\beta$], together with the dimensionless energy release rate function $g(\alpha)$, it turns possible to estimate the single solution of α_u , and thus estimate accurately the intermediate size regime, from a single size D .

In short, the analysis of the experimental data revealed the existence of a sampling problem denoted by the scattering of the initial unitary compliance, concluding for the existence of different initial damage state in the raw material used to carry out the testing. This being observed, the estimate of the asymptotic behaviour previewed for the intermediate size range, has been performed through the energetic size effect approach, based on the mean *Resistance*-curve estimated for each experimental series. The size effect on the nominal strength (in spruce) rendered possible to estimate an envelop on the bi-logarithmic scale, issuing a strength ratio estimate of approximately 35% between the highest and smallest value previewed for the structure size of major size D (according to the size effect regime previewed for LEFM).

As a final remark, it should be emphasised that most of the observations issued from the exposed approach (namely in Chapters III and IV) might be viewed in the context of any other material which exhibits a quasibrittle behaviour.

Conclusions

The quasibrittle behaviour of notched structures has been brought into the discussion in the opening Chapter of this Thesis, focussed on the observation of different stages of the development of a large Fracture Process Zone (FPZ) taking place during the crack propagation. It has been seen that the main consequence of the development of this large FPZ is the increase in the resistance to crack growth during failure, rousing from stress redistributions and stored energy release, thus leading to what came to be known as the *Resistance-curve* (*R-curve*). Focussed on the revealed curve shape, it has been seen that following the ascending branch, for which the resistance to crack growth increases with the crack length, the *R-curve* reaches a plateau, which denotes that the influence of the toughening mechanisms is not indefinite.

Finite Element simulations involving the cohesive crack modelling were then mentioned as a suitable method to mimic the quasibrittle fracture. The simulations gave rise to the establishment of the relation between the attainment of the critical extent of the cohesive zone and the plateau value of the *R-curve*. This being verified in the following Chapter, it has been underlined the importance of the ligament length to estimate accurately the plateau value of the *R-curve*. The consequence of the *Resistance-curve* behaviour of quasibrittle materials has then been addressed to the effect of the structure size on the

structure nominal strength. Particular attention arose from the observation that in the intermediate size ranges, the size effect on the nominal strength is obtained from the fitting of two asymptotic regimes (provided by the Bažant's Size Effect Law on the Strength Theory and LEM), giving thus rise to the study of this regime in a subsequent Chapter of this Thesis.

In Chapter II fracture (Mode I) has been induced through three-point-bending (TPB: under displacement control) in two wood species used in timber construction: Maritime pine (*Pinus pinaster* Ait.) and Norway spruce (*Picea abies* L.). Load-displacement curves were experimentally obtained and the R -curve has been estimated through a recently proposed LEM equivalent approach. A bilinear cohesive law based on characteristic material (stresses and crack opening) as well as energy (G_f) parameters has been adopted to simulate damage in the studied wood through interface FE disposed along the crack path. A developed inverse method based on Genetic Algorithms was employed to seek the parameters of the chosen cohesive law and a fine agreement between both numerical and experimental load-displacement (and *Resistance*) curves was achieved, thus demonstrating the soundness of the proposed model to evaluate cohesive crack properties. Further FEM simulations were performed using identified constitutive law parameters to evaluate the extent of the cohesive zone in TPB, for both wood species. Superposition of bilinear diagrams relied on gathered mean values taken from the inverse analysis revealed that the ultimate stress in Maritime pine is twice as big as in Norway spruce, and arouse suspicions that the critical cohesive zone extent in spruce might be more important than in pine. Both wood species were compared referring to released energies during crack propagation, with pine turning out to release twice as more energy in micro-cracking than in fibre-bridging. Performed FEM simulations in Norway spruce confirmed the later suspicion revealing a cohesive zone extent largely greater to the one obtained for pine. Consequently, it was observed that FPZ development in pine is less affected by boundary effects than spruce. Based on the mean trend revealed by the FEM data, a critical value of the cohesive zone extent has been approximately quantified for pine, which led to convincing G_{RC} results. Contrarily, the FPZ extent in spruce was found to be affected by boundary conditions since the early stage of crack propagation. As a result, this leads to the non-self similar propagation process, which may explain the slender rising trend observed in the R -curve of

spruce (*i.e.*, practically an absence of plateau value on the resistance to crack growth for the tested specimen size). This remark addressed to the definition of an adequate ligament size (*i.e.*, critical size) to avoid spurious boundary effects on the measured G_{Rc} values, if size effect studies are to be carried out in spruce. This is a general conclusion which may be drawn to other quasi-brittle materials, presenting a significant FPZ length.

In the third Chapter, the size effect study on the ultimate fracture properties of notched structures has been performed on an energy based asymptotic analysis. Once verified that the R -curve is unique an analytical expression has been used to characterize the resistance growth (*i.e.*, the R -curve) the investigations have been focussed in the scaling on both the relative crack length at the peak load and the corresponding resistance to crack growth. Among the conclusions emerged from the study involving intermediate structure sizes, one may detach the observed decreasing in the relative crack length at the peak load with respect to the structure size, and corresponding rise in the resistance growth. These observations led to the reported statement of the size effect on the nominal strength for both small and large structure sizes in agreement with the Bažant's Size Effect Law (SEL), though contrasting with the simple crossover regime previewed by the SEL, since an additional asymptotic regime is developed for intermediate sizes. In regards to this observed asymptotic regime, the evolution of the nominal strength with the structure size D has been quantified as a function of the R -curve curvature. As yet to the intermediate structure sizes, the performed cohesive crack modelling (CCM) involving geometrically similar structures of different sizes (single-edge-notched beam loaded in three-point-bending: SEN-TPB) put into evidence that the developed asymptotic regime can widen from 1 decade, if the R -curve curvature is found slight, up to more than 3 decades, if the R -curve exhibits a very pronounced curvature. The safety design of structures has been addressed with the optimal solution being provided by the SEL, given that the fitting is performed using the evaluated nominal strength as well as the critical energy release rate values, for accurate positioning of the LEFM's asymptote. Both later extents were estimated by means of a fracture test involving a single structure size. The proposed method appears thus more suitable to predict the position of the LEFM's asymptote than the one which is based on the maximum nominal strength, estimated for structures of small size, in the domain of the strength theory.

The ending Chapter has been reserved for the presentation of the experimental results obtained in the size effect study in wooden notched structures (SEN-TPB) following the proposed methodology exposed in preceding Sections. The self-weight compensation, first emerging as a crucial standard to the accurate evaluation of fracture parameters in structures of non-negligible size (mass), motivated the proposal of two methods based on FEM computations and the recorded experimental data. The first method was presented on the kinematic approach basis of a load equivalent to the specimen-self-weight (LSSW), defined as a function of compliance polynomials obtained with the distributed load acting on the specimen, and with the central load acting on the mid-span. The evaluated compliances, being determined through FEM computations, were used to perform the numerical zeroing (*i.e.*, shifting) operation of the load-displacement ($P-\delta$) curve, setting the new origin along the experimental linear elastic domain. A recently proposed equivalent LEFM approach was then applied to estimate the corresponding R -curve making use of the previously modified (*i.e.*, shifted) $P-\delta$ curve. In regards to the second method, expressly designated Exact self-weight compensation method (ESWCM), the numerical zeroing (*i.e.*, shifting) operation of the $P-\delta$ curve occurred subsequently to the evaluation of the displacement elapsed from the specimen accommodation on the supports, due to the self-weight, prior to the fracture test. This correctional extent, being estimated through FEM computations for the distributed load corresponding to the specimen self weight (SSW), was performed prior to the material damage onset. Additionally, the elastic strain energy release was assessed from the complementary energies and the work attributed to the distributed load associated to the SSW and to the external applied load. The corresponding R -curve was estimated dividing the resulting elastic strain energy release by the corresponding infinitesimal crack surface extent. Both SSW compensation methods (*i.e.*, the LSSW and the ESWCM) were compared through CCM using predefined cohesive crack properties, with merely the ESWCM to retrieve the exact critical energy release rate G_{Rc} used as input. The noticed outcome has been hold as the validity prove that the ESWCM is adequate to evaluate exact fracture parameters in quasibrittle fracture, with subsequent computations of the R -curve being carried out by means of this method.

A sampling problem has been detected in regards to the experimental results, first revealed by the scattering of the initial unitary compliance, thus concluding for the existence of different initial damage state in the raw material used to carry out the experiments. Applying the (validated) exact self-weight compensation method to the whole experimental $P-\delta$ curves obtained in the context of the size effect study, it has been noticed the slight rise in the mean value of the relative critical crack length of the FPZ θ , with the increase in the structure size D . The relative mean length associated to the peak load α_u in the experiments came into sight as following an identical increasing trend with D . The reported tenuous trends observed in the experimental data however, were not wholly followed by the cohesive crack modelling treated in Chapter III, since both α_u and θ had shown a consistent contrary tendency in the CCM. In any case, considering just the data issuing from specimens which exhibited undoubted plateaux on the R -curve, the revealed mean trends shown in the experiments for α_u and θ , were not absolutely convincing, since barely the biggest specimen size D seemed to force the mentioned performance. Thus, though affected by the matching problem, it has been decided to execute the numerical protocol proposed in Chapter III till the end, using the available experimental data.

The raising portion observed in the estimated R -curves which presented undoubted plateaux obtained in the experiments revealed an increasing coefficient of curvature (*i.e.*, β) with the structure size D . This behaviour made possible to take notice of the increasing range of $G_R(\alpha_u)$ with the structure size D , thus confirming the predictions issued from the CCM (Chapter III). Consequently, the size effect study on the nominal strength $\sigma_N(D)$ has been performed for each tested structure size D , revealing an envelop configuring a pattern shape composed by the superposition of both intermediate and LEFM regimes. The accurate definition of the intermediate size regime is thus possible to achieve, sufficing that the R -curve is known for a given specimen geometry.

In short, it is assumed that the size effect matter is determined. Notwithstanding this, the remaining difficulty seems to prevail associated to the dependence of the cohesive crack properties on the structure geometry.

A2.1 Material

Wood is a natural polymeric composite material which is heterogeneous, hygroscopic, porous and anisotropic, being its microstructure reflected on the macro-scale in its grain. Cells are formed of a series of layers made up of three organic components: cellulose, hemicellulose and lignin. The cell wall components are the structural members of the wood cell, and largely govern the physical properties of wood. Cellulose is the primary component of the cell wall. Structurally cellulose is a linear chain polymer forming long glucose units structurally composed by long threadlike elements known as microfibrils periodically arranged over the length into crystalline and non-crystalline portions, forming the basic structural elements of cell walls. Hemicellulose is a modified form of cellulose (Bodig J and Jayne BA 1982). Unlike cellulose, which is exclusively composed of long chains of glucose units, hemicellulose includes a variety of monosaccharide (Tsoumis G 1991), appearing as individual molecules. Lignin is basically the adhesive that binds other components together and is the most hydrophobic component in the cell wall (Smith I et al. 2003). Wood is regarded as a two-phase material with crystalline cellulose constituting the fibre while an arrangement of non-crystalline cellulose, hemicellulose and lignin is found to constitute the matrix (Bodig J and Jayne BA 1982). Compression and bending loads withstanding lead to interfacial coupling between wood cells inhibiting fibres from sliding past one another (Atkins AG and Mai YW 1985). In an undamaged state and once subjected to fairly low levels of stress during short duration room temperature, wood is markedly an elastic material (Smith I et al. 2003). With regard to time dependency wood is considered physically and mechanically as a non-linear material. Once sufficiently distant from the tree pith (Fig. A2.1.1) wood is found to exhibit an orthotropic behaviour, since the curvature in growth rings is neglected (Smith I and Vasic S 2003). Wood as a biological material has the ability to deliberately change local mechanical properties in growing structures ever since changes in load patterns are detected (Atkins AG and Mai YW 1985). Though mechanical properties can vary considerably both along the longitudinal (L) and radial (R) directions (Fig. A2.1.1), for the sake of simplicity in engineering design wood is assumed as transversally isotropic (plane RT). Harvesting and drying (Stanzl-Tschegg SE et al. 1995) processes may influence wood mechanical properties more than those of most other materials. Although drying stiffens and strengthens the material, it also makes it more

brittle, *i.e.* prone to fracture. Thus, it seems obvious that a deep understanding of fracture mechanisms is key to understanding the mechanical behaviour of wood. Very much to the purpose of the wood axis directions shown in Fig. A2.1.1, it is worth while to identify the fracture systems in wood, through the schematic representation of Fig. A2.1.2.

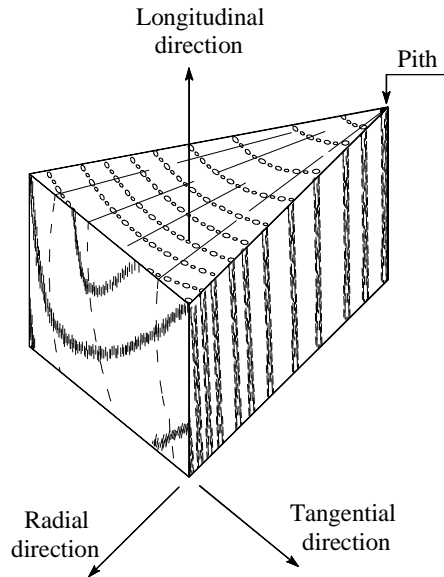


Figure A2.1.1 Axis directions in wood: Longitudinal (L), Radial (R) and Tangential (T). Adapted from Smith I et al. (2003).

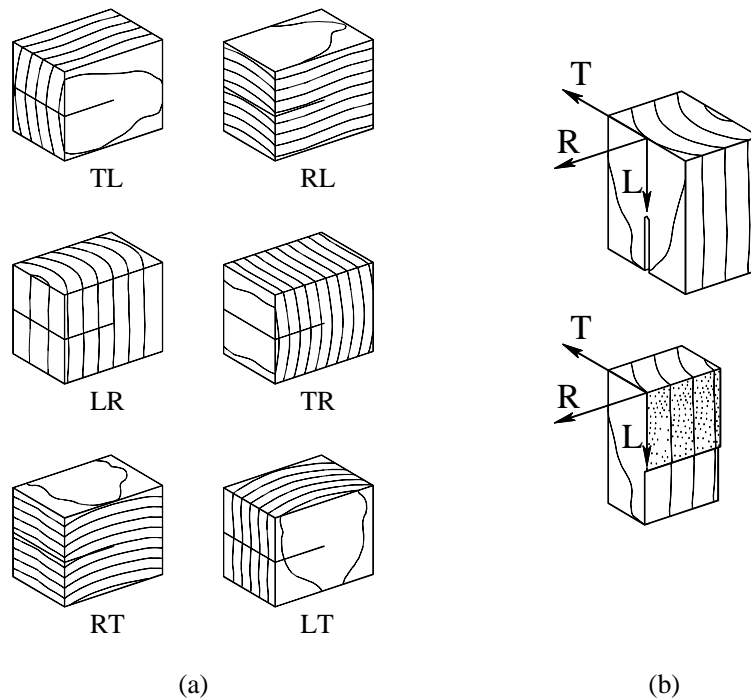


Figure A2.1.2 Identification of wood fracture systems: (a) possible to obtain and (b) studied in this Thesis.

A2.2 Formulation of the inverse problem

An inverse problem (IP) has been established as an Optimisation Strategy (OS) where the objective is to determine the bilinear parameters: w_b, f_b and f_t (design variables \mathbf{b}) which provide a numerical P - δ curve agreeing with the experimental P - δ curve (state variables \mathbf{z}). The OS was established by means of the

$$\text{Minimisation } y(\mathbf{b}) = (\mathbf{z} - \mathbf{z}^*)^T (\mathbf{z} - \mathbf{z}^*) \quad \text{with } \mathbf{z} \in D_z \quad (\text{A2.2.1})$$

$$\text{subject to } g_j(\mathbf{b}) \leq 0, \quad j = 1, \dots, N_g, \quad \underline{\mathbf{b}} \leq \mathbf{b} \leq \bar{\mathbf{b}} \quad (\text{A2.2.2})$$

in the domain D_z . The vector of prescribed values is \mathbf{z}^* , N_g the number of constraints, $\underline{\mathbf{b}}$ and $\bar{\mathbf{b}}$ are the lower and upper bounds of the design variables (Table A2.2.1), respectively. A population of solutions $P(t) = \{x_1^t, \dots, x_n^t\}$ was randomly generated constituted by x_i^t ($i=1, \dots, k$) potential solutions, encoded according to a predefined data structure S . A *fitness* evaluation was performed according to how well each solution x_i^t fulfils the objective function $y(\mathbf{b})$ defined in the problem. The binary format (*string*₂) was chosen to encode \mathbf{b} in the domain $D_i = [a_i, b_i] \subseteq R$. According to the precision p of each design variable required to determine $y(\mathbf{b})$, the length m_i attributed to each variable is evaluated considering the smallest integer (Michalewicz Z 1999) such that: $(b_i - a_i) \cdot 10^p \leq 2^{m_i} - 1$.

Table A2.2.1 Lower and upper limits of the search domain attributed to each design variable

Parameter	Maritime pine		Norway spruce		Unities
	Lower limit	Upper limit	Lower limit	Upper limit	
f_t	1.500	8.000	0.500	4.000	(MPa)
f_b	0.005	3.000	0.005	2.000	(MPa)
w_b	0.005	1.500	0.005	1.500	(mm)

Each variable x_i^t from each chromosome $\mathbf{v}_i (i=1, \dots, Pop(t))$ is decoded as follows

$$x_i^t = a_i + decimal(string_2) \times \frac{b_i - a_i}{2^{m_i} - 1} \quad (\text{A2.2.3})$$

with $decimal(string_2)$ representing the hexa-decimal value of $string_2$. Estimate of $y(\mathbf{b})$ is

$$y(\mathbf{b})_j = \frac{1}{N} \left\{ \sum_{i=1}^N \left\| z_i^* - z_i^t \right\|^2 \right\} \quad (\text{A2.2.4})$$

with N representing the total number of points composing the numerical P - δ curve, z_i^* a given point in the experimental P - δ curve (specimen j), and z_i^t the P - δ curve generated in the analysis. *Fitness* was estimated in order to Maximize $f_i(\mathbf{b}) = F_{\max} - y(\mathbf{b})_j$, with F_{\max} chosen to avoid negative values.

Regarding the *Selection* operator, a *Ranking* involving the totality of chromosomes $\mathbf{v}_i (i=1, \dots, Pop(t))$ was then performed based on the evaluation of Eq. (A2.2.4), followed by a *Scaling* operation used to improve the sensitivity (Michalewicz Z 1999) of the algorithm,

$$y'(\mathbf{b})_j = y(\mathbf{b})_j + \left(\bar{y}(\mathbf{b})_j - c \times \sigma \right) \quad (\text{A2.2.5})$$

with c chosen as a small integer, σ is the standard deviation of the current population $P(t)_j$, and $\bar{y}(\mathbf{b})_j$ the mean value of $y(\mathbf{b})$ in the current population. A new *Ranking* of solutions was then performed and three subsets (S_T, S_M, S_B) arranged into $n_T(t)$, $n_M(t)$ and $n_B(t)$ solutions (Fig. A2.2.1). In a first phase, each solution of S_T mated with a selected solution of the same group or belonging to S_M . In a second phase, S_M was divided into two equal subsets (S_{MT}, S_{MB}) with $n_{MT}(t) = n_{MB}(t)$ solutions (Conceição António CA and Dourado N 2002). Subsequently, each solution of S_{MT} mated another solution from S_{MB} , thus resulting a total of $n_M(t)/2$ couples (Fig. A2.2.2).

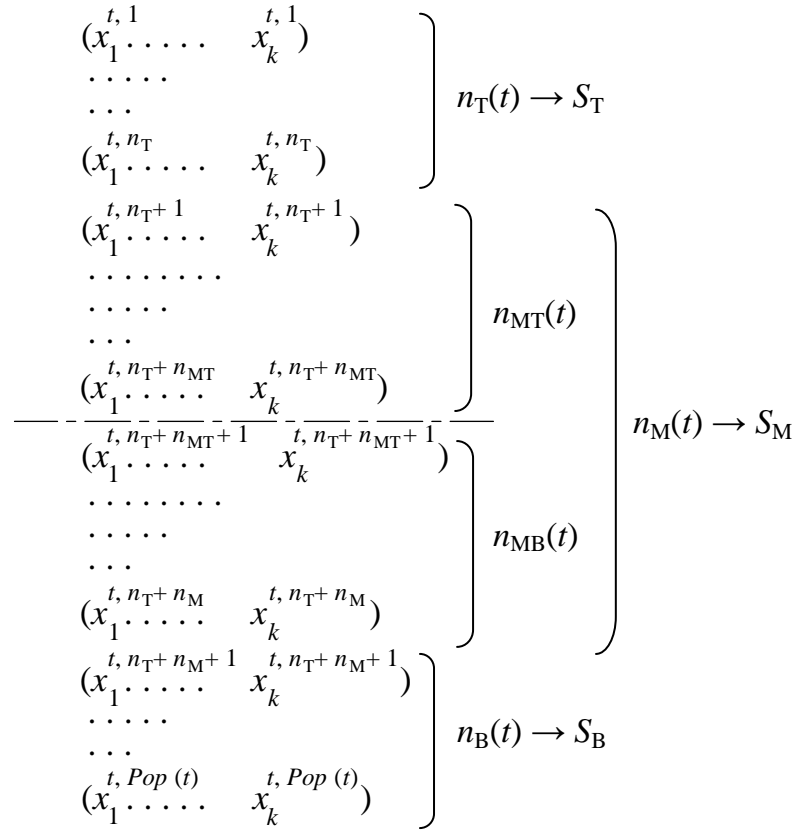


Figure A2.2.1 Ranking of solutions in generation t showing subsets disposition: S_T , S_M and S_B after the *Ranking* operation. Data represented by $x_i^{t,l}$ ($i=1, \dots, k$) are potential solutions composed by a combination of k design variables of the optimisation problem, in position l of the actual performed *Ranking* operation. The centreline divides the whole data in two equal halves. (In: Dourado N. et al. 2008).

Solutions belonging to subset S_B were not approved to generate offspring. According to the *Crossover* operator, gene r_s (offspring) is selected on a biased manner according which, gene u_s is chosen from chromosome $\bar{\mathbf{x}}_i^t$ with a probability of p_c ,

$$r_s = \begin{cases} u_s \in \bar{\mathbf{x}}_i^t & \text{if } \text{Unif}(0,1) \leq p_c \\ v_s \in \bar{\mathbf{y}}_i^t & \text{if } \text{Unif}(0,1) > p_c \end{cases} \quad s=1, \dots, m = \sum_{l=1}^k m_l \quad (\text{A2.2.6})$$

$\bar{\mathbf{x}}_i^t$ and $\bar{\mathbf{y}}_i^t$ are the chromosomes defined in Fig. A2.2.2. *Mutation* operator is used to perform transformations among the offspring with a predefined probability p_m .

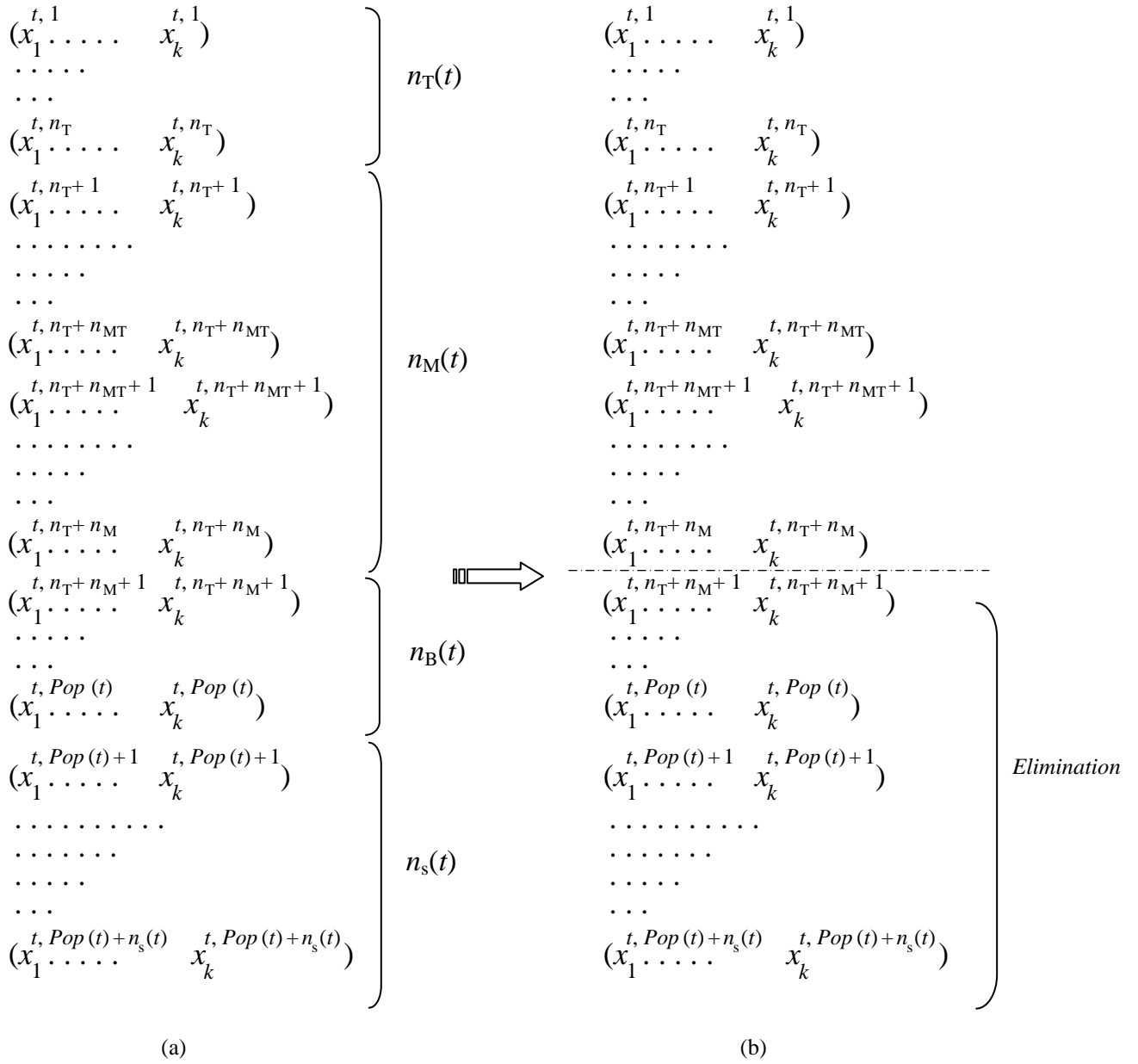


Figure A2.2.3 Arrangement of solutions performed by Elimination: (a) before and (b) after Ranking. (In: Dourado N. et al. 2008).

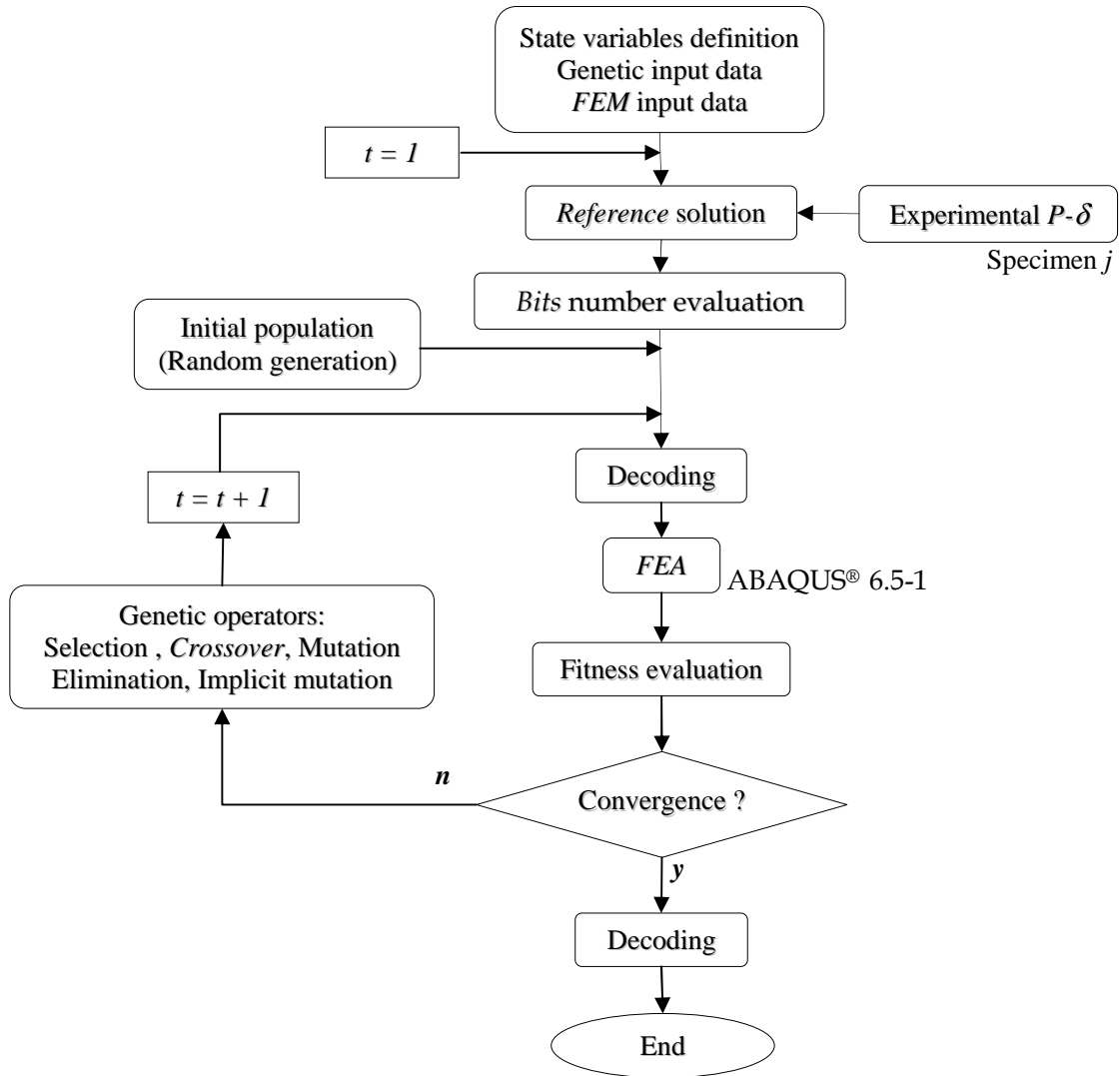


Figure A2.2.4 Sketch of the Inverse Problem. (In: Dourado N. et al. 2008).

Table A2.2.2 Resume of genetic parameters. $Pop(t)$: Population size; $n_T(t)$, $n_M(t)$ and $n_B(t)$: Number of solutions of subsets S_T , S_M and S_B ; p_m and p_c : probability of *Mutation* and *Crossover*; p ($i=1, 2, 3$): Precision of each design variable required to determine the objective function $y(\mathbf{b})$; α : Generations counter used in the stopping criterion

Parameter	Value	Parameter	Value
$Pop(t)$	10	c	3
$n_T(t)$	2	$p_{(i=1)}$	3
$n_M(t)$	6	$p_{(i=2)}$	2
$n_B(t)$	2	$p_{(i=3)}$	3
p_m	0.005	α	50
p_c	0.65		

A2.3 Fracture parameters

In the following a complete record of the main fracture parameters is presented regarding Tables 2.2, 2.3, 2.4, 2.5 and 2.6 exhibited in Chapter II.

Table A2.3.1 (Complete recording of **Table 2.2**) Resume of main values obtained in TPB for Pine wood. ψ : Multiplicative correction factor; $\lambda_{\text{exp}}(a_0)$: Initial compliance obtained in experiments; P_u : ultimate load; a_u : elastic equivalent crack length at P_u ; $G_R(a_u)$: energy release rate corresponding to P_u ; a_c : characteristic value of elastic equivalent crack length corresponding to the plateau value of the R -curve; G_{Rc} : plateau value of the R -curve

Specimen	ψ	$\lambda_{\text{exp}}(a_0)$ (10^{-3} mm/N)	P_u (N)	a_u (mm)	$G_R(a_u)$ (J/m ²)	a_c (mm)	G_{Rc} (J/m ²)
1	1.07	1.97	336.3	36.5	180.0	37.5	186.5
2	1.23	2.24	367.9	36.0	233.6	36.8	240.2
3	1.15	2.11	335.7	36.8	195.2	37.3	199.9
4	1.25	2.29	342.5	37.3	233.4	38.1	245.9
5	1.03	1.89	378.5	36.2	212.1	36.4	216.7
6	1.27	2.31	353.0	36.8	240.3	38.4	257.6
7	1.24	2.26	307.2	37.6	191.4	38.6	206.0
8	1.26	2.29	314.4	36.9	189.9	37.9	199.9
9	1.30	2.37	322.5	37.7	221.7	37.9	224.8
10	1.17	2.12	301.4	37.5	170.8	37.8	173.0
11	1.28	2.31	317.7	36.3	186.6	36.9	194.4
12	1.28	2.34	287.1	37.1	164.3	37.3	165.7
Average	1.21	2.21	330.4	36.9	201.6	37.6	209.2
St. Dev.	0.09	0.15	26.1	0.6	24.8	0.6	27.5

Table A2.3.2 (Complete recording of **Table 2.3**) Resume of main values obtained in TPB for Norway spruce. $G_R(a_i)$: Energy release rate at the slender rising trend segment of the R -curve

Specimen	ψ	$\lambda_{\text{exp}}(a_0)$ (10^{-3} mm/N)	P_u (N)	a_u (mm)	$G_R(a_u)$ (J/m ²)	a_i (mm)	$G_R(a_i)$ (J/m ²)
1	1.25	5.42	150.3	37.8	112.2	48.9	169.9
2	1.33	5.79	138.1	36.9	93.2	46.0	124.9
3	1.27	5.55	154.7	37.1	113.5	46.8	171.3
4	1.26	5.52	138.7	36.7	87.5	43.4	118.5
5	1.27	5.55	140.6	37.7	99.7	46.7	137.5
6	1.01	4.38	156.1	37.8	98.2	50.0	150.8
7	1.34	5.9	138.8	38.2	106.3	45.7	136.8
8	1.29	5.65	150.3	37.3	110.2	45.6	165.1
9	1.31	5.72	143.8	36.3	93.7	43.9	124.8
10	1.26	5.51	148.0	36.9	101.1	44.9	141.6
11	1.23	5.42	148.3	37.3	103.5	51.1	161.1
12	1.21	5.29	142.2	38.1	100.1	51.3	132.5
Average	1.25	5.48	145.8	37.3	101.6	47.0	144.6
St. Dev.	0.09	0.37	6.1	0.6	7.7	2.6	17.8

Table A2.3.3 (Complete recording of **Table 2.4**) Comparison between numerical and experimental mean values obtained for Maritime pine

Specimen	Numerical results		Experimental results			Error (%)	
	P_u (N)	$G_R(a_u)$ (J/m ²)	P_u (N)	$G_R(a_u)$ (J/m ²)	G_{Rc} (J/m ²)	P_u	$G_R(a_u)$
1	335.5	178.6	336.3	180.0	186.5	-0.24	-0.78
2	368.3	234.5	367.9	233.6	240.2	0.11	0.39
3	335.2	186.1	335.6	195.2	199.9	-0.12	-4.66
4	344.8	237.3	342.5	233.4	245.9	0.67	1.67
5	378.5	217.5	378.5	212.1	216.7	0.00	2.55
6	351.9	234.3	353.0	240.3	257.6	-0.31	-2.50
7	307.7	182.2	307.2	191.4	206.0	0.16	-4.81
8	315.6	188.9	314.4	189.9	199.9	0.38	-0.53
9	323.2	209.1	322.5	221.7	224.8	0.22	-5.68
10	301.3	166.7	301.4	170.8	173.0	-0.03	-2.40
11	318.2	185.1	317.7	186.6	194.4	0.16	-0.80
12	289.4	160.3	287.1	164.3	165.7	0.80	-2.43
Avg.	330.8	198.4	330.4	201.6	209.2	0.15	-1.67
St. Dev.	25.7	26.0	26.1	24.8	27.5		

Table A2.3.4 (Complete recording of **Table 2.5**) Comparison between numerical and experimental mean values obtained for Norway spruce

Specimen	Numerical results		Experimental results			Error (%)	
	P_u (N)	$G_R(a_u)$ (J/m ²)	P_u (N)	$G_R(a_u)$ (J/m ²)	G_{Rc} (J/m ²)	P_u	$G_R(a_u)$
1	152.5	110.3	150.3	112.2	169.9	1.46	-1.69
2	138.0	94.4	138.1	93.2	124.9	-0.07	1.29
3	157.2	118.7	154.7	113.5	171.3	1.62	4.58
4	143.6	90.4	138.7	87.5	118.5	3.53	3.31
5	144.5	89.5	140.6	99.7	137.5	2.77	-10.23
6	161.3	97.3	156.1	98.2	150.8	3.33	-0.92
7	142.3	101.9	138.8	106.3	136.8	2.52	-4.14
8	152.7	111.3	150.3	110.2	165.1	1.60	1.00
9	148.4	104.0	143.8	93.7	124.8	3.20	10.99
10	152.6	110.2	148.0	101.1	141.6	3.11	9.00
11	150.8	107.5	148.3	103.5	161.1	1.69	3.86
12	143.3	92.2	142.2	100.1	132.5	0.77	-7.89
Avg.	148.9	102.3	145.8	101.6	144.6	2.13	0.76
St. Dev.	6.5	9.1	6.1	7.7	17.8		

Table A2.3.5 (Complete recording of **Table 2.6**) Summary of main values (12 specimens of each wood species) obtained in the inverse problem regarding the bilinear constitutive model (Figure 2.7). f_t : ultimate stress value; f_b and w_b : coordinates of the break-point; $G_{f\mu}$: fracture energy attributed to micro-cracking; G_{fb} : fracture energy ascribed to fibre-bridging phenomenon; G_f cohesive fracture energy

Specimen (Pine)	f_t (MPa)	f_b (MPa)	w_b (mm)	$G_{f\mu}$ (J/m ²)	G_{fb} (J/m ²)	G_f (J/m ²)
1	5.03	0.83	0.05	128.18	58.33	186.51
2	5.96	0.81	0.06	163.26	76.93	240.19
3	5.14	1.00	0.05	128.41	71.52	199.93
4	4.44	1.15	0.07	146.56	99.33	245.89
5	5.57	0.10	0.07	185.58	31.08	216.66
6	4.87	0.86	0.07	165.77	91.80	257.57
7	4.13	1.14	0.05	110.74	95.30	206.04
8	4.26	0.71	0.06	133.19	66.72	199.91
9	4.02	0.74	0.07	149.18	75.66	224.84
10	3.80	0.74	0.06	118.57	54.42	172.99
11	4.71	0.27	0.06	146.07	48.37	194.44
12	3.98	0.23	0.06	126.44	39.23	165.67
Average	4.66	0.72	0.06	141.83	67.39	209.22
St. Dev.	0.65	0.33	0.01	20.87	21.01	27.49
(Spruce)						
1	1.62	0.34	0.09	74.83	95.06	169.89
2	1.51	0.27	0.08	63.86	61.03	124.89
3	1.70	0.36	0.09	78.09	93.16	171.25
4	1.79	0.30	0.07	61.42	57.04	118.46
5	1.94	0.33	0.06	59.58	77.89	137.47
6	1.72	0.29	0.09	76.43	74.41	150.84
7	1.51	0.29	0.09	69.40	67.38	136.78
8	1.61	0.39	0.09	73.16	93.63	166.79
9	1.70	0.22	0.09	74.69	50.10	124.79
10	1.81	0.29	0.08	73.69	69.37	143.06
11	1.51	0.29	0.10	77.71	83.34	161.05
12	1.51	0.25	0.09	68.04	64.46	132.50
Average	1.66	0.30	0.09	70.91	73.91	144.81
St. Dev.	0.13	0.05	0.01	6.12	14.38	17.97

A3.1 Polynomial functions

The effective Young modulus for orthotropic materials is given by Sih GC et al. (1965),

$$E^* = \frac{(2 E_1 E_2)^{1/2}}{\sqrt{\frac{E_2}{2 G_{12}} - \nu_{21} + \left(\frac{E_2}{E_1}\right)^{1/2}}} \quad (\text{A3.1.1})$$

According to the disposition of the specimen anatomic axis sketched in Fig. 3.9 (with the specimen occupying the central part), the indexes correspondence: 1 : T and 2 : L has been established. The elastic properties presented in Table A3.1.1 were used to compute $E^* = 709.8$ MPa .

Compliance evolution as a function of the numerical relative crack length $\lambda_{PP}(\alpha)$ has been computed through linear elastic FE in in-plane strain analyses (Fig. A3.2.1) using the set of elastic properties presented in Table A3.1.1 (for $\alpha_0 \leq \alpha < 0.85$), imposing an arbitrary vertical displacement δ to the mid-section rigid body. The unitary compliance function obtained by polynomial best fitting to the dotted curve plotted in Fig. A3.1.1. led to

$$[\lambda_{PP}(\alpha) \times b]^{-1} = -76.437 \alpha^6 + 357.578 \alpha^5 - 695.093 \alpha^4 + 725.073 \alpha^3 - 409.874 \alpha^2 + 95.589 \alpha + 3.163 \quad (\text{A3.1.2})$$

In order to fit with the Maxwell-Betty principle (referred in Chapter IV) the first index exhibited in the compliance in the former equation identifies the loading type (*i.e.*, the concentric load P), while the second denotes the loading axis (in this case index P again). Consequently, the dimensionless energy release rate function $g(\alpha)$ defined in Section 1.3 [*i.e.*, $g(\alpha) = E' b \lambda(\alpha) / 2$] has been evaluated for a given specimen size D of Table 3.1 (Fig. A3.1.2) considering the in-plane strain analysis, *i.e.*, $E' = E^* / (1 - \nu^2)$, with E^* as defined in Eq. (A3.1.1). The resulting expression has been

Table A3.1.1 Elastic properties of Norway spruce (*Picea abies* L.) Guitard D (1987)

Wood Species	E_L (MPa)	E_R (MPa)	E_T (MPa)	ν_{TL}	ν_{RL}	ν_{TR}	G_{TL} (MPa)	G_{RT} (MPa)	G_{RL} (MPa)
Norway spruce	9 900	730	410	0.018	0.032	0.306	610	22	500

obtained through the polynomial best fit of the set of results exhibited in Fig. A3.1.2, leading to

$$g(\alpha) = 7.126 \times 10^7 \alpha^6 - 2.736 \times 10^8 \alpha^5 + 4.364 \times 10^8 \alpha^4 - 3.700 \times 10^8 \alpha^3 + 1.758 \times 10^8 \alpha^2 - 4.434 \times 10^7 \alpha + 4.641 \times 10^6 \quad (\text{A3.1.3})$$

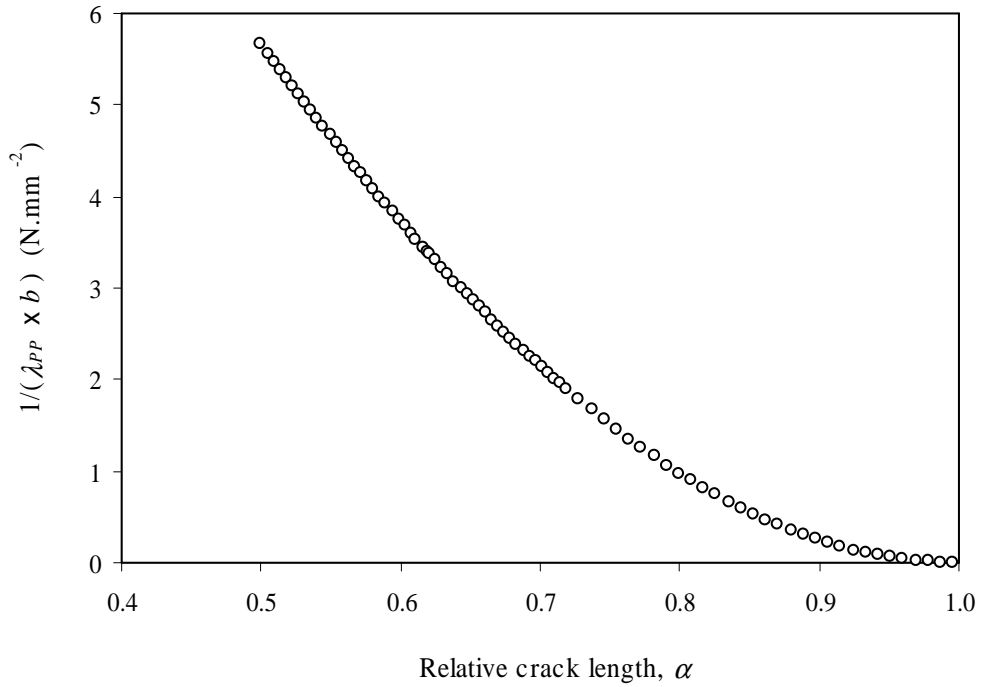


Figure A3.1.1 Stiffness calibration curve for the SEN-TPB.

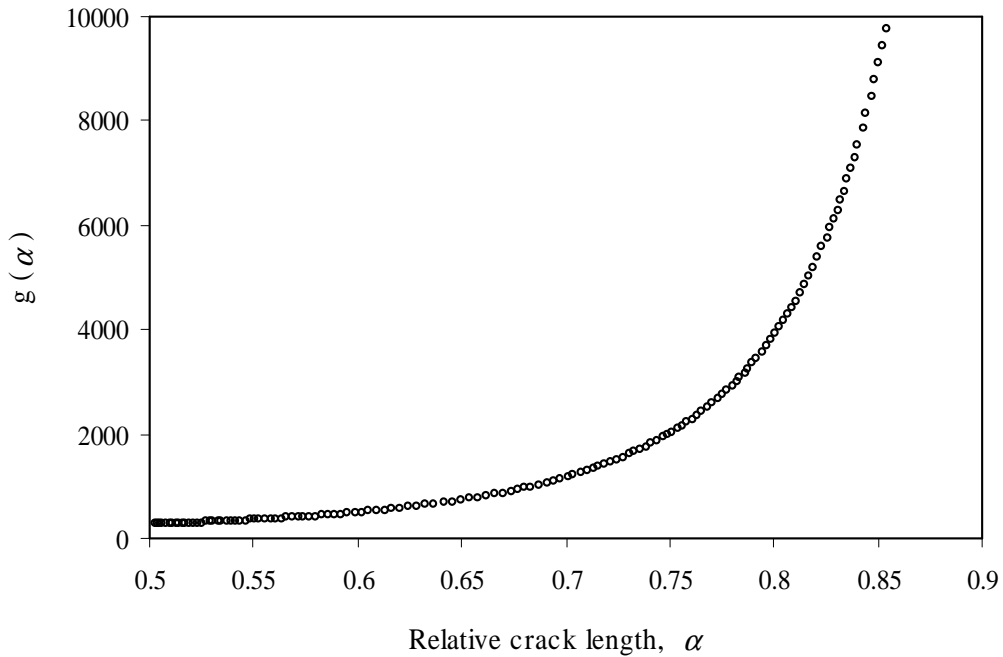


Figure A3.1.2 Dimensionless energy release rate $g(\alpha) = E' b \lambda(\alpha)/2$.

A3.2 FE-modelling

The FE-modelling is presented in more detail in this Appendix, referring to the numerical simulations performed with the SEN-TPB shape shown in Fig. 3.9.

Due to the model symmetry only a half-specimen is analyzed. The FE-mesh density shown in Fig. A3.2.1 corresponds to the series label D_2 (Table 3.1, for $h = 70$ mm) and is composed of 488 8-node and 248 6-node anisotropic in plane strain elements from ABAQUS[®] 6.5-1 library. A reasonably fine mesh, necessary to obtain a smooth load versus crack length relation is used to model the material domain in the neighbourhood of the bottom support, and in which the crack propagation occurs. Furthermore, interface plane elements (Section 2.4.1) were positioned all through an upright central line sited ahead of the initial crack notch $a_0 = h/2$ (Fig. A3.2.1) dividing the specimen ligament length in every 0.5 mm. Making use of FE rigid bodies included in ABAQUS[®] 6.5-1 library, two non-friction pairs were employed to simulate the contact with the bottom support (left-bottom rectangle in Fig. A3.2.1) and with the loading device acting on the specimen (right-top rectangle drawn in Fig. A3.2.1).

In-plane strain analyses were performed modelling Norway spruce (*Picea abies* L.) as a linear elastic orthotropic material with engineering constants exhibited in Table A3.2.1. As sketched in Fig. 3.9 the model is divided in two material domains (Fig. A3.2.1), with the left portion ($5/2h$) oriented along the orthotropic Longitudinal direction (material aligned with axis x) while the remaining portion has been oriented along the Tangential direction (material aligned with axis y). This provides a way to perform fracture simulations in the wood TL fracture system, as referred in Chapter II and Appendix A2.1.

The cohesive crack properties (Fig. 2.7) presented in Table A3.2.2 have been chosen in order to provide an equal energy distribution in the bilinear diagram ($G_{f\mu} = G_{fb}$), for $G_f = 0.1$ N/mm (Section 2.4.2), endowing with the ratios: $f_b/f_t \cong w_b/w_c \cong 0.3$.

During the simulations both load and displacement values were monitored in the top-right rigid body acting on the specimen middle-section.

Cohesive crack modelling of the remaining specimen sizes D presented in Table 3.1 were all performed according to the same numerical protocol, implementing

homothetic FE-meshes, with further mesh densification at the middle-section (crack plane) to keep the ligament length equally divided in every 0.5 mm.

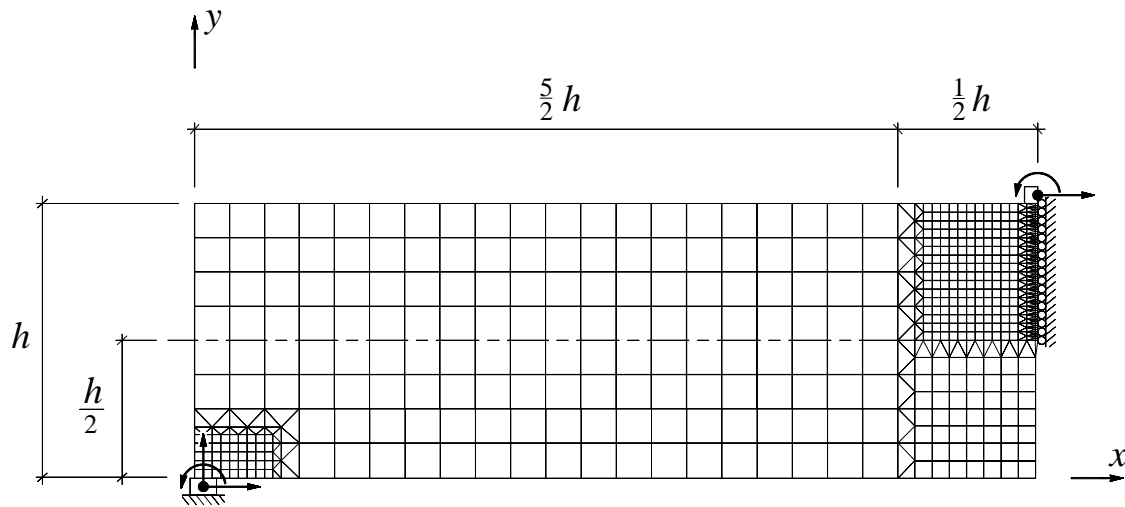


Figure A3.2.1 Symmetric FE-mesh used in ABAQUS® 6.5-1 simulations (Table 3.1 contains the nominal dimensions used in the computations).

Table A3.2.1 Elastic properties of Norway spruce (*Picea abies* L.) Guitard D (1987)

Wood Species	E_L (MPa)	E_R (MPa)	E_T (MPa)	ν_{TL}	ν_{RL}	ν_{TR}	G_{TL} (MPa)	G_{RT} (MPa)	G_{RL} (MPa)
Norway spruce	9 900	730	410	0.018	0.032	0.306	610	22	500

Table A3.2.2 Petersson's model softening properties used in the simulations (according to Fig. 2.7)

f_t (MPa)	f_b (MPa)	w_b (mm)	G_f (N/mm)
1.75	0.49	0.06	0.1

A4.1 Experimental load-displacement curves

The plotting of the load-displacement curves obtained in the experiments is exhibited in this Appendix for complete view of the achieved results.

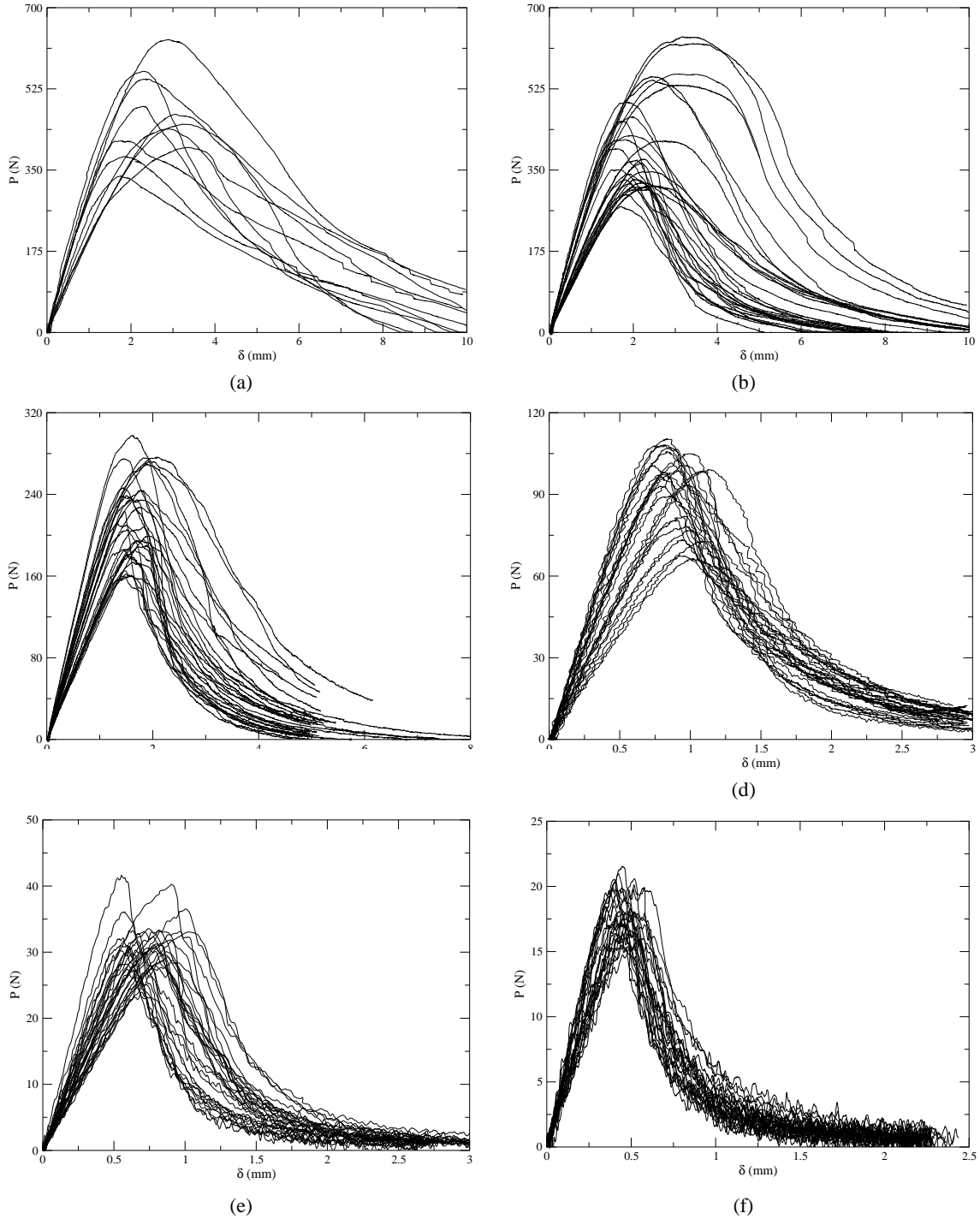


Figure A4.1.1 Load-displacement curves obtained in the experiments (displacement control). Graphics (a) to (f) correspond to sizes $D=280$ to $D=23.33$ mm (Table 4.1).

A4.2 Formulary steps of the exact self-weight compensation method

In the following a summary of the main steps detailed in Section 4.3.3 is presented according to the format which was found handier to implement in the computer code.

1. Numerical compliances (FEM-computation and polynomial fitting) :

$$\lambda_{Pq}^*(a), \lambda_{PP}^*(a) \text{ and } \lambda_{qq}^*(x,a) \text{ for } a \in [a_0, h]$$

2. Multiplicative correction factor (evaluated once per specimen):

$$\psi = \lambda_{PP \text{ exp}}(a_0) / \lambda_{PP}^*(a_0) \quad (\text{Eq. 4.14})$$

3. Correction of compliances :

$$\lambda_{PP}(a) = \psi \lambda_{PP}^*(a) \text{ and } \lambda_{Pq}(a) = \psi \lambda_{Pq}^*(a) \quad (\text{Eqs. 4.20, 4.21})$$

4. Displacement prior to the load-cell zeroing operation :

$$\delta_{Pq}(a_0) = \lambda_{Pq}(a_0) q \quad (\text{Eq. 4.29})$$

5. Shifting of the original P - δ curve (Fig. 4.9): $(P_i - \delta_i)_{\text{mod}}$:

$$\text{For each point } (P_i - \delta_i) : \delta_{\text{mod}}(a) = \delta_{\text{exp}}(a) + \delta_{Pq}(a_0) \quad (\text{Eq. 4.28})$$

6. Equivalent crack length a :

Do : For each point i :

- (a) Experimental $(P_i - \delta_i)_{\text{mod}}$ ($i \geq \text{Yield - point}$: Fig. 4.10):

$$\lambda_{\text{mod } i}(a) = \delta_{\text{mod}}(a) / P_i$$

- (b) Modified compliance :

$$\lambda_{\text{mod}}(a_i) = \lambda_{PP}(a_i) + \lambda_{Pq}(a_i) q / P_i \quad (\text{Eq. 4.31})$$

- (c) Tracking of a : (through the Bisection method) such that

$$\lambda_{\text{mod } i}(a) = \lambda_{\text{mod}}(a_i)$$

End Do

7. Energy release rate :

Uniformly pacing $(P_i - \delta_i)_{\text{mod}}$ (Fig. 4.11), with a_1, a_2 as consecutive equivalent crack-lengths,

Do: For each point i : $(P_i - \delta_i)_{\text{mod}}$ (Fig. 4.11) :

- (a) Work of the external applied load :

$$\delta W_P = (P_1 + P_2) / 2 [\delta_{\text{mod}}(a_2) - \delta_{\text{mod}}(a_1)] \quad (\text{Eq. 4.35})$$

- (b) Work of the internal body forces :

$$\delta W_q = \int_0^L [\delta(x, a_2) - \delta(x, a_1)] q dx \quad (\text{Eqs. 4.36})$$

$$\text{with: } \delta(x, a_i) = \lambda_{qP}(x, a_i) P_i + \lambda_{qq}(x, a_i) q, \quad (i = 1, 2) \quad (\text{Eq. 4.38})$$

(c) Complementary energy of the distributed load :

$$\delta U_P = 1/2 (P_2 \delta_{2_{\text{mod}}} - P_1 \delta_{1_{\text{mod}}}) \quad (\text{Eq. 4.39})$$

(d) Complementary energy of the applied load :

$$\delta U_q = 1/2 \delta W_q \quad (\text{Eq. 4.41})$$

(e) Elastic strain energy release :

$$\delta E = (\delta W_P - \delta U_P) + (\delta W_q - \delta U_q) \quad (\text{Eq. 4.44})$$

(f) Energy release rate (associated to a_1) :

$$G(a_1) = (\delta W_P - \delta U_P)/(b \delta a) + (\delta W_q - \delta U_q)/(b \delta a) \quad (\text{Eq. 4.45})$$

End do

A4.3 CCM using the load equivalent to the specimen self-weight

The plotting exhibited in Fig. A4.3.1 has been made with the data recorded in the cohesive crack modeling presented in Section 4.3.3.3. As stated in condition established through Eq. (4.8) for the self-weight compensation by means of the load equivalent to the specimen self-weight, the ratio $\lambda_{P_q}^*(\alpha)/\lambda_{P_P}^*(\alpha)$ is kept invariable over the range $a \in [D/2, 0.85D]$.

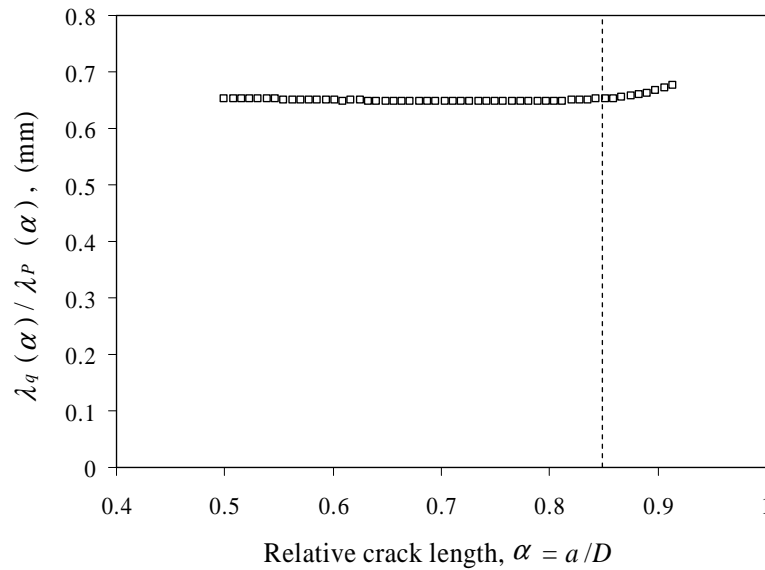


Figure A4.3.1 Plotting of the ratio $\lambda_{P_q}^*(\alpha)/\lambda_{P_P}^*(\alpha)$ obtained in the cohesive crack modeling conditions referred in Section 4.3.3.3. The dashed line establishes the range of validity of the condition stated through (Eq. 4.8), with $\alpha_{\text{expl}} \cong 0.85$ (i.e., $[D/2, 0.85D]$).

Table A4.3.1 exhibits the load equivalent to the specimen self-weight P_q evaluated through Eq. (4.7) for the specimen dimensions presented in the cohesive crack modeling (Section 4.3.3.3).

Table A4.3.1 Load equivalent to the specimen self-weight according to Eq. (4.7)

Density (kg/m ³)	Weight (N)	$\lambda_{P_q}^*(\alpha)/\lambda_{P_P}^*(\alpha)$ (mm)	q (N/m)	P_q (N)
300	46.72	0.65	37.082	24.22
400	62.30		49.44	32.29
500	77.90		61.80	40.37
600	93.45		74.16	48.44
700	109.02		86.52	56.52

Figure A4.3.2 exhibits the set of load-displacement curves first presented in Fig. 4.13 after the zeroing operation together with the compensation proposed in Section 4.3.2 (Fig. 4.7) such that $\delta_{\text{Comp}} = \delta + \lambda_{P_{\text{exp}}}(a_0)P_q$ and $P_{\text{Comp}} = P + P_q$.

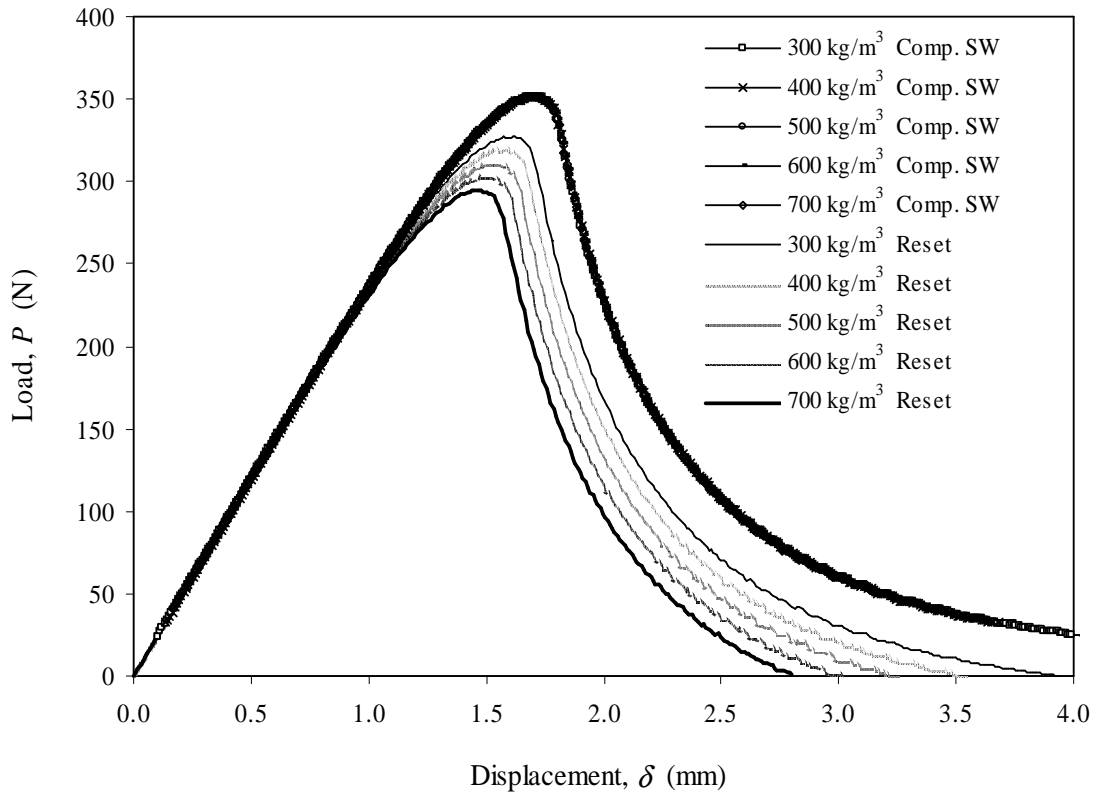


Figure A4.3.2. Load-displacement curves obtained in the cohesive crack modelling (Section 4.3.3.3) after reset and corresponding compensation as detailed in Section 4.3.3.1 (Fig. 4.7).

A4.4 Results of the exact self-weight compensation method

The compliance functions $\lambda_{PP}^*(\alpha)$ and $\lambda_{Pq}^*(\alpha)$ referred to in Section 4.3.3 ($\alpha = a/D$) were obtained through the best polynomial fitting of calculated in-plane strain elastic FE analysis (details of the *elastic analysis* in Appendix A3.2) for the interval $0 \leq \alpha \leq 0.85$ (Eqs. A4.4.1–12). The set of elastic properties used in the FEM model (Table A4.4.1) were chosen in order to provide the mean value of the multiplicative correction factor $\psi \cong 1.0$ (Eq. 4.14) (see ANNEXE). Figures A4.4.1 and A4.4.2 show the plotting of the unitary compliances $\lambda_{PP \text{ unit}}^*(\alpha)$ and $\lambda_{Pq \text{ unit}}^*(\alpha)$ obtained for each series.

As to the dimensionless energy release rate function $g(\alpha)$ defined in Section 1.4 [*i.e.*, $g(\alpha) = E' b [\partial \lambda(\alpha) / \partial \alpha] / 2$], the plane strain condition [*i.e.*, $E' = E^* / (1 - \nu^2)$] has been considered with the Effective Young modulus E^* evaluated using Eq. (A3.1.1) presented in Appendix A3.1. The compliance used to define $g(\alpha)$ (Eqs. A4.13-A4.18 and Fig. A4.4.3) is determined through the derivation of $\lambda_{PP}^*(\alpha)$.

$$\begin{aligned} [\lambda_{PP}^*(\alpha)]_{D=280} &= 9.59671 \times 10^3 \alpha^6 - 3.66348 \times 10^4 \alpha^5 + 5.81691 \times 10^4 \alpha^4 - \\ & 4.91200 \times 10^4 \alpha^3 + 2.32520 \times 10^4 \alpha^2 - 5.84743 \times 10^3 \alpha + 6.10288 \times 10^2 \end{aligned} \quad (\text{A4.4.1})$$

$$\begin{aligned} [\lambda_{PP}^*(\alpha)]_{D=210} &= 8.35491 \times 10^3 \alpha^6 - 3.19139 \times 10^4 \alpha^5 + 5.07026 \times 10^4 \alpha^4 - \\ & 4.28383 \times 10^4 \alpha^3 + 2.02891 \times 10^4 \alpha^2 - 5.10483 \times 10^3 \alpha + 5.33023 \times 10^2 \end{aligned} \quad (\text{A4.4.2})$$

$$\begin{aligned} [\lambda_{PP}^*(\alpha)]_{D=140} &= 8.43458 \times 10^3 \alpha^6 - 3.21856 \times 10^4 \alpha^5 + 5.10862 \times 10^4 \alpha^4 - \\ & 4.31244 \times 10^4 \alpha^3 + 2.04078 \times 10^4 \alpha^2 - 5.13072 \times 10^3 \alpha + 5.35342 \times 10^2 \end{aligned} \quad (\text{A4.4.3})$$

$$\begin{aligned} [\lambda_{PP}^*(\alpha)]_{D=70} &= 6.03281 \times 10^3 \alpha^6 - 2.30318 \times 10^4 \alpha^5 + 3.65718 \times 10^4 \alpha^4 - \\ & 3.08827 \times 10^4 \alpha^3 + 1.46190 \times 10^4 \alpha^2 - 3.67628 \times 10^3 \alpha + 3.83659 \times 10^2 \end{aligned} \quad (\text{A4.4.4})$$

$$\begin{aligned} [\lambda_{PP}^*(\alpha)]_{D=35} &= 8.10340 \times 10^3 \alpha^6 - 3.15527 \times 10^4 \alpha^5 + 5.11064 \times 10^4 \alpha^4 - \\ & 4.40235 \times 10^4 \alpha^3 + 2.12550 \times 10^4 \alpha^2 - 5.44987 \times 10^3 \alpha + 5.79596 \times 10^2 \end{aligned} \quad (\text{A4.4.5})$$

$$\begin{aligned} [\lambda_{PP}^*(\alpha)]_{D=23.3} &= 4.88855 \times 10^3 \alpha^6 - 1.86004 \times 10^4 \alpha^5 + 2.94397 \times 10^4 \alpha^4 - \\ & 2.47831 \times 10^4 \alpha^3 + 1.16971 \times 10^4 \alpha^2 - 2.93333 \times 10^3 \alpha + 3.05335 \times 10^2 \end{aligned} \quad (\text{A4.4.6})$$

$$\begin{aligned} [\lambda_{Pq}^*(\alpha)]_{D=280} &= 9.69787 \times 10^4 \alpha^6 - 3.67951 \times 10^5 \alpha^5 + 5.80815 \times 10^5 \alpha^4 - \\ & 4.87690 \times 10^5 \alpha^3 + 2.29604 \times 10^5 \alpha^2 - 5.74378 \times 10^4 \alpha + 5.96453 \times 10^3 \end{aligned} \quad (\text{A4.4.7})$$

$$\begin{aligned} [\lambda_{Pq}^*(\alpha)]_{D=210} &= 8.06985 \times 10^4 \alpha^6 - 3.06087 \times 10^5 \alpha^5 + 4.83041 \times 10^5 \alpha^4 - \\ & 4.05505 \times 10^3 \alpha^3 + 1.90876 \times 10^2 \alpha^2 - 4.77415 \times 10^4 \alpha + 4.95682 \times 10^3 \end{aligned} \quad (\text{A4.4.8})$$

$$\begin{aligned} [\lambda_{Pq}^*(\alpha)]_{D=140} &= 8.08082 \times 10^4 \alpha^6 - 3.06262 \times 10^5 \alpha^5 + 4.82967 \times 10^5 \alpha^4 - \\ & 4.051666 \times 10^5 \alpha^3 + 1.90594 \times 10^5 \alpha^2 - 4.76416 \times 10^4 \alpha + 4.94362 \times 10^3 \end{aligned} \quad (\text{A4.4.9})$$

$$\begin{aligned} [\lambda_{Pq}^*(\alpha)]_{D=70} &= 5.48090 \times 10^4 \alpha^6 - 2.07671 \times 10^5 \alpha^5 + 3.27413 \times 10^5 \alpha^4 - \\ & 2.74606 \times 10^5 \alpha^3 + 1.29148 \times 10^5 \alpha^2 - 3.22749 \times 10^4 \alpha + 3.34821 \times 10^3 \end{aligned} \quad (\text{A4.4.10})$$

$$\begin{aligned} [\lambda_{Pq}^*(\alpha)]_{D=35} &= 6.24033 \times 10^4 \alpha^6 - 2.36343 \times 10^5 \alpha^5 + 3.72472 \times 10^5 \alpha^4 - \\ & 3.12286 \times 10^5 \alpha^3 + 1.46820 \times 10^5 \alpha^2 - 3.66800 \times 10^4 \alpha + 3.80421 \times 10^3 \end{aligned} \quad (\text{A4.4.11})$$

$$\begin{aligned} [\lambda_{Pq}^*(\alpha)]_{D=23.3} &= 3.25487 \times 10^4 \alpha^6 - 1.58779 \times 10^5 \alpha^5 + 2.10025 \times 10^5 \alpha^4 - \\ & 2.01148 \times 10^5 \alpha^3 + 0.90221 \times 10^5 \alpha^2 - 2.00258 \times 10^4 \alpha + 2.70889 \times 10^3 \end{aligned} \quad (\text{A4.4.12})$$

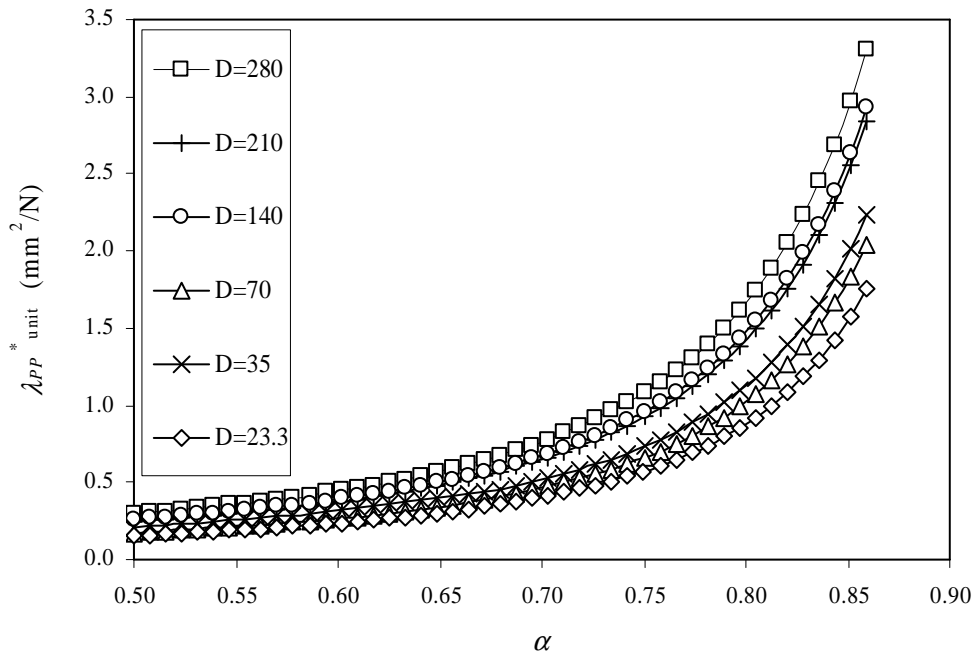


Figure A4.4.1 Plotting of unitary compliances [*i.e.*, $b \lambda_{PP}^*(\alpha)$] obtained through in-plane FEM computations (elastic strain analyses) for different values of $\alpha = a/D$ with the set of elastic properties duly chosen to retrieve, for each series (Table 4.1 and ANNEXE), the mean value of the experimental initial compliance (*i.e.*, $\psi \cong 1.0$ according to Eq. 4.14).

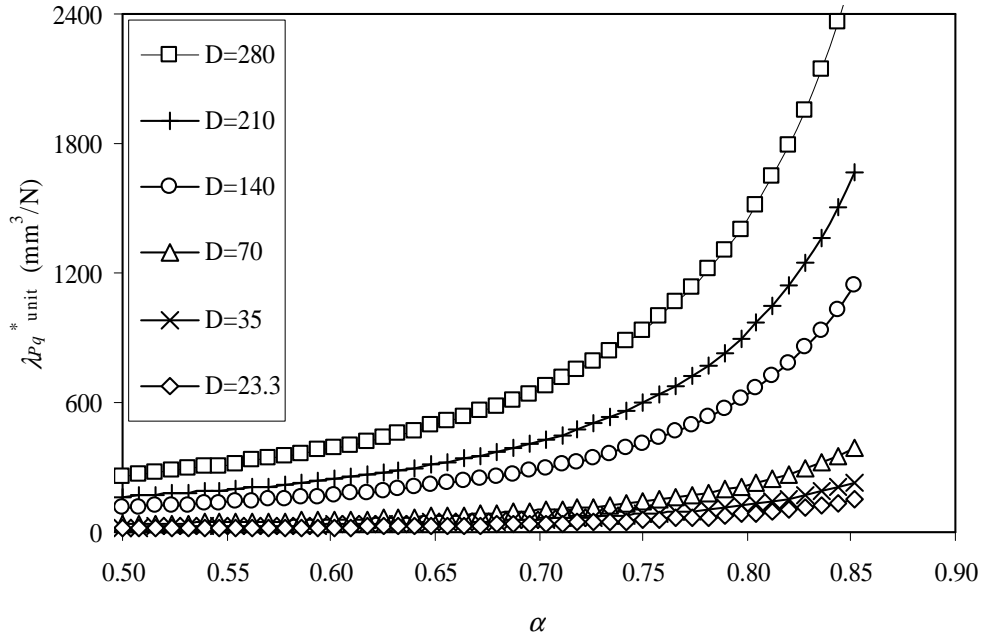


Figure A4.4.2 Plotting of unitary compliances [*i.e.*, $b\lambda_{pq}^*(\alpha)$] obtained through in-plane FEM computations (elastic strain analyses) for different values of $\alpha = a/D$ with the set of elastic properties duly chosen to retrieve, for each series (Table 4.1 and ANNEXE), the mean value of the experimental initial compliance (*i.e.*, $\psi \cong 1.0$ according to Eq. 4.14).

Table A4.4.1 Elastic properties of Norway spruce (based on Guitard D, 1987) used in the FEA for each series. E^* : Effective Young modulus for orthotropic materials (defined in Appendix 3.1)

Series	E_L (MPa)	E_R (MPa)	E_T (MPa)	ν_{TL}	ν_{RL}	ν_{TR}	G_{TL} (MPa)	G_{RT} (MPa)	G_{RL} (MPa)	E^* (MPa)
$D=280$	9 900	730	174.2	0.008	0.032	0.130	610	22	500	476.17
$D=210$	9 900	730	221.7	0.010	0.032	0.166	610	22	500	552.9
$D=140$	9 900	730	204.5	0.009	0.032	0.153	610	22	500	526.0
$D=70$	9 900	730	334.2	0.015	0.032	0.250	610	22	500	710.1
$D=35$	9 900	730	241.7	0.011	0.032	0.180	610	22	500	583.0
$D=23.3$	9 900	730	333.8	0.015	0.032	0.249	610	22	500	709.6

$$\begin{aligned}
 [g(\alpha)]_{D=280} = & 6.685535137 \times 10^7 \alpha^6 - 2.560020941 \times 10^8 \alpha^5 + \\
 & 4.074278636 \times 10^8 \alpha^4 - 3.447491086 \times 10^8 \alpha^3 + 1.635156777 \times 10^8 \alpha^2 - \\
 & 4.120693688 \times 10^7 \alpha + 4.309702616 \times 10^6
 \end{aligned} \tag{A4.4.13}$$

$$\begin{aligned}
 [g(\alpha)]_{D=210} = & 7.343019594 \times 10^7 \alpha^6 - 2.818596673 \times 10^8 \alpha^5 + \\
 & 4.494974567 \times 10^8 \alpha^4 - 3.809876119 \times 10^8 \alpha^3 + 1.809439810 \times 10^8 \alpha^2 - \\
 & 4.564344946 \times 10^7 \alpha + 4.776648717 \times 10^6
 \end{aligned} \tag{A4.4.14}$$

$$\begin{aligned}
 [g(\alpha)]_{D=140} = & 6.859530414 \times 10^7 \alpha^6 - 2.632196342 \times 10^8 \alpha^5 + \\
 & 4.197498928 \times 10^8 \alpha^4 - 3.558413921 \times 10^8 \alpha^3 + 1.690718668 \times 10^8 \alpha^2 - \\
 & 4.267585249 \times 10^7 \alpha + 4.469871586 \times 10^6
 \end{aligned} \tag{A4.4.15}$$

$$\begin{aligned}
 [g(\alpha)]_{D=70} = & 6.495297271 \times 10^7 \alpha^6 - 2.489753173 \times 10^8 \alpha^5 + \\
 & 3.965903123 \times 10^8 \alpha^4 - 3.358186428 \times 10^8 \alpha^3 + 1.593684456 \times 10^8 \alpha^2 - \\
 & 4.017756677 \times 10^7 \alpha + 4.202970175 \times 10^6
 \end{aligned} \tag{A4.4.16}$$

$$\begin{aligned}
 [g(\alpha)]_{D=35} = & 6.981172641 \times 10^7 \alpha^6 - 2.693998639 \times 10^8 \alpha^5 + \\
 & 4.314919316 \times 10^8 \alpha^4 - 3.669310399 \times 10^8 \alpha^3 + 1.746528547 \times 10^8 \alpha^2 - \\
 & 4.410580853 \times 10^7 \alpha + 4.616017443 \times 10^6
 \end{aligned} \tag{A4.4.17}$$

$$\begin{aligned}
 [g(\alpha)]_{D=23.3} = & 3.788197689 \times 10^7 \alpha^6 - 1.435002981 \times 10^8 \alpha^5 + \\
 & 2.261799914 \times 10^8 \alpha^4 - 1.897243572 \times 10^8 \alpha^3 + 8.928515735 \times 10^7 \alpha^2 - \\
 & 2.234266747 \times 10^7 \alpha + 2.322045177 \times 10^6
 \end{aligned} \tag{A4.4.18}$$

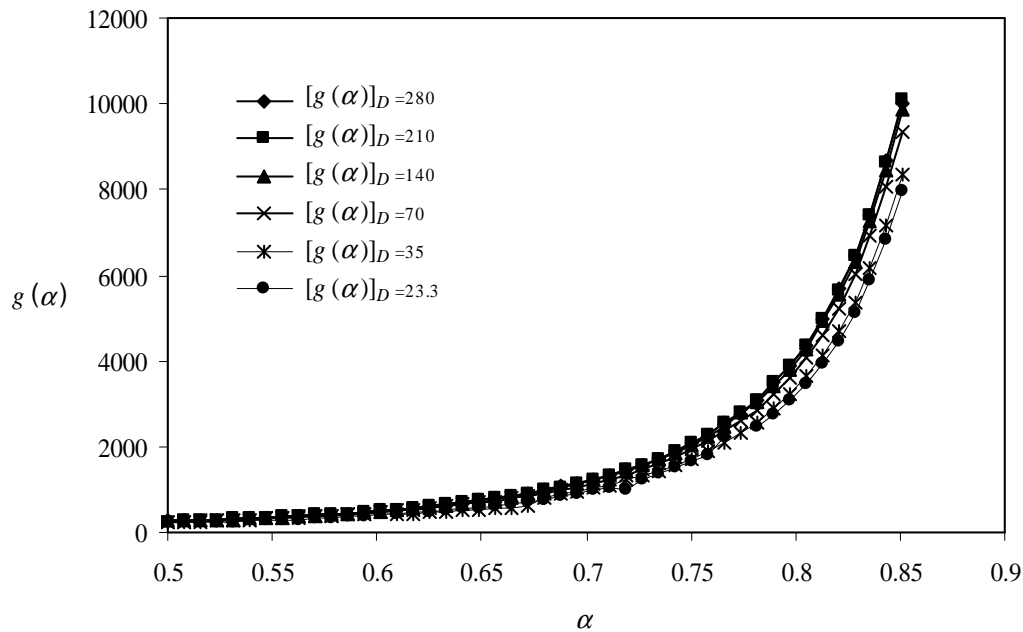


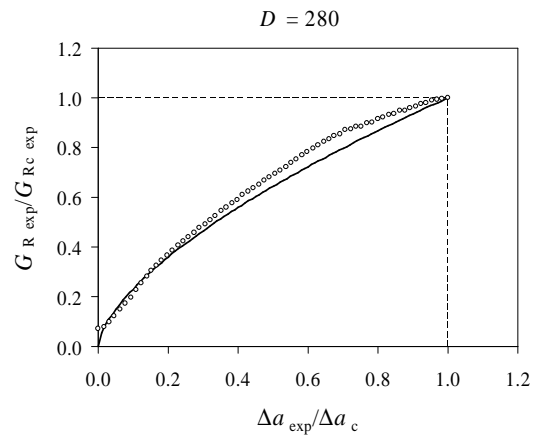
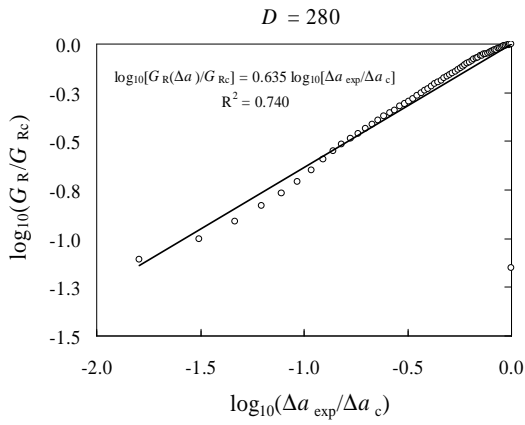
Figure A4.4.3 Plotting of the dimensionless energy release rate function for each series first presented in Table 4.1.

It should be emphasised that the evaluation of the dimensionless energy release rate function $g(\alpha)$ for each specimen size D , is barely justified by the fact that it has been

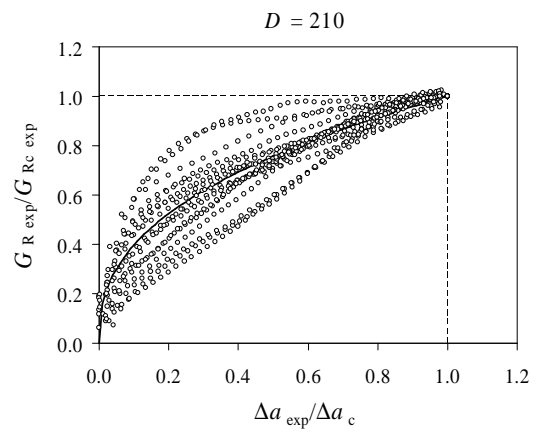
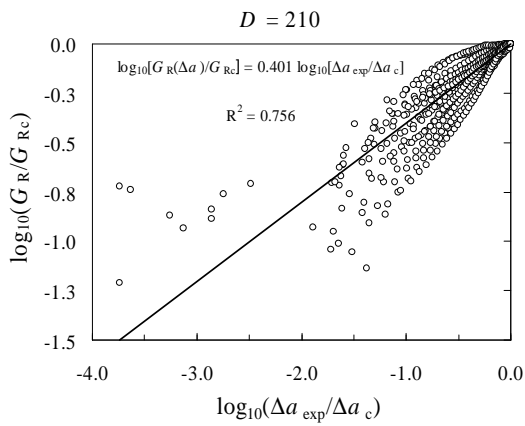
noticed that a strong scattering on the unitary compliances $\lambda_{PP \text{ unit}}(a_0)$ does exist in the experimental data (Fig. 4.19). As $g(\alpha)$ is a function of the material elastic properties (through the Effective Young modulus E^*), this procedure aims at introducing the required correction necessary for the present size effect study.

As previously described in Section 3.3, the numerical protocol establishes the polynomial fitting through the rising part of the experimental R -curves [*i.e.*, $G_R(\alpha_0)/G_{Rc} < G_R(\alpha)/G_{Rc} < 1$] which exhibit an undoubted plateau (Fig. 4.20). The curvature exponent β (of each series' R -curve) is thus revealed from the slope of the linear regression plot which passes through the graph origin (on the left side of Fig. A4.4.4). Table 4.2 resumes the set of curvature exponents β obtained for each experimental series. Pursuing the protocol, a plotting of the energy release rate G_R as a function of the crack length increment Δa (Eq. 3.1) has consequently been performed for each series, using the corresponding curvature exponent value β shown in Fig. A4.4.4 (on the right side).

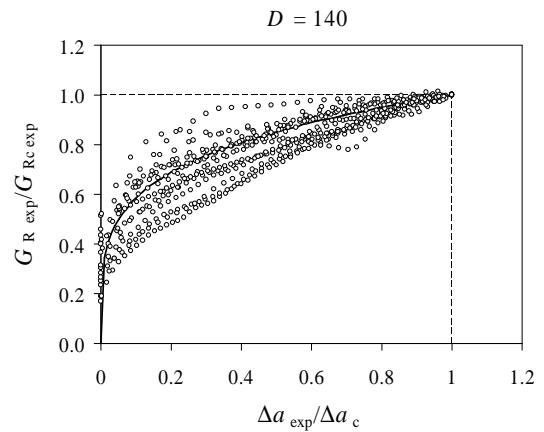
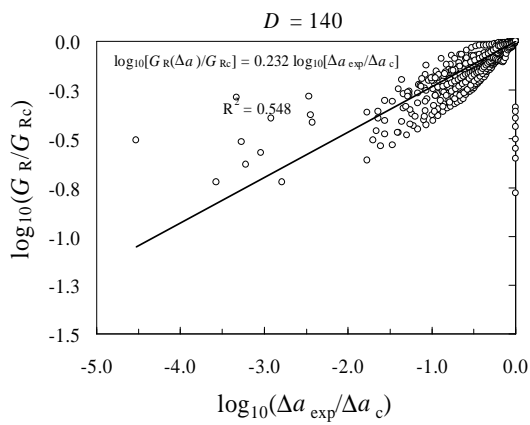
The interception between $g'/g(\alpha)$ and $G'_R/G_R(\alpha)$ shown in Figs. A4.4.5-10 provides the estimate of the single solution α_{u^*} (Section 3.2.1) shown in Table 4.2. If one excludes the series of the largest size (*i.e.*, $D=280$ mm, for non-statistical meaning) and calculate the average value taking the remaining five series in Table 4.2, the resulting solution is yields $\alpha_{u^*} = 0.536$ (COV = 2.33%). One should recognise that the value obtained for the single solution α_{u^*} (in each series) is strongly influenced by the critical energy release rate G_{Rc} obtained for each series (through β in Eq. 3.7). Therefore, if G_{Rc} in the (considered) greatest series (*i.e.*, $D=210$ mm) had been less affected by scattering, then the reliance in the obtained value (*i.e.*, α_{u^*}) would have been higher. Accordingly, working out the size limits characterizing the domain of α_{u^*} attained for each experimental series (*i.e.*, D_{\min} and D_c through Eqs. 3.9 and 3.10), one obtains the values shown in Table A4.4.2. This values are to be used in the scaling study of the relative crack length at the peak load $\alpha_u(D)$ and in the size effect on the nominal strength $\sigma_N(D)$, presented in Section 4.4.



(a)



(b)



(c)

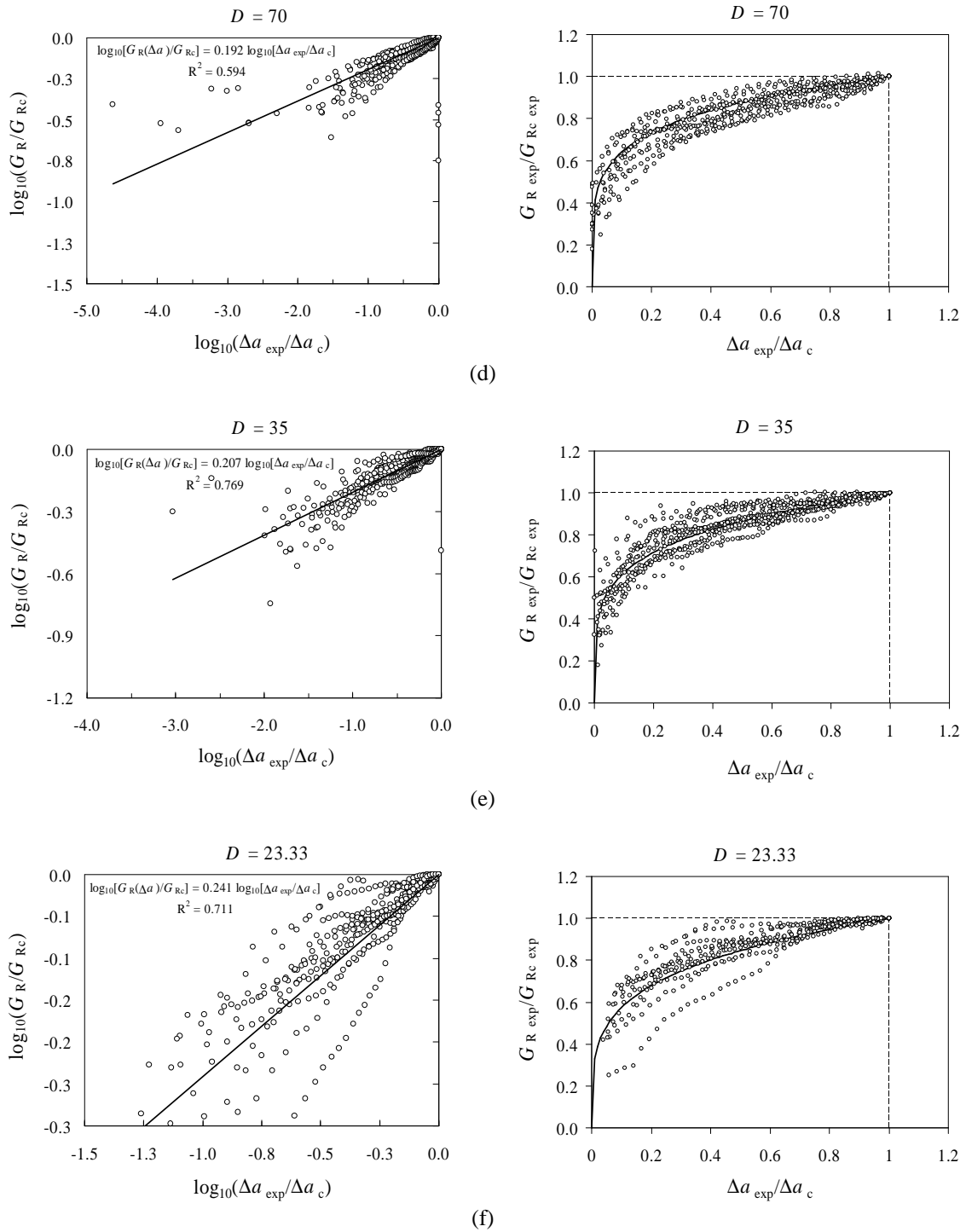


Figure A4.4.4 Linear regression plot performed on the rising part of the R -curve (as in Section 3.3) and corresponding normalized R -curve (through Eq. 3.1) for the data got in the experiments (with undoubted plateau on the R -curve). Graphics (a) to (f) correspond to characteristic sizes of $D=280$ to $D=23.33$ mm printed in Table 4.1.

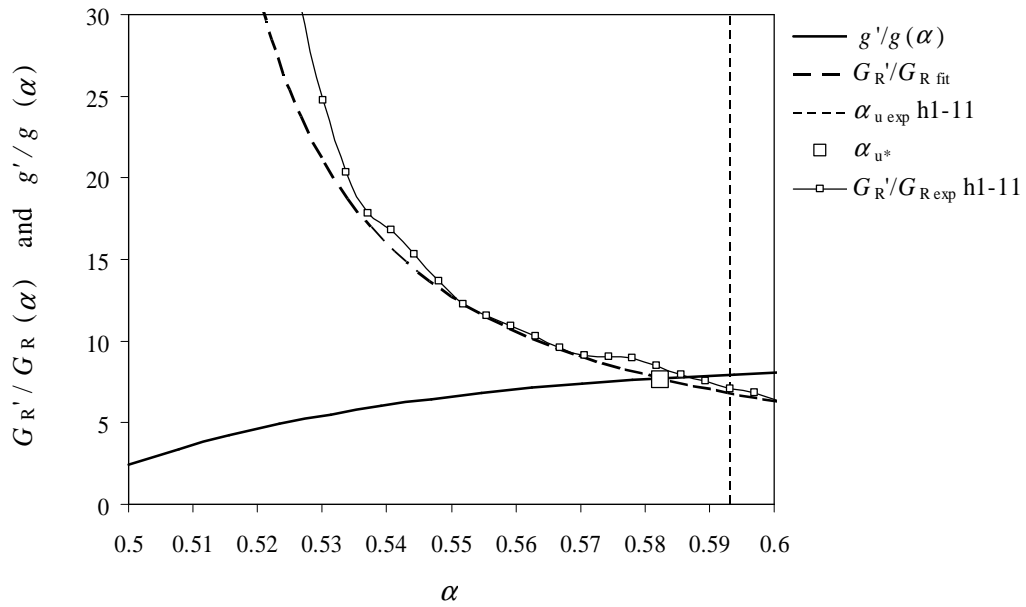


Figure A4.4.5 Plotting of Eq. (3.6) used to estimate α_{u^*} . Comparison with the plotting of Eq. (3.7) obtained from the R -curve computed for specimen size $D=280$ mm (see Fig. 4.20 a).

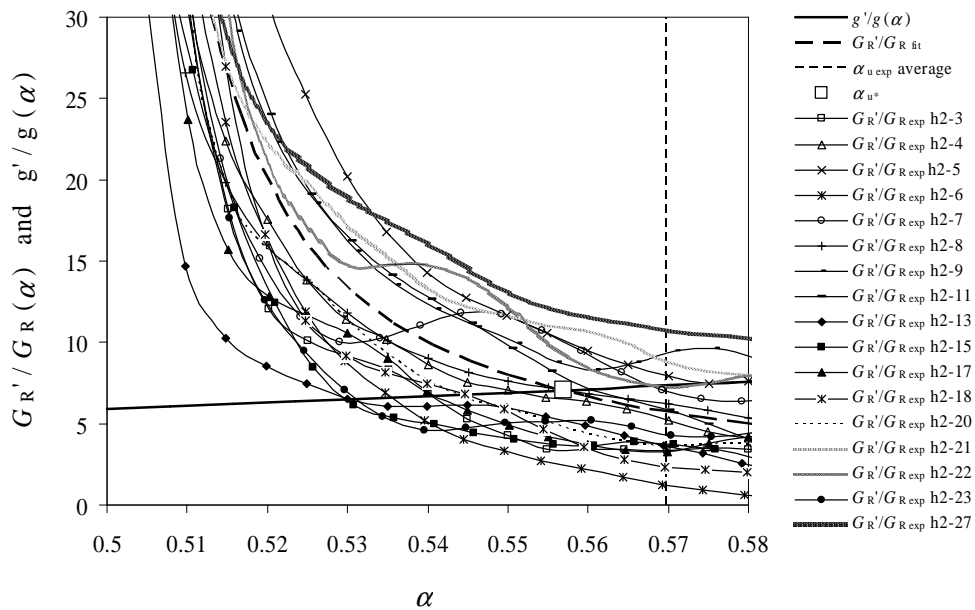


Figure A4.4.6 Plotting of Eq. (3.6) used to estimate α_{u^*} . Comparison with the plotting of Eq. (3.7) obtained from the R -curve computed for specimen size $D=210$ mm (see Fig. 4.20 b).

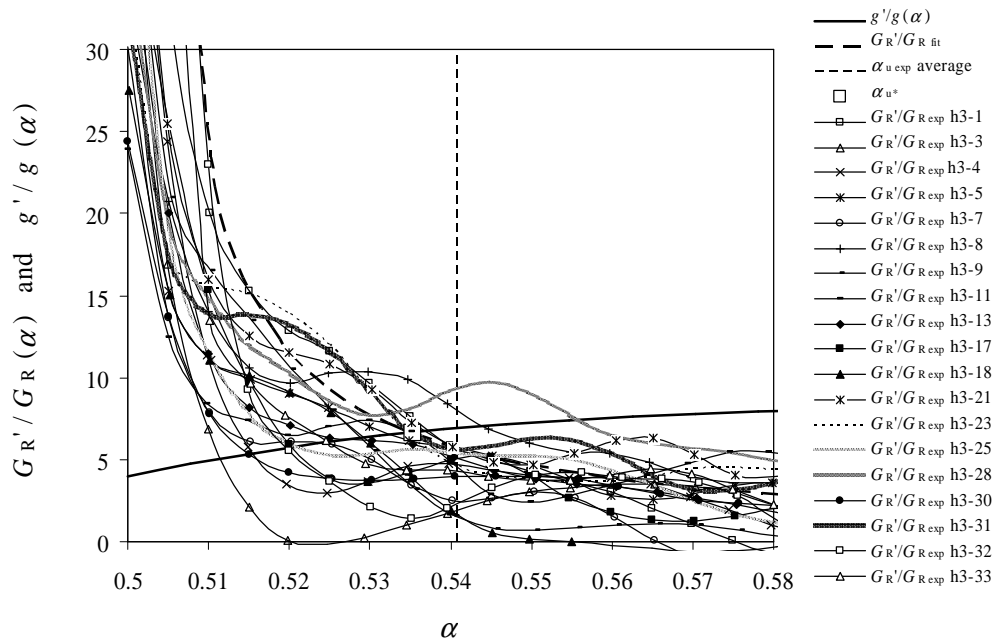


Figure A4.4.7 Plotting of Eq. (3.6) used to estimate α_{u^*} . Comparison with the plotting of Eq. (3.7) obtained from the R-curve computed for specimen size $D=140$ mm (see Fig. 4.20 c).

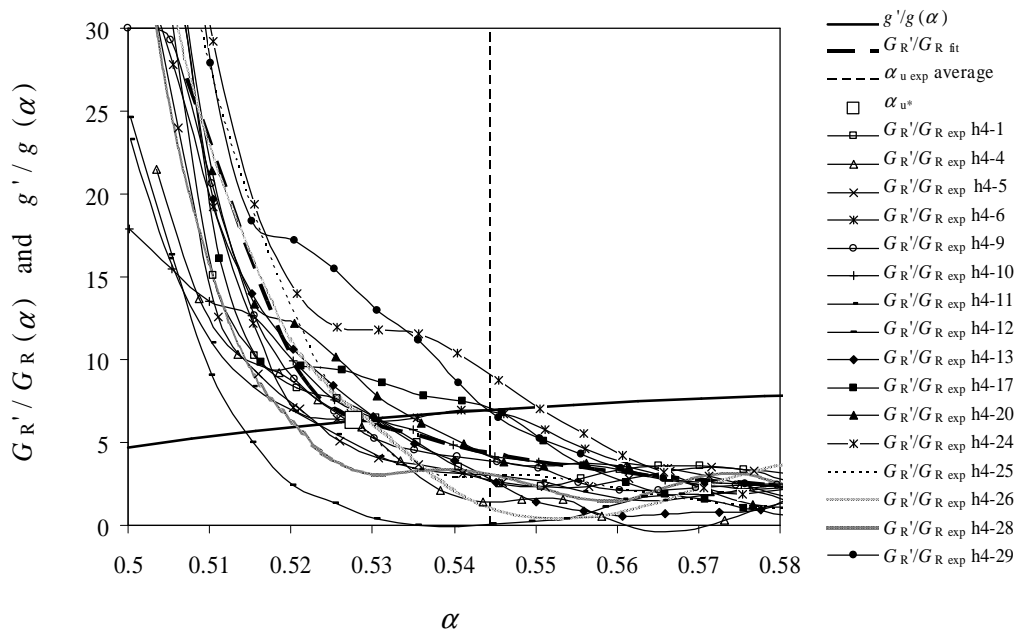


Figure A4.4.8 Plotting of Eq. (3.6) used to estimate α_{u^*} . Comparison with the plotting of Eq. (3.7) obtained from the R-curve computed for specimen size $D=70$ mm (see Fig. 4.20 d).

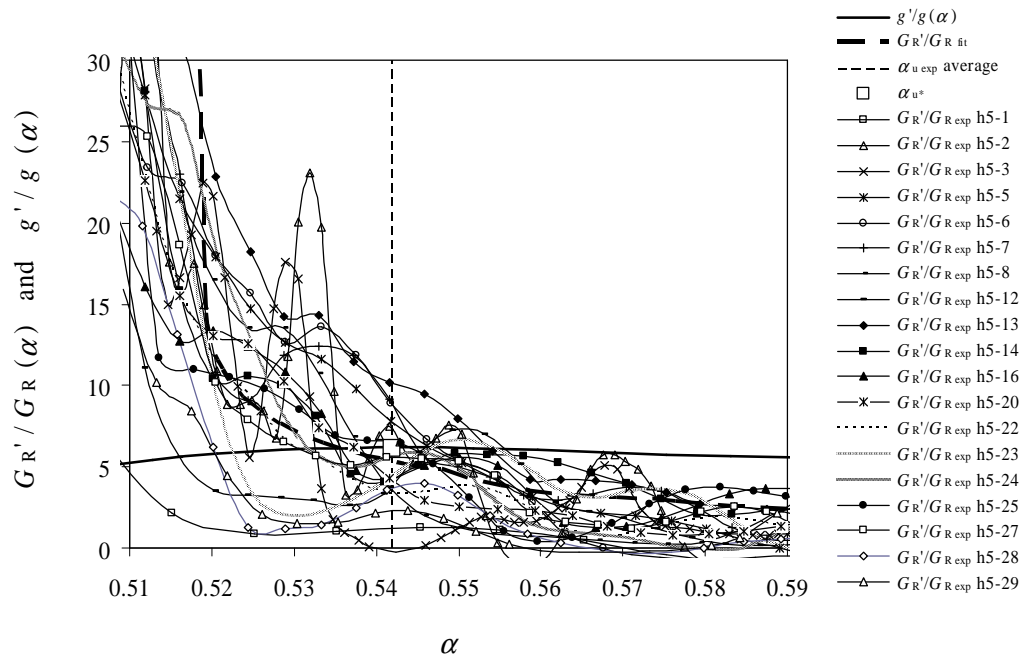


Figure A4.4.9 Plotting of Eq. (3.6) used to estimate α_{u^*} . Comparison with the plotting of Eq. (3.7) obtained from the R -curve computed for specimen size $D=35$ mm (see Fig. 4.20 e).

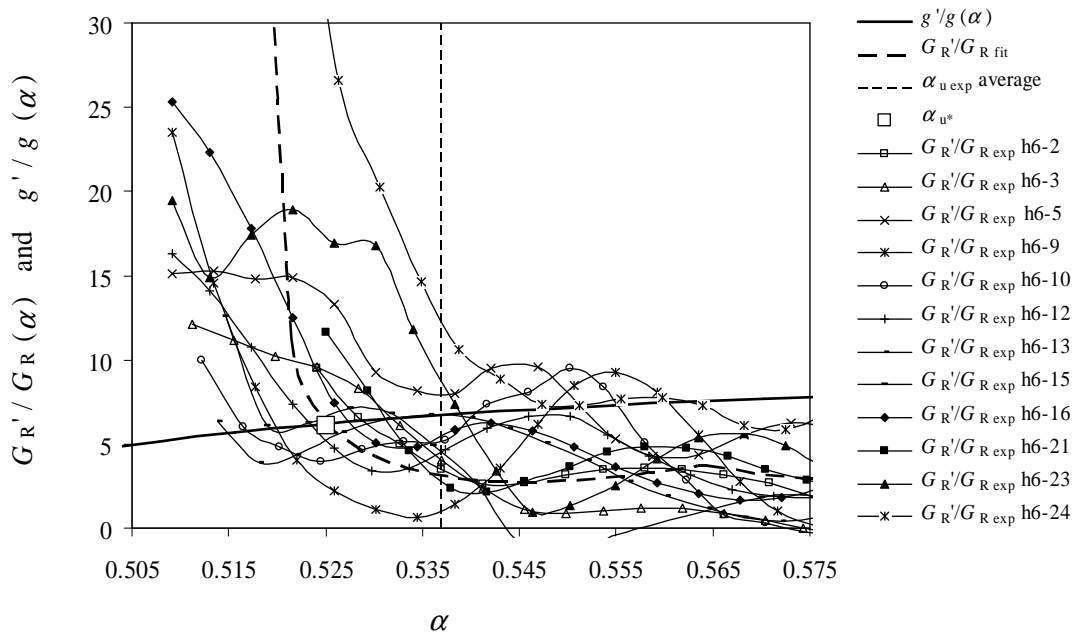


Figure A4.4.10 Plotting of Eq. (3.6) used to estimate α_{u^*} . Comparison with the plotting of Eq. (3.7) obtained from the R -curve computed for specimen size $D=23.3$ mm (see Fig. 4.20 f).

Table A4.4.2 Parameters obtained in the size effect study for the experimental data first shown in Table 4.1. Exhibited parameters: a_c characteristic equivalent crack length (mean value); Δa_c : characteristic equivalent crack length increment ($\Delta a_c = a_c - a_0$), β : Curvature exponent of the R -curve; $\phi = G_{RC} / \Delta a_c^\beta$ as in Eq. (3.1); α_{u^*} : single solution of α_u ; D_{\min} and D_c : limits characterizing the domain of α_{u^*} (Eqs. 3.9 and 3.10); $D_1^* = [g(\alpha_{u^*}) / g(\alpha_0)]^{1/\beta} D_c$ as in Eq. (3.19)

Series	a_c (mm)	Δa_c (mm)	β	ϕ (J/m ^{2+β)}	α_{u^*}	D_{\min} (mm)	D_c (mm)	D_1^* (mm)
$D=280$	208.23	68.26	0.64	1900.59	0.582	136.52	828.40	1541.40
$D=210$	153.50	48.50	0.40	1127.31	0.557	97.00	850.88	1660.10
$D=140$	93.19	23.19	0.23	463.46	0.535	46.38	656.94	740.44
$D=70$	47.80	12.80	0.19	416.58	0.528	25.60	462.09	409.01
$D=35$	22.43	4.93	0.21	521.79	0.537	9.86	133.24	255.44
$D=23.3$	15.41	3.74	0.24	588.89	0.525	7.48	149.60	163.11

A4.5 Statistics involving the experiments

The plotting of Fig. A4.5.1 shows the measured densities at 12% EMC of the set of specimens used in the experiments which provided an undoubted plateau on the R -curve (consult ANNEXE at the end of this Thesis). In the following, graphs exhibiting the mean values of the ultimate load, P_u (Fig. A4.5.2), the relative crack length associated to P_u (Fig. A4.5.3), the energy release rate associated to P_u [*i.e.*, $G_R(\alpha_u)$] (Fig. A4.5.4) and the relative crack length associated to the critical energy release rate, G_{Rc} [*i.e.*, α_c] (Fig. A4.5.5) are shown.

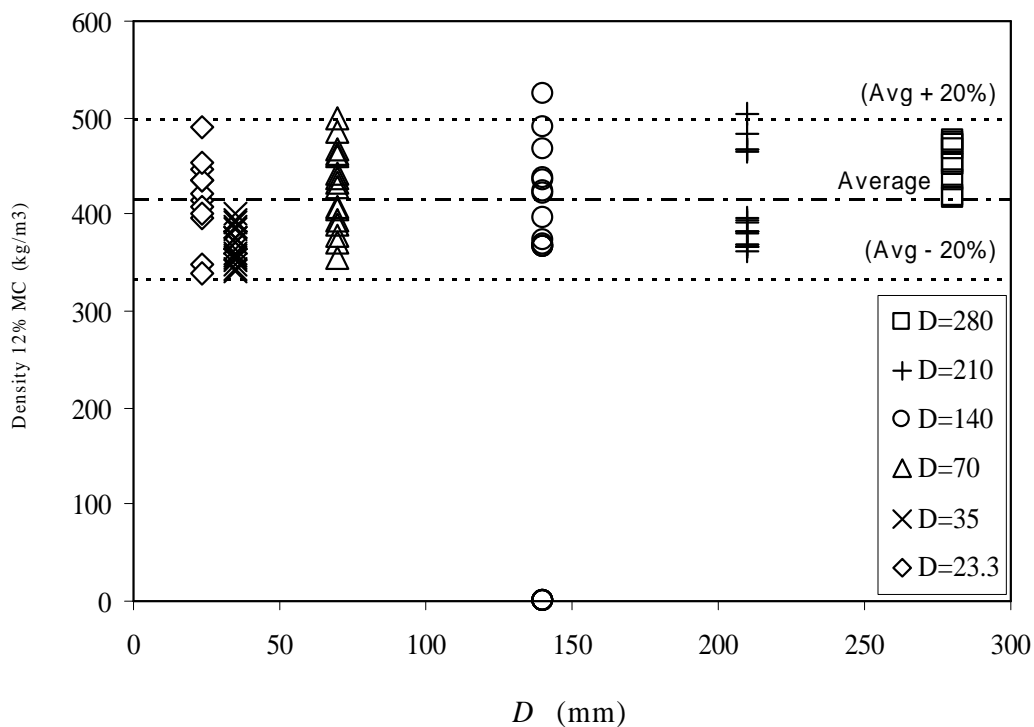


Figure A4.5.1 Measured densities at 12% EMC (*i.e.*, basic densities) in the totality of specimens (See ANNEXE) which exhibited an undoubted plateau on the *Resistance*-curve.

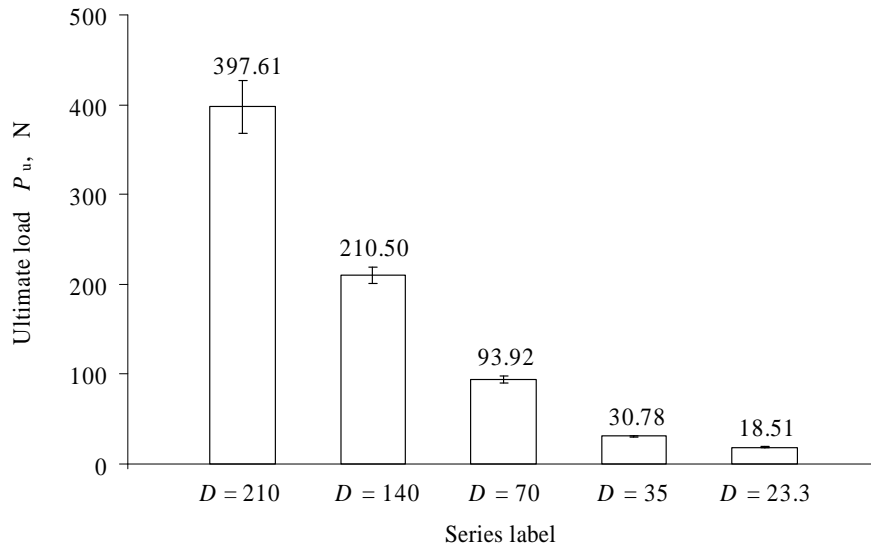


Figure A4.5.2 Mean values of the ultimate load P_u obtained in the experiments (See ANNEXE) for the specimens which exhibited an undoubted plateau on the R -curve.

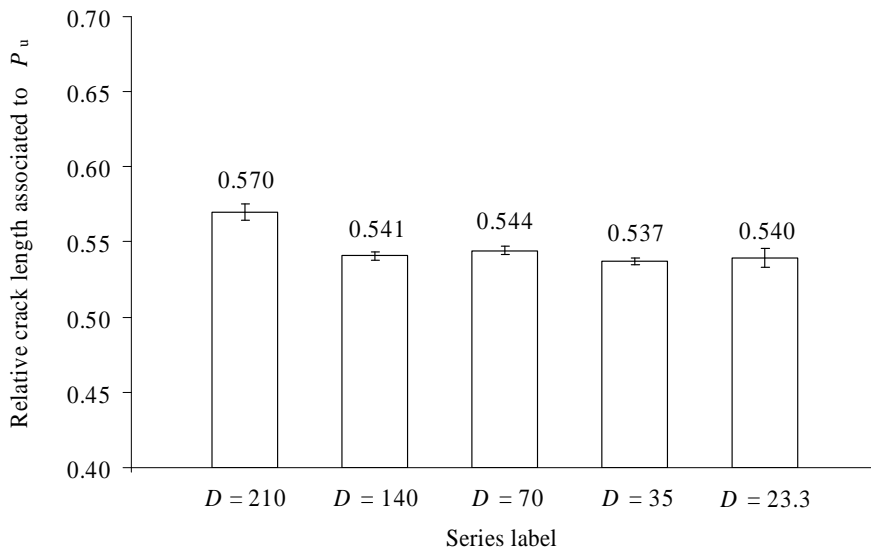


Figure A4.5.3 Mean values of the relative crack length associated to the ultimate load α_u obtained in the experiments (See ANNEXE) for the specimens which exhibited an undoubted plateau on the R -curve.

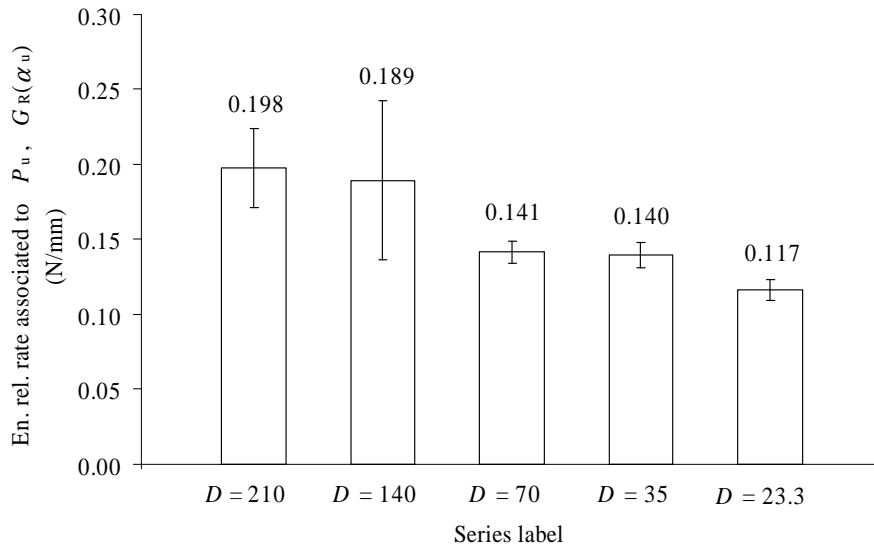


Figure A4.5.4 Mean values of the energy release rate associated to the ultimate load $G_R(\alpha_u)$ obtained in the experiments (See ANNEXE) for the specimens which exhibited an undoubted plateau on the R -curve.

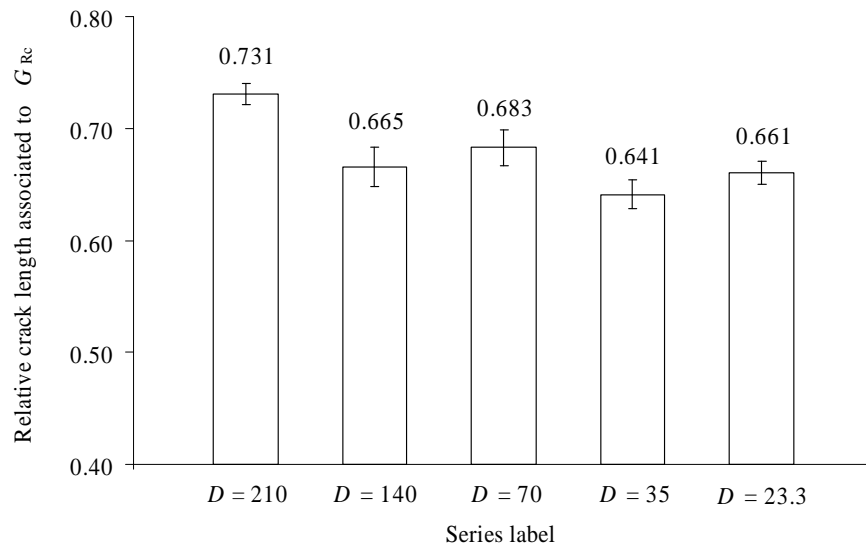


Figure A4.5.5 Mean values of the relative crack length associated to the critical energy release rate G_{Rc} , (*i.e.*, α_c) obtained in the experiments (See ANNEXE) for the specimens which exhibited an undoubted plateau on the R -curve.

References

- Atkins AG and Mai YW (1985). Elastic and Plastic Fracture. Ellis Horwood, UK ISBN 0-85312-562-7.
- Barenblatt G I (1962). The mathematical theory of equilibrium of cracks in brittle fracture. *Adv. Appl. Mech.*, **7**, 55-129.
- Bažant ZP (1984). Size Effect in Blunt Fracture: Concrete Rock, Metal. *J. Eng. Mech., Am. Soc. Civ. Eng.*, **110** [4] 518-35.
- Bažant ZP (1985). Mechanics of fracture and progressive cracking in concrete structures. In *Fracture Mechanics of Concrete: Structural Application and Numerical Calculation*. GC Sih and A. DiTommaso, eds., Martinus Nijhoff, Dordrecht, pp. 1-94.
- Bažant ZP and Mohammad T. Kazemi (1990). Size Effect in Fracture of Ceramics and its use to determine Fracture Energy and Effective Process Zone Length. *J. Am. Ceram. Soc.* **73** [7] 1841-53.
- Bažant ZP and Cedolin L (1991). *Stability of structures: Elastic, Inelastic, Fracture and Damage Theories*. Oxford University Press, New York, USA.
- Bažant ZP (1993). Scaling laws in mechanics of failure. *ASCE Journ Engrg Mech.* **119**(9). 1828-1844.
- Bažant ZP (1997 a) Scaling of structural failure. *Appl Mech Rev.* **50**(10): 593-627, and references therein.
- Bažant ZP (1997 b). Fracture of brittle solids (2nd ed). *Applied Mechanics Review*, **50**(10):593-627. and references therein.
- Bažant ZP (1997 c). Scaling of quasibrittle fracture: asymptotic analysis. *Int Journ Fract* **83**: 19-40.
- Bažant ZP and Li Y-N (1997). Cohesive crack with rate-dependent opening and viscoelasticity: I. Mathematical model and scaling. *Int Journ Fract* **86**: 247-265.
- Bažant ZP and Planas J (1998). *Fracture and size effect in concrete and other quasibrittle materials*. CRC Press LLC. ISBN 0-8493-8284-X.
- Bažant ZP (2002). Concrete fracture models: testing and practice. *Eng Fract Mech.* **69**:165-205.
- Jirásek M and Bažant ZP (2002). *Inelastic Analysis of Structures*. Wiley, London.
- Bažant ZP (2004). Scaling theory for quasibrittle structural failure. Special series of Inaugural Articles of the National Academy of Sciences (PNAS). Vol. **101**: no. 37. 13400-13407.
- Bodig J. and Jayne BA (1982). *Mechanics of Wood and Wood Composites*. Van Nostrand Reinhold. NY.
- Boström L (1992). Method for determination of the softening behaviour of wood and the applicability of a nonlinear fracture mechanics model. *Universitatis Gothorum*; CODEN: LUTVDG/(TVBM-1012) 1.

- Chapra SC and Canale RP (1985). Numerical Methods for Engineers with Personal Computer Applications. McGraw-Hill. ISBN 0-07-010664-9: 112-121.
- Coureau J-L, Morel S, Gustafsson PJ, Lespine C (2006). Influence of the fracture softening behaviour of wood on load-COD curves and R-curve. *Mat and Struct*. 40: 97-106.
- Datoo MH (1991). Mechanics of fibrous composites. Elsevier Science Publishers Ltd. ISBN 1-85166-600-1.
- de Moura MFSF, Gonc_alves JPM, Marques AT, Castro PMST (1997). Modelling compression failure after low velocity impact on laminated composites using interface elements. *J Comp Mat*; 31:1462–79.
- Dourado N, Morel S, de Moura MFSF, Valentin G, Morais J (2008). Comparison of fracture properties of two wood species through cohesive crack simulations. *Composites: Part A* 39: 415–427.
- Dugdale DS. (1960). Yielding of steel sheets containing slits. *J Mech Phys Solids*; 8:100–8.
- Ebrahimi ME, Chevalier J and Fantozzi G (2003). *R*-curve evaluation and bridging stress determination in alumina by compliance analysis. *J Europ Cer Soc*. 23: 943–949.
- Elices M, Guinea, GV, Gómez J, Planas J, (2002). The cohesive zone model: advantage, limitations and challenges. *Eng Fract Mech*; 69,137-63.
- Ferreira LET, Bittencourt TN, Sousa JLOA and Gettu R (2002). *R*-curve behavior in notched beam tests of rocks. *Eng Fract Mech*; 69: 1845–1852.
- Fett T, Munz D, Geraghty RD and White KW (2000). Influence of specimen geometry and relative crack size on the *R*-curve. *Eng Fract Mech*; 66: 375–386.
- Gettu R, B Bažant ZP and Karr ME (1990). Fracture properties and brittleness of high-strength concrete. *ACI Materials Journal* 87 (Nov.-Dec.): 608-618.
- Guitard D (1987). *Mécanique du matériaux bois et composites*. Cepadues-Editions. ISBN 2.85428.152.7: 108-123.
- Gustafsson PJ (1988). A Study of Strength of Notched Beams. Paper 21-10-1. In Proc. of CIB-W18A Meeting, Parksville, Canada.
- Hillerborg A, Modeer M, Petersson PE (1976). Analysis of crack formation and crack growth in concrete by means of fracture mechanics and finite elements. *Cem Concr Res*; 6:773–82.
- Hillerborg A (1991). Application of the fictitious crack model to different types of materials. *Int J Fract*; 51:95–102.
- Irwin GR (1960). *Structural Mechanics*. Pergamon Press, London.
- Krafft JM, Sullivan AM and Boyle RW (1961). Effect of dimensions on fast fracture instability of notched sheets. In Proc. of the Crack-Propagation Symposium. Vol. 1. pp. 8-28.
- Lawn BR (1993). *Fracture of Brittle Solids*, second ed. Cambridge University Press, Cambridge, England.

- Lespine I (2007). Influence of the structure geometry on the fracture properties of quasibrittle materials (PhD Thesis). University of Bordeaux I. France. (Available in French).
- Michalewicz Z (1999). Genetic Algorithms + Data Structures = Evolution Programs, Springer-Verlag, pp. 33-80.
- Morel S, Bouchaud E, Schmittbuhl J, Valentin G (2002 a). R-curve behaviour and roughness development of fracture surfaces. *Int J Fract*;114 (4), 307-325.
- Morel S, Bouchaud E, Valentin G (2002 b). Size effect in fracture: roughening of crack surfaces and asymptotic analysis. *Phys. Rev. B* 64 (104101), 1-8.
- Morel S, Mourot G, Schmittbuhl J (2003). Influence of the specimen geometry on the R-curve behaviour and roughening of fracture surfaces . *Int J Fract*;121, 23-42.
- Morel S, Dourado N, Valentin G and Morais J (2005). Wood: a quasibrittle material. R-curve behavior and peak load evaluation. *Int J Fract*; 131: 385-400.
- Morel S (2007). R-curve and size effect in quasibrittle fractures: Case of notched structures. *Int Journ Sol and Struct.* 44: 4272-4290.
- Morel S (2008). Size effect in quasibrittle fracture: derivation of the energetic Size Effect Law from equivalent LEFM and asymptotic analysis. Submitted to *Int J Fract*.
- Morel S, Lespine C, Coureau J-L, Planas J, Dourado N (2008). R-curve and cohesive crack properties in quasibrittle failure. Preprint to submit *Int J Sol and Str*.
- Pereira JL (2004). Mechanical behaviour of wood under traction along anatomic directions of symmetry. MSc Thesis, UTAD, Portugal (available in Portuguese).
- Petersson PE (1981). Crack growth and development of fracture zone in plain concrete and similar materials. Report No. TVBM-1006, Division of Building Materials, Lund Institute of Technology, Lund, Sweden.
- Planas J, Elices M, Ruiz G (1993). The equivalent elastic crack: 2. X-Y equivalences and asymptotic analysis. *Int J Fract*; 61:231-46.
- Planas J, Elices M, Guinea GV, Gómez FJ, Cendón DA, Arbilla I (2003). Generalizations and specializations of cohesive crack models. *Eng Fract Mech*; 70:1759-1776.
- Planas J, Elices M, Guinea GV, Gómez FJ, Cendón DA, Arbilla I (2003). Generalizations and specializations of cohesive crack models. *Engng Fract Mech*; 70:1759-76.
- Rice JR (1972). The line spring model for surface flaws. In: Sedlow JL, editor. *The surface crack: physical problems and computational solutions*. ASME.
- Smith I, Landis E and Gong M (2003). *Fracture and Fatigue in Wood*. John Wiley & Sons; ISBN 0-471-48708-2.
- Smith I and Vasic S (2003). Fracture behaviour of softwood. *Mech of Mater*, 35: 803-815.
- Stanzl-Tschegg SE, Tan DM, Tschegg EK (1995). New splitting method for wood fracture characterization. *Wood Sci Tech*; 29:31–50.
- Tanaka K, Akiniwa Y, Kimachi H and Kita Y (2003). R-curve behavior in fracture of notched porous ceramics. *Eng Fract Mech.* 70: 1101 -1113.

- Tsoumis G (1991). *Science and Technology of Wood*. Van Nostrand Reinhold. NY ISBN 0-442-23985-8.
- Vasic S, Smith I (2002). Bridging crack model for fracture of spruce. *Eng Fract Mech.* 69: 745-760.
- Xavier J, Garrido N, Oliveira M, Morais J, Camanho P, Pierron F (2004). A comparison of shear characterization of pinus pinaster Ait. with the Iosipescu and off-axis shear test methods. *Compos. Part A*; 35:7-8, pp. 827-840.
- Wang J. (2006). Cohesive zone model of intermediate crack-induced debonding of FRP-plated concrete beam. *Int Journ Sol and Struct*; 43:6630-6648.
- Weibull W (1939). Phenomenon of rupture in solids. *Proc. Royal Swedish Inst. of Eng. Res. (Ingenioersvetenskaps Akad. Handl.)* 153: 1-55.

Annexe

ANNEXE

In this ANNEXE a complete list of the experimental parameters is revealed organized according to the specimens' characteristic size D first printed in Table 4.1. As previously defined, when initially mentioned, $\lambda_{\text{exp}}(a_0)$: initial experimental unloading compliance, P_u : ultimate load, ψ : multiplicative correction factor, α_u : relative crack length corresponding to P_u , G_{Ru} : energy release rate associated to P_u , α_c : relative characteristic crack length, P_c : load corresponding to α_c , l_{Plat} : extension of the plateau in the R -curve, G_{Rc} : critical energy release rate.

Table A1 Parameters obtained in the experiments regarding series with the characteristic size $D=280$ mm (according to Table 4.1)

Label	D (mm)	$\lambda_{\text{exp}}(a_0)$ (10^{-3} mm/N)	Density (12% MC) (kg/m^3)	P_u (N)	ψ	α_u	G_{Ru} (N/mm)	α_c	P_c (N)	l_{Plat} (mm)	G_{Rc} (N/mm)
h1-1	280	3.21	471.79	487.00	1.19	0.583	0.140	-	-	-	-
h1-2	280	4.57	417.31	398.45	0.88	0.628	0.210	-	-	-	-
h1-3	280	3.80	467.66	337.10	0.94	0.564	0.080	-	-	-	-
h1-4	280	5.00	419.90	469.95	1.24	0.557	0.180	-	-	-	-
h1-5	280	4.26	434.40	438.75	0.68	0.594	0.170	-	-	-	-
h1-6	280	3.14	475.50	412.70	1.11	0.563	0.090	-	-	-	-
h1-7	280	2.95	474.62	545.80	1.23	0.584	0.160	-	-	-	-
h1-8	280	3.24	450.12	630.84	0.67	0.579	0.220	-	-	-	-
h1-9	280	2.61	451.34	562.65	1.00	0.599	0.170	-	-	-	-
h1-10	280	3.17	471.11	379.20	1.00	0.592	0.100	-	-	-	-
h1-11	280	4.66	454.19	448.75	1.19	0.593	0.200	0.744	267.96	28.4	0.341
Qtty	11										
Minimum		2.61	417.31	337.10	0.67	0.56	0.080				
Maximum		5.00	475.50	630.84	1.24	0.63	0.220				
Average		3.69	453.45	464.65	1.01	0.58	0.156				
Cov (%)		21.85	21.44	18.75	20.35	3.38	30.973				

Table A2 Parameters obtained in the experiments regarding series with the characteristic size $D=210$ mm (according to Table 4.1)

Label	D (mm)	$\lambda_{\text{exp}}(a_0)$ (10^{-3} mm/N)	Density (12% MC) (kg/m^3)	P_u (N)	ψ	α_u	G_{Ru} (N/mm)	α_c	P_c (N)	l_{Plat} (mm)	G_{Rc} (N/mm)
h2-3	210	4.71	367.19	320.00	1.15	0.555	0.126	0.700	220.66	14.9	0.208
h2-4	210	5.20	392.34	321.79	1.27	0.560	0.144	0.726	201.75	25.7	0.260
h2-5	210	3.44	466.42	622.09	0.84	0.615	0.461	0.735	464.27	14.8	0.803
h2-6	210	4.86	361.27	364.45	1.18	0.549	0.157	0.696	210.74	30.3	0.189
h2-7	210	3.19	502.72	543.55	0.78	0.579	0.264	0.819	207.35	23.7	0.563
h2-8	210	3.34	482.58	550.79	0.81	0.565	0.257	0.756	306.60	26.7	0.484
h2-9	210	3.29	466.39	637.00	0.80	0.596	0.413	0.710	507.72	16.2	0.724
h2-11	210	4.39	366.22	296.90	1.07	0.565	0.109	0.715	189.70	13.8	0.175
h2-13	210	5.46	393.86	313.24	1.33	0.550	0.135	0.650	238.00	30.2	0.172
h2-15	210	5.22	366.87	329.15	1.27	0.541	0.133	0.712	199.86	18.6	0.219
h2-17	210	4.33	369.56	329.30	1.05	0.555	0.121	0.705	207.46	19.7	0.180
h2-18	210	4.30	383.28	370.40	1.05	0.559	0.153	0.711	205.03	30.8	0.188
h2-19	210	4.41	369.78	341.01	1.07	0.555	0.132	0.789	132.18	11.2	0.240
h2-20	210	4.97	382.15	269.48	1.21	0.560	0.100	0.767	116.57	13.6	0.164
h2-21	210	4.24	395.42	412.50	1.03	0.600	0.244	0.741	269.49	13.2	0.409
h2-22	210	4.68	379.57	307.51	1.14	0.600	0.158	0.765	161.23	21.2	0.254
h2-23	210	5.22	381.86	271.05	1.27	0.540	0.094	0.735	145.77	7.0	0.162
h2-27	210	3.34	465.71	556.70	0.81	0.610	0.362	0.726	434.71	19.5	0.649
Qty	18										
Minimum		3.19	361.27	269.48	0.78	0.54	0.094	0.650	116.570	7.0	0.162
Maximum		5.46	502.72	637.00	1.33	0.61	0.461	0.819	507.720	30.8	0.803
Average		4.37	405.18	397.61	1.06	0.57	0.198	0.731	245.505	19.5	0.336
Cov (%)		17.32	11.69	31.22	17.32	4.21	56.443	5.278	45.996	36.4	63.713%

Table A3 Parameters obtained in the experiments regarding series with the characteristic size $D=140$ mm (according to Table 4.1)

Label	D (mm)	$\lambda_{\text{exp}}(a_0)$ (10^{-3} mm/N)	Density (12% MC) (kg/m^3)	P_u (N)	ψ	α_u	G_{Ru} (N/mm)	α_c	P_c (N)	l_{Plat} (mm)	G_{Rc} (N/mm)
h3-1	140	7.67	-	189.10	1.19	0.55	0.142	0.585	154.10	31.1	0.153
h3-3	140	6.03	423.44	223.27	0.94	0.52	1.142	0.615	178.11	16.2	0.148
h3-4	140	8.02	368.17	164.93	1.88	0.53	0.099	0.714	93.82	18.4	0.150
h3-5	140	4.40	525.48	274.55	0.68	0.55	0.158	0.725	163.23	8.2	0.257
h3-7	140	7.92	366.29	195.55	1.23	0.54	0.143	0.560	100.99	34.5	0.151
h3-8	140	4.29	-	297.44	0.67	0.55	0.190	0.680	214.06	17.8	0.266
h3-9	140	6.46	397.15	227.12	1.00	0.55	0.160	0.635	169.23	20.4	0.173
h3-11	140	7.64	-	158.54	1.19	0.55	0.098	0.683	107.05	17.4	0.134
h3-13	140	7.98	372.91	155.45	1.24	0.53	0.089	0.595	143.23	16.3	0.114
h3-17	140	7.83	-	193.74	1.22	0.53	0.132	0.595	172.29	21.7	0.159
h3-18	140	6.13	422.03	205.19	0.95	0.55	0.125	0.550	204.02	9.4	0.126
h3-21	140	5.23	436.26	238.59	0.81	0.55	0.143	0.795	102.93	18.1	0.316
h3-23	140	6.10	435.95	243.74	0.95	0.55	0.174	0.751	134.82	19.3	0.336
h3-25	140	8.31	-	173.52	1.29	0.53	0.114	0.604	154.74	20.8	0.147
h3-28	140	5.33	-	269.56	0.83	0.56	0.208	0.685	206.64	15.6	0.323
h3-30	140	7.65	468.07	179.61	1.19	0.53	0.109	0.796	63.30	18.2	0.196
h3-31	140	4.95	489.75	237.75	0.77	0.55	0.138	0.734	138.53	13.1	0.236
h3-32	140	7.18	366.15	186.15	1.11	0.54	0.115	0.704	109.50	8.5	0.162
h3-33	140	7.78	366.96	185.61	1.21	0.53	0.123	0.636	147.15	18.4	0.162
Qty	19										
Minimum		4.29	366.15	155.45	0.67	0.52	0.089	0.550	63.30	8.2	0.114
Maximum		8.31	525.48	297.44	1.88	0.56	1.142	0.796	214.06	34.5	0.336
Average		6.68	418.35	210.50	1.07	0.54	0.189	0.665	145.14	18.1	0.195
Cov (%)		20.05	12.50	19.57	26.27	2.15	12.280	11.337	28.52%	36.2	36.364

Table A4 Parameters obtained in the experiments regarding series with the characteristic size $D=70$ mm (according to Table 4.1)

Label	D (mm)	$\lambda_{\text{exp}}(a_0)$ (10^{-3} mm/N)	Density (12% MC) (kg/m^3)	P_u (N)	ψ	α_u	G_{Ru} (N/mm)	α_c	P_c (N)	l_{Plat} (mm)	G_{Rc} (N/mm)
h4-1	70	7.64	467.34	98.50	0.89	0.55	0.142	0.763	41.85	6.5	0.198
h4-4	70	9.87	393.36	81.85	1.16	0.54	0.125	0.740	38.77	7.3	0.153
h4-5	70	9.14	441.14	93.38	1.07	0.54	0.144	0.685	61.71	4.4	0.218
h4-6	70	5.94	484.78	107.98	0.70	0.56	0.146	0.747	58.13	7.2	0.218
h4-9	70	11.91	371.93	67.35	1.39	0.54	0.099	0.659	51.36	3.9	0.141
h4-10	70	7.82	429.31	89.27	0.92	0.55	0.123	0.638	69.16	6.7	0.145
h4-11	70	9.87	432.70	99.05	1.16	0.54	0.175	0.687	60.76	8.8	0.219
h4-12	70	7.60	407.19	98.08	0.89	0.52	0.122	0.798	31.92	7.0	0.171
h4-13	70	12.62	354.06	72.66	1.48	0.55	0.129	0.744	35.87	8.4	0.176
h4-17	70	9.67	388.41	78.08	1.13	0.56	0.125	0.588	72.58	7.6	0.131
h4-20	70	6.52	498.57	105.48	0.76	0.55	0.143	0.592	94.70	5.1	0.160
h4-24	70	7.33	460.45	104.92	0.86	0.56	0.169	0.613	90.65	7.5	0.193
h4-25	70	9.11	437.86	117.14	1.07	0.54	0.230	0.634	88.99	14.7	0.267
h4-26	70	9.28	378.95	80.30	1.09	0.54	0.112	0.727	43.66	7.0	0.156
h4-28	70	7.50	404.72	101.55	0.88	0.53	0.135	0.640	62.58	4.9	0.171
h4-29	70	6.28	461.94	107.15	0.74	0.56	0.147	0.670	64.74	8.5	0.202
Qty	16										
Minimum		5.94	354.06	67.35	0.70	0.52	0.099	0.588	31.92	3.9	0.131
Maximum		12.62	498.57	117.14	1.48	0.56	0.230	0.798	94.70	14.7	0.267
Average		8.63	425.80	93.92	1.01	0.54	0.141	0.683	60.46	7.2	0.182
Cov (%)		22.11	9.95	15.19	22.11	2.17	21.641	9.395	32.39	34.24	19.942

Table A5 Parameters obtained in the experiments regarding series with the characteristic size $D=35$ mm (according to Table 4.1)

Label	D (mm)	$\lambda_{\text{exp}}(a_0)$ (10^{-3} mm/N)	Density (12% MC) (kg/m^3)	P_u (N)	ψ	α_u	G_{Ru} (N/mm)	α_c	P_c (N)	l_{Plat} (mm)	G_{Rc} (N/mm)
h5-1	35	21.62	358.27	27.39	1.04	0.52	0.102	0.590	24.58	5.9	0.112
h5-2	35	23.63	349.06	33.22	1.13	0.55	0.201	0.574	32.29	6.2	0.201
h5-3	35	22.04	359.80	31.22	1.06	0.53	0.144	0.650	23.75	5.4	0.177
h5-5	35	25.97	387.07	33.16	1.25	0.55	0.209	0.575	31.33	12.8	0.233
h5-6	35	21.41	371.99	31.37	1.03	0.55	0.154	0.566	30.52	7.4	0.168
h5-7	35	26.91	341.03	28.92	1.29	0.54	0.157	0.608	25.60	10.7	0.190
h5-8	35	23.58	370.10	36.60	1.13	0.54	0.224	0.630	30.46	12.3	0.252
h5-12	35	26.49	376.10	28.19	1.27	0.54	0.126	0.582	19.58	8.3	0.160
h5-13	35	17.84	400.56	33.70	0.86	0.55	0.156	0.741	17.54	5.8	0.213
h5-14	35	25.74	354.69	23.84	1.24	0.54	0.100	0.668	17.51	3.5	0.144
h5-16	35	20.86	391.01	30.76	1.00	0.54	0.136	0.754	26.63	2.4	0.213
h5-20	35	21.05	370.04	33.32	1.01	0.54	0.165	0.618	27.86	8.4	0.190
h5-22	35	18.25	384.42	28.34	0.88	0.54	0.101	0.695	17.71	2.2	0.137
h5-23	35	19.84	352.30	27.54	0.95	0.52	0.095	0.657	19.33	7.1	0.126
h5-24	35	16.63	364.01	33.40	0.80	0.53	0.124	0.654	23.63	7.1	0.153
h5-25	35	15.37	394.49	31.16	0.74	0.55	0.112	0.744	16.30	2.7	0.165
h5-27	35	19.53	376.25	30.37	0.94	0.53	0.117	0.633	26.99	8.2	0.147
h5-28	35	18.81	342.72	30.73	0.90	0.52	0.109	0.639	21.62	6.9	0.127
h5-29	35	19.30	376.38	31.66	0.93	0.52	0.120	0.609	24.78	6.3	0.136
Qty	19										
Minimum		15.37	341.03	23.84	0.74	0.52	0.095	0.566	16.30	2.2	0.112
Maximum		26.91	400.56	36.60	1.29	0.55	0.224	0.754	32.29	12.8	0.252
Average		21.31	369.49	30.78	1.02	0.54	0.140	0.641	24.10	6.8	0.171
Cov (%)		15.85	4.70	9.54	15.85	1.95	27.439	9.067	21.21	43.75	22.902

Table A6 Parameters obtained in the experiments regarding series with the characteristic size $D=23.3$ mm (according to Table 4.1)

Label	D (mm)	$\lambda_{\text{exp}}(a_0)$ (10^{-3} mm/N)	Density (12% MC) (kg/m^3)	P_u (N)	ψ	α_u	G_{Ru} (N/mm)	α_c	P_c (N)	l_{Plat} (mm)	G_{Rc} (N/mm)
h6-2	23.33	23.78	348.40	15.99	1.02	0.54	0.096	0.613	13.28	1.5	0.114
h6-3	23.33	26.80	339.56	16.86	1.15	0.54	0.119	0.630	12.58	6.5	0.130
h6-5	23.33	17.20	414.06	18.55	0.74	0.56	0.100	0.653	14.61	3.6	0.137
h6-9	23.33	19.05	421.83	21.58	0.82	0.52	0.123	0.666	15.45	5.1	0.176
h6-10	23.33	27.40	433.98	15.89	1.18	0.52	0.095	0.705	9.31	3.4	0.143
h6-12	23.33	17.89	408.42	20.42	0.77	0.53	0.109	0.624	12.05	5.2	0.141
h6-13	23.33	21.75	396.46	17.61	0.93	0.52	0.091	0.678	7.61	4.0	0.134
h6-15	23.33	24.47	399.98	19.85	1.05	0.54	0.153	0.616	15.40	5.3	0.158
h6-16	23.33	26.03	445.84	18.00	1.12	0.53	0.122	0.736	10.03	2.3	0.193
h6-21	23.33	18.52	435.87	19.38	0.80	0.53	0.102	0.679	14.24	1.4	0.155
h6-23	23.33	23.47	489.18	18.14	1.01	0.54	0.119	0.670	12.73	1.8	0.161
h6-24	23.33	18.91	453.82	19.90	0.81	0.60	0.171	0.657	18.50	3.2	0.209
Qty	12										
Minimum		17.20	339.56	15.89	0.74	0.52	0.091	0.613	7.61	1.4	0.114
Maximum		27.40	489.18	21.58	1.18	0.60	0.171	0.736	18.50	6.5	0.209
Average		22.11	415.62	18.51	0.95	0.54	0.117	0.661	12.98	3.6	0.154
Cov (%)		16.71	10.14	9.60	16.71	3.97	20.734	5.588	23.09	46.62	17.780